International Journal of Photoenergy

Solar Thermal Systems Combined with Thermal Energy Storage

Lead Guest Editor: Yaxuan Xiong
Guest Editors: Binjian Nie, Chuan Li, Qian Xu, Lixin Wang, and Congcong Wang

Solar Thermal Systems Combined with Thermal Energy Storage

International Journal of Photoenergy

Solar Thermal Systems Combined with Thermal Energy Storage

Lead Guest Editor: Yaxuan Xiong
Guest Editors: Binjian Nie, Chuan Li, Qian Xu, Lixin Wang, and Congcong Wang

Chief Editor

Academic Editors

Contents

Hindawi
International Journal of Photoenergy
Volume 2023, Article ID 6838533, 12 pages
https://doi.org/10.1155/2023/6838533

Research Article

Investigation on Fluid Flow Heat Transfer and Frictional Properties of Al_2O_3 Nanofluids Used in Shell and Tube Heat Exchanger

Debabrata Barik,[1] **Sreejesh S. R. Chandran**,[2] **Milon Selvam Dennison**,[3] **T. G. Ansalam Raj**,[4] **and K. E. Reby Roy**[5]

[1]*Department of Mechanical Engineering, Karpagam Academy of Higher Education, Coimbatore 641021, India*
[2]*Department of Mechanical Engineering, Eranad Knowledge City Technical Campus, Manjeri, Malappuram, Kerala 676122, India*
[3]*Department of Mechanical Engineering, Kampala International University, Western Campus, Kampala, Uganda 20000*
[4]*Department of Mechanical Engineering, Valia koonambaikulathamma College of Engineering and Technology, Kollam, Kerala 691574, India*
[5]*Space Technology Laboratory, Department of Mechanical Engineering, TKM College of Engineering, Kollam, Kerala 691005, India*

Correspondence should be addressed to Debabrata Barik; debabrata93@gmail.com
and Milon Selvam Dennison; milon.selvam@kiu.ac.ug

Received 14 April 2022; Revised 14 October 2022; Accepted 11 March 2023; Published 31 March 2023

Academic Editor: Yaxuan Xiong

Nanofluids are generally utilized in providing cooling, lubrication phenomenon, and controlling the thermophysical properties of the working fluid. In this paper, nanoparticles of Al_2O_3 are added to the base fluid, which flows through the counterflow arrangement in a turbulent flow condition. The fluids employed are ethylbenzene and water, which have differing velocities on both the tube and the shell side of the cylinders. A shell tube-type heat exchanger is used to examine flow characteristics, friction loss, and energy transfer as they pertain to the transmission of thermal energy. The findings of the proposed method showed that the efficiency of a heat exchanger could be significantly improved by the number, direction, and spacing of baffles. With the inclusion of nanoparticles of 1% volume, the flow property, friction property, and heat transfer rate can be considerably improved. As a result, the Nusselt number and Peclet numbers have been increased to 261 and 9.14*E*+5. For a mass flow rate of 0.5 kg/sec, the overall heat transfer coefficient has also been increased to a maximum value of 13464. The heat transfer rate of the present investigation with nanoparticle addition is 4.63% higher than the Dittus–Boelter correlation. The friction factor is also decreased by about 17.5% and 11.9% compared to the Gnielinski and Blasius correlation. The value of the friction factor for the present investigation was found to be 0.0376. It is hence revealed that a suitable proportion of nanoparticles along with the base fluids can make remarkable changes in heat transfer and flow behavior of the entire system.

1. Introduction

The world of thermal engineering is centered on the term heat exchanger (HX), which is necessary for several industries that are required for heat reduction economically. Hence, the HX with low operational and management costs was designed with operating cooling fluids that extract the generated heat. The shell-tube style HX is recognized for its easiness in design; in general, it comprises the following parts: shell, tube, baffles, and fluids. The shell forms the outermost portion by enclosing all other parts and is liable for carrying the cooling fluids from entry to exit over the tubes. The tube transmits the boiling fluid generated from the system by the cooling fluid, where there is heat transfer among the fluids. Chandran et al. [1] reported that the baffles are arrayed to alter the flow course of the cooling fluid in the HX. These varieties of HX have higher reliability than the other types as they can be operated at high pressure and

possess a higher surface area to volume ratio and effectiveness that can be easily enhanced by accumulating the tubes. In general, the heat transfer calculation by CFD is a complicated process as it requires a computer with more power and space. Hence, the resolving of models is required.

Numerous sorts of cooling fluids implemented in the HXs involve varieties of water, oils, and other organic compounds. Applications of heat exchangers are vast and require a thorough knowledge to cover each aspect. Among the applications, their primary use is in the process industry, mechanical equipment, and home appliances. Heat exchangers are employed for heating district systems extensively. Air conditioners and refrigerators use heat exchangers to condense or evaporate the fluid. Moreover, it also has applications in milk processing to do pasteurization.

Nanofluids are solid-liquid compound materials comprising solid nanoparticles or nanofibers with proportions usually from 1 to 100 nm dispersed in the fluid medium. This type of fluid is not just a plain liquid-solid combination. In comparison, the utmost critical condition of a nanofluid is an agglomerate-free stable suspension over an extended period without instigating any chemical alterations to its base fluid. This could be accomplished by reducing the density amid solids and liquids or by enhancing the viscosity of fluids, i.e., through the addition of nanometer-sized particles and by inhibiting particles from agglomeration, the settling of particles could be avoided [2]. Extensive research has been carried out on alumina-water and TiO_2–water, and the appropriate nanofluid for this study was chosen as Al_2O_3–water nanofluid.

The influences of those cooling fluids on the performance of the heat exchanger were demonstrated through several pieces of research [3]. When heat flux remains constant, the Nu number of Al_2O_3 and TiO_2 increases with a surge of Re number if the experiment is conducted on horizontal circular tube underflow of turbulent nature. They also conveyed that when there is a 3% volume escalation in concentration, there is nearly a 12% decrease in convective heat transfer coefficient. In HX with two pipes by deploying copper oxide/ethylene and alumina/ethylene glycol, Zamzamian et al. [4] resolved that with an upswing in temperature and volume concentration, the heat transfer increases by 50% underflow of turbulent nature with low nanofluid concentration.

Li and Xuan [5] research on comparing the Darcy Weisbach friction factor and the heat transfer coefficient analytically on the Cu-water nanofluids determined an enhancement in heat transfer rate under laminar/turbulent flow. However, the value of f remains constant with an increase in nanofluids. The correlation stated that with an upsurge in volume concentration, heat transfer rate increases [6] based on their study deploying Al_2O_3 nanofluid under the flow of turbulent nature. Wen and Ding [7] indicated that there is progress in the heat transfer rate with improvement in Re number by consuming alumina nanoparticles. In their experiment, the addition of nanoparticles increases the thermal behavior of the nanofluid system which was unravelled by Choi and Eastman [8]. Bahiraei et al. [9] as well as Anoop et al. [10] established that the larger the particles of nanofluid, the lesser would be the rate of heat transfer and added that the shape and size of the nanoparticle with its temperature upset the performance of heat transfer corresponding to nanofluid.

The research conducted by Qi et al. [11] revealed a coincidence between the base fluid characteristics and a negligible pressure drop. The behavior of heat transfer deploying CuO/ethylene glycol nanofluid under natural convection by Abu-Nada and Chamkha [12] showed the escalation in the factor of friction and dynamic viscosity with the order of alumina nanoparticle dispersion in water. [13] illustrated the sizable improvement in heat transfer and turbulence rate when the nanoparticles were added to the base fluids. Namburu et al. [14] had led the experiment with several nanofluids added to the ethylene glycol water and analyzed that the heat transfer performance numerically concluded that nanofluid had enhanced features than base fluid. There was an increase in Re and Nu numbers when the nanoparticle concentration increased [15]. The study conducted by [16] identified that the transport property depends on the size, shape, and volume fraction of nanoparticles. Heris et al. [17] had numerically analyzed and exhibited substantial variation in the thermo-physical characteristics of base fluid when nanoparticles dispersed to it.

The dimpled helical tube was implemented by Suresh et al. [18] for experimentation on friction deploying CuO-water nanofluid to emulate the base fluid [19]. The influence of nanoparticle characteristics on thermal conductivity is listed. Concentrating on the viscosity and conductivity (thermal) as vital properties, Kumar et al. [20] determined that the nanoparticles improve thermal behavior. Nnanna [21] highlighted that at high temperature, the Nu and Re number increases correspondingly with the heat transfer rate of HX.

After the intensive literature survey, this work deals with the numerical investigation of the forced convective HX and different flow behavior of fluids and nanoparticles (Al_2O_3) with homogeneous and counterflow arrangements under the flow of turbulent nature. The analysis is done for the different flow rates with and without nanofluid having 36% baffle cut arrangements without inclination similar to the investigation carried out by Irshad et al. [22]. The study also establishes a substantial rise in the heat transfer properties when baffled with different spacing. The hot and cold fluid is considered ethylbenzene, and nanofluids have different velocities on both shell and tube optimum combination.

2. Methodology

2.1. Shell Tube Type Heat Exchanger (STHX). Shell being the wall of STHX comprises a tube arrangement which carries the hot fluid, and corresponding cooling fluid flows along the performance of the baffles in the shell side. The size and length of the shell depend primarily on the number of tubes and their arrangement. Here, the geometry modelling was carried out using ANSYS Space Claim, while the analysis was made using the finite volume method as in Computational Fluid Dynamics (CFD) tool.

This study deals with the estimation of fluid flow and friction properties of a cold fluid added with nanoparticles

Table 1: Physical and chemical properties of ethylbenzene.

Property	Information
Molecular weight	106.17
Color	Colorless
Physical state	Liquid
Boiling point	136.19°C
Melting point	-94.975°C
Density	0.8670
Partition coefficients	4.34
Vapor pressure	7 mmHg
Autoignition temperature	432°C
Flash point	15°C

Table 2: Properties of Al_2O_3 nanoparticles.

Properties	Values
Density	3.69 g/cm^3
Flexural strength	330 MPa
Elastic modulus	300 GPa
Shear modulus	124 GPa
Bulk modulus	165 GPa
Poisson's ratio	0.21
Compressive strength	2100 MPa
Thermal conductivity	18 W/(m.K)
Specific heat	880 J/(Kg.K)

of spherical dimensions in a shell and tube type heat exchanger. Here, ethyl-benzene is used as a hot fluid at a temperature of about 340 K, whereas the cold fluid is of two types, i.e., water and water-Al_2O_3 nanofluid fluid (WANF) at a temperature of 300 K. The tube parameters such as diameter, pitch layout, and counts were determined for this HX [3].

The property of ethylbenzene is flammable and explosive, and ethylbenzene can be dangerous. Vapors can travel to a source of ignition and then flashback. Ethylbenzene can spread fire by floating on water. Inflammatory and poisonous gases can be produced during combustion as given in Table 1.

The studies by Irshad et al. [22] show that pitch arrangement, number, orientation, and spacing of baffles, along with their direction, can extraordinarily alter the overall efficacy of the heat exchanger. In this present study, the triangular pitch has been selected for the tube bundles as it offers better results regarding enhanced surface area per unit length, i.e., maximum tube density. These tubes are generally built as bundles that can be easily dismounted from the tube arrangement (TFD-HE13–STHX Design). The properties of Al_2O_3 nanoparticles are given in Table 2.

The specifications of STHX have been taken from the studies of Irshad et al. [22] and are given in Table 3. The properties of base fluid and nanoparticles are given in Table 4.

The parameters of STHX were chosen according to the Tubular Exchanger Manufacturers Association (TEMA) Standards and were designed as in Figures 1(a) and 1(b).

Table 3: Geometric dimension of STHX.

Specification of STHX	Dimension
The inner diameter of the shell	90 mm
Length of the shell	600 mm
The outer diameter of the tube	20 mm
Number of tubes	7
Tube pitch geometry	30 mm, triangular
Baffle cuts	36%
Baffle spacing	86 mm
Baffle thickness	3 mm
Number of baffles	6

Table 4: Properties of base fluid and nanoparticles.

Properties	Base fluid (water)	Nanoparticle (Al_2O_3)
Density	998.2 kg/m^3	3690 kg/m^3
Thermal conductivity	0.608 W/(m.K)	18 W/(m.K)
Dynamic viscosity	0.001002 kg/(m.s)	—
Specific heat capacity	4182 J/(kg.K)	880 J/(kg.K)

The modelled STHX then meshed initially with a relatively coarser mesh, ending in 58645 elements. This mesh comprised mixed elements of both tetrahedral and hexahedral cells with triangular and quadrilateral faces at the boundaries. It was noted from the previous studies that hexahedral cells are usually advised for a fine capturing of the profile. Hence, for this criterion, a fine mesh was made with maximum care at the wall regions and edges, which are all the regions of high temperature and pressure gradients.

The contours of initially made coarse mesh were analyzed with that of the fine mesh. They observed that the latter mesh resolves better over the regions of high pressure and temperature gradient than the former. The contours depicted a refinement in meshing, particularly at the inlet and outlet regions which would help in the better acquisition of heat transfer and pressure drop. A completely grid-independent model was obtained by interpreting the temperature and pressure gradients.

During fine meshing, the aspect ratio of the elements was maintained the same as that of the aspect ratio of coarse mesh as it possesses only a negligible effect on meshing. The resulting meshed model comprised about 2184591 elements and 4473951 nodes. The different sections of the meshed model are shown in Figure 2.

The main objective of this study is to determine the fluid flow and friction properties along with the alterations in overall heat transfer due to the addition of nanoparticles in the carrier fluid.

2.2. Governing Equation of Motion. For a fluid to flow, it should obey the three governing equations of motion: continuity, momentum, and energy [23]. The three equations of motion are expressed as follows:

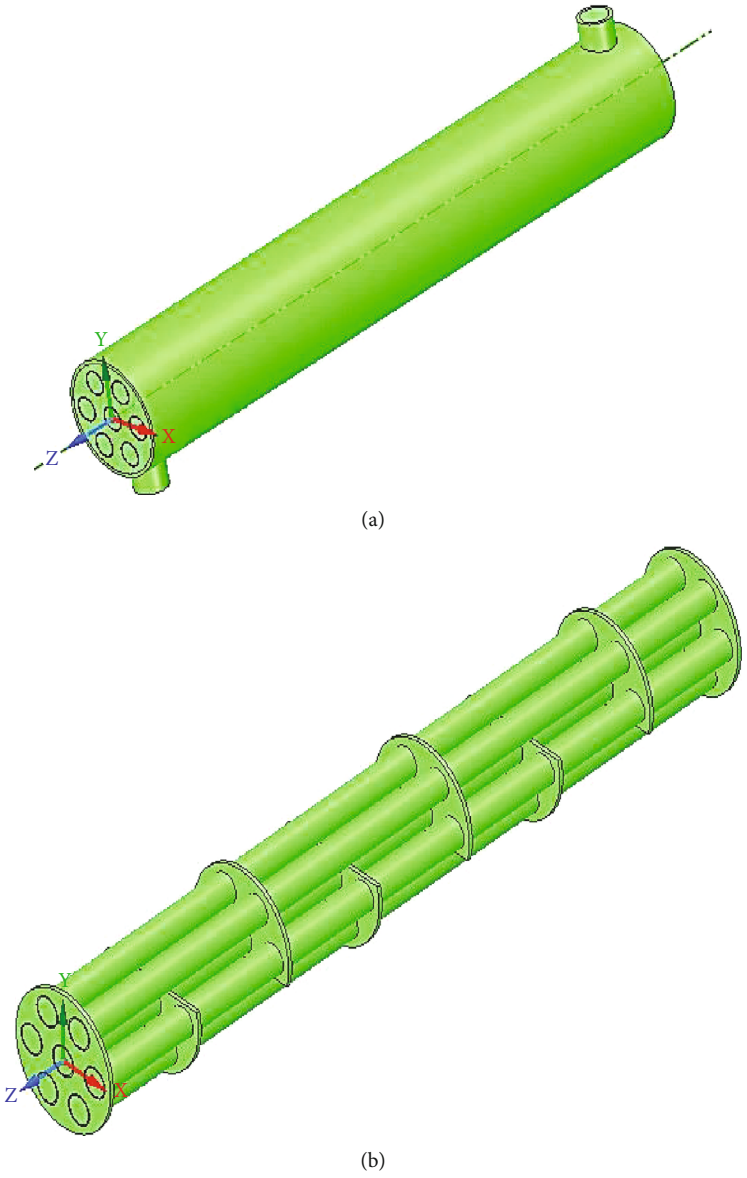

Figure 1: (a) STHX model. (b) Tube bundle arrangement with baffles inside the shell.

Continuity equation:

$$\frac{\partial \rho}{\partial t} + \nabla.(\rho V) = 0. \tag{1}$$

Momentum equation:

$$\rho \frac{DV}{Dt} = \nabla.\tau_{ij} - \nabla_p + \rho F. \tag{2}$$

Energy equation:

$$\rho \frac{De}{Dt} + p\,(\nabla.V) = \frac{\partial Q}{\partial t} - \nabla.q + \varphi, \tag{3}$$

where ρ indicates the density of the fluid, V indicates the velocity of the fluid, τ_{ij} Indicates the viscous stress tensor, p indicates pressure, F indicates body forces in the system, e indicates the internal energy of the fluid, Q indicates heat transfer, t indicates the time, φ indicates dissipation, and $\nabla .q$ indicates heat lost by conduction.

2.3. Data Analysis. The fluid flow properties and the friction properties of nanofluids are determined from the base values of particles used in the heat exchanger. These are determined using the below-mentioned formulae. Anoop et al. [10] provided the density of nanofluid resulting through the mixing of the base fluid, i.e., water and nanoparticles of Al_2O_3 is obtained through in

$$\rho_{nf} = \left[(1-\varphi)\rho_f + \varphi\,\rho_p\right]. \tag{4}$$

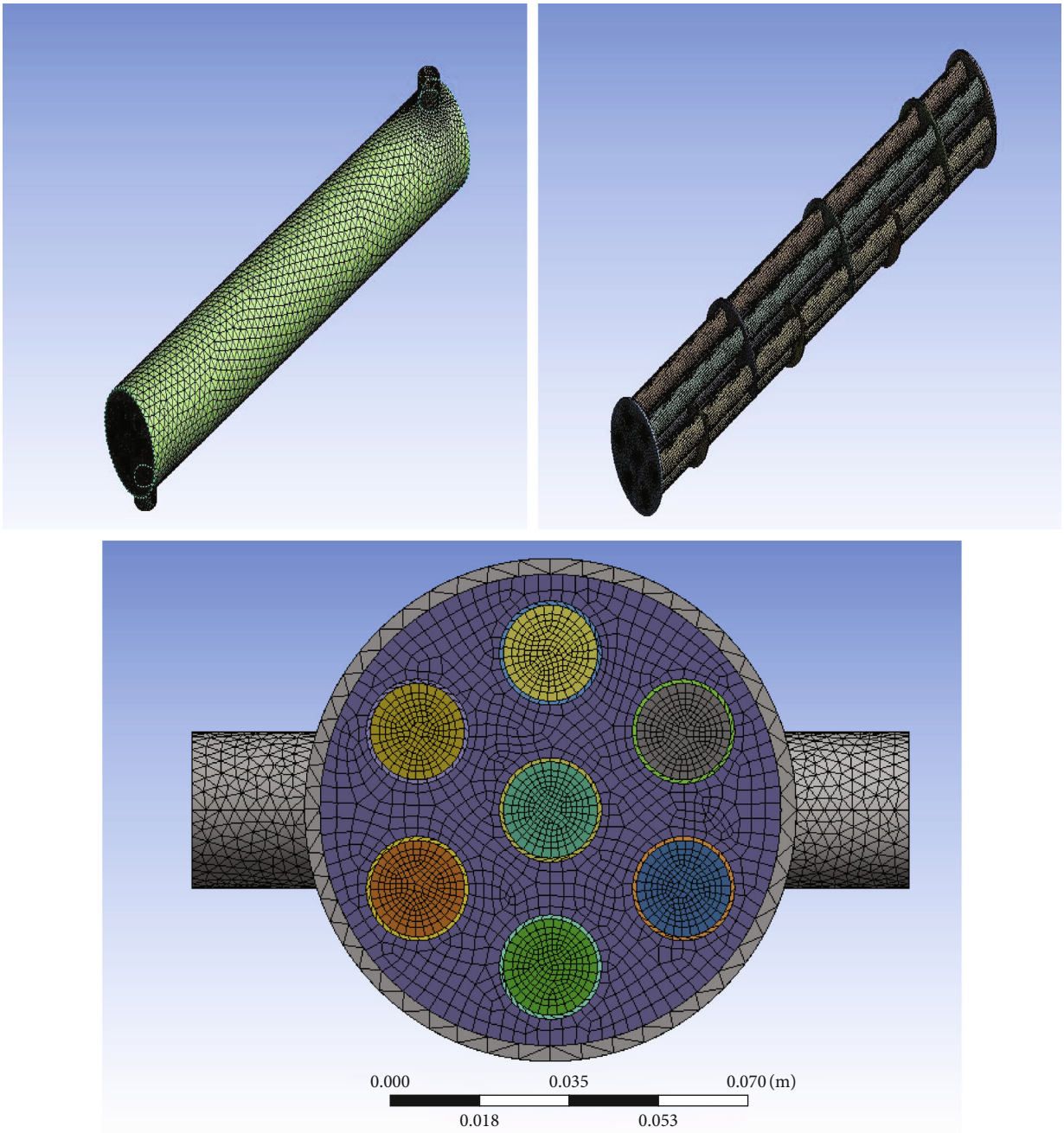

Figure 2: Meshed model.

In the same manner, the specific heat capacity of the nanofluid is given as [10]

$$\left(\rho C_p\right)_{nf} = (1-\varphi)\left(\rho C_p\right)_f + \varphi\left(\rho C_p\right)_p. \tag{5}$$

In Equation (6), the effective thermal conductivity of the resultant nanofluid comprising the solid-liquid mixture can be expressed as [24]

$$K_{nf} = K_f \frac{\left(K + 2K_f - 2\varphi\left(K_f - K\right)\right)}{\left(K + 2K_f + \varphi\left(K_f - K\right)\right)}. \tag{6}$$

Similarly, in Equation (7), the dynamic viscosity of nanofluids with very low volume concentrations of nanoparticles is given by the Einstein model of 1906 [25]:

$$\frac{\mu_{nf}}{\mu_f} = [1 + 2.5\,\varphi], \tag{7}$$

where the subscripts f, p and nf refer to the base fluid, nanoparticles, and nanofluids, respectively. The next parameter that is to be determined is the overall heat transfer rate of the system, which is given as

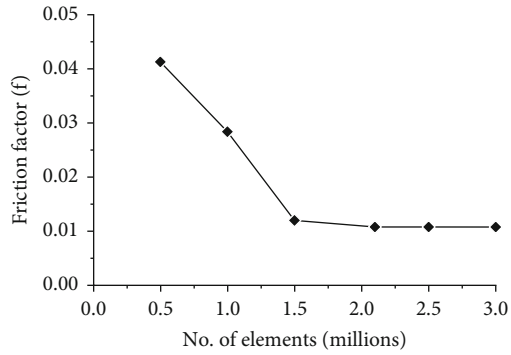

Figure 3: Grid independence study for the turbulent regime.

$$\text{The overall heat transfer rate, } Q = \dot{m} C_{p_{nf}} (T_{\text{out}} - T_{\text{in}}). \quad (8)$$

Here, $\dot{m}$ is the mass flow rate of the nanofluid system, and T_{out} and T_{in} are the outlet and inlet temperatures of the nanofluids. In the case of the friction factor of the system, it is obtained through [26]

$$f_{nf} = 0.961 \ \text{Re}^{-0.375} \varphi^{0.052}. \quad (9)$$

In Equation (9), Re is the Reynolds' number which determines the nature of the flow and is given as [27, 28]

$$\text{Re} = \frac{VD_e}{\vartheta}. \quad (10)$$

The obtained results regarding heat transfer rate and friction factor were then correlated with various models of heat transfer correlations by Dittus–Boelter (Equation (11) and Equation (12)), Gnielinski (Equation (13)), and Blasius (Equation (14)) presented as in the below equations [29, 30].

$$\frac{h_i D_i}{k} = 0.023 \left(\frac{G_i D_i}{\mu}\right)^{0.8} \left(\frac{C_p \mu}{k}\right)^{0.3}, \quad (11)$$

$$Q = h A \Delta T, \quad (12)$$

$$f = (0.79 \ln (\text{Re}) - 1.64)^{-2}, \quad (13)$$

$$f = \frac{0.316}{\text{Re}^{0.25}}. \quad (14)$$

2.4. Grid Independence Test. Grid independence study is considered an important procedure in all CFD analyses. The reason is that the solution which is delivered by the CFD software should be independent of the grid size [1]. This study helps find an optimum point for a suitable, accurate solution for the problem with reduced computational resources. With the help of the obtained optimum mesh, the accuracy of the result would be good enough to get all relevant flow features, its gradient, and so on. Grid-independent study is conducted for the turbulent flow regime for four grid quantities such as 0.5 million, 1 million, 1.5 million, 2 million, 2.5 million, and 3 million.

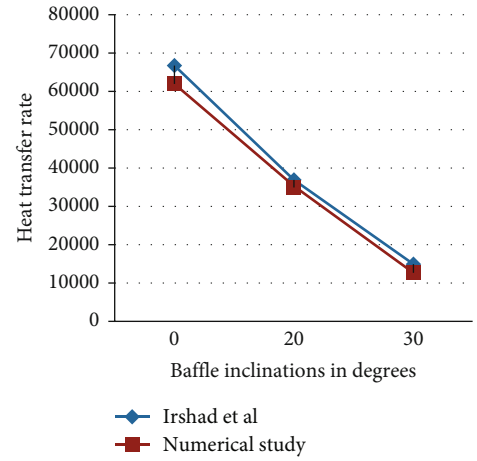

Figure 4: Validation plot of Irshad et al. with numerical study.

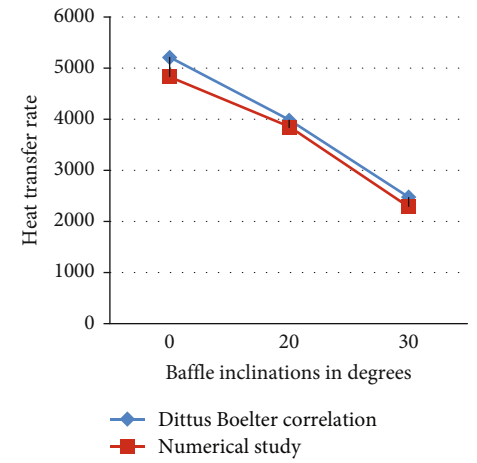

Figure 5: Validation plot of Dittus–Boelter correlation with numerical study.

The friction factor f is taken as one of the parameters to check the grid in dependency. Nusselt number evaluations are employed to discover the fewest number of grids possible without affecting numerical findings, and this procedure is known as the Grid Independence Test. From the study, the 2.1 million grid quantity is selected for further computations since the parameters with the higher mesh density of 60 (width) × 70 (depth) × 600 (length) for the fluid domain do not have appreciable variation as shown in Figure 3. Hence, a comparatively less mesh density is selected for the solid domain.

3. Validation

Figures 4 and 5 show the comparison of the heat transfer rate with baffle inclination plots for Irshad et al. [22], the Dittus–Boelter relation, and the current work. After careful observation, it is revealed that the validated results and the numerical data match pretty well, with maximum variations of 6.9% and 4.63%, respectively.

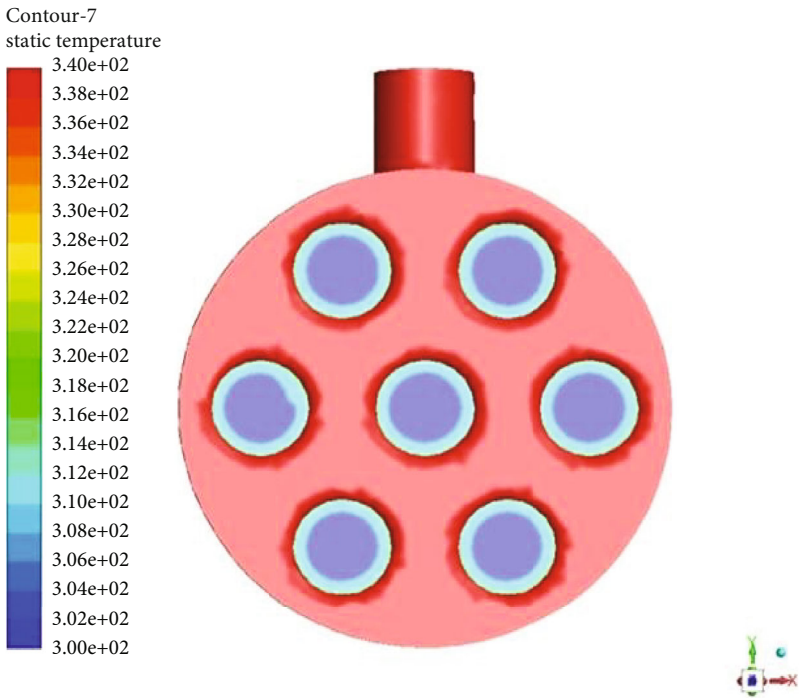

Figure 6: Temperature contour with 1% nanoparticle addition.

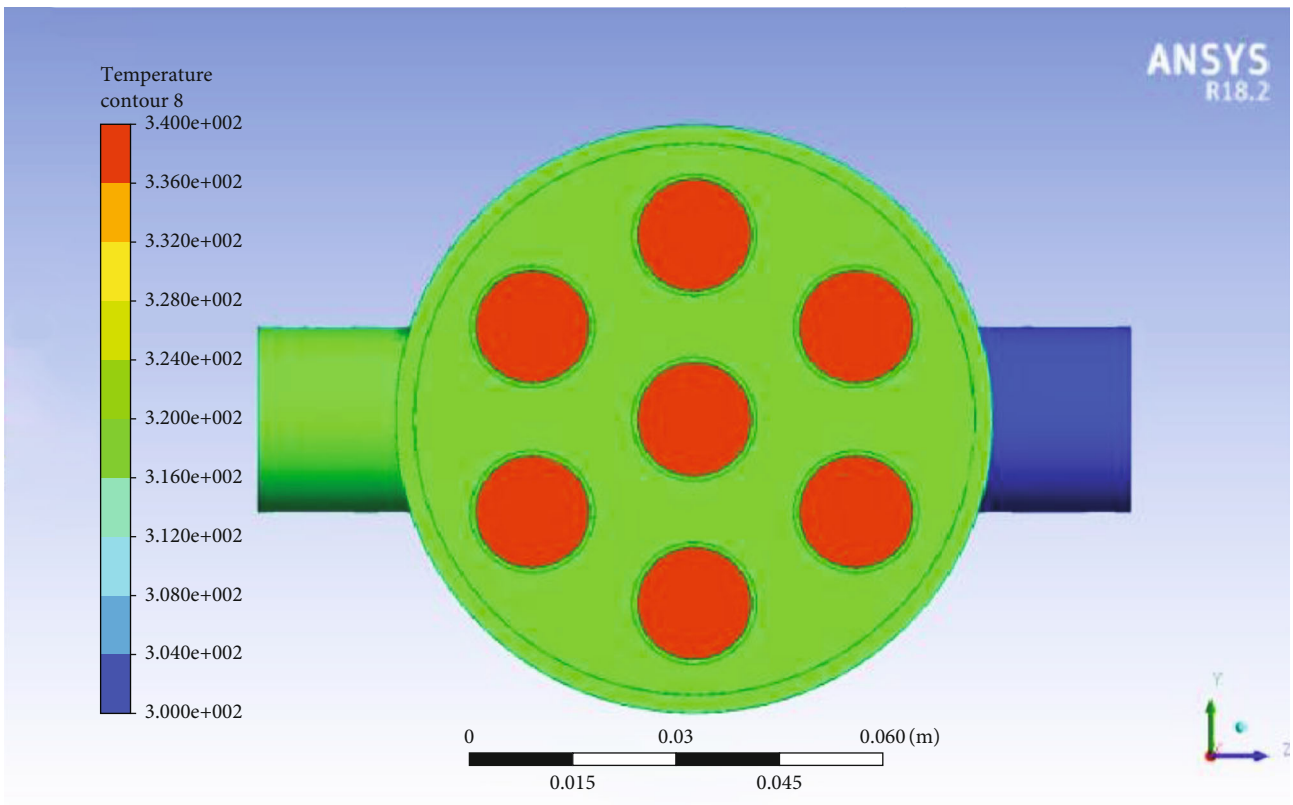

Figure 7: Temperature contour at inlet of the hot fluid.

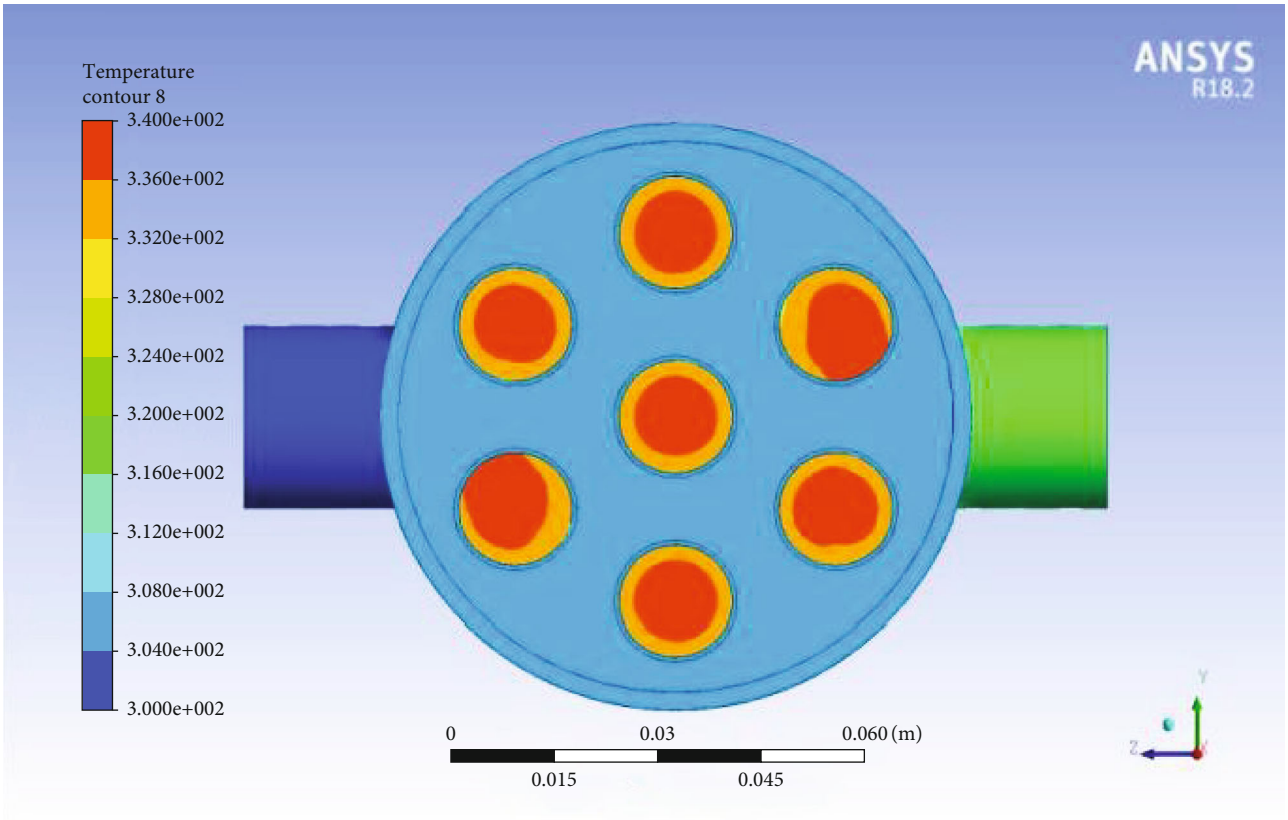

Figure 8: The temperature contour at outlet of cold fluid.

4. Results and Discussions

The present investigation portrays the inclusion of aluminium oxide nanoparticles along with the base fluid water in suitable proportion and the way it enhanced the flow property, friction property, and heat transfer rates is represented in the form of temperature contours, plots, etc.

4.1. Temperature Contour with 1% Nanoparticle Addition. The temperature contour with 1% Al_2O_3 nanoparticle addition is shown in Figure 6. It is clear that the heat gained by the cold fluid is clearly visible from the contour. From the computational domain, it is clear that cold fluid accepts the heat energy at a uniform rate from the hot fluid. Here, turbulence is fair, and heat transfer rate is appreciable.

4.2. Temperature Contour at Inlet and Outlet of Hot Fluid and Cold Fluid. The temperature contour at inlet of the hot fluid is shown in Figure 7. The temperature contour at outlet of cold fluid is shown in Figure 8.

In both inlets and outlets, the contour geometry is good, and heat is transferred perfectly between the boundaries. Even though the flow was a little bit not perfect during initial heat exchange process, it is made up and became uniform during the remaining process.

4.3. Variation of Nusselt Number with Reynolds Number with 1% Alumina. The variation of Nusselt number with Reynolds number with 1% alumina is shown in Figure 9.

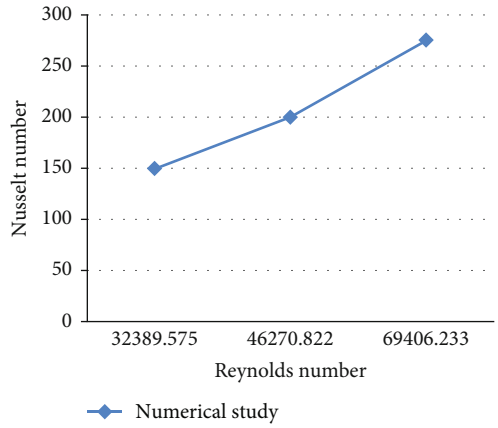

Figure 9: Variation of Nusselt number with Reynolds number with 1% alumina.

Here, the Nusselt number value is increased to 267 because of nanoparticle addition and quite higher without the application of nanoparticle. Nusselt number increases when Reynolds number is increased. Due to greater velocity rate, better heat transfer rates can be achieved. Higher heat transfer rates will lead to a higher Nusselt number.

4.4. Effect of Friction Factor with Reynolds Number for 1% Alumina. The effect of friction factor with Reynolds number for 1% alumina is shown in Figure 10. The effect of friction

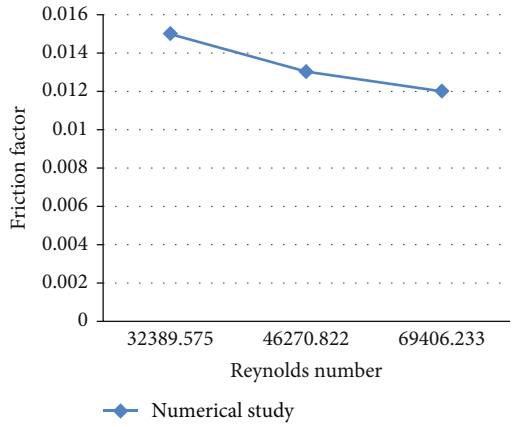

Figure 10: Effect of friction factor with Reynolds number for 1% alumina.

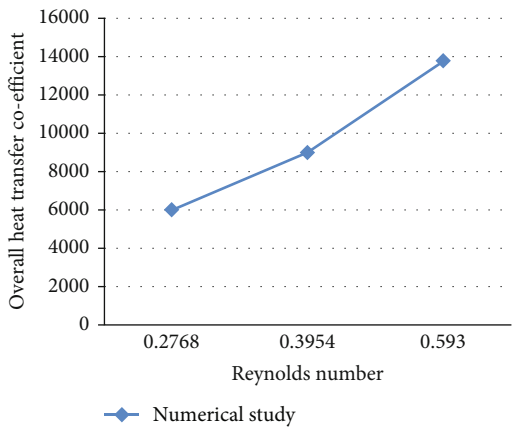

Figure 11: Variation of overall heat transfer coefficient with mass flow rate for 1% alumina.

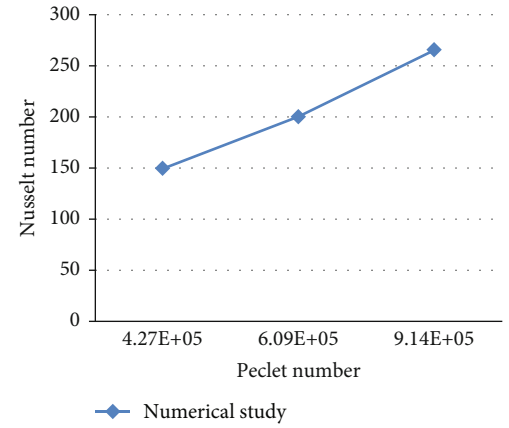

Figure 12: Nusselt number–Peclet number relationship for 1% alumina.

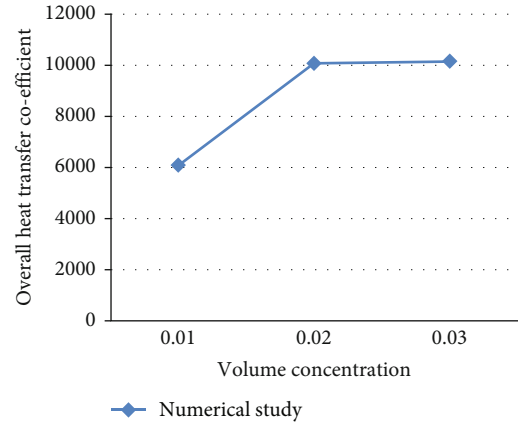

Figure 13: Effect of overall heat transfer coefficient at different concentrations of alumina at 0.7 m/sec velocity.

factor with Reynolds number for 1% alumina is shown in Figure 10. The f value is showing not much variation when Reynolds number is increased, and the value keeps on decreasing also. The above minor change can be neglected.

4.5. Variation of Overall Heat Transfer Coefficient with Mass Flow Rate for 1% Alumina. The variation of overall heat transfer coefficient with mass flow rate for 1% alumina is shown in Figure 11. Here, overall heat transfer coefficient is also found to be at its extreme value when alumina particles are used as nanoparticle. The thermal conductivity of the alumina particles is high. So, this inherent thermal conductivity resulted in a higher U value, and it will result in a higher Nusselt number too. When the mass flow rate is increased to 0.593, the U value will be at the point of 13464 which is quite significant. But the lesser mass flow rates yield a lower U value.

4.6. Nusselt Number–Peclet Number Relationship for 1% Alumina. The effect of Nusselt number with Peclet number for 1% aluminum oxide is shown in Figure 12.

The value of Peclet number and Nusselt number are directly proportional. From the analysis, the Peclet number obtained in all the four flow rates is better. The nanofluid shows greater potential in enhancing the heat transfer process. This is because the suspended ultrafine particles remarkably increase the k value, and Nusselt number is increased. The increase in the value of Peclet number resulted in an increased boundary layer thickness and a slight increase in the friction factor also.

4.7. Effect of Flow Velocity for 1% Alumina. The effect of overall heat transfer coefficient at different concentrations of alumina at 0.7 m/sec velocity is shown in Figure 13.

For a velocity of 0.7 m/sec and at a particle concentration of 1%, a higher overall heat transfer value of 10771 is attained which shows that 1% nanoparticle water combination gave appreciable results.

4.8. Effect of Tube Side Outlet Temperature for 1% Alumina at Different Baffle Inclinations. The effect of tube side outlet temperature for alumina with different baffle inclinations is shown in Figure 14. When baffle inclination increases, tube side outlet temperature also increases. The outlet temperature of the tube outlet is dependent upon the turbulence.

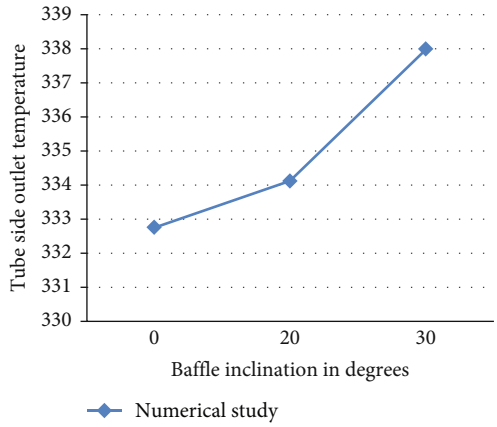

Figure 14: Effect of tube side outlet temperature for alumina with different baffle inclinations.

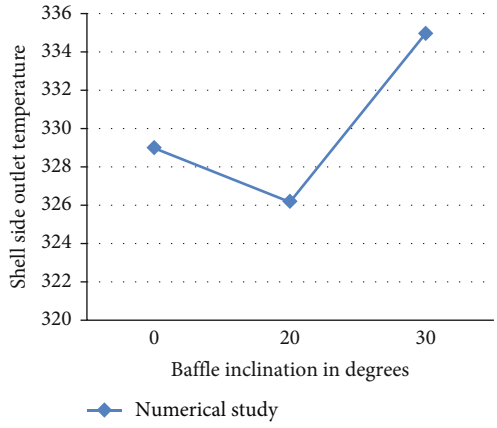

Figure 15: Effect of shell side outlet temperature for alumina with different baffle inclinations.

Tube side temperature reaches a value of 338°C which shows that heat transfer rate is appreciating.

4.9. Effect of Shell Side Outlet Temperature for 1% Alumina at Different Baffle Inclinations. The effect of shell side outlet temperature for alumina with different baffle inclinations is shown in Figure 15.

It is clear from the plot that shell side temperature shows a sudden decrease at 20° baffle inclinations because of lesser aggregation of nanoparticles with the base fluid. The optimum value of shell side temperature is closer to 335 deg. C. The heat transfer characteristics of Alumina-water nanofluid is high at 1% particle concentration.

5. Conclusions

The convective heat transfer performance of alumina-water nanofluid flowing through the shell and tube heat exchanger was investigated numerically, and the effects of nanofluid temperature, concentration and volume flow rates, friction factor, overall heat transfer coefficient, Nusselt number, Peclet number, and shell side and tube side temperatures of nanofluid were investigated. Studies revealed that water along with Al_2O_3 nanoparticles of 1% volume concentration has a better heat transfer rate compared with normal base fluid alone, i.e., only water. All studies have proved that, a substantial increase in the heat transfer rate occurs, followed by an earlier convergence history. It is also understood that addition of nanoparticle positively affects the flow and friction properties of the entire system. The following conclusions have been obtained.

(1) Studies proved that an increase in Reynolds number increases the value of Nusselt number and reaches the peak value of 261 at 1% alumina concentration. The heat exchange rate is very much higher and took reasonable iterations to make the solutions converged. The maximum time taken to complete one iteration is 2 minutes

(2) The quantitative value of the friction factor for the current investigation was observed to be 0.0376 which is not much deviating from the previous investigation which were 17.5% and 11.9% from Gnielinski and Blasius correlations

(3) The thermal conductivity of alumina nanoparticles is very high, and this inherent property enhanced the overall heat transfer coefficient (U) value to 13464 at a mass flow rate of 0.593 kg/sec. When mass flow rate decreases, overall heat transfer coefficient also decreases

(4) The value of Peclet number was seen directly proportional throughout the analysis with Nusselt number because the suspended ultrafine particles remarkably increased the value of thermal conductivity, K, and the Peclet number increases the peak value of $9.14E^{+5}$. The increase in the value of Peclet number resulted in an increased boundary layer thickness and a slight increase in the friction factor also

(5) Studies revealed that when tube side fluid velocity is increased to 0.7 m/sec led to an increase of overall heat transfer to about 10771. It is clear that when tube velocity is increased, U value would tremendously be increased

(6) The optimal values of shell side and tube side outlet temperature are 335 K and 338 K which showed that heat exchange phenomenon is good

(7) It is further concluded that the heat transfer rate can then be enhanced if twisted inserts are accommodated inside the tube side

Nomenclature

Cp: Specific heat at constant pressure, J/(kg.K)
HX: Heat exchanger
K: Thermal conductivity, W/(m.K)
P: Pressure, (N/m^2)
T: Temperature (K)

SBHX: Segmental baffle heat exchanger
STHX: Shell and tube heat exchanger
μ: Dynamic viscosity, Kg/(m.s)
ρ: Density, (kg/m^3)
υ: Kinematic viscosity (m^2/s)
φ: Nanoparticle volume concentration
f: Friction factor
D_e: Equivalent diameter for shell side, (m)
V: Velocity, (m/s).

Data Availability

The data is available in the manuscript.

Disclosure

A preprint of the present work was published [1].

Conflicts of Interest

The authors declare that they have no conflict of interest.

Acknowledgments

The authors sincerely thank the Karpagam Academy of Higher Education (KAHE), India, and Kampala International University, Western Campus, Kampala, Uganda, for providing the necessary facilities to conduct the research.

References

[1] S. S. R. Chandran, D. Barik, T. G. Ansalam Raj, and R. Roy, *Investigation on fluid flow heat transfer and frictional properties of Al_2O_3 nanofluids used in shell and tube heat exchanger*, Research Square, 2020.

[2] V. Sridhara and L. N. Satapathy, "Al_2O_3-based nanofluids: a review," *Nanoscale Research Letters*, vol. 6, no. 1, p. 456, 2011.

[3] B. C. Pak and Y. I. Cho, "Hydrodynamic and heat transfer study of dispersed fluids with submicron metallic oxide particles," *Experimental Heat Transfer an International Journal*, vol. 11, no. 2, pp. 151–170, 1998.

[4] A. Zamzamian, S. N. Oskouie, A. Doosthoseini, A. Joneidi, and M. Pazouki, "Experimental investigation of forced convective heat transfer coefficient in nanofluids of Al_2O_3/EG and CuO/EG in a double pipe and plate heat exchangers under turbulent flow," *Experimental Thermal and Fluid Science*, vol. 35, no. 3, pp. 495–502, 2011.

[5] Q. Li and Y. Xuan, "Convective heat transfer and flow characteristics of Cu-water nanofluid," *Science in China Series E: Technolgical Science*, vol. 49, no. 4, pp. 408–416, 2002.

[6] S. El Bécaye Maïga, C. Tam Nguyen, N. Galanis, G. Roy, T. Maré, and M. Coqueux, "Heat transfer enhancement in turbulent tube flow using Al2O3 nanoparticle suspension," *International Journal of Numerical Methods for Heat & Fluid Flow*, vol. 16, no. 3, pp. 275–292, 2006.

[7] D. Wen and Y. Ding, "Experimental investigation into convective heat transfer of nanofluids at the entrance region under laminar flow conditions," *International Journal of Heat and Mass Transfer*, vol. 47, no. 24, pp. 5181–5188, 2004.

[8] S. U. Choi and J. A. Eastman, *Enhancing thermal conductivity of fluids with nanoparticles*, Argonne National Lab.(ANL), Argonne, IL (United States), 1995.

[9] M. Bahiraei, M. Hangi, and M. Saeedan, "A novel application for energy efficiency improvement using nanofluid in shell and tube heat exchanger equipped with helical baffles," *Energy*, vol. 93, pp. 2229–2240, 2015.

[10] K. B. Anoop, T. Sundararajan, and S. K. Das, "Effect of particle size on the convective heat transfer in nanofluid in the developing region," *International Journal of Heat and Mass Transfer*, vol. 52, no. 9-10, pp. 2189–2195, 2009.

[11] C. Qi, T. Luo, M. Liu, F. Fan, and Y. Yan, "Experimental study on the flow and heat transfer characteristics of nanofluids in double-tube heat exchangers based on thermal efficiency assessment," *Energy Conversion and Management*, vol. 197, article 111877, 2019.

[12] E. Abu-Nada and A. J. Chamkha, "Effect of nanofluid variable properties on natural convection in enclosures filled with a CuO-EG-water nanofluid," *International Journal of Thermal Sciences*, vol. 49, no. 12, pp. 2339–2352, 2010.

[13] J. Buongiorno, "Convective transport in nanofluids," *Journal of Heat Transfer*, vol. 128, no. 3, pp. 240–250, 2006.

[14] P. K. Namburu, D. K. Das, K. M. Tanguturi, and R. S. Vajjha, "Numerical study of turbulent flow and heat transfer characteristics of nanofluids considering variable properties," *International Journal of Thermal Sciences*, vol. 48, no. 2, pp. 290–302, 2009.

[15] A. M. Ardekani, V. Kalantar, and M. M. Heyhat, "Experimental study on heat transfer enhancement of nanofluid flow through helical tubes," *Advanced Powder Technology*, vol. 30, no. 9, pp. 1815–1822, 2019.

[16] K. Subramani, K. Logesh, S. Kolappan, and S. Karthik, "Experimental investigation on heat transfer characteristics of heat exchanger with bubble fin assistance," *International Journal of Ambient Energy*, vol. 41, no. 6, pp. 617–620, 2020.

[17] S. Z. Heris, M. N. Esfahany, and G. Etemad, "Numerical investigation of nanofluid laminar convective heat transfer through a circular tube," *Numerical Heat Transfer, Part A: Applications*, vol. 52, no. 11, pp. 1043–1058, 2007.

[18] S. Suresh, M. Chandrasekar, and S. C. Sekhar, "Experimental studies on heat transfer and friction factor characteristics of CuO/water nanofluid under turbulent flow in a helically dimpled tube," *Experimental Thermal and Fluid Science*, vol. 35, no. 3, pp. 542–549, 2011.

[19] A. R. Khaled and K. Vafai, "Heat transfer enhancement through control of thermal dispersion effects," *International Journal of Heat and Mass Transfer*, vol. 48, no. 11, pp. 2172–2185, 2005.

[20] N. Kumar, S. S. Sonawane, and S. H. Sonawane, "Experimental study of thermal conductivity, heat transfer and friction factor of Al_2O_3 based nanofluid," *International Communications in Heat and Mass Transfer*, vol. 90, pp. 1–10, 2018.

[21] A. G. Nnanna, "Experimental model of temperature-driven nanofluid," *Journal of Heat Transfer*, vol. 129, no. 6, pp. 697–704, 2007.

[22] M. Irshad, M. Kaushar, and G. Rajmohan, "Design and CFD analysis of shell and tube heat exchanger," *International Journal of Engineering Science and Computing*, vol. 7, pp. 6453–6457, 2017.

[23] M. S. Ajithkumar, T. Ganesha, and M. C. Math, "CFD analysis to study the effects of inclined baffles on fluid flow in a shell

and tube heat exchanger," *International Journal of Research in Advent Technology*, vol. 2, no. 7, pp. 164–175, 2014.

[24] Q. Z. Xue, "Model for effective thermal conductivity of nanofluids," *Physics Letters A*, vol. 307, no. 5-6, pp. 313–317, 2003.

[25] K. Bashirnezhad, S. Bazri, M. R. Safaei et al., "Viscosity of nanofluids: a review of recent experimental studies," *International Communications in Heat and Mass Transfer*, vol. 73, pp. 114–123, 2016.

[26] M. H. Barzegar and M. Fallahiyekt, "Increasing the thermal efficiency of double tube heat exchangers by using nano hybrid," *Emerging Science Journal*, vol. 2, no. 1, pp. 1–10, 2018.

[27] B. Farajollahi, S. G. Etemad, and M. Hojjat, "Heat transfer of nanofluids in a shell and tube heat exchanger," *International Journal of Heat and Mass Transfer*, vol. 53, no. 1-3, pp. 12–17, 2010.

[28] J. Koo and C. Kleinstreuer, "Laminar nanofluid flow in microheat-sinks," *International Journal of Heat and Mass Transfer*, vol. 48, no. 13, pp. 2652–2661, 2005.

[29] K. V. Liu, U. S. Choi, and K. E. Kasza, "Measurements of pressure drop and heat transfer in turbulent pipe flows of particulate slurries," NASA STI/Recon Technical Report N, 89, 1988.

[30] M. Arun, D. Barik, K. Sridhar, and G. Vignesh, "Performance analysis of solar water heater using Al_2O_3 nanoparticle with plain-dimple tube design," *Experimental Techniques*, vol. 46, no. 6, pp. 993–1006, 2022.

Hindawi
International Journal of Photoenergy
Volume 2022, Article ID 4053105, 21 pages
https://doi.org/10.1155/2022/4053105

Research Article

Experimental Study on Gas-Solid Heat Transfer Characteristics for the Vertical Waste Heat Recovery Using the Inverse Problem Method

Sizong Zhang,[1] **Zhi Wen**,[1] **Yi Xing**,[1] **Xunliang Liu**,[1] **Hui Zhang**,[1] **and Yaxuan Xiong**[2]

[1]*School of Energy and Environmental Engineering, University of Science and Technology Beijing, Beijing 100083, China*
[2]*Key Laboratory of HVAC, Beijing University of Civil Engineering and Architecture, Beijing 100044, China*

Correspondence should be addressed to Sizong Zhang; zhangsizong@ustb.edu.cn and Yaxuan Xiong; xiongyaxuan@bucea.edu.cn

Received 14 April 2022; Revised 8 September 2022; Accepted 19 September 2022; Published 10 October 2022

Academic Editor: Alberto Álvarez-Gallegos

To establish an accurate model to optimize the vertical cooling process of the sinter, the inverse problem method is used to calculate the gas-solid heat transfer coefficient based on the gas outlet temperature, which is fitted into the correlation. The research indicates that the increase in the gas velocity is beneficial to the enhancement of the gas-solid heat transfer. With the gas velocity u_g increasing from 0.8 m·s^{-1} to 1.6 m·s^{-1}, the heat transfer coefficient h_v increases by about twice. But this effect will weaken with the increase in the particle size. Besides, the reduction of the particle size is conducive to improving the convective heat transfer intensity between the gas and solid. With the particle size decreasing, this enhancement effect is progressively evident. At u_g of 0.8 m·s^{-1}, the increasing extent of h_v is 1142.25 W·m^{-3}·K^{-1} with the particle size decreasing from 20~25 mm to 15~20 mm, while that is 3152.65 W·m^{-3}·K^{-1} with the particle size decreasing from 15~20 mm to 10~15 mm. In addition, the variation of the measured value of the Nusselt number with the Reynolds number has the same trend as predicted values obtained by other works. However, there is a considerable deviation in the value. Among them, the minimum value of the mean relative error is 26.81%. It is proved that the previous empirical correlations are no longer applicable, while the predicted value of this work is in good agreement with the measured value with the mean deviation of only 7.61%. Therefore, the modified correlation can accurately predict the gas-solid heat transfer characteristics in the sinter bed, which lays a foundation for the numerical design and optimization of the new process.

1. Introduction

In 2020, China has formulated the strategy of the "double Carbon." The targets of the Carbon Peak and Carbon Neutrality will be achieved in 2030 and 2060, respectively. It brings the opportunity for the development of the clean energy industry, including the solar and wind energy. Meanwhile, it has brought great challenges to the traditional industry, such as the iron and steel industry. With the formulation of the "double Carbon" strategy, the energy conservation and emission reduction have become the main theme of the development of the iron and steel industry. Although a number of advanced technologies of the energy-saving and emission reduction have been applied [1–4], the energy consumption and pollutant emission in the iron and steel industry still account for the high proportion in the whole industry, especially in the sintering process [5, 6]. Moreover, the waste heat utilization rate of the sintering process is far lower than the international level. Therefore, the waste heat utilization technology of the sinter has become an important focus for the green development of the iron and steel industry.

However, the waste heat recovery rate of the annular cooling process is less than 30% [7], as shown in Figure 1(a). Therefore, the sinter vertical cooling process [7] has been proposed recently based on the coke dry quenching process [8], as shown in Figure 1(b). The vertical process transforms the heat transfer mode from the cross flow to the countercurrent flow by changing the cooler from the horizontal structure to the vertical structure [9].

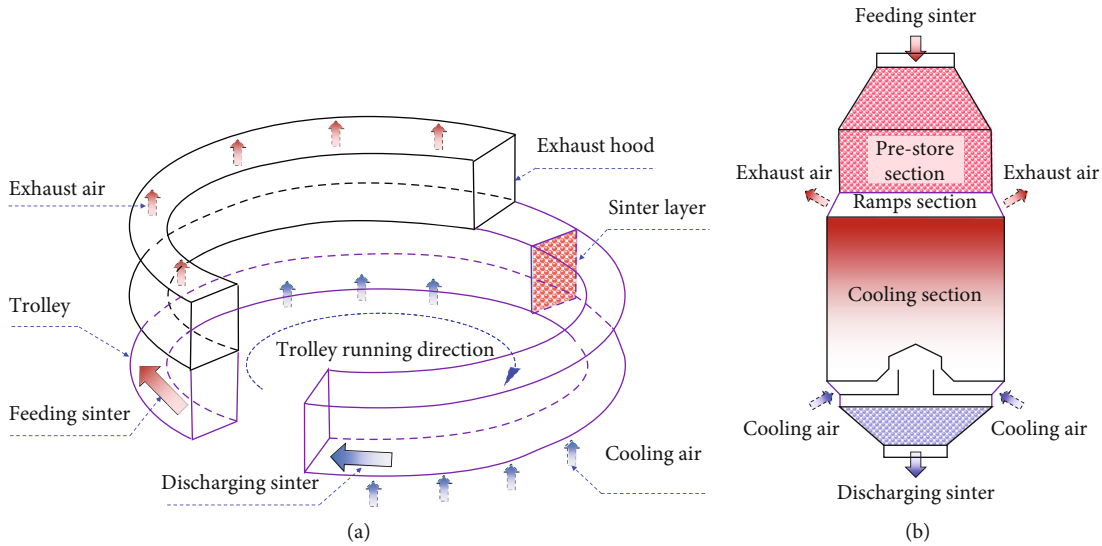

Figure 1: Comparison of two kinds of the sinter waste heat recovery processes: (a) annular cooling process; (b) vertical cooling process.

Moreover, the new process can increase the recovery rate of the waste heat to about 80%, increase the outlet temperature of the exhaust gas from 150~380°C to 500~550°C, and reduce the air leakage rate from 35~50% to nearly zero [7]. Therefore, the application of the new process is one of the important ways to improve the energy-saving and emission reduction of the iron and steel industry.

However, there are few engineering cases of the successful application at present. In addition, the test run indicates that the outlet temperatures of the sinter and exhaust gas are higher and lower than the expected value, respectively [10]. This not only causes the reduction of the sinter treatment capacity but also decreases the recovery rate and quality of the waste heat. It can be attributed to the unreasonable design of the structure and operating parameters, which reduces the heat transfer efficiency in the vertical furnace. The characteristics of the flow resistance and heat transfer are the basis of the design and optimization for the process parameter, which significantly affects the feasibility of the new process [11]. At present, a lot of work has been carried out on the experimental study of resistance characteristics in the sinter bed, and the applicable resistance correlation has been obtained [12–21]. First of all, Liu et al. considered the irregularity of the sinter to modify the resistance correlation [12]. Tian et al. also found that the flow regime in the sinter bed was very easy to be destroyed. Its turbulent degree was higher than the spherical particle, which led to a great increase in the resistance [16]. Besides, Feng et al. corrected the resistance coefficient by using the bed voidage and found that the critical Reynolds number increased as a third-order relationship with the increase of the particle diameter [13]. In addition, it was found that the pressure drop was basically the same along the radial direction except at the wall. Therefore, the wall effect was considered for the correlation correction [14, 15]. What's more, the influence of the wall on the gas flow decreased with the increase of the irregularity of the sinter [17]. In addition, Pan et al. found that the addition of the small-size sinter (0~10 mm) led to the increase of the resistance by 2~3 times [18]. Therefore, Zhang et al. considered the effect of the particle size distribution to correct the resistance correlation [19–21]. It was also found that the resistance in the sinter bed with the narrow particle size distribution is lower than that with the wide particle size distribution.

In addition, many scholars have done a lot of research on gas-solid heat transfer characteristics in the particle bed and obtained the corresponding heat transfer correlations [22–29], as shown in Table 1. First of all, Ranz et al. fitted the heat transfer correlation applicable to the packed bed of the single particle layer [27]. Wakao et al. further considered the influence of the axial fluid heat dispersion to modify the heat transfer correlation of the spherical particles [22]. What's more, Gputa et al. found that the heat transfer factor depended not only on the particle Reynolds number but also on the bed void [23, 24]. To reduce the scattering degree between the experimental data and the fitting value, the bed voidage should be introduced to modify the correlation [24]. However, Singhal et al. thought that previous studies did not consider very dense particle ensembles, i.e., having the bed voidage of less than 0.4 [28]. Previous correlations were more suitable for fluidized beds than packed beds. For large particles, the gas-particle heat transfer in packed beds was typically a much more important limiting factor than in fluidized beds. Therefore, Singhal et al. present a new numerical methodology for deriving heat transfer correlations of very dense particle packed beds [28]. In addition, Will et al. corrected the correlation by considering the thermal radiation and natural convection and expanded the application range of the Reynolds number [29]. It was also found that when the Reynolds number was greater than 2.9×10^5, the heat transfer coefficient suddenly increased. Besides, the studies of Ref. [30–33] indicated that the packing structure of particles had a significant impact on the heat transfer. The comprehensive heat transfer performance of the ordered packing mode is better than that of the disordered packing mode. In the ordered packing mode, the gas

Table 1: Summary of previous correlations in the Nusselt number form for the gas-solid heat transfer in the particle packed bed.

Researcher	Heat transfer correlation	Equation
Wakao et al. [22]	$Nu = 2 + 1.1\mathrm{Re_p}^{0.6}\mathrm{Pr}^{1/3}$	(1)
Thodos et al. [23]	$Nu = (1/\varepsilon)\left(2.876 + 0.3023\mathrm{Re_p}^{0.65}\right)\mathrm{Pr}^{1/3}$	(2)
Gputa et al. [24]	$Nu = (1/\varepsilon)\left(0.0108 + \left(0.929/\mathrm{Re_p}^{0.65} - 0.483\right)\right)\ \mathrm{Re_p}\mathrm{Pr}^{1/3}$	(3)
Ramos et al. [25]	$Nu = 2 + 0.7\mathrm{Re_p}^{0.5}\mathrm{Pr}^{1/3}$	(4)
Handley and Heggs [26]	$Nu = (1/\varepsilon)0.255\mathrm{Re_p}^{2/3}\mathrm{Pr}^{1/3}$	(5)
Ranz [27]	$Nu = 2 + 0.6\mathrm{Re_p}^{0.5}\mathrm{Pr}^{1/3}$	(6)
Singhal et al. [28]	$Nu = 2.67 + 0.53\mathrm{Re_p}^{0.77}\mathrm{Pr}^{0.53}$	(7)
Will et al. [29]	$Nu = 2 + 0.493\mathrm{Re_p}^{1/2} + 0.0011\ \mathrm{Re_p}$	(8)

channel is more uniform, which makes the gas-solid contact more sufficient. Yang et al. [30, 34] and Wu et al. [31] also analyzed the influence of the particle size distribution. They found that the temperature field and flow field in the bed with non-uniform particles were more uneven than that of uniform particles. It resulted in a significant reduction in the comprehensive heat transfer performance. This may be attributed to that the packing structure of non-uniform particles is more disordered than that of uniform particles.

However, the previous research mainly focuses on spherical or regular particles, while there are few studies on the extremely irregular particles such as the sinter. Also, Yang [35, 36] found that the bed of ellipsoidal particles not only had lower gas resistance than the spherical particle bed but also had higher heat transfer performance. In addition, Tavasoli et al. [37] showed that the heat transfer correlation of spherical particles could be applied to spherocylinder particles only by modifying the particle diameter of spherocylinder. The above research indicates that the influence of the particle shape on the heat transfer cannot be ignored, and the previous correlation of regular particles is no longer applicable. Therefore, it is very necessary to study the gas-solid heat transfer characteristics in the irregular sinter bed.

In recent years, scholars have also carried out some related research on the heat transfer characteristics of the sinter. First of all, Zheng et al. [9] obtained the gas-solid heat transfer coefficient of the sinter by the logarithmic mean temperature difference (LMTD) method with using the moving bed. It can be found that the change trend of the heat transfer coefficient with the Reynolds number was consistent with the predicted value of Wakao's correlation [22]. However, there was a large deviation in the value, which was caused by the difference of the particle shape. Due to the limitation of the discharge device, the particle size range in the study was only 5~20 mm, which was far smaller than the typical particle size in the actual engineering production. Besides, Jang and Chiu [38] proposed the heat transfer correlation by combining experiment and numerical methods. But it was aimed at the cross-flow heat exchange mode of the annular cooling process. This was not suitable for the countercurrent heat exchange mode of the vertical cooling process. In addition, Pan et al. [18], Huang et al. [39], and Feng et al. [40] used the fixed bed to study the heat transfer characteristics of the sinter based on LMTD method, and put forward the heat transfer correlation. When calculating the heat transfer coefficient by LMTD method, the arithmetic mean of the inlet and outlet temperatures was regarded as the average temperature of the whole bed. They considered that the temperature in the bed changed linearly with the height, which was inconsistent with the actual situation of the exponential change. Based on the above shortcomings, this paper studies heat transfer characteristics of the sinter with the typical particle size in the actual production by using the fixed bed. The inverse heat transfer problem method [41–43] is adopted to calculate the heat transfer coefficient, which is fitted as the heat transfer correlation suitable for the sinter.

2. Experimental Method and Data Processing

2.1. Experimental Apparatus and Procedure. To measure the temperature during the cooling process of the sinter, a hot test-bed is constructed, as shown in Figure 2. The test-bed consists of five parts, which are the packed bed, air supply system, heating control system, measurement system, and data acquisition system, respectively. Firstly, the inner diameter and height of the packed bed are 209 mm and 900 mm, respectively. Secondly, the air supply system includes the frequency conversion blower and two ball valves. The flow rate and flow direction of the gas can be controlled by adjusting the blower frequency and valve switch, respectively. Thirdly, the heating control system includes the temperature control cabinet, two temperature-controlled thermocouples, and electric heating wire. The sinter is heated to the design temperature by controlling the heating program. Fourthly, the measurement system is composed of the vortex flowmeter and K-type thermocouples, which are used to measure the flow rate of the gas and the temperature of the gas and solid, respectively. Fifthly, the data acquisition system is the Agilent data acquisition instrument, recording the temperature and flow rate of the gas during the cooling process.

The sinter used in the experiment comes from the production site of an iron and steel company. After screening, the heat transfer characteristics of seven kinds of typical particle sizes [16, 20, 21] are studied, as shown in Table 2. The equivalent particle diameter and bed voidage

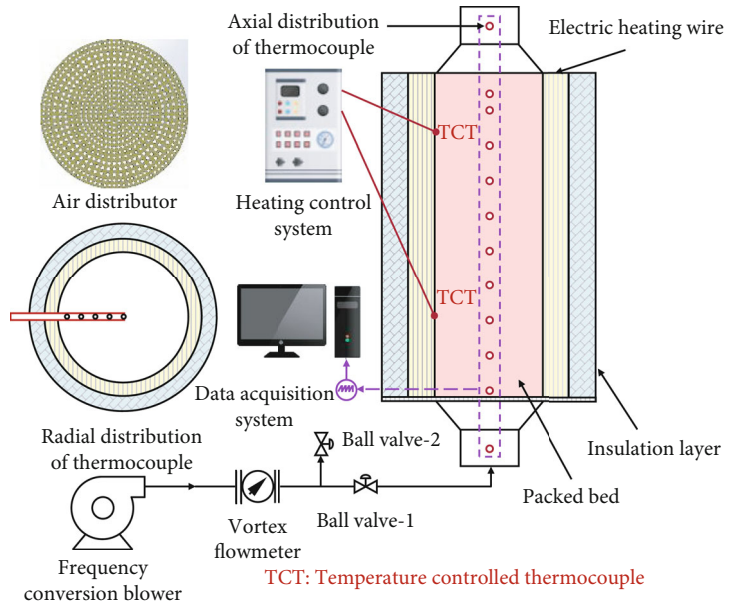

Figure 2: Schematic diagram of the gas-solid heat transfer test-bed for the sinter.

Table 2: Experimental conditions and characteristic parameters for 7 kinds of particle sizes.

Particle size d (mm)	Equivalent particle diameter d_p (mm)	Bed voidage ε	Bed height L (m)	Gas velocity u_g (m·s^{-1})
5~10	5.76	0.5728	0.5673	0.8, 1.0, 1.2, 1.4, 1.6
10~15	11.11	0.5939	0.6162	0.8, 1.0, 1.2, 1.4, 1.6
15~20	14.72	0.6038	0.6434	0.8, 1.0, 1.2, 1.4, 1.6
20~25	19.50	0.6073	0.6576	0.8, 1.0, 1.2, 1.4, 1.6
25~30	23.55	0.6118	0.6748	0.8, 1.0, 1.2, 1.4, 1.6
35~40	30.97	0.6203	0.6945	0.8, 1.0, 1.2, 1.4, 1.6
45~50	38.80	0.6293	0.7149	0.8, 1.0, 1.2, 1.4, 1.6

are characterized by the equal volume method and weighing method, respectively [19, 20]. To provide accurate thermophysical properties for the calculation of the heat transfer coefficient, Figure 3 shows the specific heat and thermal conductivity of the sinter measured by the methods of the scanning calorimetry and laser flash, respectively. Besides, the mass and heating process under different particle sizes are the same to ensure the comparability of the experimental results. First of all, the sinter is heated from the room temperature to 500°C at the heating rate of 10 K·min^{-1}. Secondly, it is kept at 500°C for 3 h. Then, the gas is blown into the bed at the set flow rate to cool the sinter for 1 h. During the cooling process, the gas outlet temperature shall be recorded as the original data for calculating the heat transfer coefficient. Finally, the above process is repeated to measure the gas outlet temperature under different flow rates and particle sizes, so as to analyze the influence of the flow rate and particle size.

2.2. Calculation Method of the Volumetric Heat Transfer Coefficient. The sinter cooling process is essentially the forced convection heat transfer of the gas in the porous medium formed by the accumulation of sinter particles, as shown in Figure 4.

Therefore, this paper adopts the inverse heat transfer problem method in the porous media [41–43] to calculate the heat transfer coefficient. First of all, the forward problem model is established based on the reasonable assumptions:

(1) It is considered that the gas flows only along the axial direction of the bed, ignoring the heat transfer in the circumferential and radial directions. Therefore, the cooling process can be regarded as the one-dimensional unsteady process

(2) The bed formed by the accumulation of sinter particles can be regarded as the homogeneous and isotropic porous medium

(3) The heat transfer between the sinter and air is carried out by the convection, which is in the local non-thermal equilibrium

According to the above assumptions, the following mathematical model can be established [41–43].

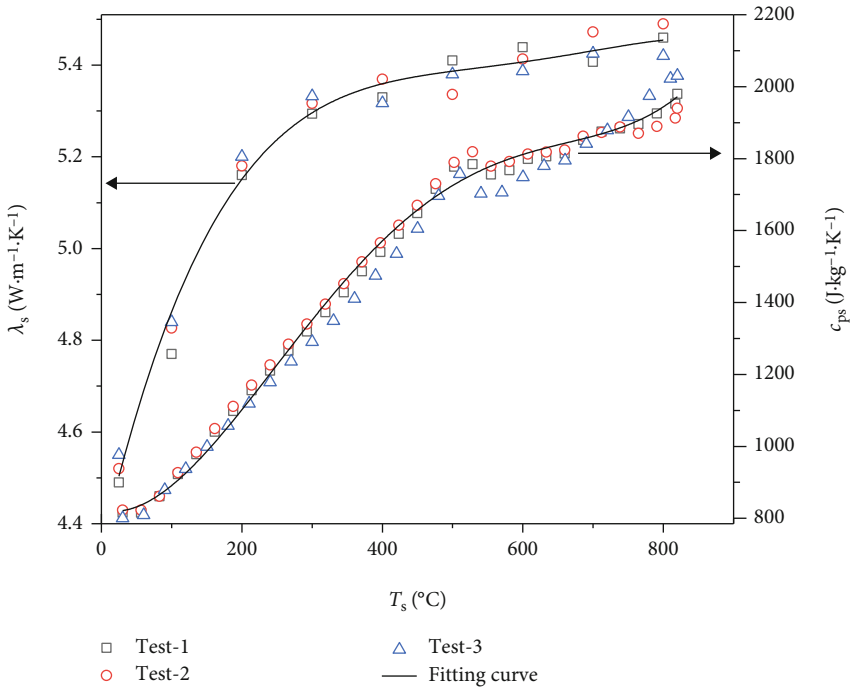

Figure 3: Measured data of the thermal conductivity λ_s and specific heat c_{ps} of the sinter at different temperatures.

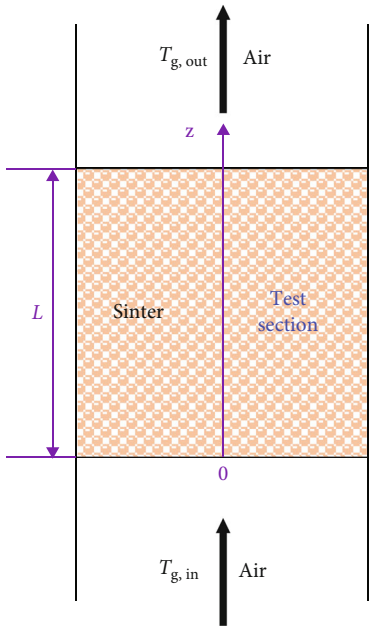

Figure 4: Schematic diagram of the physical model for the sinter cooling process.

(1) Energy equation of the gas:

$$\frac{\partial\left(\varepsilon\rho_g c_{pg} T_g\right)}{\partial t} + \frac{\partial\left(\varepsilon\rho_g v_g c_{pg} T_g\right)}{\partial z} = \varepsilon\frac{\partial}{\partial z}\left(\lambda_g \frac{\partial T_g}{\partial z}\right) + h_v\left(T_s - T_g\right), \quad (1)$$

where ρ_g is the density of the gas, kg·m^{-3}; c_{pg} is the specific heat of the gas, J·kg^{-1}·°C^{-1}; λ_g is the thermal conductivity of the gas, W·m^{-1}·°C^{-1}; T_g is the temperature of the gas, °C; T_s is the temperature of the sinter, °C; h_v is the volumetric heat transfer coefficient, W·m^{-3}· °C^{-1}.

(2) Energy equation of the sinter:

$$\frac{\partial\left((1-\varepsilon)\rho_s c_{ps} T_s\right)}{\partial t} = (1-\varepsilon)\frac{\partial}{\partial z}\left(\lambda_s \frac{\partial T_s}{\partial z}\right) + h_v\left(T_g - T_s\right), \quad (2)$$

where ρ_s is the density of the sinter, kg·m^{-3}; c_{ps} is the specific heat of the sinter, J·kg^{-1}·°C^{-1}; λ_s is the thermal conductivity of the sinter, W·m^{-1}·°C^{-1}.

At the beginning of the cooling process, the temperature of the gas and solid is the same, which is the temperature measured by the thermocouple at the end of the insulation stage. The boundary conditions of energy equations for the gas and solid are as follows:

$$\begin{aligned} T_g(t, z=0) &= T_{g,in}, \\ -(1-\varepsilon)\lambda_s \frac{\partial T_s(t, z=0)}{\partial z} &= h_v\left(T_{g,in} - T_s(t, z=0)\right), \\ \lambda_g \frac{\partial T_g(t, z=L)}{\partial z} &= 0, \\ \lambda_s \frac{\partial T_s(t, z=L)}{\partial z} &= 0, \end{aligned} \quad (3)$$

where $T_{g,in}$ is the inlet temperature of the gas, which is the same as the ambient temperature, °C.

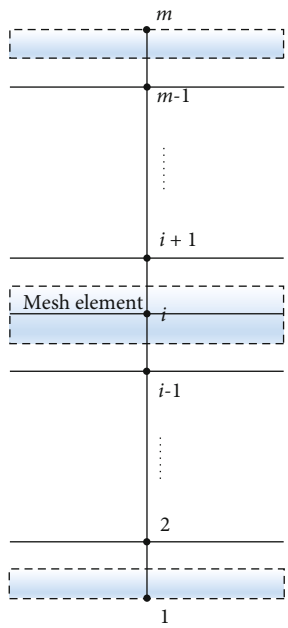

Figure 5: Schematic diagram of the mesh discretization of the physical model.

Next, the method of the numerical solution is introduced. First of all, the physical model is discretized by the outside node method to determine the mesh element, node position, and control volume, as shown in Figure 5.

Besides, the energy equation is discretized by the control volume integration method to obtain the discrete equation. The algebraic equation of each element after discretization is shown in Eqs. (4) and (5).

(1) Discretization equation of the gas:

$$\begin{aligned}&\left[\varepsilon_i\left(\rho_g c_{pg}\right)_i^{j-1}\Delta z+\left(\rho_g v_g\right)_0 c_{pg,i}^{j-1}\Delta t+\varepsilon_i\lambda_{g,i+1}^{j-1}\frac{\Delta t}{\Delta z}+\varepsilon_i\lambda_{g,i-1}^{j-1}\frac{\Delta t}{\Delta z}+h_v\Delta t\Delta z\right]\\&\cdot T_{g,i}^{j}-\left[\varepsilon_i\lambda_{g,i-1}^{j-1}\frac{\Delta t}{\Delta z}+\left(\rho_g v_g\right)_0 c_{pg,i-1}^{j-1}\Delta t\right]T_{g,i-1}^{j}-\varepsilon_i\lambda_{g,i+1}^{j-1}\frac{\Delta t}{\Delta z}T_{g,i+1}^{j}\\&=\varepsilon_i\left(\rho_g c_{pg}\right)_i^{j-1}\Delta z T_{g,i}^{j-1}+h_v\Delta t\Delta z T_{s,i}^{j-1}.\end{aligned}\tag{4}$$

(2) Discretization equation of the solid:

$$\begin{aligned}&\left[(1-\varepsilon_i)\left(\rho_s c_{ps}\right)_i^{j-1}\Delta z+(1-\varepsilon_i)\lambda_{s,i+1}^{j-1}\frac{\Delta t}{\Delta z}+(1-\varepsilon_i)\lambda_{s,i-1}^{j-1}\frac{\Delta t}{\Delta z}+h_v\Delta t\Delta z\right]\\&\cdot T_{s,i}^{j}-(1-\varepsilon_i)\lambda_{s,i-1}^{j-1}\frac{\Delta t}{\Delta z}T_{s,i-1}^{j}-(1-\varepsilon_i)\lambda_{s,i+1}^{j-1}\frac{\Delta t}{\Delta z}T_{s,i+1}^{j}\\&=(1-\varepsilon_i)\left(\rho_s c_{ps}\right)_i^{j-1}\Delta z T_{s,i}^{j-1}+h_v\Delta t\Delta z T_{g,i}^{j-1},\end{aligned}\tag{5}$$

where j and $j-1$ represent this moment and the last moment; $i-1$, i, and $i+1$ represent the last node, this node, and the next node, respectively; Δz and Δt represent the time step and space step, m and s, respectively.

By discretizing the controlling equation of each element, a series of algebraic equations can be obtained to form an algebraic equation system similar to Eq. (6).

$$\begin{cases}b_1x_1+c_1x_2=d_1\\a_2x_1+b_2x_2+c_2x_3=d_2\\\cdots\\a_ix_{i-1}+b_ix_i+c_ix_{i+1}=d_i\\\cdots\\a_{m-1}x_{m-2}+b_{m-1}x_{m-1}+c_{m-1}x_m=d_{m-1}\\a_mx_{m-1}+b_mx_m=d_m\end{cases}.\tag{6}$$

The algebraic equation system is solved by the tridiagonal matrix algorithm (TDMA) based on the Gauss elimination method. Finally, the computer language C# is used to write the calculation program to realize the above algorithm, thereby solving the sinter cooling process.

To obtain the solution independent of the space and time, the temperature field in the bed under different time and space steps is calculated by the numerical model. The change of the gas outlet temperature $T_{g,out}$ with the time is shown in Figure 6. It is found that the change of $T_{g,out}$ is no longer significant when Δz and Δt are less than 0.35 mm and 3 s, respectively. However, the further reduction of the time step and space step would greatly increase the amount of the calculation, while the improvement of the calculation accuracy is limited. Therefore, Δz and Δt are set to 0.35 mm and 3 s in this paper, respectively.

To verify the accuracy of the numerical model, the experimental data in Ref. [39] are compared with the calculated value of this model, as shown in Figure 7. First of all, Figure 7(a) shows that the variation trend of the measured value and calculated value with the time is basically consistent. Besides, Figure 7(b) indicates that the relative error between the measured value and predicted value is less than 5%. Therefore, the numerical model established can well predict the cooling process of the sinter.

Figure 8 shows the whole process of calculating the heat transfer coefficient by using the inverse problem method. Firstly, the value of the convective heat transfer coefficient h_v is assumed. Combined with conditions of the geometric parameters, physical properties, gas inlet temperature, and initial temperatures of the gas and solid, the calculated value of the gas outlet temperature $(T_{g,out})_{cal}$ is solved by the numerical model. Then, the absolute deviation δ is obtained by comparing the calculated value of the gas outlet temperature $(T_{g,out})_{cal}$ with the measured value $(T_{g,out})_{exp}$. If δ is less than 1×10^{-3}, the assumed value is the measured value of the heat transfer coefficient at this moment. Otherwise, the heat transfer coefficient h_v is modified based on the deviation δ between $(T_{g,out})_{cal}$ and $(T_{g,out})_{exp}$ [42]. Using the

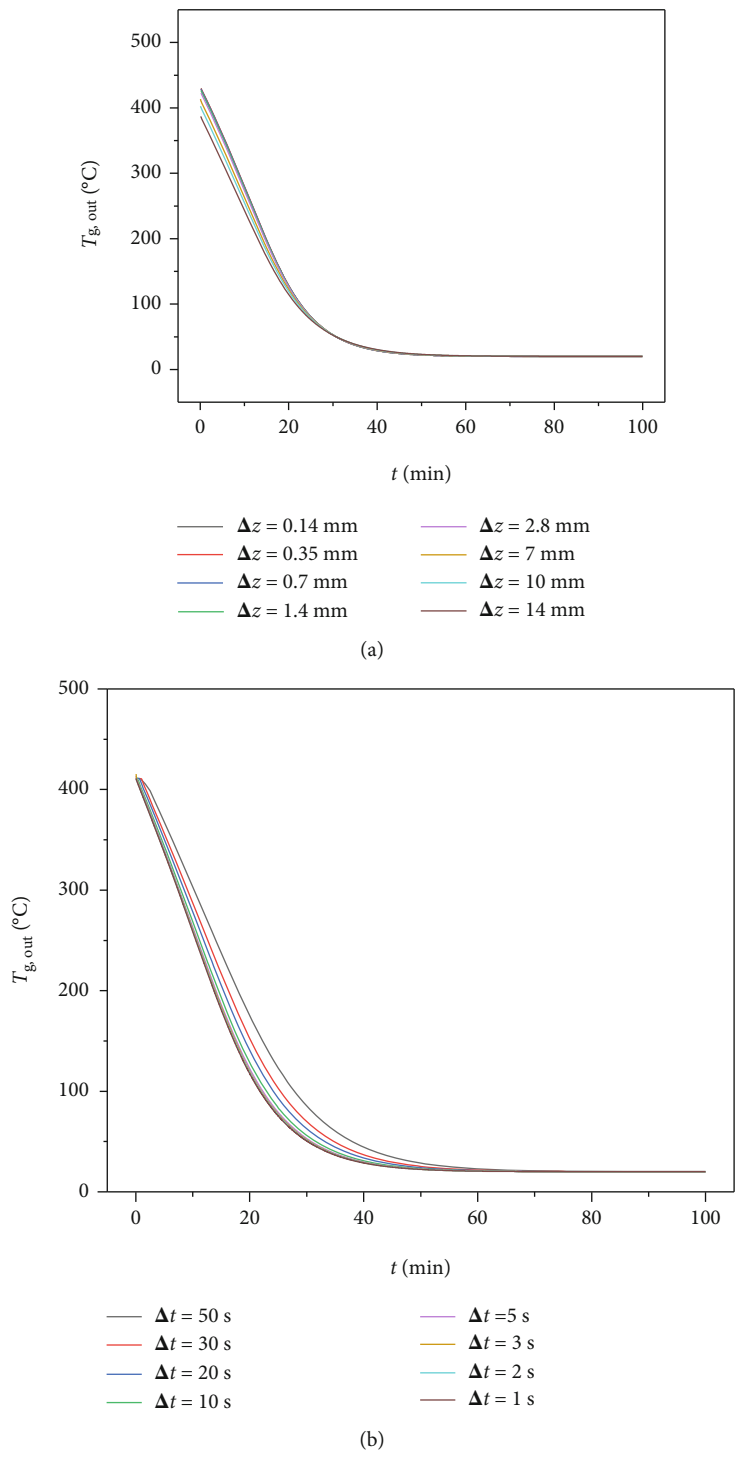

FIGURE 6: The change of the gas outlet temperature $T_{g,out}$ with the time t: (a) different space steps Δz; (b) different time steps Δt.

modified heat transfer coefficient, the energy equation is resolved until δ is less than 1×10^{-3}.

2.3. Analysis of the Uncertainty. Since this paper uses the inverse problem method to calculate the heat transfer coefficient, it is difficult to use the error transfer theory to directly analyze the uncertainty [44]. For the inverse problem method, the uncertainty analysis generally adopts the method of setting the manual error [44]. The error of this experiment mainly comes from the measurement of the temperature, flow rate of the gas, and height of the sinter bed. The measurement accuracy of the thermocouple and flowmeter is class I, and the measurement errors of the temperature and flow rate are 0.4% and 1.0%, respectively.

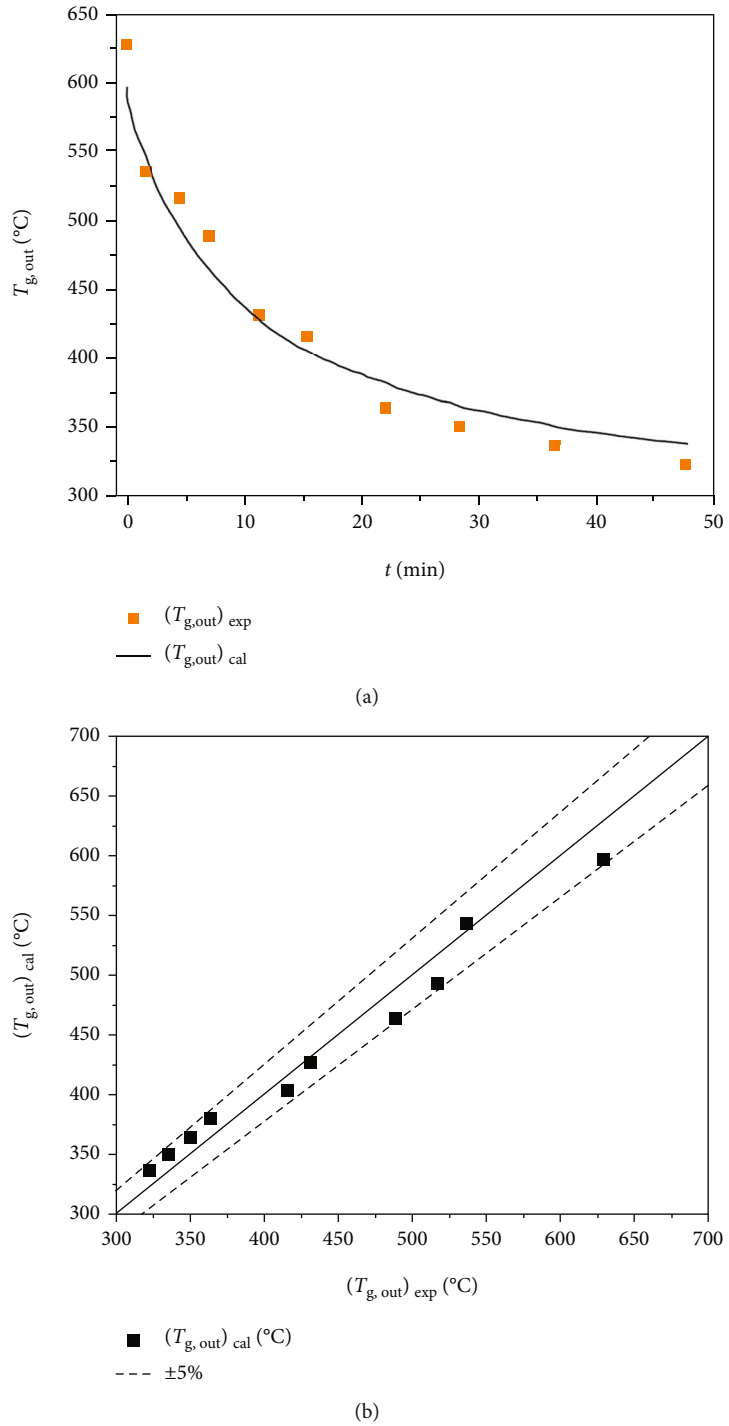

FIGURE 7: Verification of the numerical model: (a) change of the calculated value and measured value of the gas outlet temperature $T_{g,out}$ with time t; (b) comparison between the calculated value $(T_{g,out})_{cal}$ and measured value $(T_{g,out})_{exp}$ of the gas outlet temperature.

The accuracy of the straight rule used to measure the bed height is 1 mm. Since the minimum height of the bed layer of seven kinds of sinters is greater than 500 mm, the maximum error is less than 0.2%. Then, the uncertainty caused by these three parameters on the heat transfer coefficient h_v is analyzed by the method of setting manual error.

First of all, the heat transfer coefficient h_v of three different particle sizes under the gas velocity of 0.8 $m \cdot s^{-1}$ is set, as shown in Figure 9. Based on the heat transfer coefficient, the outlet temperature of the gas is calculated by the numerical model, as shown in Figure 10. Besides, the standard deviation corresponding to the relative error is used to generate the random number of the normal distribution as the

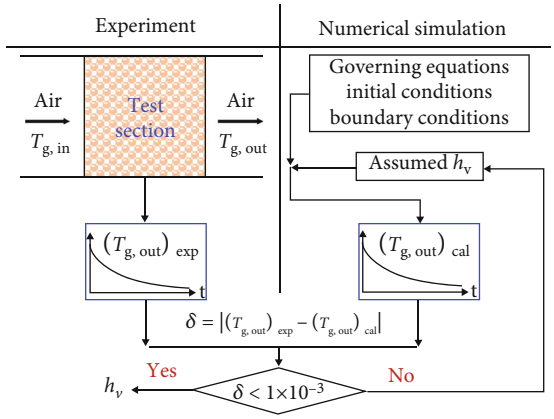

FIGURE 8: The whole process of calculating the heat transfer coefficient by the inverse problem method.

manual error [44]. Then, the error is added to the exact value as the input parameter of the inverse problem to recalculate the heat transfer coefficient. Finally, the influence of the measurement error is estimated by comparing the recalculated heat transfer coefficient with the set value.

The following is a brief description of the temperature measurement error as an example. The gas outlet temperature with the error can be obtained by Eq. (7):

$$\left(T_{g,out}\right)_{err} = \left(T_{g,out}\right)_{exact} + \xi_{T_{g,out}}, \tag{7}$$

where $(T_{g,out})_{exact}$ is the outlet temperature of the gas without the error, ˚C; $(T_{g,out})_{err}$ is the outlet temperature of the gas with the error, ˚C; ξ_{T_g} is the normally distributed random number. The standard deviation σ of the normal distribution function is 0.08, corresponding to the temperature measurement error of 0.4% [44]. Figure 11(a) compares the heat transfer coefficient based on $(T_{g,out})_{exact}$ and $(T_{g,out})_{err}$. It is found that calculation errors of the heat transfer coefficient with the particle size of 5~10 mm, 25~30 mm, and 45~50 mm are 11.75%, 5.13%, and 3.67%, respectively. In addition, the measurement errors of the gas flow rate and bed height are estimated by the same method, as shown in Figures 11(b) and 11(c), respectively. The errors caused by the flow rate on the heat transfer coefficient for the sinters of 5~10 mm, 25~30 mm, and 45~50 mm are 6.11%, 3.96%, and 2.32%, respectively. The errors caused by the bed height for the sinters of 5~10 mm, 25~30 mm, and 45~50 mm are 0.89%, 0.38%, and 0.31%, respectively. The comparison indicates that the temperature measurement has the greatest impact on the heat transfer coefficient, followed by the flow rate of the gas. The influence of the bed height can be almost ignored.

3. Experimental Results and Discussions

3.1. Effect of the Gas Velocity on Gas-Solid Heat Transfer Characteristics. Figure 12 illustrates the change of the gas outlet temperature $T_{g,out}$ and its change rate $dT_{g,out}$ with the cooling time t in the sinter bed of the 5~10 mm under different gas velocities u_g. Since the gas outlet temperature is repeatedly measured three times under each condition, the curve in Figure 12(a) is the average value of the three results. Since the number of experiments is small, the error bar should be calculated by using the t-distribution. The significance level selected in this paper is 0.05, that is, the confidence probability is 95%. Firstly, the t-distribution table shows that $t_{0.05/2}(2)$ is 4.3027. Besides, the standard error $S_{\bar{x}}$ is calculated as follows:

$$S_{\bar{x}} = \sqrt{\frac{\sum_{i=1}^{3}(x_i - \bar{x})^2}{3\times(3-1)}}, \tag{8}$$

where x_i represents the gas outlet temperature measured by each time; $\bar{x}$ represents the mean value of the three results. Therefore, the error bar is $t_{0.05/2}S_{\bar{x}}$, as shown in Figure 12(a).

Firstly, the curve of $T_{g,out}$ moves to the left side of the time axis with the increase of u_g. This indicates that the time required for the cooling process decreases with the increase in u_g. The completion time for the cooling process decreases from about 39 min to 22 min with u_g increasing from 0.8 m·s^{-1} to 1.6 m·s^{-1}, which is shortened by 43.59%. Besides, both the steep degree of the $dT_{g,out}$ curve and the peak value of $dT_{g,out}$ increase with the increase of u_g. The peak value of $dT_{g,out}$ increases from 29.16˚C·min^{-1} to 55.28˚C ·min^{-1} with u_g increasing from 0.8 m·s^{-1} to 1.6 m·s^{-1}, which increases by about 1 time. The above result shows that the increase of u_g is conducive to improve the heat transfer between the gas and solid.

For the cooling process of the sinter, the heat transfer mode between the gas and solid is mainly the convective heat transfer. The viscous force caused by the viscosity occupies an absolute advantage at the wall. This results in the existence of the laminar flow boundary layer on the particle surface, also known as the heat transfer boundary layer. The heat transfer in this area mainly depends on the heat conduction. Due to the small thermal conductivity of the gas, the temperature difference in the laminar flow area is large. Therefore, the heat transfer resistance mainly concentrated in the boundary layer. But the heat transfer in the turbulent region outside the boundary layer mainly depends on the mixing effect caused by the velocity fluctuation. As a result of the violent mixing of fluid particles, there is basically no temperature difference in the turbulent area, which can be considered no heat transfer resistance. Therefore, the thermal resistance of the convective heat transfer mainly depends on the boundary layer. The thicker the boundary layer, the greater the thermal resistance and the weaker the convective heat transfer. The increase of the gas velocity increases the degree of the gas turbulence, which thins the boundary layer and reduces the heat transfer resistance [11]. Consequently, the intensity of the gas-solid convective heat transfer is improved.

Figure 13 shows the change of the mean value $(dT_{g,out})_{mean}$ and peak value $(dT_{g,out})_{peak}$ of the change rate

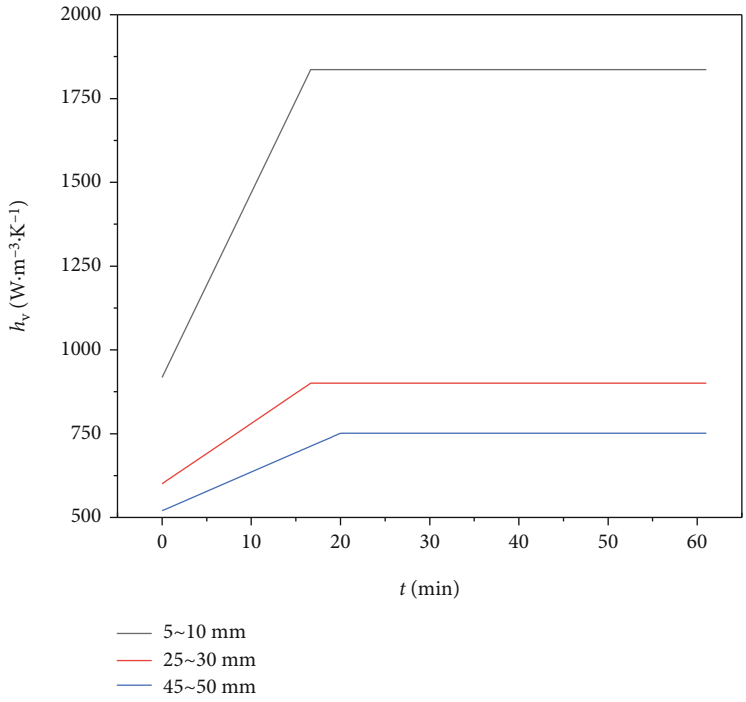

FIGURE 9: Volumetric heat transfer coefficients h_v set for three different kinds of sinters.

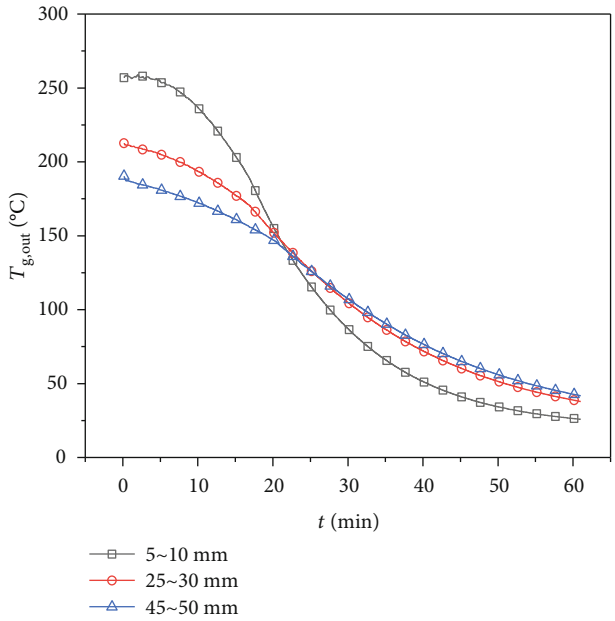

FIGURE 10: Gas outlet temperatures $T_{g,out}$ of three kinds of sinters based on the set heat transfer coefficient.

of the gas outlet temperature with the gas velocity u_g under different kinds of sinters. It is found that the steep degree of the fitting curve reduces with the increase in the particle size. When the particle size increases from 5~10 mm to 45~50 mm, the slopes of the $(dT_{g,out})_{mean}$ curve and $(dT_{g,out})_{peak}$ curve decrease by 55.61% and 70.36%, respectively. This indicates that the increase in the particle size will weaken the effect of the gas velocity on the gas-solid heat transfer. This is attributed to the increase of the heat conduction resistance within the particle [45].

Figure 14 illustrates the variation of the volumetric heat transfer coefficient h_v with the cooling time t in the sinter bed of the 5~10 mm at different gas velocities u_g. Firstly, it is observed that h_v increases with the increase of u_g. At the cooling time of 40 min, h_v increases from 16288 W·m^{-3}·K^{-1}

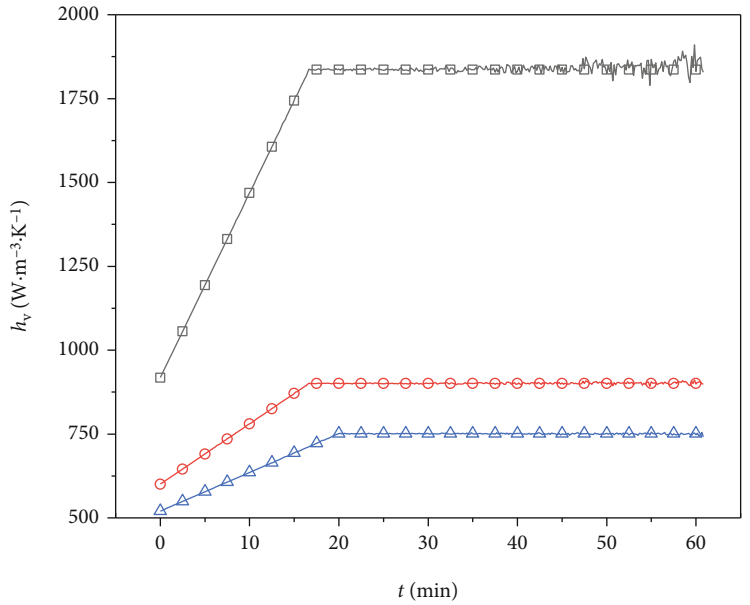

(a)

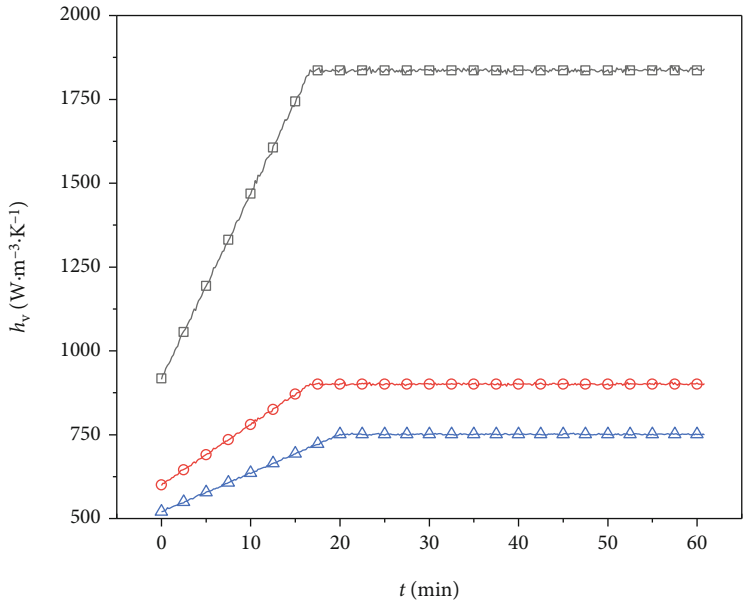

(b)

Figure 11: Continued.

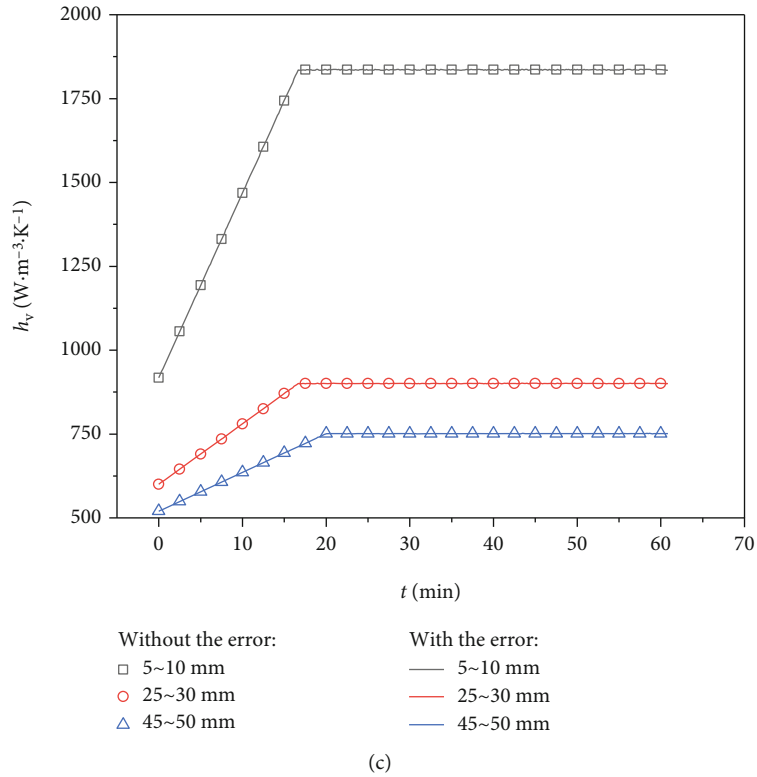

(c)

FIGURE 11: Influence of the measurement error on the heat transfer coefficient h_v: (a) error of the temperature; (b) error of the gas flow rate; (c) error of the bed height.

to 49599 W·m^{-3}·K^{-1} with u_g increasing from 0.8 m·s^{-1} to 1.6 m·s^{-1}, which increases by about twice. Since the turbulent degree of the gas increases with the increase in u_g, the thickness of the boundary layer decreases. This would decrease the thermal resistance. Besides, h_v is smaller in the initial stage of the cooling process but increases gradually with the cooling continuing. Since the gas temperature in the bed is high at the initial stage, the viscosity coefficient is large, which is about 1.8 times that of the room temperature. Therefore, the viscous resistance of the gas on the particle surface increases, which increases the thickness of the boundary layer and heat transfer resistance. As the cooling process continues, the gas temperature decreases. At this time, the viscosity coefficient of the gas decreases, thereby reducing the thickness of the boundary layer. Therefore, the heat transfer resistance decreases, improving the convective heat transfer coefficient. In addition, the greater the gas velocity u_g, the faster the heat transfer coefficient h_v increases in the initial stage. The time of the initial stage at u_g of 0.8 m·s^{-1} and 1.6 m·s^{-1} is about 25 min and 8 min, respectively, which is shortened by 68%. As shown in Figure 12, the decreasing rate of the gas temperature with the cooling time increases with the increase in u_g. This would increase the decreasing range of the viscosity coefficient. Therefore, the faster the gas temperature in the bed decreases with the increase in u_g, the greater the decrease of the viscosity coefficient. Therefore, the decreasing extent of the thickness of the boundary layer increases with the increase in u_g, which makes the increase of the heat transfer coefficient faster in the initial stage.

3.2. Effect of the Equivalent Particle Diameter on Gas-Solid Heat Transfer Characteristics. According to the experimental data under the gas velocity u_g of 0.8 m·s^{-1}, the change curves of the gas outlet temperature $T_{g,out}$ and its change rate $dT_{g,out}$ for sinters with different particle sizes are plotted in Figure 15. Firstly, the smaller the particle size, the higher the gas outlet temperature in the initial stage. At the cooling time of 1 min, $T_{g,out}$ with the particle size of 45~50 mm and 5~10 mm are 305.91°C and 453.54°C with an increase of 147.63°C, respectively. Besides, the steepness of the $dT_{g,out}$ curve increases with the reduction of the particle size, indicating that the time required for cooling is shortened. The cooling time with the particle size of 15~20 mm and 5~10 mm is about 51.5 min and 39.0 min with the reduction of 12.5 min, respectively. In addition, the peak value $(dT_{g,out})_{peak}$ of the $dT_{g,out}$ increases with the particle size decreasing. $(dT_{g,out})_{peak}$ increases from 8.27°C min^{-1} to 29.25°C min^{-1} with the particle size decreasing from 45~50 mm to 5~10 mm, which increases by about 2.5 times. The above results show that the reduction of the particle size is beneficial to improve the intensity of the gas-solid convective heat transfer. This is attributed to the following two main reasons [9, 40, 45]. Firstly, the bed voidage reduces with the decrease in the particle size. It makes the real

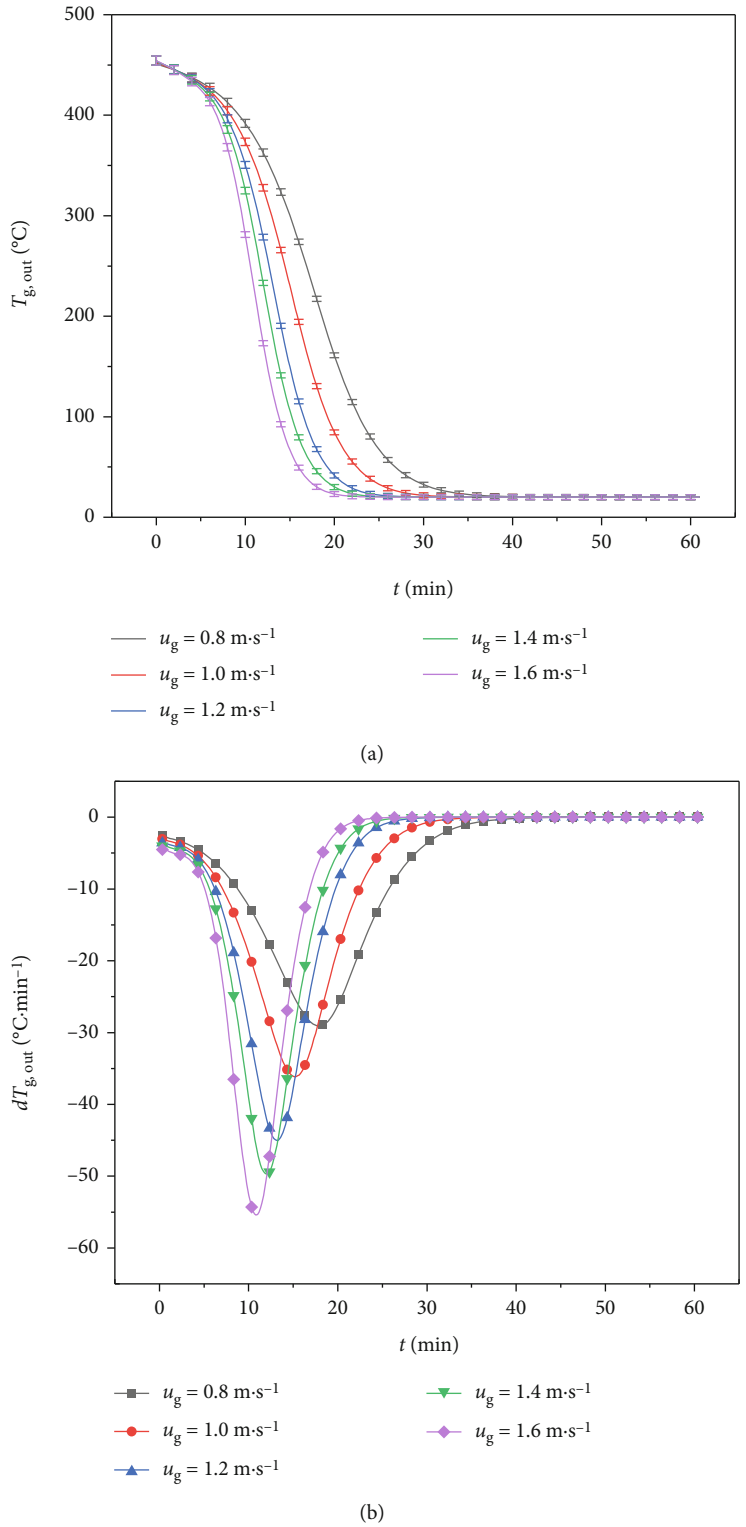

FIGURE 12: Variations of the gas outlet temperature $T_{g,out}$ and its change rate $dT_{g,out}$ with the cooling time t in the sinter bed of the 5~10 mm under different gas velocities u_g.

velocity of the gas in the bed increase under the same flow rate of the gas. Therefore, the boundary layer of the heat transfer will become thin with the increase in the gas turbulence. This makes the thermal resistance decrease. Secondly, the specific surface area of particles increases with the particle size decreasing. It makes the gas-solid contact more sufficient, resulting in an increase in the total heat exchange area.

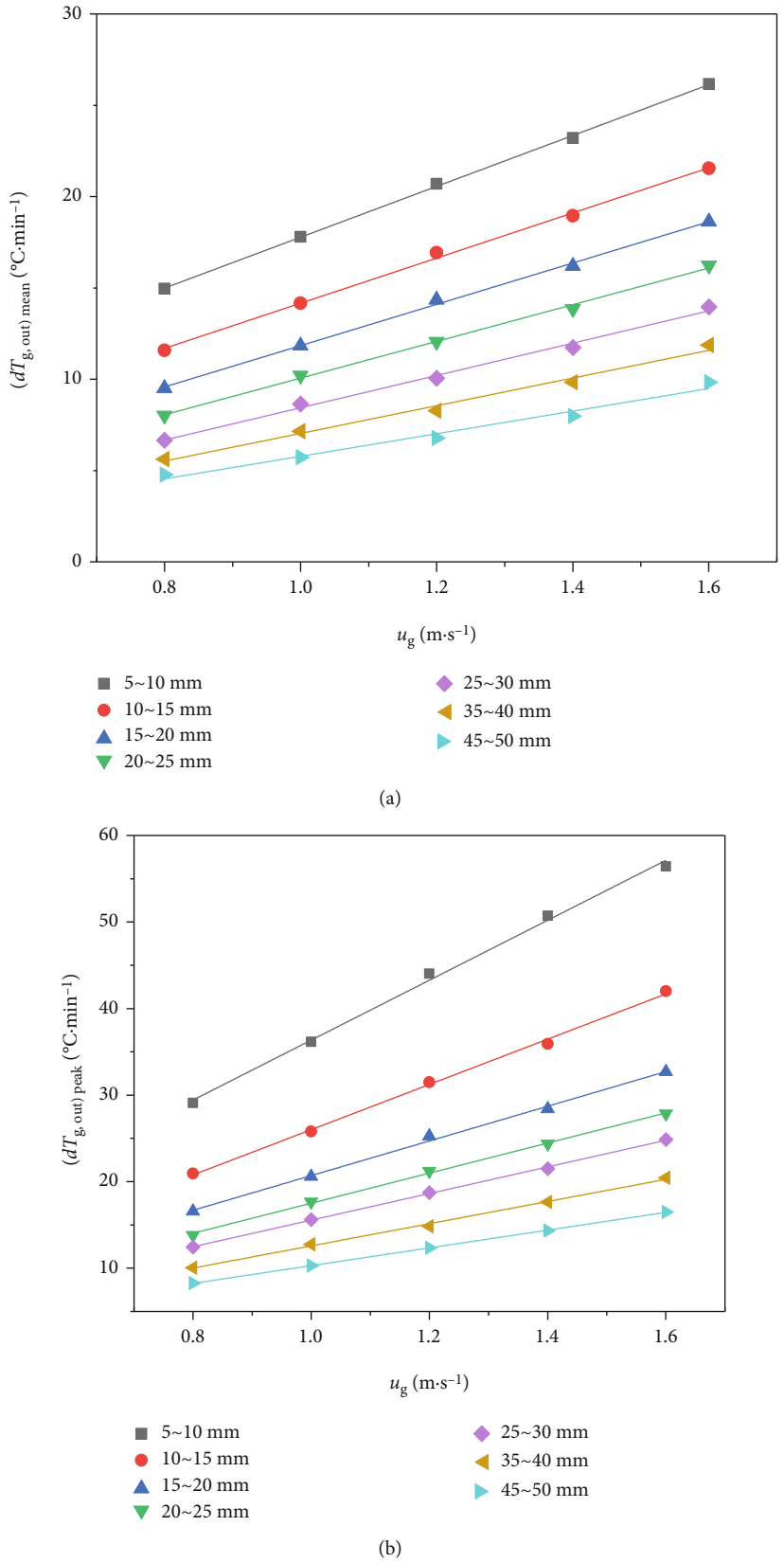

FIGURE 13: Change of the mean value $(dT_{g,out})_{mean}$ and peak value $(dT_{g,out})_{peak}$ of the change rate of the gas outlet temperature with the gas velocity u_g under different kinds of sinters.

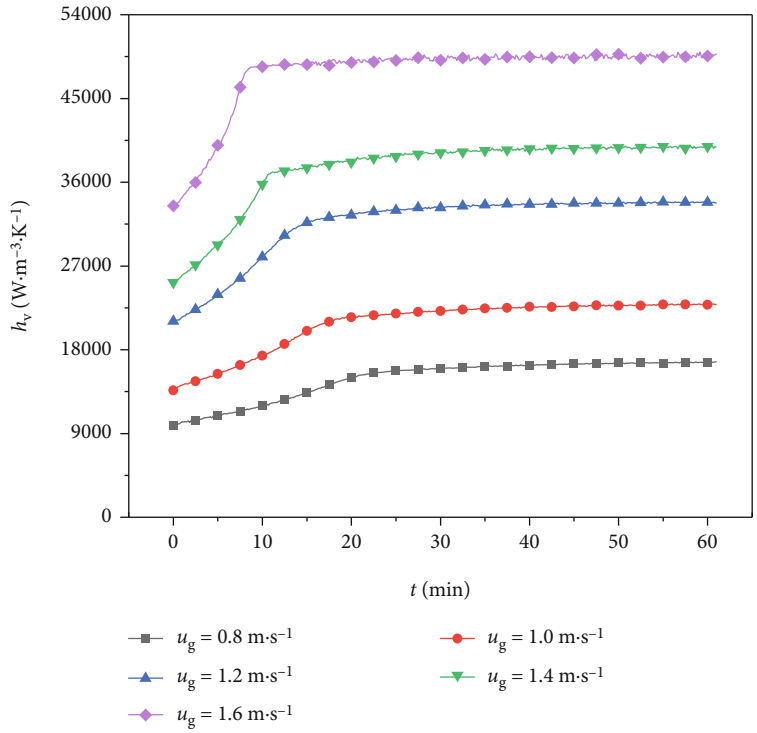

Figure 14: Variation of the heat transfer coefficient h_v of different sinters with the cooling time t at different gas velocities u_g.

Figure 16 illustrates the mean value $(dT_{g,out})_{mean}$ and peak value $(dT_{g,out})_{peak}$ of the change rate of the gas outlet temperature with the equivalent particle diameter d_p under different gas velocities u_g. It can be seen that $(dT_{g,out})_{mean}$ and $(dT_{g,out})_{peak}$ not only increase with the reduction of d_p but also show the growth trend in the increasing extent. In addition, Figure 17 shows that the heat transfer coefficient h_v increases with the reduction of d_p, and the increasing extent also increases. When the sinter is cooled to 40 min, the increasing extent is 1142.25 W·m^{-3}·K^{-1} with the particle size decreasing from 20~25 mm to 15~20 mm, while that is 3152.65 W·m^{-3}·K^{-1} with the particle size decreasing from 15~20 mm to 10~15 mm. The above results indicate that the reduction of d_p is beneficial to improve the gas-solid convective heat transfer, which is more and more significant. First, Figure 18 shows that the specific surface area increases with the particle size decreasing, which makes the gas-solid contact more sufficient. Besides, the reduction in the bed voidage ε with the particle size decreasing makes the turbulent degree of the gas increase. This reduces the heat transfer resistance. Finally, the variation range of the specific surface area and bed voidage also increases with the reduction in the particle size.

4. Modification of the Gas-Solid Heat Transfer Correlation

For the cooling process of the sinter, the main factors affecting the gas-solid heat transfer characteristics include the bed voidage ε, equivalent particle diameter d_p, gas velocity u_g, specific heat of the gas c_{pg}, viscous coefficient of the gas μ_g, thermal conductivity of the gas λ_g, density of the gas ρ_g, and volumetric coefficient of the gas-solid heat transfer h_v. To fit the heat transfer correlation, the following expressions are usually used for the dimensionless treatment of the above factors.

$$Nu = \frac{h_a d_p}{\lambda_g}, \tag{9}$$

where Nu is the Nusselt number representing the intensity of the convective heat transfer; $h_a = h_v/S_{pv}$ is the area heat transfer coefficient of the gas-solid convection, W·m^{-2}·K^{-1}; $S_{pv} = 6(1-\varepsilon)/d_p$ is the specific surface area of particles, m^2·m^{-3}.

$$\mathrm{Pr} = \frac{\mu_g c_{pg}}{\lambda_g}, \tag{10}$$

where Pr is the Prandtl number, which is the ratio of the dynamic viscosity coefficient to the thermal diffusivity.

$$\mathrm{Re}_p = \frac{\rho_g u_g d_p}{\mu_g}, \tag{11}$$

where Re_p is the particle Reynolds number, representing the gas flow state in the particle bed.

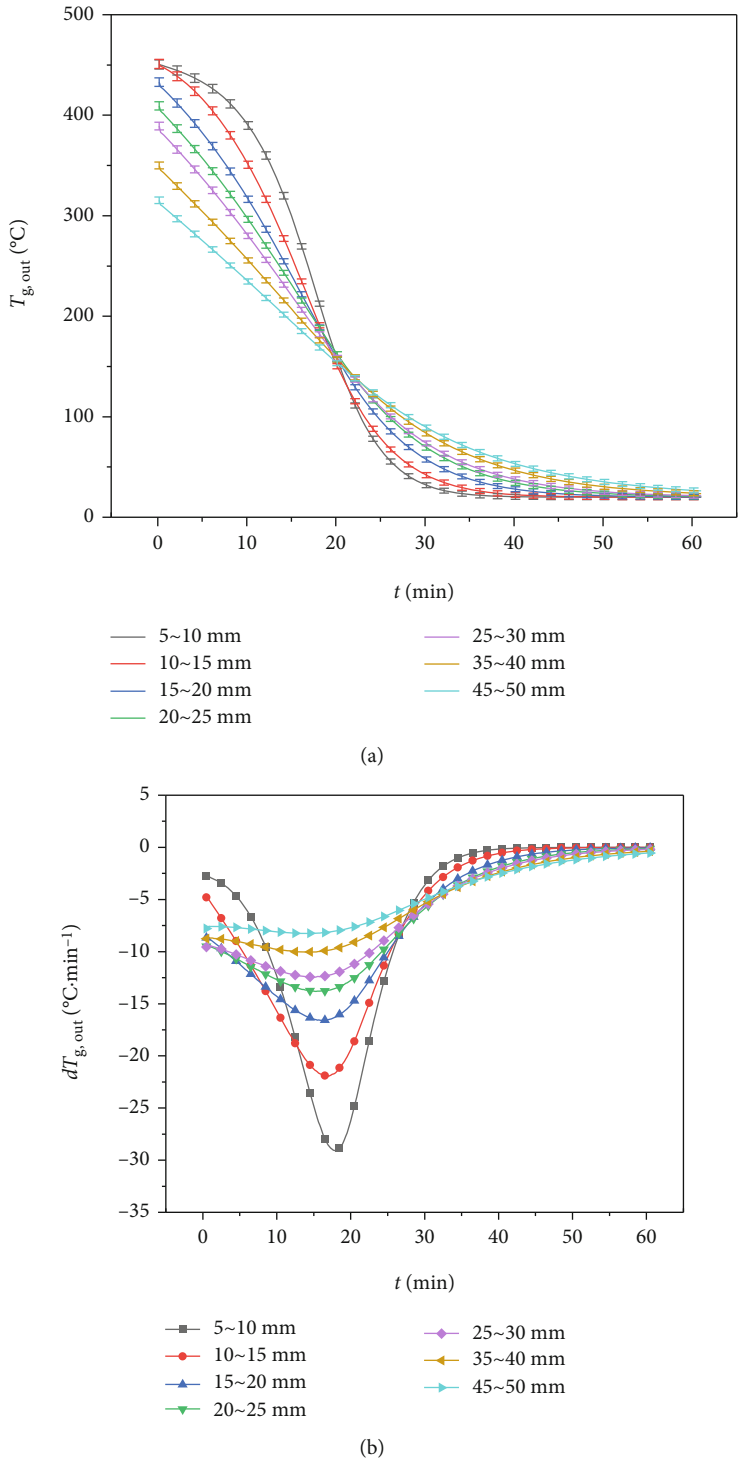

FIGURE 15: Variation of the gas outlet temperature $T_{g,out}$ and its change rate $dT_{g,out}$ with the cooling time t for the different kinds of sinters at the gas velocity of 0.8 m·s^{-1}.

Based on the form of previous correlations [23, 24, 26], the dimensionless gas-solid heat transfer correlation of the sinter is fitted according to the experimental data as follows:

$$Nu = \frac{1}{\varepsilon^{0.356}}\left(1.779 + 0.0256\mathrm{Re_p}^{0.851}\right)\mathrm{Pr}^{1/3}. \quad (12)$$

The fitting correlation coefficient R^2 of the above formula is 0.99015. Figure 19 compares the measured value of the Nusselt number Nu with the predicted value calculated by this work and other works. Furthermore, the comparison is made by means of the mean relative deviation (MRD), as given by

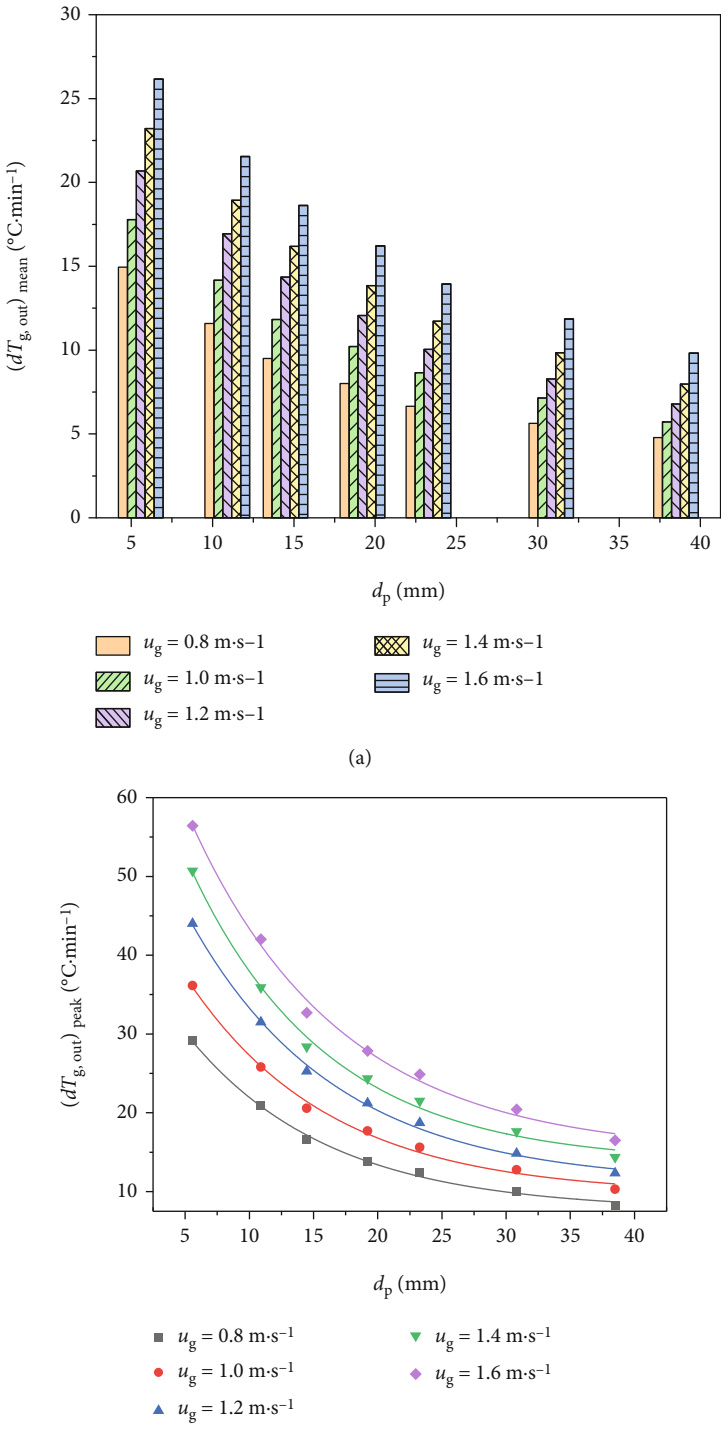

FIGURE 16: Change of the mean value $(dT_{g,out})_{mean}$ and peak value $((dT_{g,out})_{peak})$ of the change rate of the gas outlet temperature with the equivalent particle diameter d_p under different gas velocities u_g.

$$\mathrm{MRD}(\%) = \frac{1}{N}\sum_{i=1}^{N}\left|\frac{Nu_{cal,i} - Nu_{exp,i}}{Nu_{exp,i}}\right| \times 100, \qquad (13)$$

where Nu_{exp} and Nu_{cal} are the measured value and calculated value of the Nusselt number Nu, respectively.

First of all, the change trend of the measured value of the Nusselt number Nu is consistent with the predicted value obtained by this work, that is, it increases with the increase of the Reynolds number Re. Besides, the measured value is evenly distributed on both sides of the predicted curve with the mean relative deviation of only 7.61%. Therefore, the heat transfer correlation obtained by this paper can be used

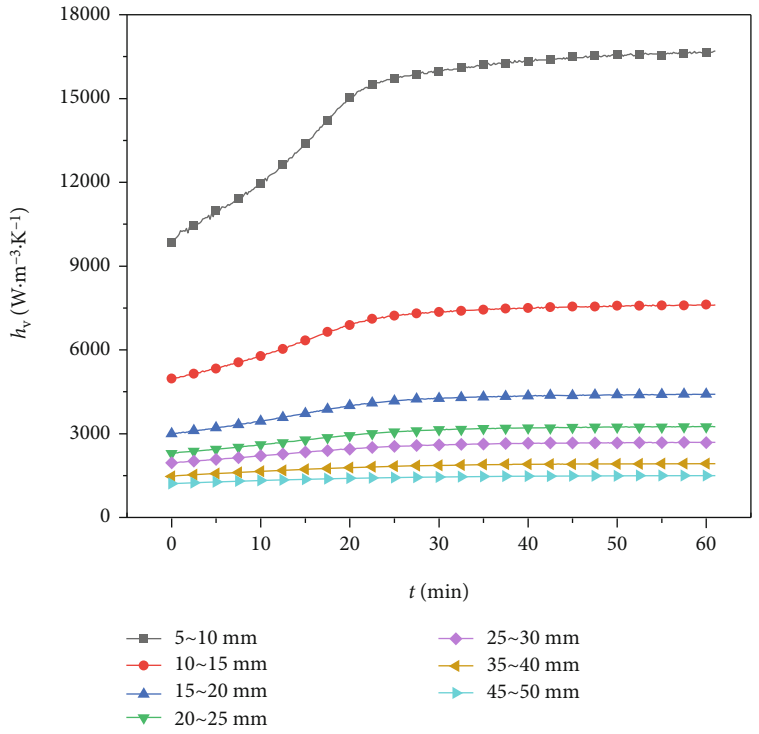

Figure 17: Variation of the volumetric heat transfer coefficient h_v with the cooling time t for the different kinds of sinters at the gas velocity of 0.8 m·s^{-1}.

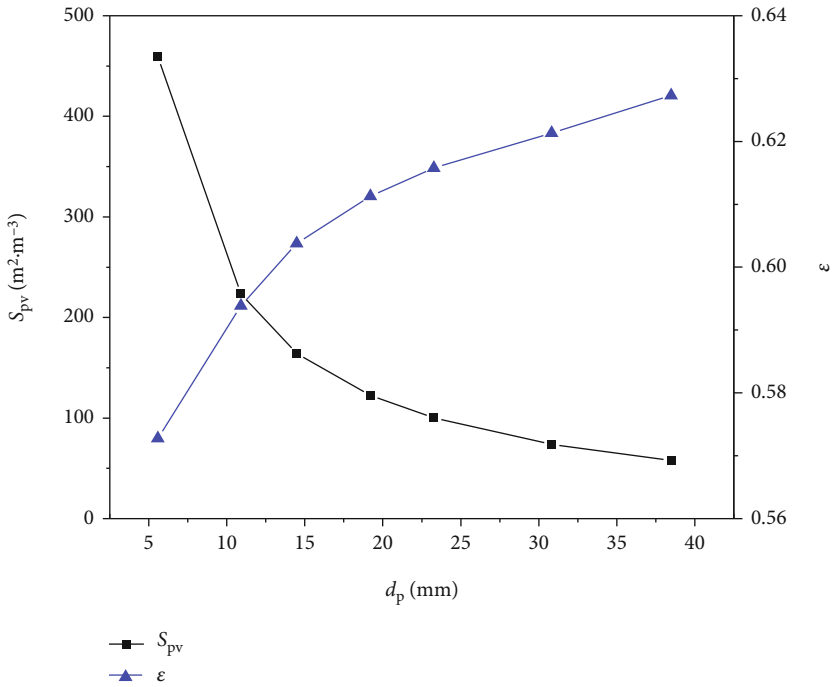

Figure 18: Variation of the specific surface area S_{pv} and bed voidage ε of sinter particles with the equivalent particle diameter d_p.

to accurately predict the gas-solid heat transfer characteristics in the sinter bed.

In addition, it is found that the variation of the measured value of the Nusselt number with the Reynolds number has the same trend as predicted values obtained by other works [9, 22–26, 40]. However, there is a considerable deviation in the value. Among them, the minimum value of MRD is 26.81%, and the maximum value of MRD is as high as 177.32%. This may be attributed to the different shape of packed particles in the bed. Compared with the previous

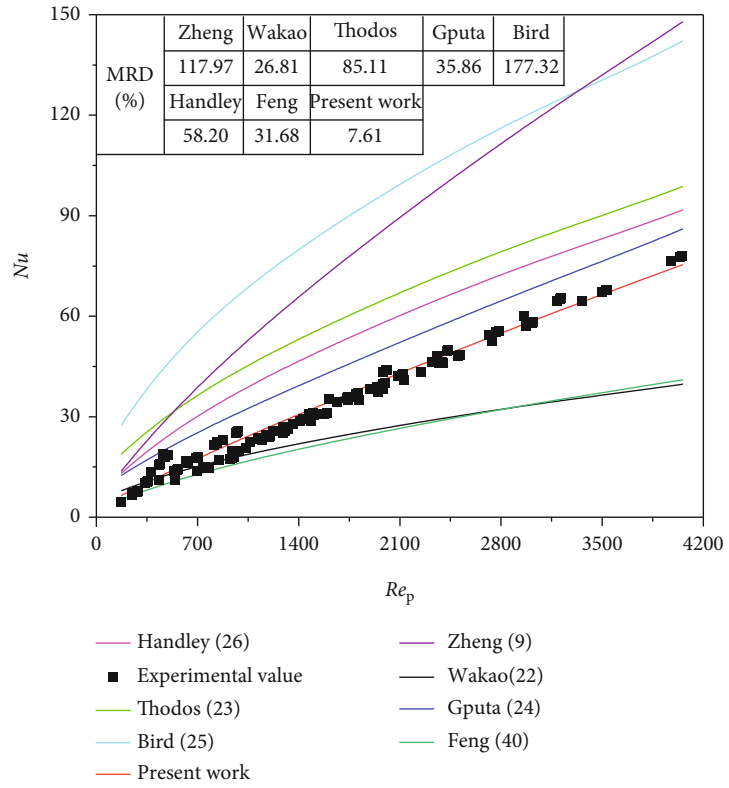

Figure 19: Comparison between the measured value of the Nusselt number Nu and predicted value of this work and other works.

particles, the shape of sinter particles is more irregular, resulting in different gas channels from regular particles [9]. Therefore, the heat transfer correlation of regular particles is no longer applicable to the sinter.

5. Conclusions

To establish an accurate model to optimize the vertical cooling process of the sinter, the key is to apply an accurate heat transfer correlation. Therefore, the heat transfer characteristics in the sinter bed with the typical particle size are experimentally studied. The inverse problem method is used to calculate the gas-solid heat transfer coefficient based on the gas outlet temperature, which is fitted into the correlation.

The results show that the heat transfer between the gas and sinter is significantly enhanced with the increase in the gas velocity. At the cooling time of 40 min, h_v increases from 16288 $W \cdot m^{-3} \cdot K^{-1}$ to 49599 $W \cdot m^{-3} \cdot K^{-1}$ with u_g increasing from 0.8 $m \cdot s^{-1}$ to 1.6 $m \cdot s^{-1}$, which increases by about twice. But this effect is gradually weakened with the increase in the particle size. With the particle size increasing from 5~10 mm to 45~50 mm, the slopes of the $(dT_{g,out})_{mean}$ curve and $(dT_{g,out})_{peak}$ curve decrease by 55.61% and 70.36%, respectively. In addition, the reduction of the particle size is also conducive to the enhancement of the heat transfer intensity. With the particle size decreasing, this effect is progressively evident. When the sinter is cooled to 40 min, the increasing extent of h_v is 1142.25 $W \cdot m^{-3} \cdot K^{-1}$ with the particle size decreasing from 20~25 mm to 15~20 mm, while that is 3152.65 $W \cdot m^{-3} \cdot K^{-1}$ with the particle size decreasing from 15~20 mm to 10~15 mm.

In addition, it is found that the variation of the measured value of the Nusselt number with the Reynolds number has the same trend as predicted values obtained by other works [9, 22–26, 40]. However, there is a considerable deviation in the value. Among them, the minimum value of MRD is 26.81%, and the maximum value of MRD is as high as 177.32%. It is proved that the previous empirical correlations are no longer applicable due to the difference of the shape. While the predicted value of this work is in good agreement with the measured value with the mean deviation of only 7.61%. Therefore, the modified correlation can accurately predict the gas-solid heat transfer characteristics in the sinter bed.

Nomenclature

c_p:	Specific heat capacity ($J \cdot kg^{-1} \cdot K^{-1}$)
d:	Particle size (m)
d_p:	Equivalent particle diameter (m)
h_v:	Volumetric heat transfer coefficient ($W \cdot m^{-3} \cdot K^{-1}$)
h_a:	Surface heat transfer coefficient ($W \cdot m^{-2} \cdot K^{-1}$)
L:	Bed height (m)
Nu:	Nusselt number (–)
Pr:	Prandtl number (–)
Re_p:	Particle Reynold number (–)
S_{pv}:	Specific surface area ($m^2 \cdot m^{-3}$)

T: Temperature (°C)
T_g, $T_{g,in}$, $T_{g,out}$: Gas temperature, inlet gas temperature, outlet gas temperature, respectively (°C)
$dT_{g,out}$: Change rate of the gas outlet temperature (°C·min^{-1})
T_s: Sinter temperature (°C)
t: Time (s)
u_g: Gas velocity (m·s^{-1})
z: Ordinate (m).

Greeks

ε: Bed voidage (−)
λ: Thermal conductivity (W·m^{-1}·K^{-1})
δ: Absolute error (−)
σ: Standard error (−)
ξ: Random number of the normal distribution (−)
ρ: Density (kg·m^{-3})
μ: Dynamic viscosity of the gas (Pa·s).

Subscripts

p: Particle
s: Sinter
g: Gas
err: Error
cal: Calculation
exp: Experiment.

Data Availability

The data used to support the findings of this study are included within the article.

Conflicts of Interest

The authors declare that they have no known competing financial interests or personal relationships that could have appeared to influence the work reported in this paper.

Acknowledgments

This work is supported by Fundamental Research Funds for the National Natural Science Foundation of China (Nos. 52006008 and 62033014).

References

[1] Q. Xu, K. Wang, Z. W. Zou et al., "A new type of two-supply, one-return, triple pipe-structured heat loss model based on a low temperature district heating system," *Energy*, vol. 218, article 119569, 2021.

[2] K. He and L. Wang, "A review of energy use and energy-efficient technologies for the iron and steel industry," *Renewable and Sustainable Energy Reviews*, vol. 70, pp. 1022–1039, 2017.

[3] Q. Xu, L. Liu, J. X. Feng et al., "A comparative investigation on the effect of different nanofluids on the thermal performance of two-phase closed thermosyphon," *International Journal of Heat and Mass Transfer*, vol. 149, article 119189, 2020.

[4] R. Q. Wang, L. Jiang, Y. D. Wang, and A. P. Roskilly, "Energy saving technologies and mass-thermal network optimization for decarbonized iron and steel industry: a review," *Journal of Cleaner Production*, vol. 274, article 122997, 2020.

[5] W. Chen, X. Yin, and D. Ma, "A bottom-up analysis of China's iron and steel industrial energy consumption and CO_2 emissions," *Applied Energy*, vol. 136, pp. 1174–1183, 2014.

[6] X. H. Zhang, Z. Chen, J. Y. Zhang, P. X. Ding, and J. M. Zhou, "Simulation and optimization of waste heat recovery in sinter cooling process," *Applied Thermal Engineering*, vol. 54, no. 1, pp. 7–15, 2013.

[7] H. Dong, L. Li, W. J. Liu, B. Wang, Y. S. Suo, and J. J. Cai, "Process of waste heat recovery and utilization for sinter in vertical tank," *China Metallurgy*, vol. 22, no. 1, pp. 6–11, 2012.

[8] K. Sun, C. Tseng, D. S. Wong et al., "Model predictive control for improving waste heat recovery in coke dry quenching processes," *Energy*, vol. 80, pp. 275–283, 2015.

[9] Y. Zheng, H. Dong, J. J. Cai et al., "Experimental investigation of volumetric heat transfer coefficient in vertical moving-bed for sinter waste heat recovery," *Applied Thermal Engineering*, vol. 151, pp. 335–343, 2019.

[10] C. G. Bi and J. J. Sun, "Application of process to recycle sensible heat of sinter using vertical cooling furnace in Meisteel," *Sintering and Pelletizing*, vol. 43, no. 4, pp. 69–72, 2018.

[11] J. S. Feng, H. Dong, J. Y. Liu, and K. Liang, "Gas-solid heat transfer characteristics in vertical tank for sinter," *CIESC Journal*, vol. 66, no. 11, pp. 4418–4423, 2015.

[12] Y. Liu, J. Y. Wang, Z. L. Cheng, J. Yang, and Q. W. Wang, "Experimental investigation of fluid flow and heat transfer in a randomly packed bed of sinter particles," *International Journal of Heat and Mass Transfer*, vol. 99, pp. 589–598, 2016.

[13] J. S. Feng, H. Dong, J. Y. Liu, K. Liang, and J. Y. Gao, "Experimental study of gas flow characteristics in vertical tank for sinter waste heat recovery," *Applied Thermal Engineering*, vol. 91, pp. 73–79, 2015.

[14] J. S. Feng, H. Dong, and H. D. Dong, "Modification of Ergun's correlation in vertical tank for sinter waste heat recovery," *Powder Technology*, vol. 280, pp. 89–93, 2015.

[15] J. S. Feng, S. Zhang, H. Dong, and G. Pei, "Frictional pressure drop characteristics of air flow through sinter bed layer in vertical tank," *Powder Technology*, vol. 344, pp. 177–182, 2019.

[16] F. Y. Tian, L. F. Huang, L. W. Fan et al., "Pressure drop in a packed bed with sintered ore particles as applied to sinter coolers with a novel vertically arranged design for waste heat recovery," *Journal of Zhejiang University-SCIENCE A*, vol. 17, no. 2, pp. 89–100, 2016.

[17] F. Y. Tian, L. F. Huang, L. W. Fan, H. L. Qian, and Z. T. Yu, "Wall effects on the pressure drop in packed beds of irregularly shaped sintered ore particles," *Powder Technology*, vol. 301, pp. 1284–1293, 2016.

[18] L. S. Pan, X. L. Wei, Y. Peng, X. B. Shi, and H. L. Liu, "Experimental study on convection heat transfer and air drag in sinter layer," *Journal of Central South University*, vol. 22, no. 7, pp. 2841–2848, 2015.

[19] S. Z. Zhang, Z. Wen, X. L. Liu, Y. Xing, and H. Zhang, "Gas flow characteristics through irregular particle bed with the vertical confined wall for waste heat recovery," *International Journal of Photoenergy*, vol. 2022, Article ID 1890541, 16 pages, 2022.

[20] S. Z. Zhang, "Effects of the layered distribution pattern on the gas flow resistance through the bed with the multisize irregular

particle for the waste heat recovery," *International Journal of Photoenergy*, vol. 2022, Article ID 3727937, 15 pages, 2022.

[21] S. Z. Zhang, Z. Wen, X. L. Liu, X. Liu, S. Wang, and H. Zhang, "Experimental study on the permeability and resistance characteristics in the packed bed with the multi-size irregular particle applied in the sinter vertical waste heat recovery technology," *Powder Technology*, vol. 384, pp. 304–312, 2021.

[22] N. Wakao, S. Kaguei, and T. Funazkri, "Effect of fluid dispersion coefficients on particle-to-fluid heat transfer coefficients in packed beds: correlation of nusselt numbers," *Chemical Engineering Science*, vol. 34, no. 3, pp. 325–336, 1979.

[23] A. S. Gupta and G. Thodos, "Mass and heat transfer in the flow of fluids through fixed and fluidized beds of spherical particles," *AICHE Journal*, vol. 8, no. 5, pp. 608–610, 1962.

[24] S. N. Gputa, R. B. Chaube, and S. N. Upadhyay, "Fluid–particle heat transfer in fixed and fluidized beds," *Chemical Engineering Science*, vol. 29, no. 3, pp. 839–843, 1974.

[25] M. V. Ramos, E. Kasai, J. Kano, and T. Nakamura, "Numerical simulation model of the iron ore sintering process directly describing the agglomeration phenomenon of granules in the packed bed," *ISIJ International*, vol. 40, no. 5, pp. 448–454, 2000.

[26] D. Handley and P. J. Heggs, "Momentum and heat transfer mechanisms in regular shaped packings," *Transactions of the Institution of Chemical Engineers*, vol. 46, pp. 251–264, 1968.

[27] W. E. Ranz, "Friction and transfer coefficients for single particles and packed beds," *Chemical Engineering Progress*, vol. 48, pp. 247–253, 1952.

[28] A. Singhal, S. Cloete, S. Radl, Q. F. Rosa, and S. Amini, "Heat transfer to a gas from densely packed beds of monodisperse spherical particles," *Chemical Engineering Journal*, vol. 314, pp. 27–37, 2017.

[29] J. B. Will, N. P. Kruyt, and C. H. Venner, "An experimental study of forced convective heat transfer from smooth, solid spheres," *International Journal of Heat and Mass Transfer*, vol. 109, pp. 1059–1067, 2017.

[30] J. Yang, J. Q. Wu, L. Zhou, and Q. W. Wang, "Computational study of fluid flow and heat transfer in composite packed beds of spheres with low tube to particle diameter ratio," *Nuclear Engineering & Design*, vol. 300, pp. 85–96, 2016.

[31] J. Q. Wu, J. Yang, L. Zhou, and Q. W. Wang, "Numerical analysis of fluid flow and heat transfer in various composite packed beds," *CIESC Journal*, vol. 66, pp. 111–116, 2015.

[32] J. Y. Wang, Q. Guo, J. Yang, Y. Liu, and Q. Wang, "Experimental study of convective heat transfer in grille-sphere composite structured packed bed," *Energy Procedia*, vol. 105, pp. 4782–4787, 2017.

[33] J. Y. Wang, J. Yang, Z. L. Cheng, Y. Liu, Y. Chen, and Q. Wang, "Experimental and numerical study on pressure drop and heat transfer performance of grille-sphere composite structured packed bed," *Applied Energy*, vol. 227, pp. 719–730, 2018.

[34] J. Yang, J. Wang, S. S. Bu, M. Zeng, and Q. W. Wang, "Experimental study of forced convective heat transfer in structured packed porous media of particles," *Journal of Engineering Thermophysics*, vol. 33, no. 5, pp. 851–855, 2012.

[35] J. Yang, Q. Wang, M. Zeng, and A. Nakayama, "Computational study of forced convective heat transfer in structured packed beds with spherical or ellipsoidal particles," *Chemical Engineering Science*, vol. 65, no. 2, pp. 726–738, 2010.

[36] J. Yang, J. Wang, S. S. Bu, M. Zeng, Q. Wang, and A. Nakayama, "Experimental analysis of forced convective heat transfer in novel structured packed beds of particles," *Chemical Engineering Science*, vol. 71, pp. 126–137, 2012.

[37] H. Tavassoli, E. A. J. F. Peters, and J. A. M. Kuipers, "Direct numerical simulation of fluid-particle heat transfer in fixed random arrays of non-spherical particles," *Chemical Engineering Science*, vol. 129, pp. 42–48, 2015.

[38] J. Jang and Y. Chiu, "3-D transient conjugated heat transfer and fluid flow analysis for the cooling process of sintered bed," *Applied Thermal Engineering*, vol. 29, no. 14-15, pp. 2895–2903, 2009.

[39] Z. C. Huang, Y. Yang, R. H. Zhong, Z. K. Liang, and B. Hu, "Heat transfer characteristics in process of hot sinter vertical cooling," *Iron and Steel*, vol. 54, no. 11, pp. 9–15, 2019.

[40] J. S. Feng, H. Dong, J. Y. Gao, J. Y. Liu, and K. Liang, "Experimental study of gas-solid overall heat transfer coefficient in vertical tank for sinter waste heat recovery," *Applied Thermal Engineering*, vol. 95, pp. 136–142, 2016.

[41] L. B. Younis and R. Viskanta, "Experimental determination of the volumetric heat transfer coefficient between stream of air and ceramic foam," *International Journal of Heat and Mass Transfer*, vol. 36, no. 6, pp. 1425–1434, 1993.

[42] J. J. Hwang, G. J. Hwang, R. H. Yeh, and C. H. Chao, "Measurement of interstitial convective heat transfer and frictional drag for flow across metal foams," *Journal of Heat Transfer*, vol. 124, no. 1, pp. 120–129, 2002.

[43] P. X. Jiang, R. N. Xu, and W. Gong, "Particle-to-fluid heat transfer coefficients in miniporous media," *Chemical Engineering Science*, vol. 61, no. 22, pp. 7213–7222, 2006.

[44] Q. Guo, Z. Wen, and R. Dou, "Experimental and numerical study on the transient heat-transfer characteristics of circular air-jet impingement on a flat plate," *International Journal of Heat and Mass Transfer*, vol. 104, pp. 1177–1188, 2017.

[45] J. S. Feng, H. Dong, S. Zhang, and L. Zhao, "Experimental study on gas-solid exergy transfer process in sinter vertical tank," *Journal of Iron and Steel Research*, vol. 32, no. 7, pp. 556–562, 2020.

Hindawi
International Journal of Photoenergy
Volume 2022, Article ID 8632826, 13 pages
https://doi.org/10.1155/2022/8632826

Research Article

Numerical Study on the Optimization Design of Photovoltaic/Thermal (PV/T) Collector with Internal Corrugated Channels

Xiangrui Kong[1], **Yuhan Zhang**[2], **Jinshun Wu**[1] and **Song Pan**[3]

[1]*School of Architecture Engineering, North China Institute of Science and Technology, Yanjiao, 065201, China*
[2]*Beijing Uni-Construction Group Company, LTD, Beijing 100029, China*
[3]*School of Civil Engineering and Architecture, Beijing University of Technology, Beijing 100022, China*

Correspondence should be addressed to Jinshun Wu; wujinshun2005@163.com

Received 19 March 2022; Revised 1 August 2022; Accepted 5 September 2022; Published 17 September 2022

Academic Editor: Congcong Wang

This study presents a theoretical study on the super thin and conductive thermal absorber with built-in corrugated channels on the basis of previous field experiments. The flow and heat transfer characteristics of the corrugated channels are simulated to identify the factors affecting photovoltaic/thermal (PV/T) system efficiency. The influences of the structural parameters such as the corrugation number, the corrugation area, and the flow channel width on the water outlet temperature and heat collection are discussed in order to support the structural optimization design of the hybrid PV/T system. The simulation results were validated to be in good agreement with experimental results. The results indicate that increasing inlet water velocity leads to a decrease in the outlet temperature. It was found that the corrugation area and the flow channel width have impacts on the outlet temperature of the hybrid PV/T collector panel. When the flow channel width of the absorber plate is reduced from 4 mm to 3 mm, the outlet temperature attained is between 298 and 302 K, and the heat collection is in the range of 16.2–51.4 MJ/h. This led to an increase in the amount of heat collected by 18.6%.

1. Introduction

The solar photovoltaic/thermal (PV/T) system is one of the key research focuses of the solar energy utilization field due to its high thermal energy output and comprehensive utilization compared with PV or solar thermal systems alone [1, 2]. It was widely used in several industries, like power generation stations [3–5], dryers [6, 7], building heating [8, 9, 10], and desalination systems [11–13]. In recent years, great progress has been made in the optimization and application of solar photovoltaic/thermal (PV/T) systems. No matter in what field the PV/T system is used, improving its performance is the key and final objective. Many studies have been conducted to investigate the PV/T system performance involving utilizing PCM [14–16], using nanofluids [17, 18], concentrated application [19, 20], and air and water configurations [1, 21, 22] by various methodologies such as experimental, analytical, numerical, and simulation techniques. Due to the structure and performance improvement of the heat collector having a great influence on the whole PV/T system components' efficiency, technologies for this purpose, including the cooling channel design or modifications of the PV/T systems, have been developed substantially. This includes using single and double pass and using fins, suspended plates, concentrating plates, etc.

Hissouf et al. [23] investigated the theoretical performance of a PV/T solar collector employing three different geometrical shapes of fluid circulation channels (circular tube, half tube, and square tube) and a heat transfer fluid of pure water and ethylene glycol-water (EG-W) mixture. The half tube design is found to provide the best photovoltaic cooling effect and the highest efficiency. The use of pure water as working fluid improves thermal and electrical yields by 4.5% and 1.85%, respectively, compared to the EG-W mixture. A new type (double pass) of photovoltaic/thermal panel and a novel latent heat storage unit integrated with the condenser of the heat pump were designed and manufactured in Kosan and Aktas' study [8]. The numerical analysis was performed using the Ansys Fluent program to characterize the thermal behavior of the phase change material in the latent heat storage unit.

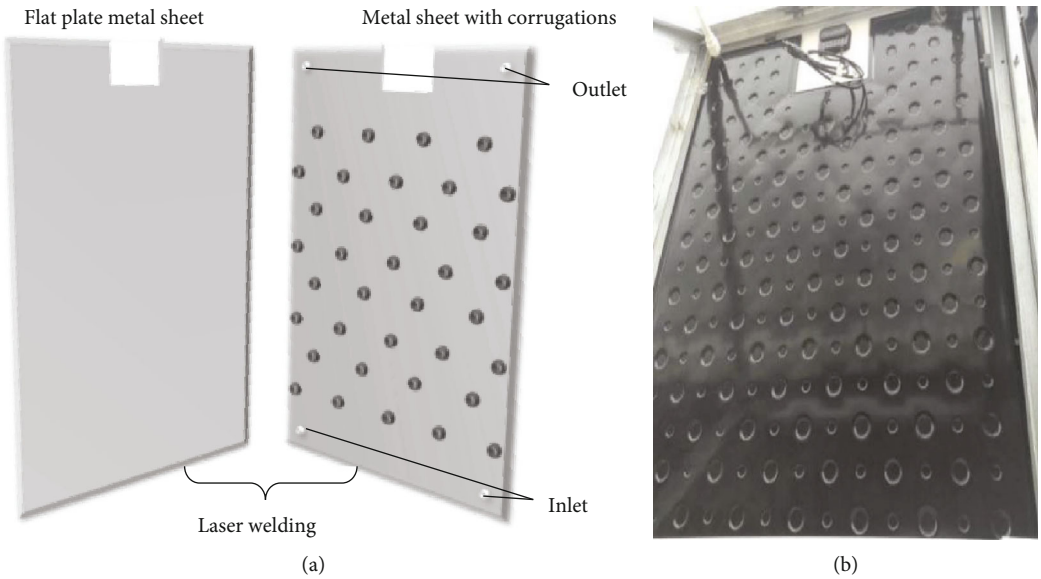

Figure 1: Schematic of the thermal absorber (a) and the associated PV/T prototypes (b).

Table 1: Relevant parameters of the heat absorber plate core.

Items	Parameters
Absorber plate material	Iron
Large corrugation's diameter	35 mm, 25 mm
Small corrugation's diameter	20 mm, 15 mm
Inlet/outlet diameters	20 mm
Inlet/outlet lengths	50 mm
Flow channel width	4 mm

Table 2: Material parameters.

Items	Density (kg/m^3)	Specific heat volume (J/kg·K)	Thermal conductivity (W/m·K)	Coefficient viscosity (kg/m)
Water	998.2	4182	0.6	0.001003
Iron	8030	502.48	16.27	—

It was observed that the heat pump system's average coefficient of performance varied between 2.93 and 3.18. The photovoltaic/thermal panel was able to store 1.07 kWh of electrical energy and produce 9.59% more electricity than the photovoltaic panel alone. Yu et al. [24] investigated a novel solar Micro-Channel Loop-Heat-Pipe Photovoltaic/Thermal (MC-LHP-PV/T) system through experimental measurements. A prototype MC-LHP-PV/T system employing R-134a as working fluid was designed and measured to evaluate its solar thermal and electrical efficiencies and its impact factors. The results found that a lower inlet water temperature, a higher water flow rate, a higher ambient temperature, and a larger height difference between the condenser and the evaporator can help to increase the solar thermal efficiency of the system. Compared to existing PV/T and BIPV/T systems, the new MC-LHP-PV/T system achieved 17.20% and 33.31% higher overall solar efficiency. By utilizing numerical and experimental approaches, Çiftçi et al. [25] developed and analyzed a vertical hybrid PV/T solar dryer. Their results showed that the thermal efficiency values of the finned vertical PV/T collector were much higher than those of the finless vertical PV/T collector. The sustainability index values of finless and finned drying systems were between 2.16-2.75 and 2.38-3.25, respectively. Arslan et al. [26] designed a new type of finned air fluid photovoltaic/thermal collector and performed numerical and experimental analysis on it. It was reported that 0.42% improvement in electrical efficiency occurred due to the cooling of PV. The average thermal and electrical efficiency obtained for the PV/T was 49.5% and 13.98%, respectively, with a mass flow rate of 0.04553 kg/s. To achieve higher thermal and electrical efficiencies, Yao et al. [27] designed and optimized the fluid channel pattern of the solar-assisted PV/T heat pump. The optimized two-phase flow channel pattern had significant improvements in temperature uniformity, thermal and electrical efficiencies, and hydraulic behavior. Fan et al. [28] developed a multiobjective design optimization strategy for hybrid photovoltaic/thermal collector- (PV/T-) solar air heater (SAH) systems with fins to maximize thermal energy generation and net electricity gains. To improve the cooling capacity and required pump power of parallel cooling channels (PCCs), Yu et al. [29] studied the heat transfer in parallel cooling channels with periodically expanded grooves (PEGs).

The hybrid photovoltaic/thermal (PV/T) collector with internal corrugated channels studied in this work has the characteristics of using pass or fins mentioned above. It was developed by Xu et al. [30] to retrofit the existing PV panel into a photovoltaic/thermal (PV/T) panel. The current study is thus built up on top of the previously reported works in the literature [30, 31] which conducted a parallel comparative investigation on the PV and PV/T panel systems through both laboratory and field experiments. The previous study [30] has shown that the electrical efficiency of the PV/T unit can be improved by 16.8% through the

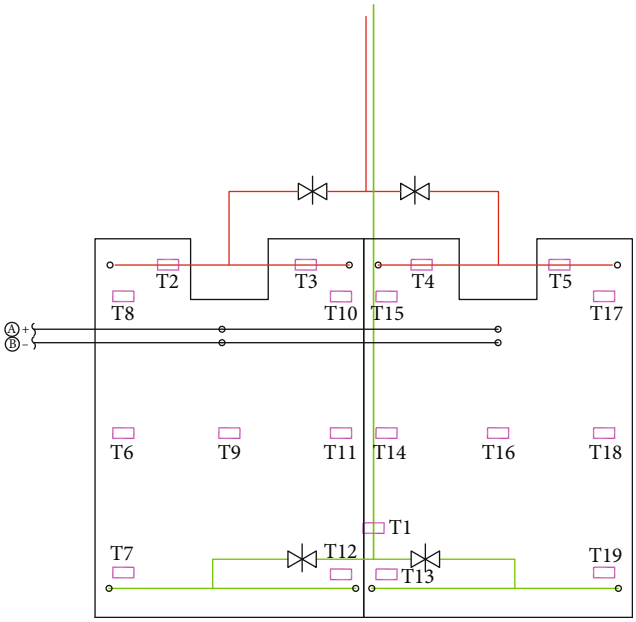

Figure 2: Location of the measuring points set on the absorber plate.

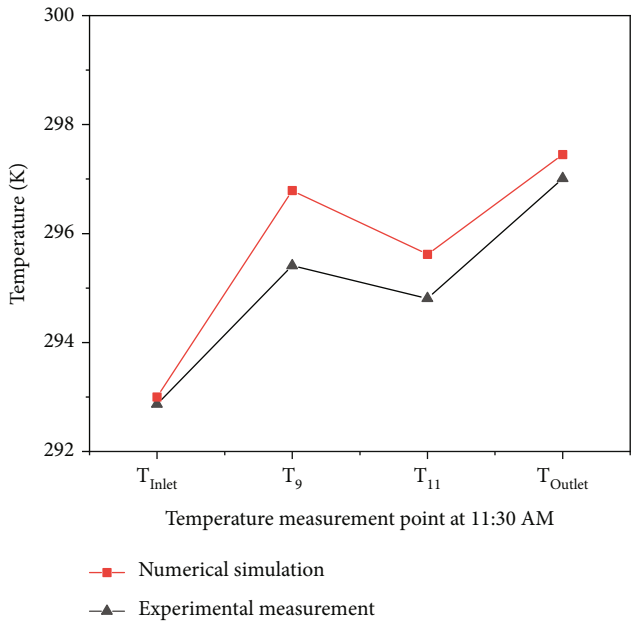

Figure 3: Temperature comparison of different measurement points between experimental measurements and numerical simulation.

use of a super thin-conductive thermal absorber, and the thermal efficiency reaches 65%. Compared with the same PV, the hybrid PV/T panel could enhance the electrical return by nearly 3.5% and increase the overall energy output by nearly 324.3%.

The overall energy output of hybrid PV/T panels is mainly related to heat collection efficiency. To improve the efficiency of solar energy conversion of PV/T systems, it is necessary to investigate the factors affecting the heat transfer performance of the absorber plate. The geometric characteristics of the absorber plate are also key factors affecting the internal flow and heat transfer characteristics. In addition, the optimized structural parameters should meet the demands of different sizes and thicknesses of a wall body and installation convenience. However, it is difficult to achieve the temperature and velocity of the working medium in the plate through laboratory measurements and identify the influence of factors on the absorber plate's heat transfer performance due to its complex structure. In this work, a CFD model of the super thin-conductive thermal absorber was established on the basis of the previous field experiment [31]. The flow and heat transfer characteristics of the corrugated channels are simulated to identify the key factors affecting the PV/T system efficiency. Finally, the influences of the structural parameters, such as corrugation areas, corrugation numbers, and flow channel width, on the flow and heat transfer characteristics are discussed to support the structural optimization design of the hybrid PV/T panel with corrugated cooling channels.

2. Methodology

2.1. Photovoltaic/Thermal (PV/T) Panel with Corrugated Cooling Channels. The PV/T in this article is designed by attaching the PV panel to a super thin-conductive thermal absorber through a series of U-shaped resilient metal clips. The thermal absorber was laser-welded together through two parallel thin flat plate metal sheets with a 1 mm thickness. One sheet was extruded by a machinery mold to formulate arrays of mini corrugations while the other sheet remained smooth. These two metal sheets form the built-in turbulent flow channels with a 4 mm width, which engenders high heat transfer capacity. The corner holes are cut on the four corners of the corrugated sheet as the working medium water's inlet and outlet channels with a spacing of 4 cm. The physical map and plane schematic diagram of the heat-absorbing core are shown in Figure 1, and the relevant parameters of the heat absorber plate are shown in Table 1.

2.2. Mathematical Model. In this article, a CFD model was established using the hybrid PV/T panel with large and small corrugations as the research objects. To simplify the simulation, the following assumptions are made:

(1) The irradiance, ambient temperature, and inlet water temperature are constant

(2) The working medium water is considered to be an incompressible liquid

(3) The materials' properties are constant

(4) The flow is fully developed

The solid boundary involved in the simulation model is iron. The physical property parameters of water and iron are shown in Table 2. The same boundary condition as in the reference experiment [31] was adopted; that is, the front of the collector was kept as a constant heat source.

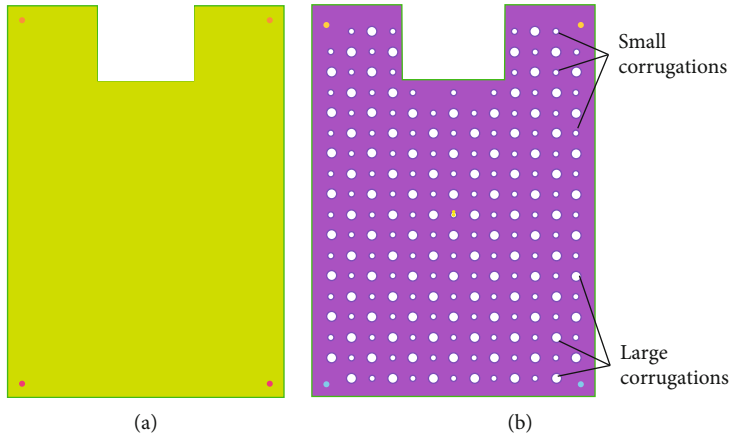

Figure 4: The metal sheet with smooth surface (a) and metal sheet with corrugations (b).

2.2.1. Model Equations. Considering that the heat absorber is an ultrathin type of superconducting tablet, the internal flow of fluid had streamline curvature and vortex due to the corrugations. The fluid was affected largely by the wall in the internal, and its turbulence developed insufficiently near the wall surface. The realizable k-ε model was chosen for this study because it more accurately predicts the performance of the flat plate absorber. Its specific expression was as follows:

$$\rho\frac{\partial k}{\partial \tau}+\rho u_j\frac{\partial k}{\partial x_i}=\frac{\partial}{\partial x_i}\left[\left(\mu+\frac{\mu_t}{\sigma_k}\right)\frac{\partial k}{\partial x_j}\right]+G_k+G_b-\rho\varepsilon-Y_M+S_k, \tag{1}$$

where ρ and μ are the density and viscosity of the water, respectively; τ is the time; k is the turbulent energy; μ_t is the turbulent viscosity; x_i and x_j are the displacement in the x and y directions, respectively; u and v are the velocity of water along the x and y axis, respectively; G_k is the turbulent kinetic energy term that is generated by the laminar velocity gradient; G_b is the turbulent kinetic energy term that is generated by buoyancy; ε is the turbulent dissipation rate; Y_M refers to the wave generated by the transition diffusion in compressible turbulence; S_k is defined as the turbulent kinetic energy; and σ_k is the turbulent Prandtl number in the k equation.

The governing equation for the dissipation ratio ε is as follows:

$$\rho\frac{\partial \varepsilon}{\partial \tau}+\rho u_j\frac{\partial \varepsilon}{\partial x_j}=\frac{\partial}{\partial x_j}\left[\left(\mu+\frac{\mu_t}{\sigma_\varepsilon}\right)\frac{\partial \varepsilon}{\partial x_j}\right]+\rho C_1 S_\varepsilon-\rho C_2\frac{\varepsilon^2}{k+\sqrt{\nu\varepsilon}}+C_{1\varepsilon}\frac{\varepsilon}{k}C_{3\varepsilon}G_k+S_\varepsilon \tag{2}$$

where σ_ε is the turbulent Prandtl number in ε equation, S_ε is defined as the turbulent dissipation source, $C_{1\varepsilon}$ and C_2 are constants, and $C_{3\varepsilon}$ is the influence term of buoyancy on the dissipation rate:

$$C_1=\max\left[0.43,\frac{\eta}{\eta+5}\right],\qquad \eta=S\frac{k}{\varepsilon}, \tag{3}$$

where S is the influence term of average strain rate on turbulence.

2.2.2. Numerical Method and Boundary Conditions. The ICEM module of commercial computational fluid dynamics (CFD) software Ansys Fluent was used to establish the geometric model and carry out the structural mesh division. Three-dimensional single precision was selected. The SIMPLE algorithm and an uncoupled implicit solver were used for the solution. The heat transfer surface grid encryption technology, boundary layer mesh technology, and general grid interface (GGI) mesh link technology were used. Grid independence verification was also conducted. When the number of grids is about 2.17 million, the outlet temperature error is less than 2%.

For the incompressible flow in channels, the following boundary conditions are set according to the actual operating conditions of the experimental platform [31]:

(1) The inlet velocity v ranges from 0.2 to 1.5 m/s, and the inlet water temperature T_{in} is 293 K

(2) The outlet was the outflow of quality

(3) The wall surface was chosen to be made of iron. To simplify the simulation, when simulating the influence of temperature difference on the water's flow and heat transfer characteristics inside the plate, all the wall surfaces were assumed adiabatic, except the outer heating surface, which was set at a corresponding constant temperature

2.3. Model Validation. To validate the numerical model developed in this work, the numerical simulation results

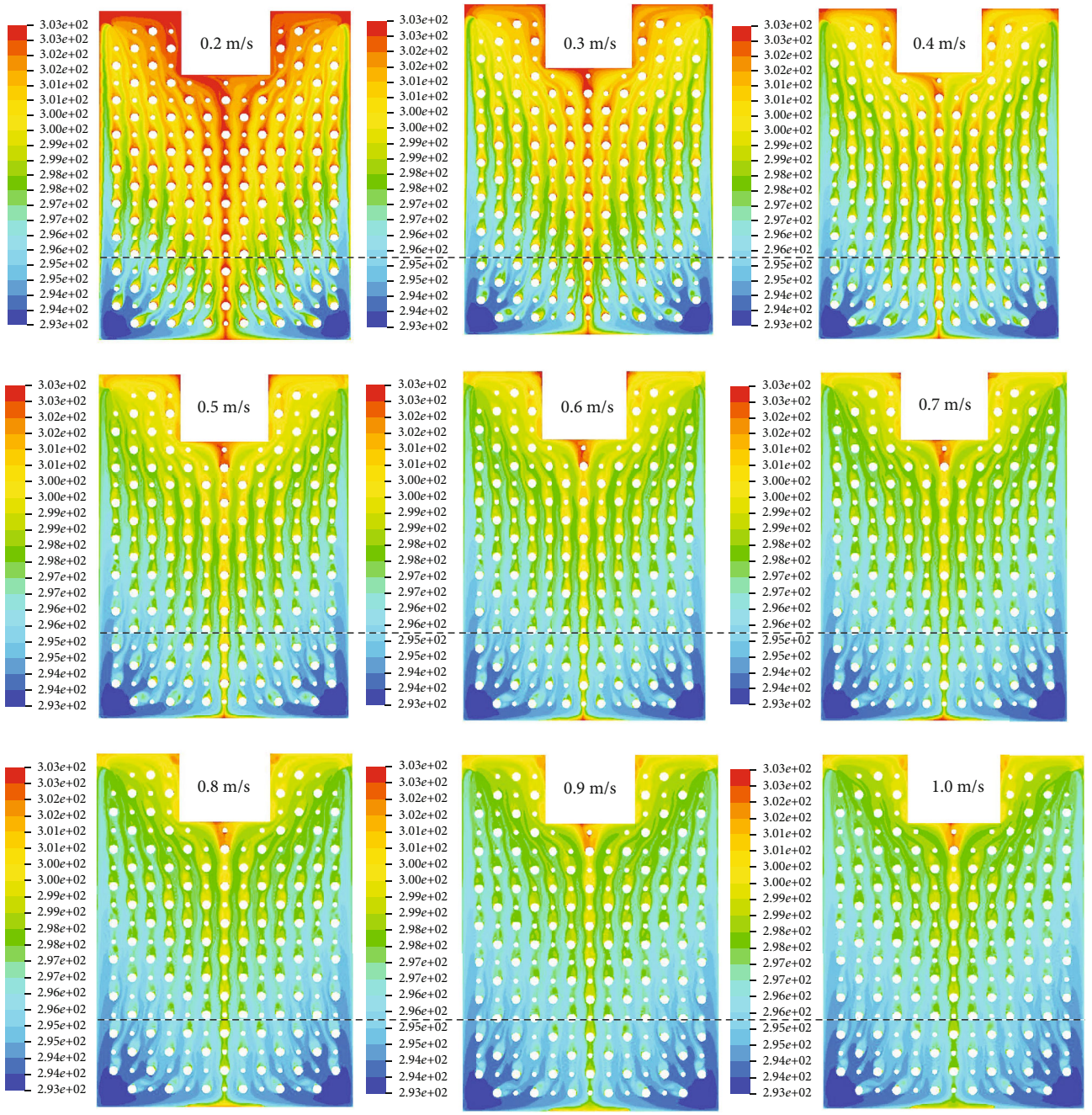

Figure 5: Temperature distribution (in K) at different inlet flow velocities.

for the inlet water temperature, the outlet temperature, and the temperature near the plate center (T9) and two sides (T11), considering an inlet flow velocity of 1.5 m/s, are compared with the experimental data from Li et al. [31]. The experimental temperature was obtained by setting 14 measuring points (T6-T19) on the back board of the hybrid plate (as shown in Figure 2). The minimum and maximum temperatures recorded by the temperature sensor are -323~473 K, respectively. At 11:30, it is noted that the experimental and numerical simulation inlet water temperatures are approximate and are selected for comparison, as illustrated in Figure 3.

Overall, the temperature distribution at the different measurement points is similar in the case of experimental and numerical simulations. The maximum reported discrepancy is around 0.5%, exhibited at point T9. The differences may be due to the positions of the experimental measurement points. The flow channel is too narrow to install a temperature monitor to get the temperature of the water inside. Except for the inlet and outlet temperatures, the rest of the measuring points are arranged on the back board of the hybrid plate during the experiment. The thermal absorber is made up of two super thin metal sheets. It was considered that the back board temperature is approximately equal to

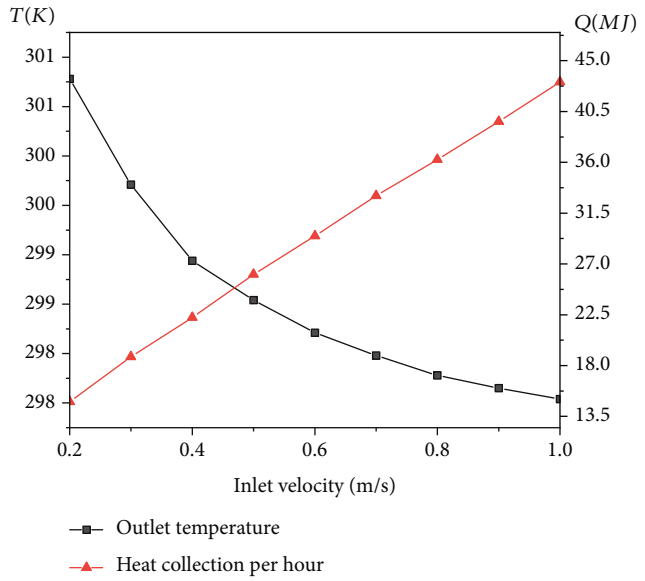

Figure 6: Outlet temperature and hourly heat collection of heat absorber.

the internal water temperature at steady state conditions. It is noted that when the inlet flow velocity is high, the rate of heat removal from the PV panel is low, which leads to insufficient heat transfer by the internal working medium. Therefore, the simulated outlet temperature is higher than the experimentally measured one. In a previous study presented in the literature [22], the water outlet temperature was found to drop as the inlet water velocity increased. In general, the temperature distributions by simulation show reasonable agreement with the test results. Hence, the numerical model can accurately predict the heat transfer of the hybrid absorber's internal flow channels.

3. Results and Discussions

This study firstly analyzed the flow and heat transfer characteristics of the water in the present absorber plate under different inlet velocities and heating surface temperatures. Then, the flow and heat transfer characteristics were simulated by changing the structural parameters of the hybrid PV/T panel, such as corrugation numbers, corrugation areas, and flow channel width, while other conditions were maintained constant. Finally, the optimization direction was given by comparing it with the previous hybrid heat collector and the flat plate heat collector. The flat plate collector is laser-welded together by two parallel metal sheets with a smooth surface (Figure 4(a)). The hybrid collector is laser-welded together by two parallel metal sheets. One sheet has corrugations (Figure 4(b)), while the other sheet remains smooth.

3.1. Effect of the Internal Temperature and Inlet Velocity. When the inlet velocity is greater than 1.0 m/s, the water outlet temperature drops very little. The water outlet temperature is 297.54 K when the inlet flow velocity is 1.0 m/s, and it drops to 297.45 K when the inlet flow velocity is 1.5 m/s. The temperature distribution in the parallel heating surface direction is similar. Therefore, in order to identify the influence of inlet velocity and heating surface temperature on the heat absorber, this study simulated the water temperature and velocity distributions at different conditions: the inlet velocity was increased by a 0.1 m/s increment from 0.2 to 1.0 m/s, and the heating surface temperature was 298, 303, 308, and 313 K, respectively. The geometry parameters and other conditions are constant.

The water temperature inside the PV/T panel drops as the inlet water velocity increases (Figure 5). At a low inlet flow velocity (0.2 m/s), it can be seen that the water temperature is high due to the fact that the rate of heat removal from the PV panel is high at low inlet flow rates. The temperature distribution in the parallel heating surface direction is similar no matter how the water inlet velocity changes (Figure 5). The temperature near the plate exit is high, while the part near the entrance is low. The temperature of the absorber plate is symmetrical about the symmetry axis, and the temperature on both sides is lower than at the center.

According to the temperature difference between the collector inlet and outlet, heat collection at different water inlet velocities can be obtained (Figure 6). The outlet temperature decreases with the increase in the water inlet velocities. This is due to the fact that at low flow velocities, the working fluid will take more time to absorb heat from a PV panel compared to the case at high speeds. In general, increasing the flow rate will lead to a decrease in the PV temperature [32], and thus, the rate of heat removal from the PV panel is thus low. As the inlet velocity increases, the heat collection per hour increases, and the amplitude decreases gradually. When the velocity varies from 0.2 to 1.0 m/s, the heat collection is in the range of 14.8-43.1 MJ/h.

Figure 7 shows the water temperature distribution at different heating surface temperatures with water inlet velocity being 0.5 m/s. All the temperature distributions at different heating surfaces have a similar trend. The temperature near the middle is slightly higher than it is on either side. The temperatures near the two exits are high, and the temperatures near the entrances are low. This may also be due to the flow velocity distribution of the working medium inside the plate (Figure 8). The water velocity on both sides is high, while it is low near the middle part. Compared to the sides, the water in the middle has a longer flow path and a lower velocity. This relatively low velocity, along with the high rate of heat removal from the PV panel, results in sufficient heat exchange between the PV panel and the water.

Figure 9 shows the outlet temperature and heat collection under different heating surface temperatures with the inlet velocity being 0.5 m/s. The outlet temperature and heat collection per hour increase with the rise of the heating surface temperatures. The trend is linear, and the rate is decreasing. Under this condition, the outlet temperature of the heat collector is between 298 and 313 K, and the heat collection per hour is in the range of 12.3~53.5 MJ. An increase in the PV panel temperature leads to an increase in the outlet temperature due to the rise in the work medium temperature, which was also reported in the study conducted by

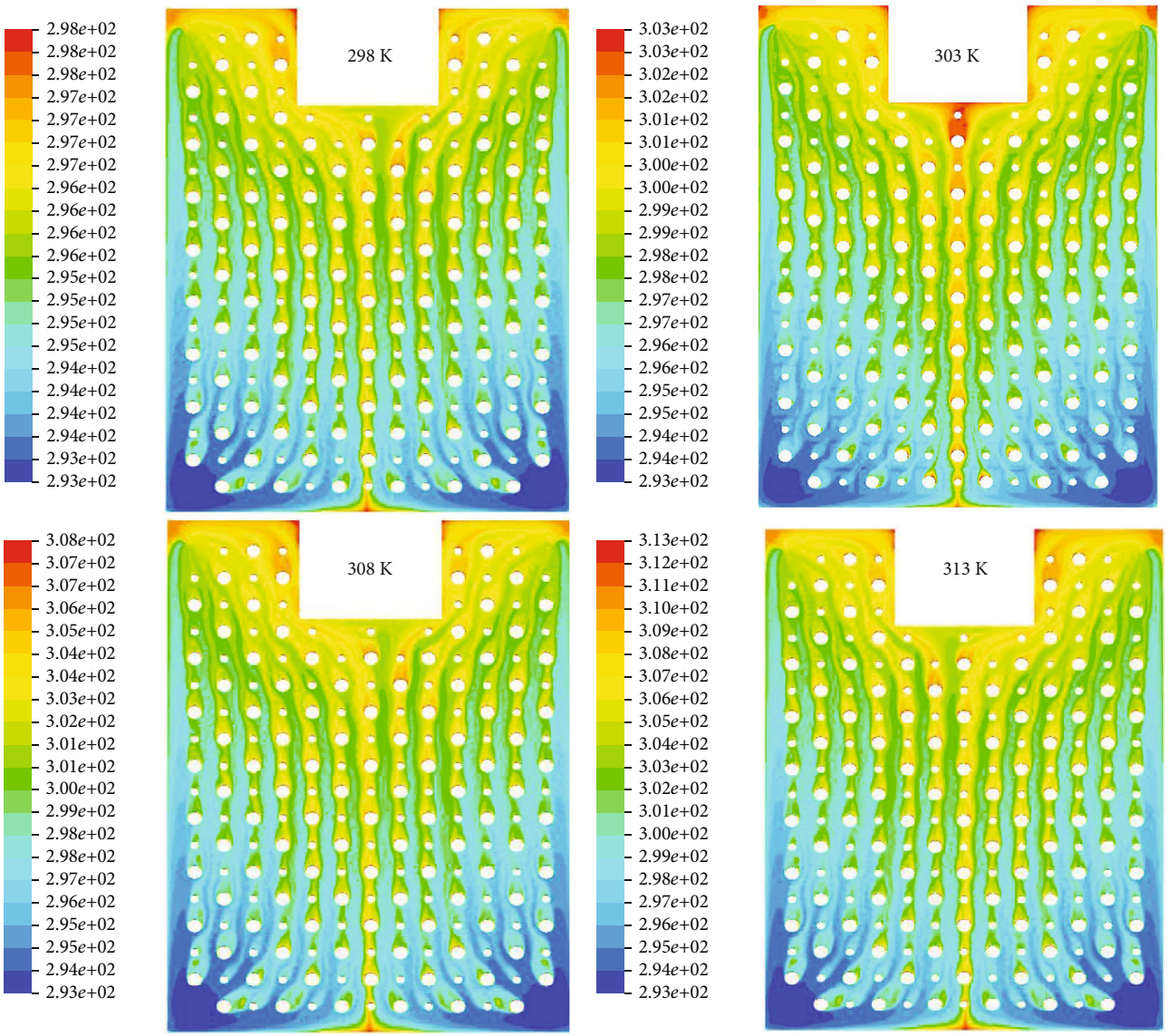

Figure 7: Temperature distribution of water (in K) at different heating surface temperatures.

Abdin and Rachid [33]. It was also found that the PV efficiency drops with the rise in the PV panel temperature.

3.2. Effect of the Geometry Parameters

3.2.1. Corrugation Number. Two ways to change the corrugation number were investigated in this study. One is removing all the small corrugations and keeping all the large corrugations retained (Figure 10), and the other is removing all the large corrugations and keeping all the small corrugations retained. The panel size, other geometric parameters, model, and boundary conditions remain constant. The outlet temperatures of three types of plates under different inlet velocities are shown in Figure 11.

No matter how the corrugation number changes, the heat transfer performance of the hybrid PV/T collector with corrugations is higher than the flat plate collector, and the changing trend of the outlet temperature is similar. As the inlet velocity increases, the outlet temperature decreases while the heat collection increases. When the water inlet velocity changes from 0.2 to 1.0 m/s, the heat collection is between 15.0 and 44.0 MJ per hour.

The changes in the corrugation number on the hybrid PV/T collector performance are not so significant. The impact of the corrugation number on the outlet temperature and heat collection has a certain relationship with the inlet velocity. The outlet temperature of the absorber plate after removing all the small corrugations is slightly higher compared with the original absorber plate when the inlet velocity is less than 0.4 m/s or more than 0.7 m/s. However, when the inlet velocity is between 0.4 m/s and 0.6 m/s (Figure 11), the outlet temperature of the absorber plate after removing all the small corrugations becomes slightly lower than the original absorber plate. While the outlet temperature of the absorber plate after removing all the large corrugations is slightly higher when the inlet velocity is less than 0.45 m/s, it is slightly lower when the inlet velocity is more than 0.45 m/s (Figure 11).

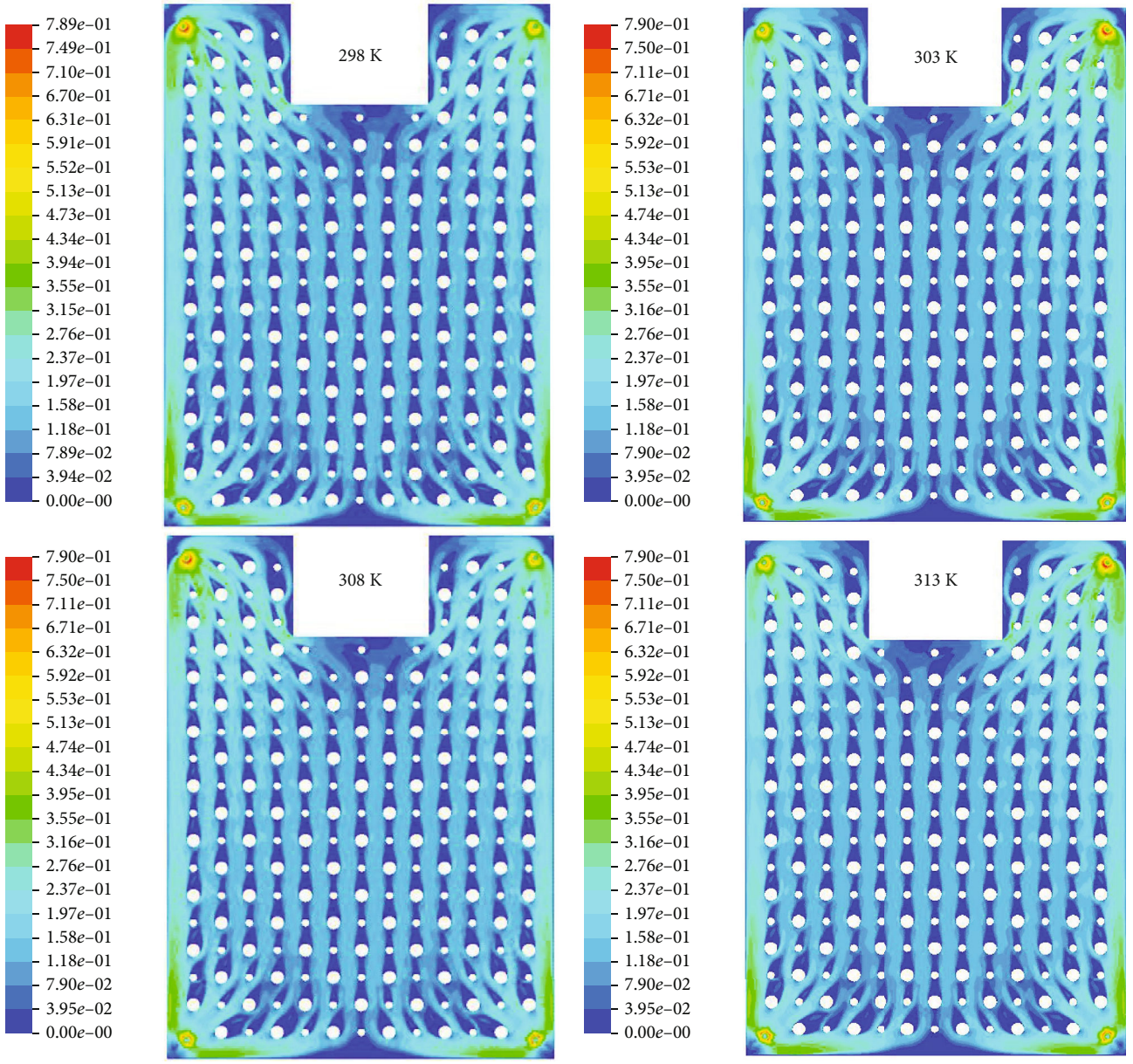

Figure 8: Velocity distribution of internal working fluids (in m/s) at different heating surface temperatures.

The differences in the shape of the collector surface have a direct impact on the flow of the heat transfer fluid and the overall heat transfer coefficient [32]. Removing all the small or large corrugations will increase the contact area between the fluid and the absorber plate and thus lead to sufficient heat transfer. However, it also decreases the flow disturbances between the two panels, leading to a weakened heat transfer. A previous study [34] also reported that the presence of sinusoidal corrugations provides higher flow disturbances, resulting in a significant enhancement in heat transfer. On the other hand, the influence of the corrugation number on the outlet temperature could be offset by the changes in the inlet velocity. That is why the impact of the changes in the corrugation number on the hybrid PV/T collector performance is not so significant.

3.2.2. Corrugation Area. Two ways to change the corrugation area were studied in this work. One is changing all the small corrugations to the large ones (Figure 12), and the other is changing all the large corrugations to the small ones. The panel size, other geometric parameters, model, and boundary conditions are the same as with the original absorber plate. The outlet temperature and heat collection of three types of plates under different inlet velocities are shown in Figure 13.

As shown in Figure 13, as the inlet velocity increases, the outlet temperature gradually decreases, and the decreasing amplitude comes to a lower level. When the inlet velocity changes from 0.2 to 1.0 m/s, the outlet temperature of the absorber plate with all small corrugations changed to the large ones is between 301 and 298 K, and the heat collection

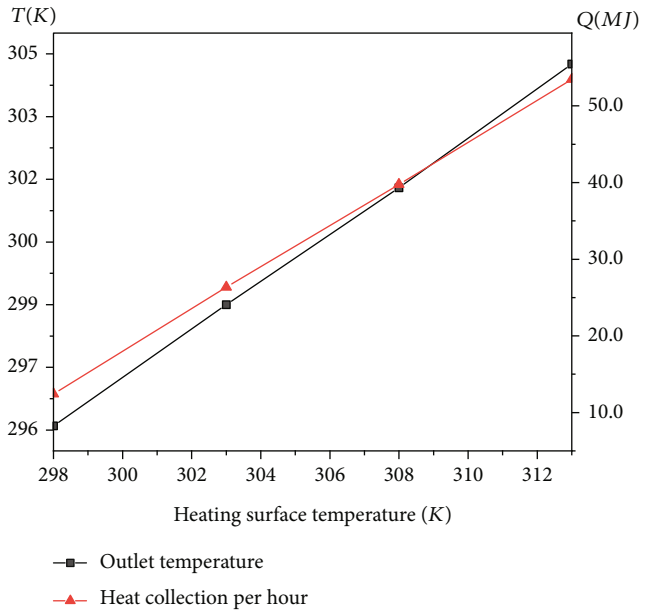

Figure 9: Outlet temperature and heat collection at different heating temperatures.

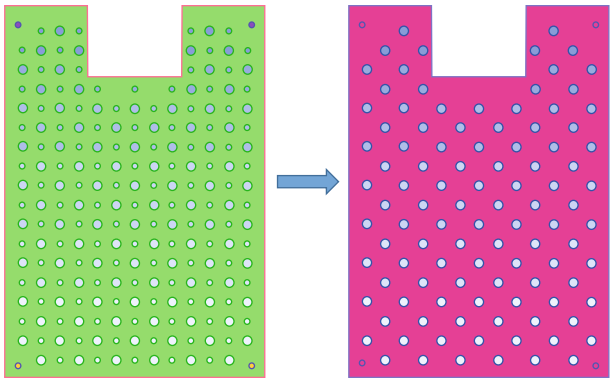

Figure 10: Heat absorber plate with removing all the small corrugations (right).

is in the range of 14.8 to 46.2 MJ/h. Compared with the original heat absorber plate, the heat collection per hour increases gradually at the same flow velocity, and the maximum increment of heat collection is 6.6%. While the absorber plate's outlet temperature is between 301 and 297 K after changing all large corrugations to the small ones, the heat collection is in the range of 14.7-35.7 MJ/h (Figure 13).

With the inlet velocity changing, the outlet temperature of the original plate and the plate with changing corrugation area is significantly higher than the flat plate. When the inlet velocity is greater than 0.4 m/s, the outlet temperature of the heat absorber plate with all small corrugations changing to the large ones is higher than the original plate (Figure 13). However, when the inlet velocity is greater than 0.5 m/s, the outlet temperature of the present absorber plate after changing all large corrugations to the small ones is lower than the original plate (Figure 13).

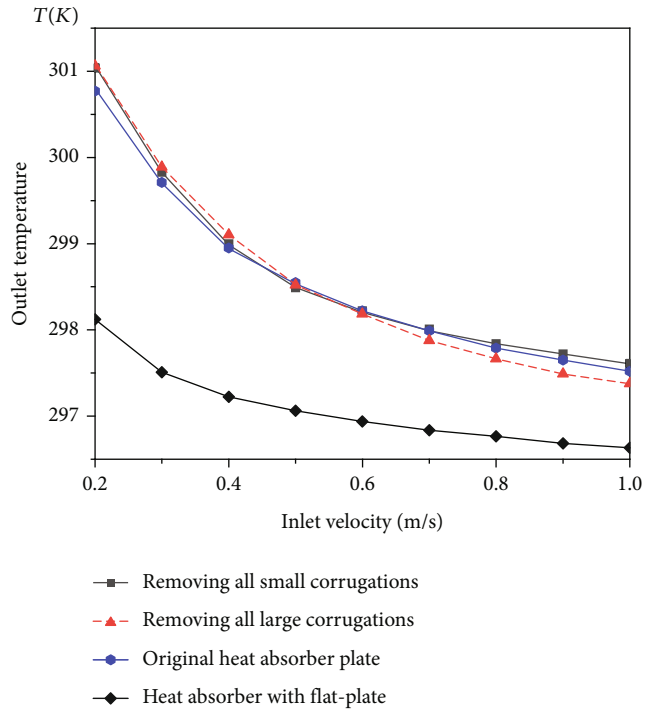

Figure 11: Outlet temperature comparison of three types of absorber plates after changing the corrugation number.

The outlet temperature increased after changing the corrugation area, especially after changing all small corrugations to the large ones when the inlet flow velocity was greater than 0.4 m/s. Besides, due to the flow around the corrugations, the internal water was heated by the back-facing of the PV plate, which was also heated by the increased corrugations. The PV temperature decreases with the increase in the water inlet velocity. Moreover, changing the corrugation area especially changing all large corrugations to the small ones could increase the contact area between the water and the absorber panel. However, it also reduces the flow disturbances caused by the corrugations.

The mass flow rate considered in this study is based on the previously reported experimental evaluation of the PV/T panel, employing a nominal mass flow rate of 0.83 L min^{-1} m^{-2} and a maximum mass flow rate of 3.83 L min^{-1} m^{-2}. Previous studies [22, 30] reported that increasing the fluid flow rate leads to a lower outlet temperature and a higher thermal efficiency of the PV/T panel. It also reported that the experimental thermal efficiency will reach its "optimum point" at a mass flow rate of 5 L/min [22]. Therefore, the PV/T panel exhibits an optimal mass flow rate at a certain solar irradiance. The optimal mass flow rate and the structural parameters, such as the corrugation number and the area, will be considered in the subsequent applied study, referring to the local solar irradiance in combination with the mass flow rate to obtain the high thermal efficiency. Therefore, changing corrugation area does affect the absorber plate performance to a certain extent, but the optimal corrugation area that improves the heat transfer characteristics should be further studied.

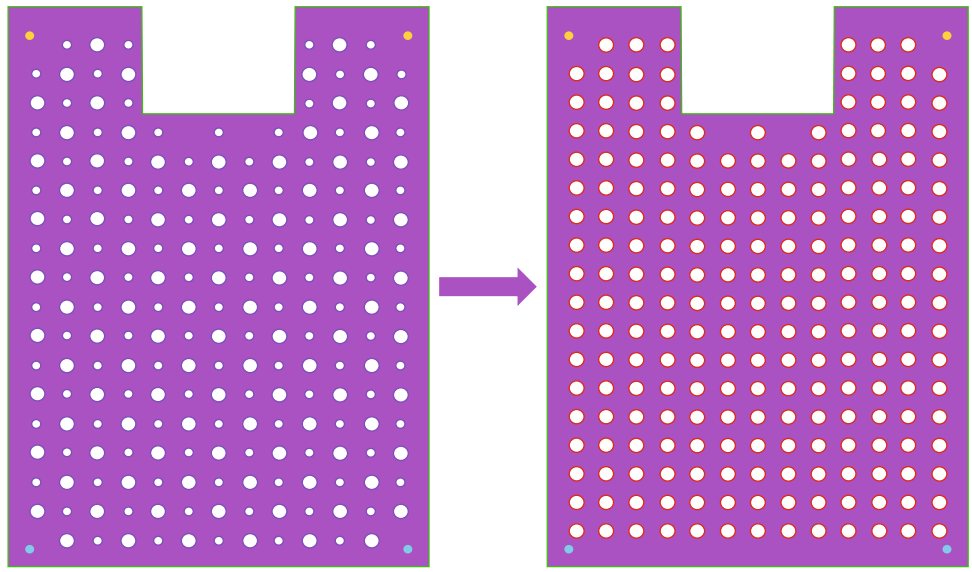

Figure 12: Heat absorber plate with changing all small corrugations to large ones (right).

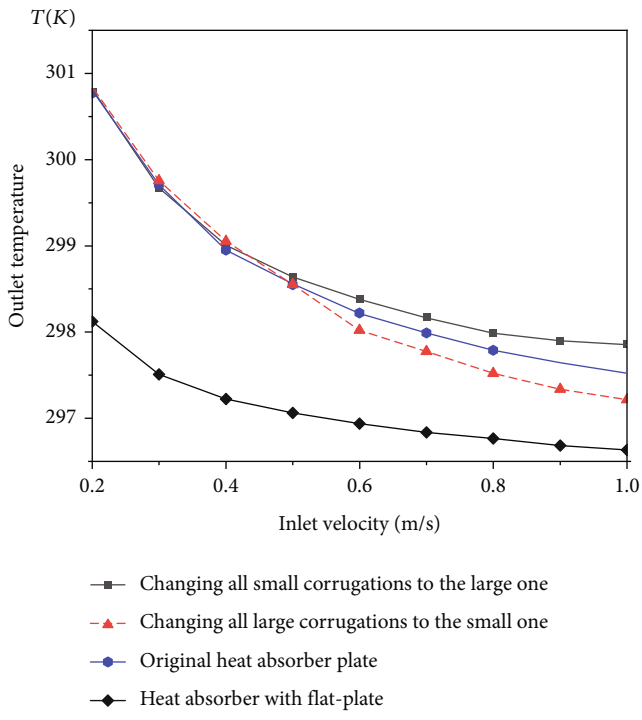

Figure 13: Outlet temperature comparison of three types of absorber plates after changing corrugation area.

3.2.3. Flow Channel Width. Two ways to change the flow channel width were implemented in this study. One is changing the width from 4 to 5 mm (Figure 14(a)), and the other is changing to 3 mm (Figure 14(b)). The plate size, other geometric parameters, model, and boundary conditions are the same as for the original plate. The outlet temperature and heat collection of three types of absorber plates under different inlet velocities are shown in Figure 14.

As shown in Figure 15, as the flow velocity increases, the outlet temperature gradually decreases. When the inlet velocity changes from 0.2 to 1.0 m/s, the outlet temperature of the plate with a 5 mm width is between 297 and 302 K, and the heat collection is in the range of 16.1-39.2 MJ/h. Compared to the original absorber plate, when the inlet velocity is less than 0.3 m/s, the outlet temperature of the plate with a 5 mm width flow channel is higher. On the other hand, the outlet temperature is lower than that of the original absorber plate when the inlet velocity is greater than 0.4 m/s.

The outlet temperature of the absorber plate with a 3 mm width flow channel is significantly higher than both the flat plate and the original plate at different inlet velocities, which is between 298 and 302 K. The heat collection is in the range of 16.3-51.4 MJ/h. Compared with the original PV/T panel, the heat collection per hour increases gradually at the same flow velocity, and the maximum increment in heat collection is 18.6%. This may be owing to the corrugations and narrow flow channel increasing flow obstruction. The presence of corrugations provides higher flow disturbances and pressure drop increases with the decrease in the fin spacing, leading to significant enhancement in heat transfer [34, 35].

The heat transfer characteristics of the hybrid PV/T panel could be improved by changing the flow channel width from 4 mm to 3 mm. Regardless of the employed velocity, the outlet temperature of the absorber plate with a 3 mm flow channel width is higher than that of an absorber plate with a 4 mm channel width. However, the best channel width to enhance the performance of the heat absorber plate should match the corrugation number and area. The collector structure could be optimized when the heat collection generated by changing corrugation area and corrugation number, combined with the heat caused by changing the flow channel width, is positive, which will be carried out in the follow-up study.

Above all, the flow channel width has influences on outlet temperature and heat collection of the hybrid PV/T panel. The heat transfer performance of the hybrid PV/T

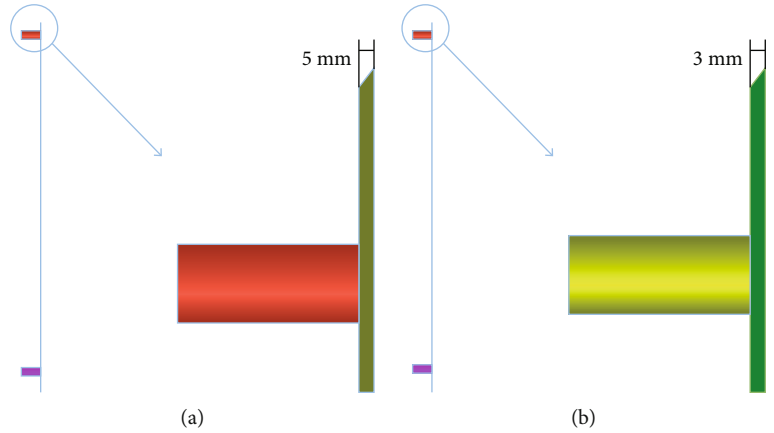

Figure 14: (a) 5 mm width flow channel and (b) 3 mm width flow channel.

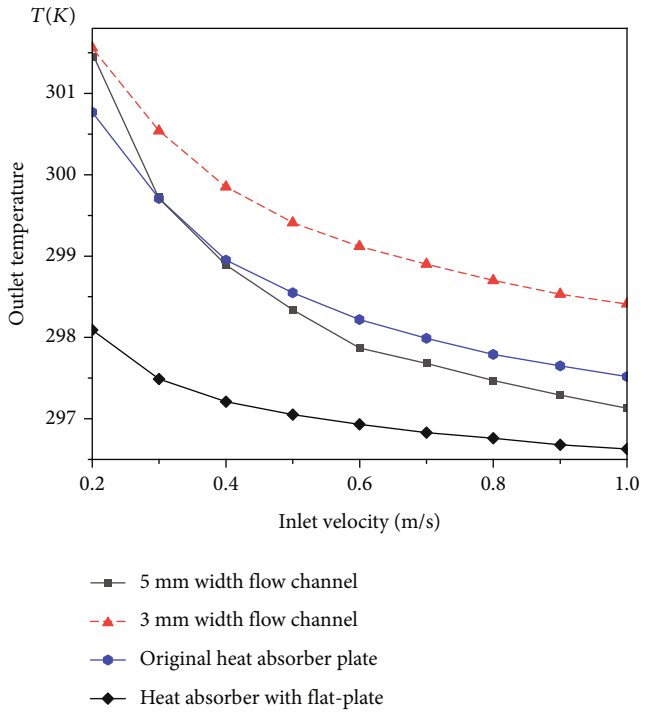

Figure 15: Outlet temperature comparison of three types of absorber plates after changing the flow channel width.

collector with corrugations is higher than the flat plate collector no matter how to change its relevant parameters, which accords with the previous study [34] that also reported that the PV/T panel could enhance thermal efficiency compared to the stand-alone PV panel.

4. Conclusion

In this study, the steady-state flow and heat transfer characteristics of a hybrid PV/T collector with corrugated channels were investigated numerically to investigate the influence of the inlet velocity and heating surface temperature on the thermal performance of the PV/T collector. In order to support the structural optimization of the heat absorber plate to improve the heat collection efficiency, the influences of the structural parameters such as corrugation number, corrugation area, and flow channel width on the heat transfer characteristics were also discussed. The numerical results indicated that

(1) compared with the collector with a flat plate, the outlet temperature of the hybrid PV/T panel with the added corrugations is significantly increased

(2) the outlet temperature and heat collection of the hybrid PV/T panel are affected by the water inlet velocity, corrugated area, and flow channel width

(3) when the inlet velocity is greater than 0.4 m/s, the outlet temperature of the collector plate with all the small corrugations changed to the large ones is higher than the original heat absorber plate, enhancing the heat collection

(4) as the width between the two plates of the hybrid PV/T collector decreases from 4 mm to 3 mm, the improvement of flow heat transfer characteristics significantly leads to the performance enhancement of the heat collection

This study is complementary to the previous studies [30, 31], is limited to the comprehensive effect of the structure parameters of the built-in corrugated channels on the flow and heat transfer, and expands the library of comprehensive evaluation and optimal design of the built-in corrugated channels. The use of a particular absorber is considered based on its uniformity, pressure drop, heat transfer area, mass flow rates, etc. In future investigations, the optimal corrugation number, corrugation area, and flow channel width will be combined with laboratory measurements for a more comprehensive and detailed evaluation.

Data Availability

Some or all data, models, or codes that support the findings of this study are available from the corresponding author upon reasonable request.

Conflicts of Interest

The authors declare that they have no conflicts of interest.

Acknowledgments

This work was funded by the Fundamental Research Funds for the Central Universities (Nos. 3142019017 and 3142021005) and supported by the Higher Education Teaching Reform Research and Practice Project of Hebei Province (No. 2018GJJG479).

References

[1] M. Chandrasekar and T. Senthilkumar, "Five decades of evolution of solar photovoltaic thermal (PVT) technology - a critical insight on review articles," *Journal of Cleaner Production*, vol. 322, article 128997, 2021.

[2] A. Herez, H. El Hage, T. Lemenand, M. Ramadan, and M. Khaled, "Review on photovoltaic/thermal hybrid solar collectors: classifications, applications and new systems," *Solar Energy*, vol. 207, pp. 1321–1347, 2020.

[3] N. Goel, R. A. Taylor, and T. Otanicar, "A review of nanofluid-based direct absorption solar collectors: design considerations and experiments with hybrid PV/thermal and direct steam generation collectors," *Renewable Energy*, vol. 145, pp. 903–913, 2020.

[4] S. Kiwan and I. Salim, "A hybrid solar chimney/photovoltaic thermal system for direct electric power production and water distillation," *Sustainable Energy Technologies and Assessments*, vol. 38, article 100680, 2020.

[5] C. Zhang, J. Li, and Y. Chen, "Improving the energy discharging performance of a latent heat storage (LHS) unit using fractal-tree-shaped fins," *Applied Energy*, vol. 259, article 114102, 2020.

[6] A. Fudholi, K. Sopian, M. Gabbasa et al., "Techno-economic of solar drying systems with water based solar collectors in Malaysia: a review," *Renewable and Sustainable Energy Reviews*, vol. 51, pp. 809–820, 2015.

[7] L. Sahota and G. N. Tiwari, "Review on series connected photovoltaic thermal (PVT) systems: analytical and experimental studies," *Solar Energy*, vol. 150, pp. 96–127, 2017.

[8] M. Kosan and M. Aktas, "Performance investigation of a double pass PVT assisted heat pump system with latent heat storage unit," *Applied Thermal Engineering*, vol. 199, article 117524, 2021.

[9] P. Mi, J. Zhang, Y. Han, and X. Guo, "Study on energy efficiency and economic performance of district heating system of energy saving reconstruction with photovoltaic thermal heat pump," *Energy Conversion and Management*, vol. 247, article 114677, 2021.

[10] S. Tiwari, J. Bhatti, G. N. Tiwari, and I. M. al-Helal, "Thermal modelling of photovoltaic thermal (PVT) integrated greenhouse system for biogas heating," *Solar Energy*, vol. 136, pp. 639–649, 2016.

[11] A. Giwa, A. Yusuf, A. Dindi, and H. A. Balogun, "Polygeneration in desalination by photovoltaic thermal systems: a comprehensive review," *Renewable and Sustainable Energy Reviews*, vol. 130, article 109946, 2020.

[12] A. A. Monjezia, Y. Chen, R. Vepa et al., "Development of an off-grid solar energy powered reverse osmosis desalination system for continuous production of freshwater with integrated photovoltaic thermal (PVT) cooling," *Desalination*, vol. 495, article 114679, 2020.

[13] S. T. Pourafshar, K. Jafarinaemi, and H. Mortezapour, "Development of a photovoltaic-thermal solar humidifier for the humidification- dehumidification desalination system coupled with heat pump," *Solar Energy*, vol. 205, pp. 51–61, 2020.

[14] M. Carmona, A. P. Bastos, and J. D. García, "Experimental evaluation of a hybrid photovoltaic and thermal solar energy collector with integrated phase change material (PVT-PCM) in comparison with a traditional photovoltaic (PV) module," *Renewable Energy*, vol. 172, pp. 680–696, 2021.

[15] M. Khodadadi and M. Sheikholeslami, "Numerical simulation on the efficiency of PVT system integrated with PCM under the influence of using fins," *Solar Energy Materials and Solar Cells*, vol. 233, article 111402, 2021.

[16] A. S. Abdelrazik, F. A. Al-Sulaiman, R. Saidur, and R. Ben-Mansour, "A review on recent development for the design and packaging of hybrid photovoltaic/thermal (PV/T) solar systems," *Renewable and Sustainable Energy Reviews*, vol. 95, pp. 110–129, 2018.

[17] G. Wang, B. Wang, X. Yuan, J. Lin, and Z. Chen, "Novel design and analysis of a solar PVT system using LFR concentrator and nano-fluids optical filter," *Case Studies in Thermal Engineering*, vol. 27, article 101328, 2021.

[18] I. Nkurikiyimfura, Y. Wang, B. Safari, and E. Nshingabigwi, "Electrical and thermal performances of photovoltaic/thermal systems with magnetic nanofluids: a review," *Particuology*, vol. 54, pp. 181–200, 2021.

[19] S. Kumar, R. Thakur, A. Singhy, R. K. Tripathi, and M. Sethi, "A review of heat removal mechanism in concentrated PVT systems using beam splitter," *Materials Today: Proceedings*, vol. 50, pp. 952–961, 2022.

[20] R. Tripathi and G. N. Tiwari, "Annual performance evaluation (energy and exergy) of fully covered concentrated photovoltaic thermal (PVT) water collector: an experimental validation," *Solar Energy*, vol. 146, pp. 180–190, 2017.

[21] A. N. Ozakin and F. Kaya, "Effect on the exergy of the PVT system of fins added to an air-cooled channel: a study on temperature and air velocity with ANSYS Fluent," *Solar Energy*, vol. 184, pp. 561–569, 2019.

[22] A. L. Abdullah, S. Misha, N. Tamaldin, M. A. M. Rosli, and F. A. Sachit, "Theoretical study and indoor experimental validation of performance of the new photovoltaic thermal solar collector (PVT) based water system," *Case Studies in Thermal Engineering*, vol. 18, article 100595, 2020.

[23] M. Hissouf, M. Feddaoui, M. Najim, and A. Charef, "Performance of a photovoltaic-thermal solar collector using two types of working fluids at different fluid channels geometry," *Renewable Energy*, vol. 162, pp. 1723–1734, 2020.

[24] M. Yu, F. Chen, S. Zheng et al., "Experimental investigation of a novel solar micro-channel loop-heat-pipe photovoltaic/thermal (MC-LHP-PV/T) system for heat and power generation," *Applied Energy*, vol. 256, article 113929, 2019.

[25] E. Çiftçi, A. Khanlari, A. Sözen, İ. Aytaç, and A. D. Tuncer, "Energy and exergy analysis of a photovoltaic thermal (PVT) system used in solar dryer: a numerical and experimental investigation," *Renewable Energy*, vol. 180, pp. 410–423, 2021.

[26] E. Arslan, M. Aktas, and O. F. Can, "Experimental and numerical investigation of a novel photovoltaic thermal (PV/T)

collector with the energy and exergy analysis," *Jouranl of Cleaner Production*, vol. 276, article 123255, 2020.

[27] J. Yao, W. Liu, Y. Zhao, Y. Dai, J. Zhu, and V. Novakovic, "Two-phase flow investigation in channel design of the roll-bond cooling component for solar assisted PVT heat pump application," *Energy Conversion and Management*, vol. 235, article 113988, 2021.

[28] W. Fan, G. Kokogiannakis, and Z. J. Ma, "A multi-objective design optimisation strategy for hybrid photovoltaic thermal collector (PVT)-solar air heater (SAH) systems with fins," *Solar Energy*, vol. 163, pp. 315–328, 2018.

[29] C. Yu, H. Li, J. Chen, S. Qiu, F. Yao, and X. Liu, "Investigation of the thermal performance enhancement of a photovoltaic thermal (PV/T) collector with periodically grooved channels," *Journal of Energy Storage*, vol. 40, article 102792, 2021.

[30] P. Xu, X. X. Zhang, J. C. Shen, X. Zhao, W. He, and D. Li, "Parallel experimental study of a novel super-thin thermal absorber based photovoltaic/thermal (PV/T) system against conventional photovoltaic (PV) system," *Energy Report*, vol. 1, pp. 30–35, 2015.

[31] Q. P. Li, J. S. Wu, G. J. Wang et al., "Numerical simulation and experimental test of a novel compact solar collector with internally extruded pin-fin flow channel (in Chinese)," *HV & AC*, vol. 50, pp. 103–110, 2020.

[32] A. K. Hussein, T. C. Miqdam, A. H. Al-Waeli, and K. Sopian, "Comparison and evaluation of solar photovoltaic thermal system with hybrid collector: an experimental study," *Thermal Science and Engineering Progress*, vol. 22, article 100845, 2021.

[33] Z. U. Abdin and A. Rachid, "Bond graph modeling of a water-based photovoltaic thermal (PV/T) collector," *Solar Energy*, vol. 220, pp. 571–577, 2021.

[34] M. S. Manjunath, K. V. Karanth, and N. Y. Sharma, "Numerical investigation on heat transfer enhancement of solar air heater using sinusoidal corrugations on absorber plate," *International Journal of Mechanical Sciences*, vol. 138-139, pp. 219–228, 2018.

[35] A. Priyam and P. Chand, "Thermal and thermohydraulic performance of wavy finned absorber solar air heater," *Solar Energy*, vol. 130, pp. 250–259, 2016.

Hindawi
International Journal of Photoenergy
Volume 2022, Article ID 4912922, 14 pages
https://doi.org/10.1155/2022/4912922

Research Article

Insights into the Enhancement Mechanisms of Molten Salt Nanofluids

Xiong Yaxuan,[1] **Wang Huixiang**,[1] **Wang Zhenyu**,[1] **Wu Yuting**,[2] **Xu Qian**,[3] **Wang Gang**,[1] **Li Chuan**,[2] **Ding Yulong**,[4] **and Ma Chongfang**[2]

[1]*Beijing Key Lab of Heating, Gas Supply, Ventilating and Air Conditioning Engineering, Beijing University of Civil Engineering and Architecture, Beijing 100044, China*
[2]*College of Environmental and Energy Engineering, Beijing University of Technology, Beijing 100124, China*
[3]*School of Energy and Environmental Engineering, University of Science and Technology Beijing, Beijing 100083, China*
[4]*Birmingham Center for Energy Storage, University of Birmingham, Birmingham B15 2TT, UK*

Correspondence should be addressed to Xiong Yaxuan; xiongyaxuan@bucea.edu.cn, Xu Qian; qianxu@ustb.edu.cn, and Li Chuan; lichuan@bjut.edu.cn

Received 13 January 2022; Revised 1 June 2022; Accepted 18 August 2022; Published 13 September 2022

Academic Editor: Daniel T. Cotfas

The addition of nanomaterials to molten salts can significantly improve their thermal performance. To explore the enhancement mechanisms, this work prepared carbonate salt nanofluids with binary carbonate as base salt and 20 nm SiO_2 and 20 nm MgO nanoparticles as additives by the commonly used aqueous solution method. Then, the key performance and micromorphology of the carbonate salt nanofluids are characterized by differential scanning calorimetry, thermal gravimetric analysis, laser flash analysis, and micromorphology analysis. Results showed that the 20 nm SiO_2 nanomaterials instead of the 20 nm MgO nanomaterials exerted higher effects on latent heat while the 20 nm MgO nanomaterials instead of the 20 nm SiO_2 nanomaterials exerted higher effects on the sensible heat, thermal conductivity, and high-temperature stability of carbonated salt. In addition, different nanostructures were observed in SiO_2-based and MgO-based molten salt nanofluids, respectively. Innovatively, formation mechanisms of molten salt nanofluids were proposed based on cloud nuclei to explain the different enhancements in this work.

1. Introduction

As efficient thermal energy storage (TES) materials, molten salt has been widely used in the fields of waste heat recovery, concentrating solar power, and valley power utilization [1, 2]. In recent years, researchers observed that nanomaterials can further improve the TES performance of molten salts and reduce the size of TES systems which will save initial investment cost greatly from investors [3].

In the development process of molten salt nanofluids, Shin and Banerjee conducted the first work and found the anomalous effect of nanomaterials on carbonate salt [3]. In their innovative work [3], Shin and Banerjee added SiO_2 nanoparticles to binary carbonate salt (61.5 mol.% Li_2CO_3-37.5 mol.% K_2CO_3) and found a maximal increase of 24% in specific heat. Moreover, they attributed the anomalous increase to the percolation networks observed in their carbonate salt nanofluid. Later, nanomaterials like SiO_2, MgO, Al_2O_3, SiC, carbon nanotubes (CNTs), graphene, TiO_2, and their mixtures have also been used as additives [4]. Shin and Banerjee [5] added 1.0 wt.% of 10 nm Al_2O_3 nanoparticles to the above binary carbonate salt by the aqueous solution (AS) method, and they obtained that the maximum specific heat increased by about 33% as well as a large number of chain-like nanostructures. Shin and Banerjee [6] prepared carbonate salt nanofluids by dispersing 1.0 wt.% of SiO_2 nanoparticles to the binary carbonate eutectic via the AS method. They observed maximal increases of 14.59% in specific heat and 47% in thermal conductivity, respectively. Shin and Banerjee [7] found high-dense network

substructures in alkali chloride nanofluids with SiO_2 nanoparticles and proposed the three-mode mechanism: (a) the specific heat of nanoparticles is higher than that of the bulk of SiO_2; (b) solid-fluid interaction energy; and (c) liquid molecules are layered on the surface of the nanoparticles, forming a semi-solid layer. Now, the first mode has been confirmed to be not applicable to some molten salt nanofluids. Tiznobaik and Shin [8] found needle-like structures in binary carbonate salt nanofluids with SiO_2 nanoparticles, and they concluded that the high specific surface area of the embedded nanoparticles and the nanoparticle-induced needle-like structures appear to be related to the enhancement of specific heat. Shin and Banerjee [5] considered that the chain-like nanostructures in molten salt nanofluids were responsible for the improvement of specific heat of molten salt nanofluids and that the specific heat can only be improved by the secondary long-range nanostructures formed in carbonate salt nanofluids. Shin and Banerjee [6] attributed the increased thermal conductivity of carbonate salt nanofluids to the observed percolation networks with a higher density phase. Shin et al. [9] considered that a salt component electrostatically interacts with nanoparticles to lead to a microseparation phenomenon of the molten salt mixture, and then, the separated component salt crystallizes on the nanoparticle surface to form the fractal-like fluid nanostructures, which enhance the specific heat of molten salt nanofluids. They also observed the theoretical thermodynamic mixing model [10], thermal conductivity by Hamilton-Crosser model [11], and Maxwell-Garnett model [12] for traditional nanofluids that do not match with the molten salt nanofluids. Rizvi and Shin [4] proposed the theory "development of dendritic structure" to describe the formation of molten salt nanofluids based on theories of the electric double layer and the microsegregation of a binary mixture due to electrostatic interaction and explained how the specific heat of molten salt nanofluids is increased. This theory considers that the dendritic structure on nanoparticles is only one component salt molecule in the molten salt mixture. However, this mechanism is difficult to explain other enhancements like the heat of fusion and the thermal conductivity. Tiznobaik and Shin [13] dispersed 1.0 wt.% of SiO_2 nanoparticles to binary carbonate (62 mol.% lithium carbonate-38 mol.% potassium carbonate) and observed that the specific heat was increased by about 26%. They also concluded that the carbonate salt nanofluids are a mixture of solid nanoparticles, solid nanostructures near nanoparticles, and liquid salt while nanostructures are the cause of increase of specific heat.

Moreover, researchers all over the world are devoted to molten salt nanofluids. Tiznobaik et al. [14] compared the specific heat of the above binary carbonate salt with 1.0 wt.% of different 10 nm nanoparticles, and they observed that the specific heat of MgO, SiO_2, and Al_2O_3 nanoparticles increased by 22%, 27%, and 33%, respectively. Tiznobaik et al. [14] considered that the great specific surface of nanoparticles induced the secondary long-range nanostructures in molten salt nanofluids, and the secondary long-range nanostructures primarily dominated the improvement of specific heat of carbonate salt nanofluids. Jo and Banerjee [15] dispersed 0.1 wt.% of 50 nm graphite nanoparticles to the above binary carbonate and obtained the maximum increase of specific heat of 57%. They also found dense compressed layers on the surface of graphite nanoparticles by scanning electron microscopy (SEM). Jo and Banerjee [16] investigated the effect of multiwalled CNTs on the specific heat of above carbonate salt and found the maximal increases of 15% and 12% in specific heat in liquid and solid state, respectively. Kwak et al. [17] added 2.5 wt.% of SiO_2 nanoparticles to a binary carbonate (62 mol.% lithium carbonate-38 mol.% potassium carbonate) by the AS method, and a maximal increase of 14.59% in specific heat was observed. Based on their research results, Keblinski et al. [18] considered that both the ballistic and the direct or fluid-mediated clustering effects provide a way for rapid heat transport. In addition, they thought that the liquid layer at the liquid/particle interface should be at least several nanometers. Xue et al. [19] found that the thickness of layering of the simple liquid atoms at the liquid-solid interface was several atoms using molecular dynamic simulations and thought that the layering of the simple liquid atoms at the liquid-solid interface did not have any noticeable effect on the heat transport properties. Nevertheless, they also thought that the thickness of the complex liquid atom layering at the liquid-solid interface could extend over longer distances from the interfaces. Oh et al. [20] found the ordered molecule layer at the liquid aluminum/sapphire interface by TEM tests. Using $LiNO_3$ liquid and 10-nm Al_2O_3 nanoparticles, Matthew [21] calculated the thickness of adsorbed layer on the interface. A thickness of 7.1 ± 0.6 nm for enthalpy of fusion and a thickness of 5.3 ± 0.5 nm for specific heat are obtained for 1.0% Al_2O_3 nanoparticles while a thickness of 7.1 ± 0.6 nm for enthalpy of fusion and a thickness of 6.7 ± 0.6 nm for specific heat are obtained for 2.0% Al_2O_3 nanoparticles. This thickness is in the order as what has been reported in literatures [20, 22]. Hentschke [23] argued that the impact of nanoparticles on surrounding liquid was of long range (100 nm or farther) and the formed interfacial mesolayers interacted with each other, which improved the specific heat of molten salt nanofluids. Our recent work [24] found that SiO_2 nanoparticles can also enhance the heat of fusion, specific heat, thermal conductivity, and upper operating temperature of single component salts. Sang and Liu [25] studied the effect of different nanoparticles on a ternary carbonate salt (40 wt.% K_2CO_3-40 wt.% Li_2CO_3-20 wt.% Na_2CO_3), and maximal increases of 116.8%, 73.9%, 56.5%, and 66.5% in specific heat were observed by adding SiO_2, CuO, TiO_2, and Al_2O_3 nanoparticles. Meanwhile, they attributed the increase of specific heat to the dispersion state and quantities of the formed needle-like nanostructures.

It is concluded from the above review that the increased levels in latent heat, specific heat, and thermal conductivity obtained by different researchers are quite different while different microstructures are observed although the nanoparticle, the base salt, and the preparation method employed by these researchers are the same. Therefore, explanations on the enhancement mechanisms of nanoparticles on base salt by different authors are abhorrent.

To explain the enhancement mechanisms of nanoparticles on molten salts, innovatively, this work proposed the formation mechanisms of molten salt nanofluids from the perspective of molecules according to the experimental results in this work and publications and attempted to interpret the mechanism of enhancing the thermal performance of molten salts by adding nanoparticles.

2. Materials and Methods

To provide a basis for the formation mechanisms proposed in Section 3.4, some experiments have been done based on the existing composition of molten salt nanofluid in published literatures.

2.1. Material Preparation. In this work, analytical reagents (Li_2CO_3 and K_2CO_3) were used as component salts to prepare base salt. MgO nanoparticles and SiO_2 nanoparticles were added as additives to prepare carbonate nanofluids, respectively. The purity of the component salts is above 99.0% while the SiO_2 nanoparticles and the MgO nanoparticles were selected with the purity of over 99.8%. MgO and SiO_2 nanoparticles with a mass fraction of 1.0 were dispersed into the base salt (62 mol.% Li_2CO_3-38 mol.% K_2CO_3), respectively. Table 1 shows the specific properties of component salts and nanomaterials.

In this work, the base salt (binary carbonate salt) is prepared with the following steps:

(1) Dried component salts of sodium carbonate and potassium carbonate in a muffle furnace at 300 ˚C for at least 24 h

(2) Weight the dried component salts based on the appropriate mass ratio by an analytical balance (ME 104/02, Mettler Toledo, 0.1 mg) [24], respectively

(3) Ground the component salts in a high-speed disintegrator for 10 s to form a base salt to prepare molten salt nanofluids

(4) Dried the base salt in a drying oven at 170 ˚C for the next preparation process

Molten salt nanofluids containing SiO_2 and MgO nanoparticles are prepared by the AS method, respectively, as described below (Figure 1):

(1) Weighted the base salt and nanoparticles according to preset mass ratio by an analytical balance, respectively

(2) Dispersed different mass ratios of nanoparticles into deionized water at a mass ratio of 1 : 10 and then stirred the solution for 2 h through an ultrasonic agitator to form a homogeneous suspension

(3) Dissolved the base salt into the nanoparticle suspension and stirred until completely dissolved

Table 1: Specific properties of the component carbonates and nanomaterials.

Materials	Purity	Size, nm	T_m, ˚C	ΔH_m, kJ/kg	λ, W/(m·K)	Manufacturer
K_2CO_3	≥99%	—	898	200	1.88	Ref. [26]
Na_2CO_3	≥99%	—	858	280	1.84	
SiO_2	≥99.8%	20	—	—	—	
MgO	≥99.8%	20	—	—	—	

(4) Evaporated the suspension in a vacuum drying oven at 95 ˚C for dehydration to form carbonate salt nanofluid powers

(5) Further dried the carbonate salt nanofluid powers at 170 ˚C for 24 h to ensure complete dehydration of material

Carbonate nanofluids containing SiO_2 nanoparticles are coded as SiO_2-nfs, and carbonate nanofluids containing MgO nanoparticles are coded as MgO-nfs.

To evaluate homogeneity of nanoparticle dispersion in molten salt nanofluids, three samples were taken from three different locations (P1, P2, and P3), as illustrated in Figure 2. For SiO_2-nfs, samples taken from the three locations were coded as samples s11, s12, and s13 while samples taken from the three places were coded as samples s21, s22, and s23 for MgO-nfs.

2.2. Characterization Methods and Uncertainty Analysis. To analyze the dispersion uniformity of nanoparticles in molten salt nanofluids, three samples were taken from different locations of the beaker for every carbonate salt nanofluid. In this work, a synchronous thermal analyzer (STA 449 F3, NETSCH) [24]) was performed to obtain the specific heat, melting point, and heat of fusion of the base salt and molten salt nanofluids using high-purity nitrogen (99.999%) as protective gas and purge gas. Three melting-solidification cycles were carried out at 10 K/min intervals for each sample, and aluminum crucibles were used for the tests. The continuous thermal cycle experiment of the sample is carried out in STA 449 F3, and measurements were repeated seven times for each sample under the same conditions. The sample was heated from 200 to 550 ˚C and then cooled to 200 ˚C in the furnace of the STA 449 F3, during which the heating rate and cooling rate were both 10 K/min.

A laser flasher (LFA 467, NETSCH) was performed to obtain the thermal diffusivity of the base salt and molten salt nanofluids using high-purity nitrogen (99.999%) as protective gas and purge gas, and the thermal conductivity of sample was calculated according to the formula in the literature [27]. Each temperature point was measured seven times, and platinum-rhodium crucibles were used for the tests. Scanning electron microscopy (SEM, SU8000, Hitachi) was performed to observe the micromorphology of base salt and molten salt nanofluids to find potential reasons for the differences in the samples.

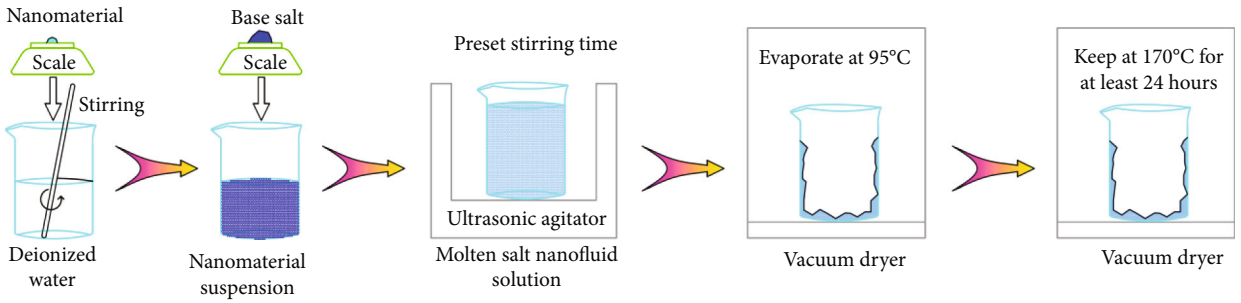

Figure 1: Preparation process of molten salt nanofluids by the AS method.

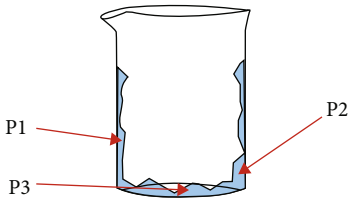

Figure 2: Carbonate nanofluid sampling locations inside the beaker.

The experimental measurement uncertainty was calculated according to the method in the literature [28]; with comprehensive consideration of the standard uncertainty of classes A and B, the measurement uncertainties of the melting point, latent heat, specific heat, and thermal conductivity were calculated to be 0.31 °C, 0.55 J/g, 0.025 J/(g·K), and 0.023 W/(m·K), respectively, in this work.

2.3. Homogeneity and Thermal Stability of Molten Salt Nanofluids

2.3.1. Homogeneity of Nanoparticles. To evaluate the dispersing homogeneity of nanoparticles in carbonate nanofluids, three samples are taken from the three different locations for each nanofluid as described in Section 2.1, and their specific heats are measured, respectively. Table 2 shows the average solid and liquid state specific heats of carbonate nanofluids. In this table, the test results in the first three lines are the average of three cycles.

Table 2 shows that by adding MgO nanoparticles, the average specific heats of the three samples from the three locations are 27.5% and 34.1% higher than those of the base salt in solid state and liquid state, while by adding SiO_2 nanoparticles, the average specific heats of the three samples from different places are only 11.0% and 20.7% higher than those of the base salt in both solid and liquid states. Especially, the standard deviations of the three samples of MgO-nfs are 0.012 J/(g·K) in solid state and 0.054 J/(g·K) in liquid state, while the standard deviations of the three samples of SiO_2-nfs are 0.022 J/(g·K) in solid state and 0.036 J/(g·K) in liquid state. These standard deviations indicate that the dispersion of nanoparticles in the three locations is homogeneous.

2.3.2. Thermal Stability. To investigate the thermal stability of both carbonate nanofluids, the carbonate nanofluid samples were measured repeatedly through ten continuous heating-cooling cycles of 200-560-200 °C. Excluding the phase change process, the average specific heat of carbonate salt nanofluids in solid state and liquid state is shown in Figure 3.

Figure 3 indicates that the average specific heat of both carbonate salt nanofluids keeps generally constant and no obvious variation is found in the specific heats of both carbonate nanofluids after undergoing ten continuous heating-cooling cycles. This indicates that both carbonate nanofluids have excellent thermal stability.

The thermogravimetric curves of both carbonate nanofluids during the heating process are shown in Figure 4. It is observed that the mass losses are 3.49% for MgO-nfs and 4.32% for SiO_2-nfs, respectively, as the carbonate nanofluids are heated up to 1000 °C. The mass loss of base salt is greater than that of both carbonate nanofluids. Obviously, during the heating process, the mass loss of MgO-nfs is less than that of SiO_2-nfs, especially, as the heating temperature is above 800 °C. This indicates that MgO-nfs has better thermal stability than SiO_2-nfs.

3. Results and Discussion

3.1. TES Capacity. To investigate the influence of nanoparticles on the phase change process, the melting point and the latent heat have been measured. Figure 5 depicts the heat flow of the base salt and nanofluids over temperature.

It is clear from Figure 5 that the heat flow curve of SiO_2-nfs moves obviously to the right while the heat flow curve of MgO-nfs keeps nearly unchanged. However, the melting peaks of the base salt are lower than the melting peaks of both nanofluids. Figure 5 indicates that both the MgO nanoparticles and the SiO_2 nanoparticles have an effect on the melting process, but the effects are obviously different.

To verify the equipment, the melting temperature and the latent heat of the base salt were measured and are listed in Table 3, which are consistent with those in refs. [29, 30].

Table 3 indicates the melting temperature and mean latent heat of the carbonate nanofluids. It is observed that the change of the melting point of SiO_2-nfs is significantly smaller than that of MgO-nfs. On the contrary, the increase of the latent heat of SiO_2-nfs is larger than that of MgO-nfs. This confirms the fact again that SiO_2 nanoparticles have little impact on the melting point of molten salts [28].

Table 2: Specific heat of the carbonate salt nanofluids.

Material	Base salt + MgO, J/(g·K)		Base salt + SiO_2, J/(g·K)	
	Solid	Liquid	Solid	Liquid
S11/S21	1.576	2.090	1.378	1.913
S12/S22	1.599	2.141	1.362	1.849
S13/S23	1.586	2.033	1.405	1.908
Average value	1.587	2.088	1.382	1.880
SD	0.012	0.054	0.022	0.036
Increment by	27.5%	34.1%	11.0%	20.7%

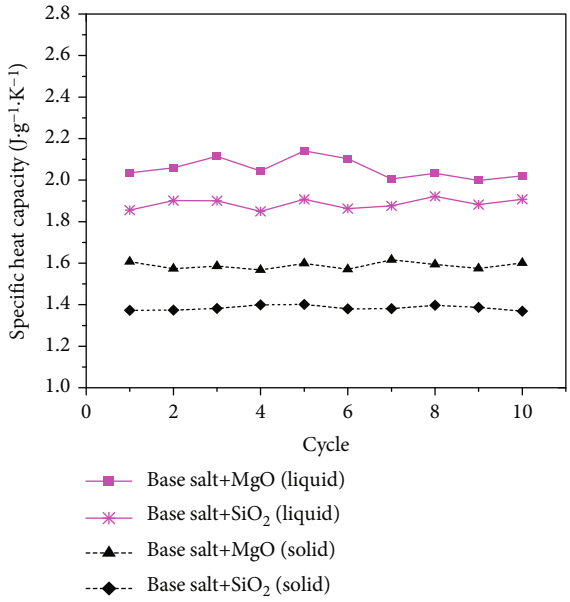

Figure 3: Specific heat of nanofluids after solid-liquid cycles.

Apparently, to increase the TES capacity, the SiO_2-nfs is more beneficial than the MgO-nfs.

In addition, higher specific heat means larger sensible heat to be stored in a TES system. Figure 6 illustrates the specific heat of the base salt, SiO_2-nfs, and MgO-nfs. It is observed that the specific heat of both carbonate nanofluids is all larger than that of the base salt either before or after the phase change. However, the specific heat of MgO-nfs is much higher than that of SiO_2-nfs. This means that the MgO nanoparticles have a greater influence on the sensible heat storage capacity of carbonate nanofluids than that of the SiO_2 nanoparticles. Further, the increases in specific heat of both carbonate nanofluids before the phase change are smaller than those after the phase change, respectively. In addition, the specific heat of both nanofluids increases near linearly over temperature in liquid state.

Figure 6 illustrates that the addition of MgO nanoparticles is superior to the SiO_2 nanoparticles to the binary carbonate for the purpose of sensible heat improvement.

The total TES capacity by the carbonate salt nanofluids consists of the specific heat of the low-temperature ramp-up section, the specific heat of the high-temperature ramp-up section, and the latent heat and the latent heat. Therefore, the total TES capacity can be calculated by equation (1):

$$q_{\mathrm{TES}} = q_{\mathrm{L}} + q_{\mathrm{s,s}} + q_{\mathrm{s,l}}, \tag{1}$$

where

$q_{\mathrm{s,s}} = \int_{T_{\mathrm{init}}}^{T_{\mathrm{melt}}} c_{\mathrm{p,s}} \mathrm{d}T$, $q_{\mathrm{s,l}} = \int_{T_{\mathrm{melt}}}^{T_{\mathrm{max}}} c_{\mathrm{p,l}} \mathrm{d}T$, $q_{\mathrm{L}} = h_{\mathrm{m.}}$

In this work, the initial calculating temperature for TES calculation was 350 °C and the terminal calculating temperature was 550 °C. Figure 7 presents the TES capacity of carbonate nanofluids prepared in this work at different temperatures in the test temperature range.

It is observed that the TES capacity of MgO-nfs increases faster than that of SiO_2-nfs in solid state. This is because the former has higher specific heat than the latter. However, since the latent heat of the MgO-nfs is smaller than that of SiO_2-nfs, the TES capacity of MgO-nfs is close to that of SiO_2-nfs with the termination of the melting process. Further, MgO-nfs also has higher specific heat than SiO_2-nfs in liquid state; therefore, the TES capacity of MgO-nfs increases still faster than that of SiO_2-nfs in the liquid state.

In all, from the point of view of total TES capacity, MgO-nfs are superior to SiO_2-nfs.

3.2. Thermal Conductivity. Thermal conductivity of samples has a decisive influence on heat conduction and convective heat transfer in TES devices, and an improvement in thermal conductivity significantly enhances the heat transfer performance. The thermal conductivity of samples in this work was calculated according to the equations in the literature [27]. The average measured thermal diffusivity of binary carbonate salt is 0.217 mm^2/s. The average thermal diffusivity and the thermal conductivity at different temperatures are illustrated in Figure 8. Obviously, the thermal diffusivities of binary carbonate salt nanofluids are all higher than those of their base salt while the thermal diffusivity of MgO-nfs is higher than that of SiO_2-nfs. Similarly, the thermal conductivities of the binary carbonate salt nanofluids are all far higher than those of their base salt while the thermal conductivity of MgO-nfs is far higher than that of SiO_2-nfs.

Table 4 indicates the detailed values of thermal diffusivity and thermal conductivity. From Table 4, it was observed that the thermal conductivity of MgO-nfs increased by a maximum of 55.7%, which is 26.1% higher than that of SiO_2-nfs. Therefore, MgO-nfs is superior to SiO_2-nfs in terms of heat transfer performance.

3.3. Microscopic Analysis. In Section 2.3, the homogeneity of nanoparticles in molten salt nanofluids has been verified by at least 18 measurements of the specific heat of 6 samples. To determine the micromorphological differences between the two molten salt nanofluids, a SEM was performed to observe the micromorphological of both carbonate nanofluids. The microstructures of binary carbonate salt and carbonate nanofluids are shown in Figure 9.

Figures 9(a) and 9(b) show the microstructure of the base salt at different magnifications. It is observed that the surface of the binary carbonate salt is relatively smooth and dense with an ice-like surface. There is no other special

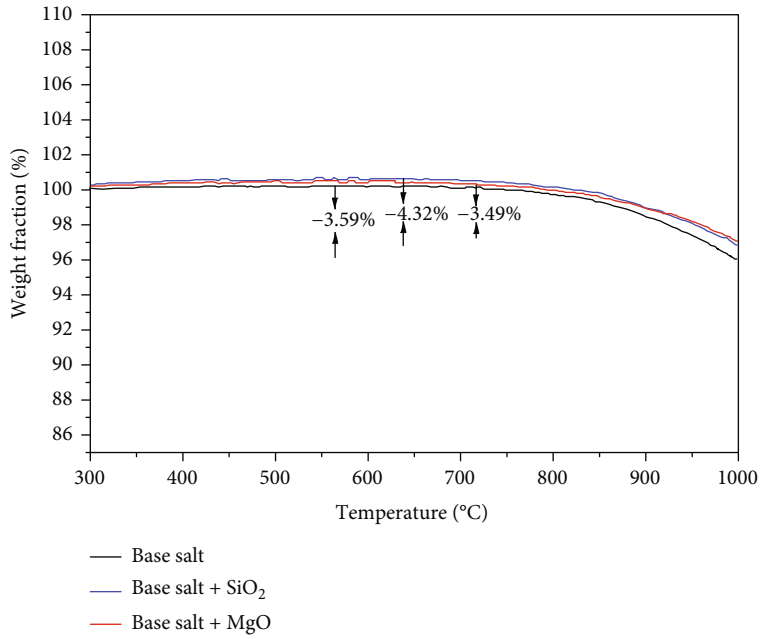

Figure 4: Thermogravimetric curves of the base salt, SiO_2-nfs, and MgO-nfs.

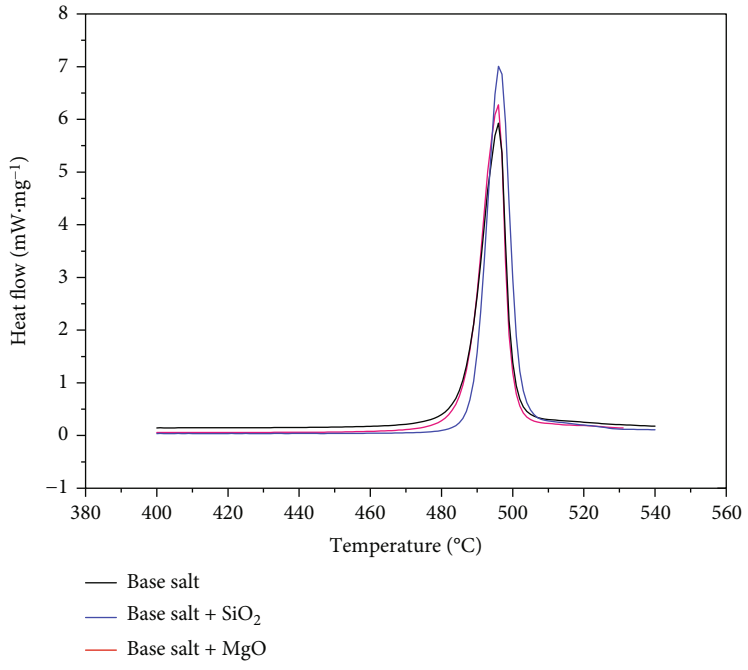

Figure 5: Heat flow of the base salt, SiO_2-nfs, and MgO-nfs.

Table 3: Latent heat and melting temperature of base salt, SiO_2-nfs, and MgO-nfs.

Material	Melting temperature			Latent heat, J/g		
	Avg. value, ˚C	SD	Increase by, ˚C	Avg. value	SD	Increased by, %
Base salt	488.1	0.32	—	351.2	0.64	—
+1.0 wt.% SiO_2 (20 nm)	488.7	0.57	+0.6	381.4	0.8	8.6
+1.0 wt.% MgO (20 nm)	486.9	0.75	−1.2	355.2	0.95	1.1

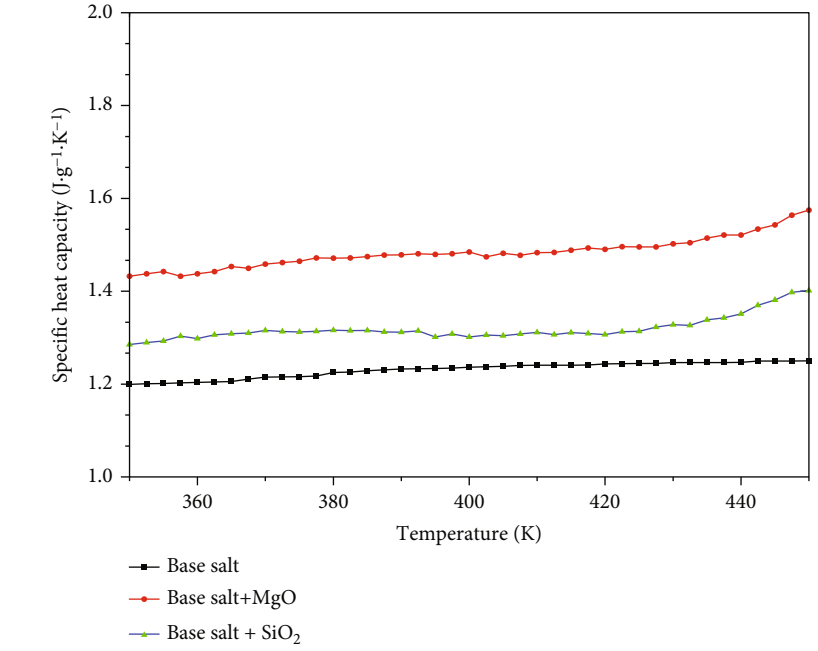

(a) Solid state

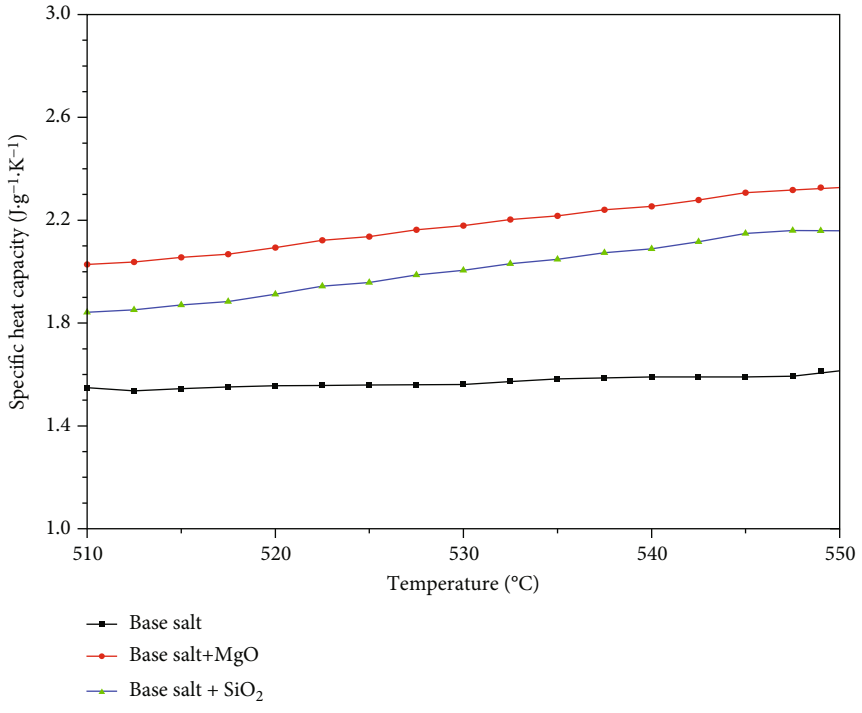

(b) Liquid state

Figure 6: Specific heat of the base slat, SiO_2-nfs, and MgO-nfs.

structure found in the base salt. Figures 9(c) and 9(d) show the microstructure of MgO-nfs. Compared to the binary carbonate salt, massive honeycomb-like crystals are observed. These crystals are almost uniformly distributed. In addition, this carbonate salt nanofluid seems sparse with pore-like structures. Therefore, the specific surface area is increased greatly. It seems that nanoparticles were evenly dispersed in molten salt. Figures 9(e) and 9(f) show the micromorphology of SiO_2-nfs. For this carbonate nanofluid, the microstructure is completely different from the base salt and MgO-nfs. These crystals are with sharp thorns and are covered by the emulsion-like substance, which seems to be raised stalactite. Moreover, these crystals are evenly distributed. Obviously, the specific surface area of this molten salt

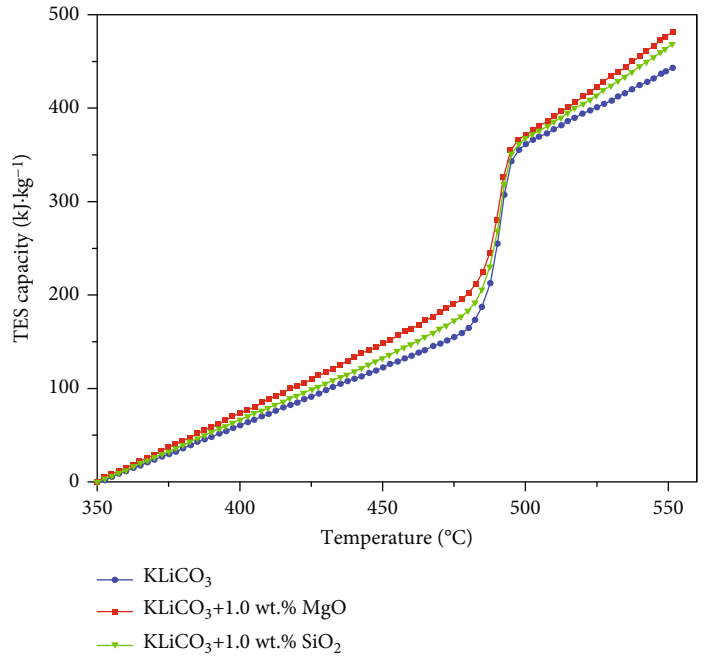

Figure 7: TES capacity of base salt, SiO_2-nfs, and MgO-nfs variates over temperature.

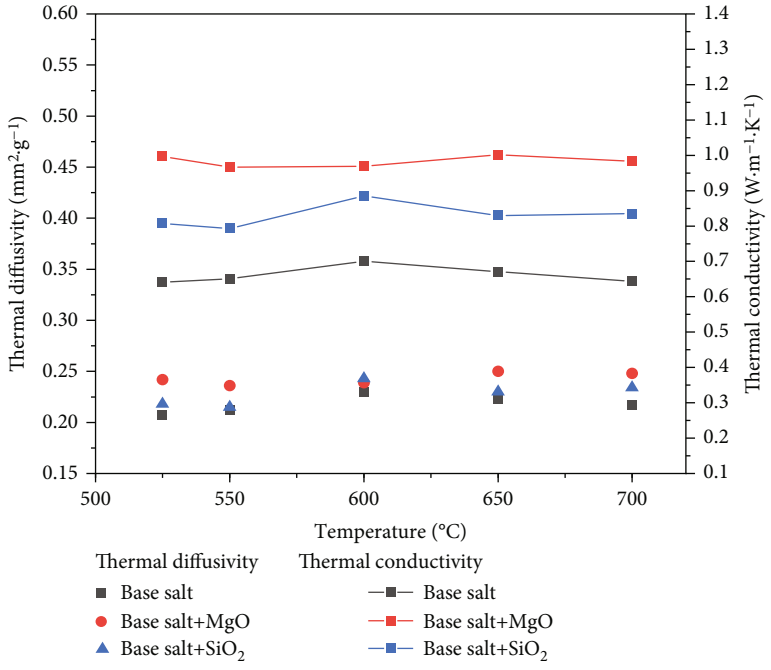

Figure 8: Thermal diffusivity and thermal conductivity of base salt, SiO_2-nfs, and MgO-nfs variates over temperatures.

nanofluid is between the base salt and MgO-nfs. In addition, it is found that no obvious agglomeration of nanoparticles is observed in both carbonate nanofluids.

3.4. Mechanisms of Formation and Performance Enhancement. The above results show that both types of nanoparticles have significant but different impacts on the thermal performance and the micromorphology of base salt. However, how do the molten salt nanofluids form? What is the mechanism of enhancement?

3.4.1. Formation of Molten Salt Nanofluid. As nanoparticle size approaches atom size, atom density on the nanoparticle surface is very high. Therefore, there are a lot of free bonds

Table 4: Thermal conductivity and thermal diffusivity of base salt, SiO_2-nfs, and MgO-nfs.

Material		525 ˚C	550 ˚C	600 ˚C	650 ˚C	700 ˚C
Base salt	α (mm^2/s)	0.207	0.212	0.230	0.223	0.217
	λ (W/(m·K))	0.641	0.651	0.700	0.671	0.644
MgO-nfs	α (mm^2/s)	0.242	0.236	0.239	0.250	0.248
	λ (W/(m·K))	0.997	0.967	0.969	1.002	0.983
	Enhancement (%)	55.7	48.6	38.4	49.3	52.5
SiO_2-nfs	α (mm^2/s)	0.218	0.215	0.243	0.230	0.234
	λ (W/(m·K))	0.807	0.793	0.885	0.830	0.835
	Enhancement (%)	26.0	21.9	26.4	23.7	29.6

connecting free atoms which lack coordination atoms. This causes the nanoparticles to have high unsaturation, high chemical activity, high specific surface energy, and strong hydrophilicity. Therefore, nanoparticles can easily interact with water and form hydroxyl groups on their surface.

According to the AS method presented in Section 2.1, nanoparticles (as illustrated in Figure 10(a)) firstly are dispersed into deionized water by ultrasonic agitation.

As nanoparticles meet water molecules, free atoms on nanoparticle surface will split water molecules into -OH groups and -H atoms to fill unsaturated free bonds and form the first layer, namely, the hydroxyl group layer, on the nanoparticle surface (from Figure 10(b)). Meanwhile, the ultrasonic agitation accelerates the formation of hydroxyl groups. This layer is also depicted by the green annulus in Figures 10(d)–10(f).

SiO_2 nanoparticles with amorphous space structure have irregular Si-O tetrahedral branched network. As can be seen from Figure 10(c), hydroxyl groups with space distance less than 3 Å in a nanoparticle and between adjacent nanoparticles will interact with each other to form hydrogen bonds while water molecules will also interact with isolated hydroxyls and pair hydroxyls on nanoparticle surface to form additional hydrogen bonds with the increase of mixing time. However, for MgO nanoparticles, the free atoms and the formed hydroxyl groups are equal in the pace distance, which is more than 3 Å. Therefore, there are no hydrogen bonds formed by adjacent hydroxyl groups on the same nanoparticle. This is one of the main differences between SiO_2 nanoparticles and MgO nanoparticles during the interaction with water molecules. Moreover, during the ultrasonic agitation process, the soft-agglomerated nanoparticle clusters will break up into individual nanoparticles and smaller nanoparticle clusters, while some individual nanoparticles will collide with each other and form hard-agglomerated nanoparticle clusters with different sizes. They also form hydroxyl groups and then hydrogen bonds on the surface of hard nanoparticle clusters. At this stage, the interaction flux between nanoparticles and water molecules reduces to zero while the nanoparticle surface is full of water molecules connected by hydrogen bonds.

As we know, it is not easy for molten salt ions to interact with hydrogen bonds on nanoparticle surface. As base salts are added, under the interaction of Van der Waals between nanoparticle and molten salt ions and the electrostatic force between hydrogen bonds and molten salt ions, the molten salt ions move closer to the nanoparticle surface, as illustrated in Figure 10(e). Figure 10(e) shows that the molten salt ions are adsorbed to the nanoparticle surface layer by layer to form cloud nuclei. Massive cloud nuclei, centered with nanoparticles and surrounded by molten salt ions, form in molten salt nanofluid until the interaction between the outermost molten salt ions and surrounding nanoparticles reaches a dynamic thermodynamic equilibrium [24]. However, more potassium ions will be adsorbed by the centered nanoparticles due to their larger zeta potential. Therefore, the ratio of potassium ions to sodium ions in cloud nuclei is larger than that in the base salt, which has been verified by the literature [4]. These cloud nuclei suspend in salt-water solution which appears translucent. During the mixing process, insufficient agitation time cannot produce the maximum number of cloud nuclei and some nanoparticles may not form saturated cloud nuclei while too long agitation would destroy some cloud nuclei and cause some cloud nuclei to agglomerate hardly.

In engineering applications, to produce molten salt nanofluid for convenient transportation, water must be evaporated completely. During this process, the molten salt nanofluid will crystallize and the solid cloud nuclei will form as the water evaporates completely. Before molten salt nanofluids are charged into the TES tanks, the molten salt nanofluids have to be melted into liquid at first.

As mentioned above, molten salt ions located at the edge of cloud nuclei are in dynamic equilibrium. When the temperature of the molten salt nanofluid rises to its terminal melting temperature, the molten salt ions located outside the cloud nuclei melt completely. With a further increase of the molten salt nanofluid temperature, molten salt ions inside the cloud nuclei gradually lose their dynamic equilibrium and melt starting from the edge to the center of the cloud nuclei. As the temperature of molten salt nanofluid rises to some level above the melting point, the molten salt ions adsorbed by Van der Waals force inside the cloud nuclei melt completely. At this time, water molecules are still adsorbed by the hydrogen bonds between hydroxyl groups and water molecules and the Van der Waals force between the nanoparticle and water molecules. Therefore, water molecules are still difficult to leave the nanoparticle surface. When the temperature of molten salt nanofluid rises to a higher level, the hydrogen bonds start to break. As the

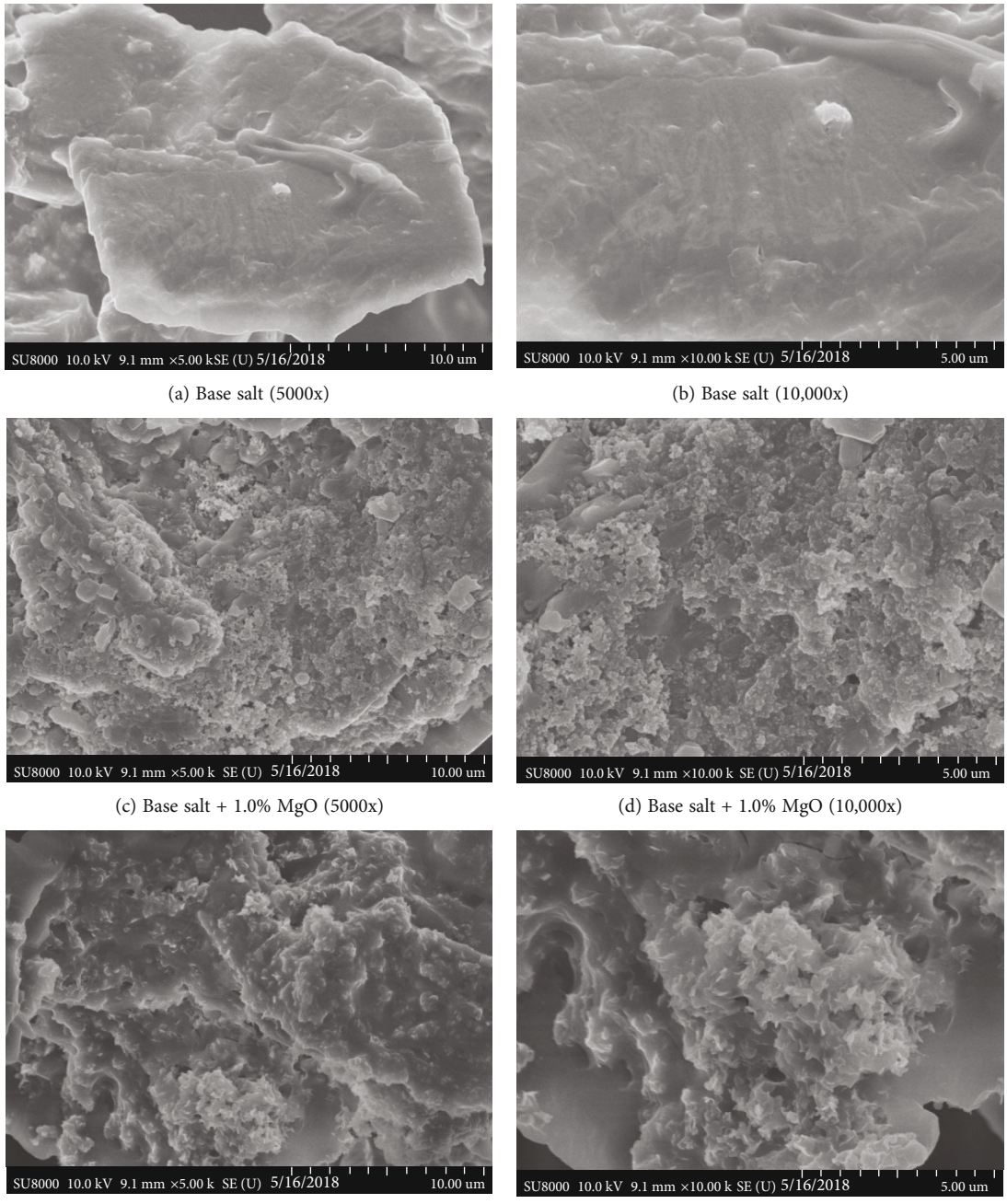

(a) Base salt (5000x)

(b) Base salt (10,000x)

(c) Base salt + 1.0% MgO (5000x)

(d) Base salt + 1.0% MgO (10,000x)

(e) Base salt + 1.0% SiO_2 (5000x)

(f) Base salt + 1.0% SiO_2 (10,000x)

Figure 9: Micromorphology of the base salt, SiO_2-nfs, and MgO-nfs.

hydrogen bonds inside the cloud nuclei are broken, the adsorbed water molecules will leave the cloud nuclei and evaporate from molten salt nanofluid while hydroxyl groups will form again on the nanoparticle surface. However, as the temperature for hydroxyl groups to leave the nanoparticle is far higher than the operating temperature of the molten salt nanofluid, hydroxyl groups will keep being adsorbed on the nanoparticle surface. Therefore, the cloud nuclei in the molten salt nanofluid prepared by the AS method consist of three parts: the centered nanoparticle, the hydroxyl groups (middle layer), and the molten salt (outer layer), as illustrated in Figure 11.

The other difference between the SiO_2 nanoparticles and the MgO nanoparticles is that both types of nanoparticles have completely different physicochemical properties. Therefore, the cloud nuclei that they formed in their molten salt nanofluids are completely different in size and structure. This also leads to the difference of cloud nuclei in micromorphology in SiO_2-nfs and MgO-nfs.

3.4.2. Enhancement of Specific Heat. The carbonate nanofluids are prepared to undergo some melting/high-temperature-heating/solidification cooling cycles. Through the above experiments, the authors observed that the specific heat of

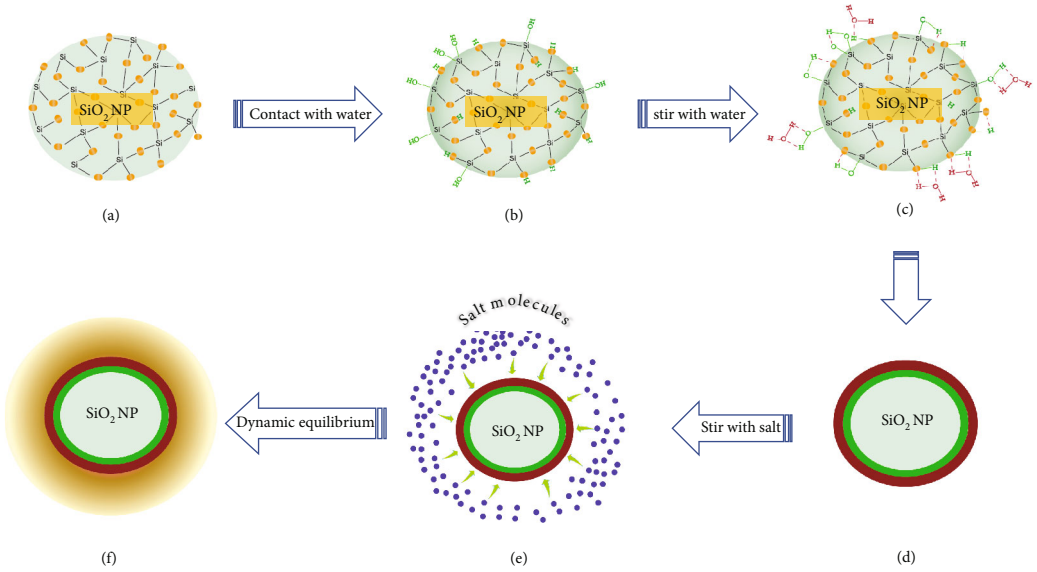

Figure 10: Formation mechanism of molten salt nanofluids prepared by AS method. (a) SiO_2 nanoparticle. (b) SiO_2 nanoparticle with hydroxyl groups. (c) SiO_2 nanoparticle with hydroxyl groups and water molecules. (d) Thumbnail of Figure 10(c). (e) Molten salt ions move toward nanoparticle. (f) Formed cloud nucleus with three attached layers.

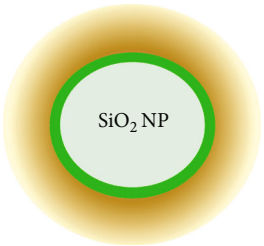

Figure 11: Structure of cloud nuclei in the molten salt nanofluid by the AS method after a high-temperature heating/solidification cycle.

the carbonate nanofluids increased abnormally. Based on the formation mechanisms proposed in Section 3.4.1, the anomalous increase in the specific heat can be explained as follows.

After the bulk salt melts completely with the temperature increase of bulk salt, the salt inside the cloud nuclei starts to melt gradually from the edge to the inside of the cloud nuclei due to the total interaction between the centered nanoparticle and the molten salt ions inside the cloud nuclei that is larger than that between the centered nanoparticle and the bulk molten salt ions outside the cloud nuclei. In addition, with the reduction of distance between the centered nanoparticle and the molten salt ions inside the cloud nuclei, the total interaction between the centered nanoparticle and the molten salt ions inside the cloud nuclei increases rapidly.

As we know, when the temperature rises up to some level, the molten salt nanofluid system will reach a new molecular dynamic equilibrium. With the further increase of bulk nanofluid temperature, the distance between nanoparticles and molten salt ions inside the cloud nuclei will become larger and larger. Then, molten salt ions will leave the cloud nuclei and the diameter of cloud nuclei will be smaller and smaller, as illustrated in Figure 12, which is consistent with the layer-by-layer desorption scenario [21]. During this process, much more heat is needed, which explains why the specific heat of molten salt nanofluid increases. Otherwise, more heat will be released during the overall temperature reduction. Due to the formation of the cloud core structure, the specific heat of carbonate nanofluids prepared by the aqueous solution method increases sharply after layer-by-layer analysis, with an increase of ~121.85% [31].

3.4.3. Enhancement of Heat of Fusion. Undeniably, when the molten salt nanofluid system reaches some molecular dynamic equilibrium, the centered nanoparticles interact not only with molten salt ions inside the cloud nucleus but also with those molten salt ions in the bulk salt. The main difference between the molten salt ions inside the cloud nuclei and the bulk molten salt ions is that molten salt ions in both fields are in different molecular dynamic equilibria. Once pure thermal energy is input into the molten salt nanofluid system, the equilibria will be broken and new equilibria tend to form. Therefore, the melting of bulk molten salt has to overcome the interaction force between nanoparticles and bulk molten salt ions. At this moment, some more thermal energy has to be supplied. This means that the latent heat of molten salt nanofluid increases. However, because the interaction force between nanoparticles and bulk molten salt ions is very weak, this increase of the heat of fusion is very small. The review shows that the latent heat increases by 33% when different nanoparticles are added to binary carbonate [14]. The increase in latent heat is much smaller compared to the increase in specific heat.

3.4.4. Enhancement of Thermal Conductivity. As can easily be imagined, there is an interaction force between different

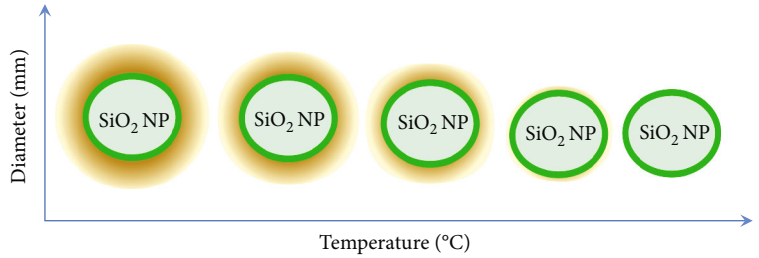

Figure 12: Diameter change of cloud nuclei over temperature.

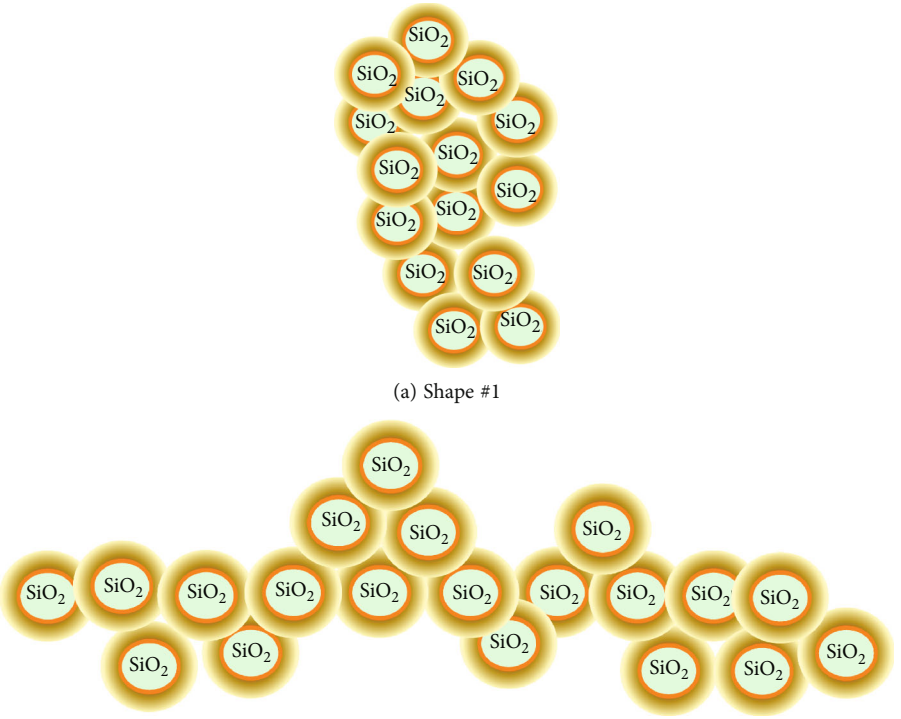

(a) Shape #1

(b) Shape #2

Figure 13: Diameter change of cloud nuclei over temperature.

cloud nuclei. This interaction force will cause some adjacent cloud nuclei to approach and form different shapes of chains made up of cloud nuclei, as illustrated in Figure 13. These chains are very small relative to the great volume of the carbonate salt nanofluid, and therefore, the distribution of these chains in the carbonate salt nanofluid is random.

According to the ballistics in nanoparticles and the direct or fluid-mediated clustering effects [18], phonons can transport heat through nanoparticles and cloud nuclei and finally transport through the chains of cloud nuclei rapidly. Therefore, the thermal diffusivity and the thermal conductivity of carbonate salt nanofluids are increased greatly.

However, because the cloud nuclei formed in SiO_2-nfs are different from those formed in MgO-nfs, the increased levels of both carbonate salt nanofluids are different. In addition, different mixing times, different evaporation containers, ratio of water to nanoparticles, and other factors will form different cloud nuclei in size and structure, which will cause the different increase levels of carbonate salt nanofluids. It indicated that the addition of nanoparticles (SiO_2 and carbon nanotubes) to carbonate increased the thermal conductivity by 50% [32]. The increase in thermal conductivity is also different with the addition of different nanoparticles.

3.4.5. Effect on Microstructure. As we know, SiO_2 is an atom crystal while magnesia is an ionic crystal. Also, as mentioned above, SiO_2 nanoparticles with an amorphous space structure have an irregular Si-O tetrahedral branched network while MgO nanoparticles have a regular space structure. In addition, both the SiO_2 nanoparticles and the MgO nanoparticles have different physicochemical properties. Therefore, the cloud nuclei in both molten salt nanofluids have different sizes and different crystal structures though structures of the cloud nuclei in both molten salt nanofluids look similar. The difference in structure inevitably leads to the

difference in micromorphology of SiO_2-nfs and MgO-nfs. This is also sure for molten salt nanofluids with the same type but different concentrations of nanoparticles by different mixing times. Though the base salt and nanoparticles are the same, the cloud nuclei also have different sizes and different structures in these molten salt nanofluids, which are caused by the different mixing time and other factors.

4. Conclusions

This work innovatively proposed the formation mechanisms of molten salt nanofluids based on a molecular perspective, and the formation mechanisms were used to explain the enhancement mechanisms of nanomaterials on carbonate salt based on experimental data obtained in this work. Some conclusions are made as follows:

(1) Specific heat is improved by maximal 20.7% and 34.1% by SiO_2 and MgO nanoparticles while the thermal conductivity is increased by maximal 29.6% and 55.7%, respectively. The high-temperature stability of MgO-nfs is better than that of SiO_2-nfs while the two types of molten salt nanofluids have excellent homogenization

(2) Different nanostructures have been observed in SiO_2-nfs and MgO-nfs, which are formed because of the different sizes and structures of cloud nuclei and led to the different enhancement of their thermal energy storage performance

(3) Cloud nuclei formed in the molten salt nanofluid during the preparation process by the AS method, which is made of four parts: the centered nanoparticle, the hydroxyl groups (middle layer), the water molecules, and the molten salt (outer layer). After a high-temperature heating/solidification cycle, the cloud nuclei are simplified into three parts: the centered nanoparticle, the hydroxyl groups (middle layer), and the molten salt (outer layer). These cloud nuclei are different due to the different nanomaterials, mixing time, and some other factors

(4) Interaction between nanoparticles and bulk molten salt enhances the heat of fusion while the process of molten salt molecules leaving or approaching the cloud nuclei enhances the specific heat of molten salt nanofluids and the chains of cloud nuclei enhance the thermal conductivity of molten salt nanofluids

4.1. Future Work. In the following work, we will further investigate homogenization after a long-time static placement and fluid flow. More detailed formation mechanisms will be explored and analyzed further.

Data Availability

This article includes all the data used to support the research results. If necessary, you can contact the author to provide data.

Conflicts of Interest

The author declares that this article is published without any conflict of interest.

Acknowledgments

The authors are grateful to the financial support of the Scientific Research Program of Beijing Municipal Education Commission under Project (Grant No. KM201910016011), the National Nature Science Foundation of China under Project (Grant No. 51206004), and the Beijing Municipal Natural Science Foundation (3151001).

References

[1] M. Aneke and M. Wang, "Energy storage technologies and real life applications—a state of the art review," *Applied Energy*, vol. 179, pp. 350–377, 2016.

[2] Q. Yu, Z. Jiang, L. Cong et al., "A novel low-temperature fabrication approach of composite phase change materials for high temperature thermal energy storage," *Applied Energy*, vol. 237, pp. 367–377, 2019.

[3] D. Shin and D. Banerjee, "Enhanced specific heat of silica nanofluid," *Journal of Heat Transfer*, vol. 133, no. 2, article 024501, 2011.

[4] S. M. M. Rizvi and D. Shin, "Mechanism of heat capacity enhancement in molten salt nanofluids," *International Journal of Heat and Mass Transfer*, vol. 161, article 120260, 2020.

[5] D. Shin and D. Banerjee, "Specific heat of nanofluids synthesized by dispersing alumina nanoparticles in alkali salt eutectic," *International Journal of Heat and Mass Transfer*, vol. 74, pp. 210–214, 2014.

[6] D. Shin and D. Banerjee, "Enhanced thermal properties of SiO_2 nanocomposite for solar thermal energy storage applications," *International Journal of Heat and Mass Transfer*, vol. 84, pp. 898–902, 2015.

[7] D. Shin and D. Banerjee, "Enhancement of specific heat capacity of high-temperature silica-nanofluids synthesized in alkali chloride salt eutectics for solar thermal-energy storage applications," *International Journal of Heat and Mass Transfer*, vol. 54, no. 5-6, pp. 1064–1070, 2011.

[8] H. Tiznobaik and D. Shin, "Enhanced specific heat capacity of high-temperature molten salt-based nanofluids," *International Journal of Heat and Mass Transfer*, vol. 57, no. 2, pp. 542–548, 2013.

[9] D. Shin, H. Tiznobaik, and D. Banerjee, "Specific heat mechanism of molten salt nanofluids," *Applied Physics Letters*, vol. 104, no. 12, article 121914, 2014.

[10] J. Buongiorno, "Convective transport in nanofluids," *ASME Journal of Heat Transfer*, vol. 128, no. 3, pp. 240–250, 2006.

[11] R. Hamilton and O. Crosser, "Thermal conductivity of heterogeneous twocomponent systems," *Industrial & Engineering Chemistry Fundamentals*, vol. 1, no. 3, pp. 187–191, 1962.

[12] C. Nan, R. Birringer, D. Clarke, and H. Gleiter, "Effective thermal conductivity of particulate composites with interfacial thermal resistance," *Journal of Applied Physics*, vol. 81, no. 10, pp. 6692–6699, 1997.

[13] H. Tiznobaik and D. Shin, "Experimental validation of enhanced heat capacity of ionic liquid-based nanomaterial," *Applied Physics Letters*, vol. 102, no. 17, article 173906, 2013.

[14] H. Tiznobaik, D. Banerjee, and D. Shin, "Effect of formation of "long range" secondary dendritic nanostructures in molten salt nanofluids on the values of specific heat capacity," *International Journal of Heat and Mass Transfer*, vol. 91, pp. 342–346, 2015.

[15] B. Jo and D. Banerjee, "Enhanced specific heat capacity of molten salt-based nanomaterials: effects of nanoparticle dispersion and solvent material," *Acta Materialia*, vol. 75, pp. 80–91, 2014.

[16] B. Jo and D. Banerjee, "Enhanced specific heat capacity of molten salt-based carbon nanotubes nanomaterials," *Journal of Heat Transfer*, vol. 137, no. 9, article 091013, 2015.

[17] H. E. Kwak, D. Shin, and D. Banerjee, "Enhanced sensible heat capacity of molten salt and conventional heat transfer fluid based nanofluid for solar TES application," in *ASME 2010 4th International Conference on Energy Sustainability*, vol. 2, pp. 735–739, Phoenix, Arizona, USA, 2010.

[18] P. Keblinski, S. R. Phillpot, S. U. S. Choi, and J. A. Eastman, "Mechanisms of heat flow in suspensions of nano-sized particles (nanofluids)," *International Journal of Heat and Mass Transfer*, vol. 45, no. 4, pp. 855–863, 2002.

[19] L. Xue, P. Keblinski, S. R. Phillpot, S. U. S. Choi, and J. A. Eastman, "Effect of liquid layering at the liquid-solid interface on thermal transport," *International Journal of Heat and Mass Transfer*, vol. 47, no. 19-20, pp. 4277–4284, 2004.

[20] S. Oh, Y. Kauffmann, C. Scheu, W. Kaplan, and M. Ruhle, "Ordered liquid aluminum at the interface with sapphire," *Science*, vol. 310, no. 5748, pp. 661–663, 2005.

[21] W. Matthew, *Adsorption at the nanoparticle interface for increased thermal capacity in solar thermal systems*, MIT, Cambridge, Massachusetts, 2012.

[22] W. Kaplan and Y. Kauffmann, "Structural order in liquids induced by interfaces with crystals," *Annual Review of Materials Research*, vol. 36, no. 1, pp. 1–48, 2006.

[23] R. Hentschke, "On the specific heat capacity enhancement in nanofluids," *Nanoscale Research Letters*, vol. 11, no. 1, p. 88, 2016.

[24] Y. Xiong, Z. Wang, M. Sun et al., "Enhanced thermal energy storage of nitrate salts by silica nanoparticles for concentrating solar power," *International Journal of Energy Research*, vol. 45, no. 4, pp. 5248–5262, 2021.

[25] L. Sang and T. Liu, "The enhanced specific heat capacity of ternary carbonates nanofluids with different nanoparticles," *Solar Energy Materials and Solar Cells*, vol. 169, pp. 297–303, 2017.

[26] Y. Xiong, M. Sun, Y. Wu et al., "Effects of synthesis methods on thermal performance of nitrate salt nanofluids for concentrating solar power," *Energy & Fuels*, vol. 34, no. 9, pp. 11606–11619, 2020.

[27] Y. Xiong, C. Song, J. Ren et al., "Sludge-incinerated ash based shape-stable phase change composites for heavy metal fixation and building thermal energy storage," *Process Safety and Environmental Protection*, vol. 162, pp. 346–356, 2022.

[28] Y. Xiong, Z. Wang, Y. Wu et al., "Performance enhancement of bromide salt by nano-particle dispersion for high- temperature heat pipes in concentrated solar power plants," *Applied Energy*, vol. 237, pp. 171–179, 2019.

[29] Y. Tao, C. Lin, and Y. He, "Preparation and thermal properties characterization of carbonate salt/carbon nanomaterial composite phase change material," *Energy Conversion and Management*, vol. 97, pp. 103–110, 2015.

[30] M. Kenisarin, "High-temperature phase change materials for thermal energy storage," *Renewable and Sustainable Energy Reviews*, vol. 14, no. 3, pp. 955–970, 2010.

[31] B. Jo and D. Banerjee, "Effect of solvent on specific heat capacity enhancement of binary molten salt- based carbon nanotube nanomaterials for thermal energy storage," *International Journal of Thermal Sciences*, vol. 98, pp. 219–227, 2015.

[32] L. Sang, W. Ai, Y. Wu, and C. Ma, "SiO_2-ternary carbonate nanofluids prepared by mechanical mixing at high temperature: enhanced specific heat capacity and thermal conductivity," *Solar Energy Materials and Solar Cells*, vol. 203, article 110193, 2019.

Hindawi
International Journal of Photoenergy
Volume 2022, Article ID 8595591, 14 pages
https://doi.org/10.1155/2022/8595591

Research Article

Thermal Performance of a Dimpled Tube Parabolic Trough Solar Collector (PTSC) with SiO_2 Nanofluid

M. Arun,[1] Debabrata Barik,[1] K. P. Sridhar,[2] and Milon Selvam Dennison[3]

[1]*Department of Mechanical Engineering, Karpagam Academy of Higher Education, Coimbatore 641021, India*
[2]*Department of Electronics and Communication Engineering, Karpagam Academy of Higher Education, Coimbatore 641021, India*
[3]*Department of Mechanical Engineering, Kampala International University, Western Campus, Kampala 20000, Uganda*

Correspondence should be addressed to Debabrata Barik; debabrata93@gmail.com
and Milon Selvam Dennison; milon.selvam@kiu.ac.ug

Received 7 April 2022; Revised 24 June 2022; Accepted 11 August 2022; Published 28 August 2022

Academic Editor: Chuan Li

In this research work, dimple texture tubes and silicon dioxide (SiO_2) nanofluid were used to analyze the performance parameters of a solar water heater. For this purpose, SiO_2 was mixed with deionized (DI) water using an ultrasonic dispersion device to prepare the nanofluids (SiO_2/DI-H_2O). The size of the nanoparticle was in the range of 10-15 nm. Different volume concentrations of the nanoparticles in the range of 0.1% to 0.5%, in steps of 0.1%, were chosen to prepare the nanofluids to carry out the experiments. Apart from this, computational fluid dynamics (CFD) tool was used to numerically analyze the parameters affecting the performance of the solar water heater, as well as the fluid flow pattern in the dimple texture tube. During the experiment, the mass flow rate of the base fluid (water) varied in the range of 0.5 kg/min to 3.0 kg/min in steps of 0.5 kg/min. The added advantage of the dimple texture tube design led to an increase in turbulence in the flow pattern, resulting 34.2% increase in the convective heat transfer efficiency compared with the plain tube. Among all experimental modules, SiO_2/DI-H_2O with a mass flow rate of 2.5 kg/min and 0.3% volume concentration gives overall optimized results in absolute energy absorption, gradient temperature, and efficiency of the solar water heater. The efficiency metrics of the experimental results were compared with the simulation results, and it was in the acceptable range with an overall deviation of ±7.42%.

1. Introduction

Based on the global energy consumption rate, 86% of the global energy is produced from fossil fuels which demands a continuous rise in the requirement for fossil fuels. Consequently, CO_x and NO_x emissions from fossil fuels significantly influence global warming [1]. This circumstance demands the development of renewable energy technology to reduce greenhouse gas emissions and air pollution simultaneously. Solar thermal, geothermal, biomass, marine, solar, and hydropower are a few renewable energy sources globally [2]. A solar collector is an efficient device to capture the maximum solar energy from the sun [3]. The performance of solar thermal systems can be further improved by system optimization, heat transfer enhancement, and operation optimization. The efficient operation of solar thermal systems combined with thermal energy storage systems is the most important aspect of a large-scale solar energy utilization. It should be noted that the utilization of solar thermal energy will substantially impact the building environment.

Flat-plate collectors, evacuated tubes, and parabolic collectors are the common types of solar collectors, and each has its advantages and disadvantages based on the heat transfer rate. Based on the application, the heat transfer tubes in flat-plate and evacuated tube solar collectors vary in shape and size. A vacuum is used to keep the absorption plate within a glass tube in an evacuated solar collector to decrease heat loss due to convection. A greater temperature may be maintained in the evacuated tube solar collector than in the flat-plate collector, which has a lower efficiency [1, 4, 5]. When erection costs are taken into account for solar panels, the solar collector's energy efficiency remains less

[6, 7]. Hence, an increase in the efficiency of the different solar collectors is a prime aspect to be focused on.

The solar thermal systems' effectiveness entirely relies on their collectors' performance. Thermal and photovoltaic systems in the solar collectors are utilized to convert sunlight into heat with the help of working fluids like air or water [8, 9]. From an economic point of view, flat-plate collectors are used to heat the working fluids. But the efficiency and performance are poor. Several researchers have conducted considerable research to increase the efficiency and performance of flat-plate collectors without affecting the cost [10]. Most researchers suggested that utilizing nanofluids in place of ordinary fluids in solar collectors can increase the performance of the flat-plate collectors. Bai et al. [11] investigated nanofluids which are the suspensions of water and nanoparticles in the range of 1–100 nm in size. They identified that this kind of working fluid has a higher thermal conductivity than its base fluid. The use of nanofluids in solar thermal systems has significant positive impacts on environmental, economic, and thermal aspects.

Moravej et al. [12] experimentally investigated the impact of substituting water with surfactant-free water using flat-plate solar collectors with rutile TiO_2–water nanofluids as a working fluid. They followed the ASHRAE standard; as per the standard, the flow rate of the heat transfer fluid (HTF), the sun irradiation, and the temperature difference between the intake and outflow were analyzed. They concluded that the thermal efficiency could be improved by using TiO_2–water nanofluids instead of water alone. Mahian et al. [13] investigated the usage of four different nanofluids (Al_2O_3water, TiO_2/water, SiO_2/water, and Cu/water) in a mini-channel-based solar collector. They found that Cu/water nanofluid exhibits the optimum temperature at the exit and the lowest entropy at the source with an increase in thermal efficiency. Parvin et al. [14] conducted a numerical study to examine the direct absorption collector, direct convection heat transfer efficacy, and entropy production using Cu–water nanofluid as the working fluid. They analyzed the effect of the Nusselt number, entropy generation Bejan number, collector efficiency, and solid volume fraction of nanoparticles on the collector's performance. They identified that isotherms and heat functions for varied solid volume fractions and inertia forces significantly affect the collector's performance.

Noghrehabadi et al. [15] investigated the direct absorption of a flat-plate solar collector by a low-temperature SiO_2/water nanofluid. They evaluated the influence of one of the stable nanofluids on the efficiency of a symmetric collector in light of the previous results. In a flat-plate collector, water and a SiO_2/water nanofluid with a mass fraction of 1% are tested as coolants. They concluded that employing SiO_2/water nanofluid as a coolant increases the collector efficiency by improving its optical and thermophysical characteristics. Ghalambaz et al. [16] investigated the viscosity and thermal conductivity fluctuation of Al_2O_3 nanofluid as a working fluid. They reported that with the increase in the concentration of Al_2O_3 nanofluid, the thermal conductivity increased, and the viscosity of the working fluid decreased. Furthermore, they observed a 12.8% improvement in thermal efficiency while the volume concentration of the nanoparticle was 1%. Sujith et al. [17] studied the thermal conductivity of Al_2O_3 and copper oxide (CuO) nanofluids, and they revealed that the increase in the concentration of the nanofluids significantly affects the thermal conductivity. Furthermore, they observed that the thermal conductivity of CuO nanofluid was greater than that of Al_2O_3 nanofluid at the same concentration ratio.

Verma et al. [18] inspected the effect of thermal performance of a flat-plate solar collector, employing nanofluids of Al_2O_3, CuO, SiO_2, TiO_2, and graphene with multiwall carbon nanotube (MWCNT). They reported that thermal efficiency was enhanced by 23.5% with MWCNT nanofluid as the working medium. Yan et al. [19] investigated the thermal conductivity and transmissivity of the nanofluid of SiO_2 and water with a mass fraction of 1%, 3%, and 5%. They also numerically analyzed the solar-collector vacuum tubes filled with water (5 wt. %) and nanofluid of SiO_2 using a computer model. They identified that the heat transfer properties of the SiO_2/water nanofluid were improved. Also, it was absorbed that the temperature and velocity distributions of the nanofluid of SiO_2 had a significant impact on the heat transfer than that of the ordinary fluids. Yousefi et al. [20] experimentally studied the effects of Al_2O_3/water nanofluid as a working fluid in a flat-plate solar collector. Their study employed the nanofluid with 0.2% and 0.4% weight fraction and 15 nm particle size and a controlled mass flow rate of nanofluid in the range of 1 to 3 litres per minute, giving an increase in thermal efficiency of 28.3% in comparison to pure water.

Sundar and Sharma [21] experimentally investigated the effect of Al_2O_3 nanoparticles in deionized water as working fluid in a solar heater inserted with and without a twisted tap. They conclude that the copper tube channels' thermal efficiency was significantly inserted with a twisted tap. Ekiciler [22] numerically investigated the heat transfer phenomenon of Al_2O_3 nanoparticles with a volume fraction of 1% to 5% in a duct with a backwards-facing step. They observed that the Nusselt number and Reynolds numbers were directly proportional to the increase in the volume percentage of the Al_2O_3 nanoparticles. Thansekhar and Anbumeenakshi [23] studied the effect of nanofluids on the improvement of heat transfer rate in a microchannel heat sink. They identified that a higher volume concentration of Al_2O_3 nanoparticles in the nanofluid exhibits an enhanced heat transfer rate compared to SiO_2 nanoparticles.

Kalidoss et al. [24] focused on Therminol 55-TiO_2 nanofluids for solar energy storage. They utilized Fresnel lenses, secondary reflectors, and a glass-type evacuated absorber tube to improve the photothermal conversion efficiency. They suggested that improvement in nanofluid concentration enhances the thermal conductivity, and the significance of optical absorbance indicates nanofluids' stability. Cardoso et al. [25] evaluated the influence of TiO_2/SiO_2 nanoparticles in terms of surface area, SEM/TEM morphology, and phase transaction temperature. They found that photoanodes with 3% SiO_2 are more efficient due to increased surface area, and SiO_2 passivation of imperfections increases the photocurrent. Ayoobi and Ramezanizadeh [26] documented the performance and efficiency of the solar still combined with a flat-plate collector in terms of energy, exergy, economic,

and productivity. They observed that maximum efficiency of 60% was obtained in the flat-plate collector by improving the evaporation rate with the aid of six microcompartments in the collector basin. Cao et al. [27] numerically investigated the entropic properties of flat-plate solar collector (FPSC) with the number of swirls generating nozzles. They predicted the overall system performance using N_E, N_S, Nu, and heat transfer improvement (HTI). They found that the maximum value of HTI and efficiency were 1.7 and 0.9, respectively, for the quad nozzle.

From the extensive literature review on the relevance to the present works, it was observed that many authors had adopted various methods to improve the performance of solar water heaters by using the following techniques such as varying nanoparticles size, use of mini-channel-based solar collector, adoption of multiwall carbon nanotube, use of twisted tap design, and use of microchannel heat sink. It was clear that none of the researchers has used dimple texture tubes with nanoparticles for performance improvement analysis and has not documented computational analysis for dimpled tube texture using CFD.

In the present investigation, the authors have presented a numerical and experimental analysis of a parabolic plate solar water heater using a tube in tube type heat exchanger, with a dimple inner tube having a P/D ratio of 3. Also, the authors have used deionized water and nanoparticles of SiO_2 of size 10-15 nm at volume concentrations of 0.1 to 0.5% in steps of 1% to prepare the nanofluid. During the investigation, the mass flow rate of the water in the tube was varied in the range of 0.5 kg/min to 3.0 kg/min in steps of 0.5 kg/min to analyze the absolute energy of the parabolic collector, heat loss from the dimpled tube, parabolic collector efficiency, gradient temperature of the dimpled tube, friction factor for the working fluid, Reynolds number, Nusselt number, and convective heat transfer coefficient of the dimpled tube. Also, the velocity, temperature, and pressure contour of the PTSC were analyzed using CFD.

2. Material and Methods

In the present investigation, the performance parameters of a parabolic trough solar collector (PTSC) were analyzed using SiO_2 nanoparticles with deionized water. The concentration of the nanoparticles varied in the range of 0.1 to 0.5% in steps of 1%. Apart from this, the copper tube of the solar water heater was modified to make dimples on it to create more turbulence in the working fluid. Also, the mass flow rate of the water in the tube was varied as 0.5 kg/min, 1.0 kg/min, 1.5 kg/min, 2.0 kg/min, 2.5 kg/min, and 3.0 kg/min to analyze the absolute energy of the parabolic collector, heat loss from the dimpled tube, parabolic collector efficiency, gradient temperature of the dimpled tube, friction factor for the working fluid, Reynolds number, Nusselt number, and convective heat transfer coefficient of the dimpled tube. Also, the performance parameters of a PTSC were analyzed by using the CFD tool (Fluent 18.0). The experimental and the numerical results were compared and presented in subsequent sections.

2.1. Design and Experimental Setup. The experimental setup used in this present research is a geometric model consisting of a dimpled tube of 1200 mm in length and 50 mm in diameter, connected to a circular 1500-litre reservoir containing working fluids, as shown in Figure 1. The solar radiation strength of the outer dimpled tube was 847 W/m^2, and it provided a steady heat flow with a turbulent flow of 500 W/m^2. SiO_2/DI-H_2O was used as nanofluid in the present investigation, and it has a volume concentration of 0.1-0.5% in steps of 0.1%. The dimple diameter chosen for making the dimple was 0.05 mm. The dimples were fabricated on the outer surface of the tube with the help of a screw-type punching die made of cast iron.

The specification of the experimental setup is given in Table 1. The temperature measurements of the glazed solar collector were recorded at an inclination angle of 45°. Two mercury-bar thermometers were fitted to measure the working fluid temperature at the inlet and outlet of the PTSC separately. A positive displacement pump was used to maintain the flow across the PTSC, and the flow was regulated with the help of control valves. The mass flow rate of the working fluid flow was measured with a flow meter, and it varied from 0.5 kg/min to 3.0 kg/min depending on the valve regulation and the stages of the experiment. A sun meter was used to measure the solar radiation intensity, and it was found to be 847 W/m^2.

2.2. Nanofluid Preparation. The nanofluid was made of nanopowder of SiO_2 of 99.7% purity, 20 nm average size, and pH 7, and density was 4170 kg/m^3. The nanofluids were made with 0.1 to 0.5 percent volume of nanoparticles in steps of 0.1% each. The ultrasonic dispersion setup for the nanofluid preparation is shown in Figure 2. By using this setup, the dispersion of the nanoparticles takes place in DI water to avert accumulation and assures a pH of 7. The specifications of the nanoparticles are given in Table 2. SiO_2 nanoparticles have been purified in the ambient air with a mesh size of 0.5 μm. The thermophysical features of nanofluids were compared theoretically and experimentally and explained in subsequent sections. The properties of nanofluids are given in Table 3.

2.3. Governing Equation. The problem statement can be expressed in the form of governing equations [9, 18], as shown below:

$$\frac{du}{dx} + \frac{dv}{dy} + \frac{dw}{dz} = 0. \tag{1}$$

The momentum equations in x, y, and z are as follows [9, 18]:

$$\rho_{SiO_2}\left(\frac{\partial u}{\partial t} + u\frac{\partial u}{\partial x} + v\frac{\partial u}{\partial y} + w\frac{\partial w}{\partial z}\right) = -\frac{\partial p}{\partial x} + \mu\left(\frac{\partial^2 u}{\partial x^2} + \frac{\partial^2 u}{\partial y^2} + \frac{\partial^2 u}{\partial z^2}\right) - \rho_{SiO_2}\propto_{SiO_2} g_x(T - T_{ref}), \tag{2}$$

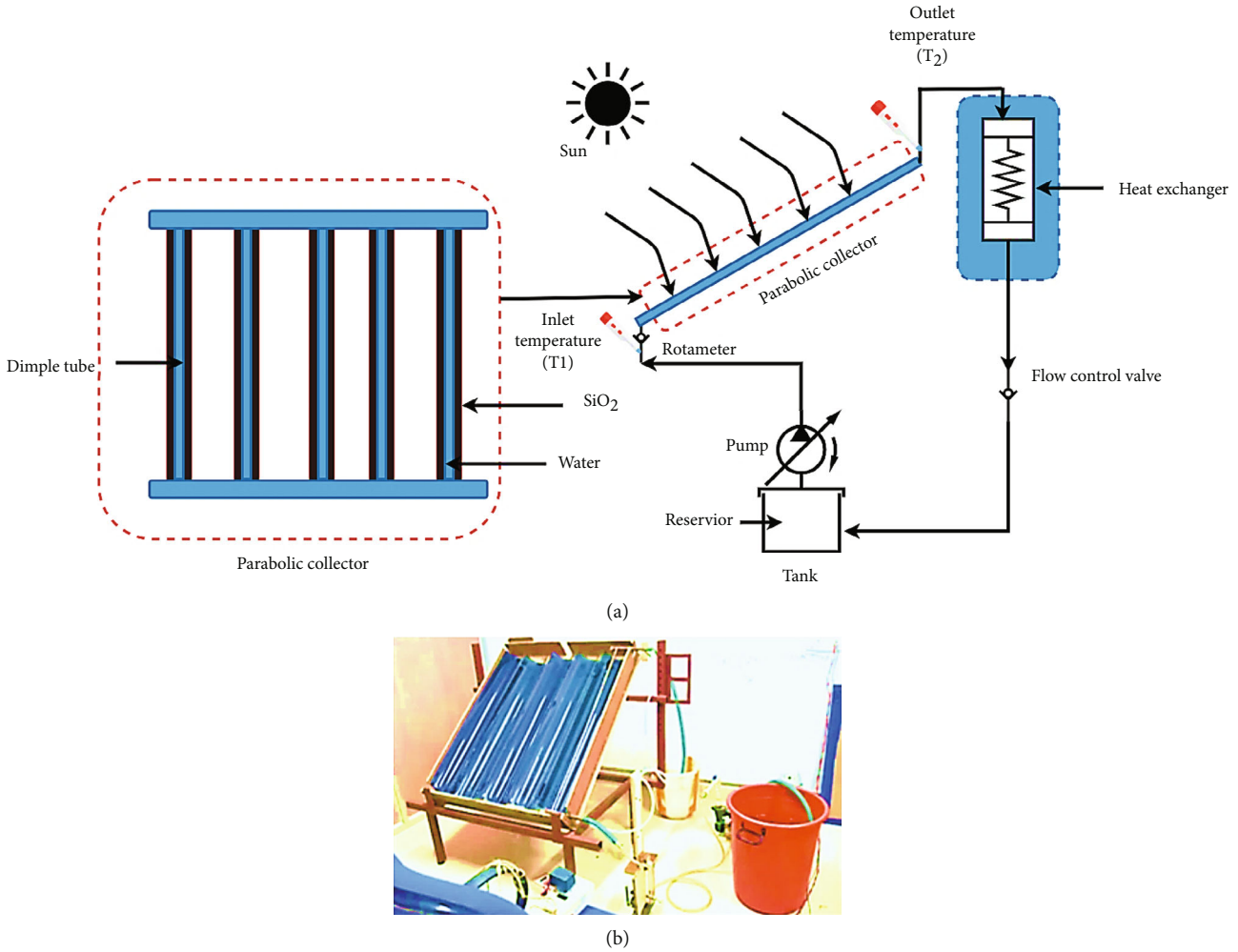

Figure 1: (a) Layout of the experimental setup. (b) Photograph of the experimental setup.

$$\rho_{SiO_2}\left(\frac{\partial v}{\partial t}+u\frac{\partial v}{\partial x}+v\frac{\partial v}{\partial y}+w\frac{\partial v}{\partial z}\right) = -\frac{\partial p}{\partial x}+\mu\left(\frac{\partial^2 v}{\partial x^2}+\frac{\partial^2 v}{\partial y^2}+\frac{\partial^2 v}{\partial z^2}\right)-\rho_{SiO_2}\propto_{SiO_2} g_x(T-T_{ref}), \tag{3}$$

$$\rho_{SiO_2}\left(\frac{\partial w}{\partial t}+u\frac{\partial w}{\partial x}+v\frac{\partial w}{\partial y}+w\frac{\partial w}{\partial z}\right) = -\frac{\partial p}{\partial x}+\mu\left(\frac{\partial^2 w}{\partial x^2}+\frac{\partial^2 w}{\partial y^2}+\frac{\partial^2 w}{\partial z^2}\right)-\rho_{SiO_2}\propto_{SiO_2} g_x(T-T_{ref}). \tag{4}$$

The energy is given by [9, 18]

$$\rho_{SiO_2}\left(\frac{\partial T}{\partial t}+u\frac{\partial T}{\partial x}+v\frac{\partial T}{\partial y}+w\frac{\partial T}{\partial z}\right) = \frac{k_{eff}}{(C_P\cdot\rho)_{SiO_2}}\left(\frac{\partial^2 T}{\partial x^2}+\frac{\partial^2 T}{\partial y^2}+\frac{\partial^2 T}{\partial z^2}\right). \tag{5}$$

The density for both the base fluid and the SiO_2 nanoparticles can be calculated using the correlation presented below [9, 18]:

$$\rho_{SiO_2} = \varphi(C_P\cdot\rho)+(1-\varphi)(\beta\rho)_{SiO_2}. \tag{6}$$

SiO_2 nanofluid's thermal conductivity was calculated using the Maxwell model, which can be expressed in terms of the following equation [9]:

$$\frac{k_{SiO_2}}{k_f} = \frac{2k_f+k_s+2\varphi k_f-2\varphi k_s}{2k_f+k_s-\varphi k_f-\varphi k_s}. \tag{7}$$

The successful dynamic viscosity association of Brinkman has been used in this analysis [9]

$$\mu_{SiO_2} = \frac{\mu_f}{(1-\varphi)^{2.5}}. \tag{8}$$

The evacuated tunnel was cut up and down. Hence, the

Table 1: Specification of the experimental setup.

Specification	Dimensions
Collector length	1800 mm
Width of collector	1200 mm
Length of absorber plate	1650 mm
Thermal conductivity of absorber plate	387 W $(mK)^{-1}$
Width of the absorber plate	1000 mm
Plate thickness	5 cm
The density of plate material	8954 kg/m^3
The diameter of the riser pipe	0.0125 m
The diameter of the header pipe	2.5 cm
The riser and head of thickness	7 cm
Tube centre to centre distance	11.25 cm
Glass and absorber plate between the spacing	30 cm
Thermal conductivity of insulation material	0.044 W $(mK)^{-1}$
The density of the insulation material	200 kg/m^3
The thickness of the insulation material	0.05 m
Area of the absorber plate	960 × 1000 mm
The thickness of the riser tube	1 mm

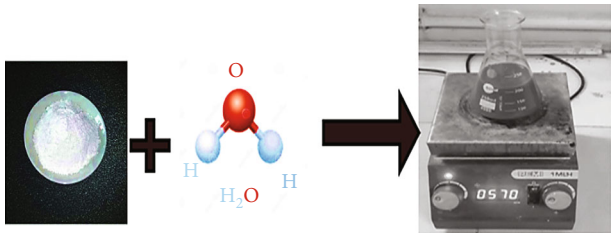

SiO_2 nano power Di-H_2O (De-ionized water) Nanofluid in UP 400S ultrasonic processor

Figure 2: Ultrasonic dispersion setup for the preparation of nanofluid.

heat was applied only to the upper part, where the lower part was unheated. The top portion of the dimpled tube is expected to receive 50% to 57% of solar radiation, while the bottom receives less radiation unless the solar water heater uses the reflector. The solar radiation intensity was recorded from 8 am morning to 5 pm the evening using a sun meter. 952 W/m^2 maximum sunlight radiation intensity had been reached in the afternoon. The heated stream around the dimpled tube has been considered to be 847 W/m^2 in this analysis.

2.4. Grid Independence Test. Fine mesh size and shape are the critical parameters to ensure the accuracy and quick computational time of the CFD numerical calculation. In this analysis, 3D meshes were utilized in the ANSYS platform to analyze the influence of grid numbers on the maximum inside tank temperature. Figure 3 shows the highest temperature within the tank converged at 308 K. In the computational domain, the element size was maintained in the range of 586275.

Table 2: Specification of the nanoparticle.

Properties	Values
Nanoparticle material	SiO_2
Density	4170 kg/m^3
Molar mass of SiO_2	60.0843 g/mol
Nanoparticle size	10-15 nm
Melting point	1986 K
Boiling point	2503 K
Thermal conductivity	1.38 W/mK
Crystal structure	Cristobalite
Purity of nanoparticle	99.7%
Specific surface area	160 m^2/g
Volume density	4170 kg/m^3
Specific heat	880 kJ/kg K

2.5. Performance Analysis. The performance analysis was carried out using two different techniques, and the estimation readings were recorded from 8 am to 5 pm. SiO_2 levels and flow speeds are measured in the dimples tube. The experiments were carried out in six stages to achieve consistency, and each stage consisted of 30 minutes. The collection time constant of 64.25% complies with ASHRAE requirements; each 60-minute cycle was further separated into 20-minute subcycles. Furthermore, the PTSC collector performance was determined by linear regression at a minimum of 20 data points at different inlet water temperatures to carry out the steady-state model. Data was collected regularly for several months.

2.6. Analysis of Collector Efficiency. The collector efficiency reveals the entire radiation of the incident from the opening area, and the collector produces the available heat gain as shown in [9]

$$Q_g = C_{P_{SiO_2}}(T_O - T_I). \tag{9}$$

In Equation (10), the efficiency of solar collector for PTSC has been obtained by [9]

$$\eta_c = \frac{Q_g}{A_a} = \frac{C_{P_{SiO_2}}(T_O - T_I)}{A_a}. \tag{10}$$

The collector performance curve is plotted for a sequence of 16 data points. A linear reverse fitting procedure is used to locate the slope and intercepts. The following equations denote the collector's productivity as shown in [9]

$$\eta_c = \alpha\tau(F_R) - \frac{U_L F_R}{C}\left(\frac{T_O - T_I}{I}\right). \tag{11}$$

As shown in Equation (11), where $F_R(\eta_c) = \alpha\tau(F_R)$ indicates the energy parameter is consumed, $U_L F_R/C$ indicates the parameter of removal energy, and $(T_O - T_I)/I$ indicates the parameter of heat loss or collector's function curve. The relationship between the heat loss parameter and

Table 3: Properties of nanofluids.

Properties	DI H_2O-SiO_2 0.1%	DI H_2O-SiO_2 0.2%	DI H_2O-SiO_2 0.3%	DI H_2O-SiO_2 0.4%	DI H_2O-SiO_2 0.5%
Density, kg/m^3	1014	1025	1029	1035	1042
Specific heat, kJ/kgK	410.6	414.8	418.5	422.7	427.8
Convective heat transfer coefficient, W/m^{2}K	0.6723	0.7562	0.7825	0.8251	0.8452
Viscosity, m^2/s	$0.411e^{-6}$	$0.388e^{-6}$	$0.377e^{-6}$	$0.286e^{-6}$	$0.257e^{-6}$
Boiling point, ˚C	2950	2958	2960	2968	2970
Molar mass, g/mol	60.08	62.72	64.28	66.82	69.86

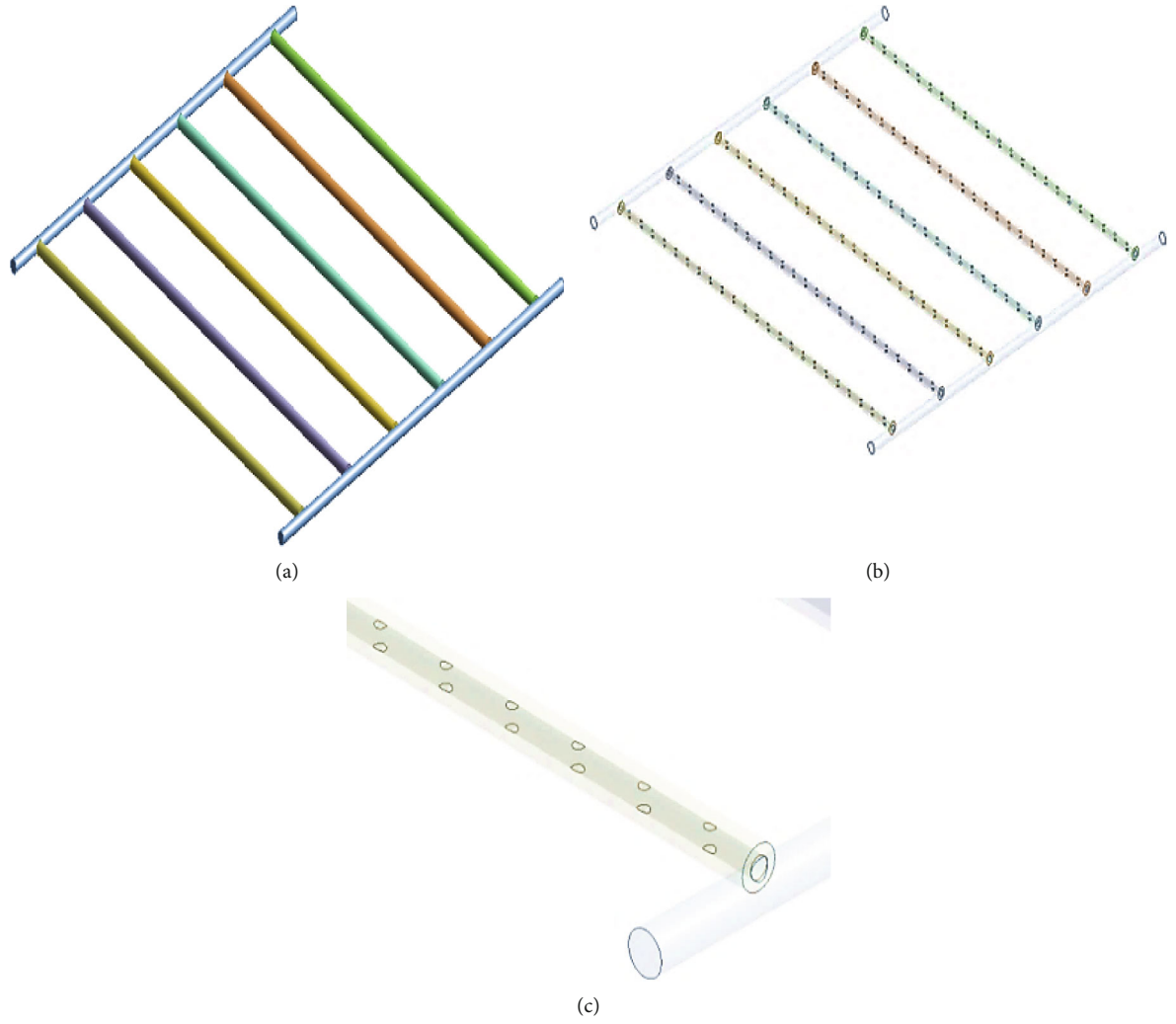

Figure 3: (a) Plain tube. (b) Dimpled tube. (c) Dimpled tube with nanofluid.

collector efficiency is shown in Equation (11). These values were compared to prior versions using the new one. The $F_R(\eta_c)$ and $\alpha\tau(F_R)$ intercept component with a linear regression approach. The collector's overall efficiency for SiO_2 at 0.3% has been 62.25% increased from 54.25% on the level of base fluid at a comparable flow rate based on the regression equation of the DI water and quality of the SiO_2 nanofluids. Experimental studies suggest that the highest exit temperate of $T = 93.15$˚C has been recorded due to the higher period of interaction between the recipient surface and the working fluid at a lower mass flow rate (0.5 kg/min–3.0 kg/min). In comparison, the temperature graduate of $\Delta T = (T_O - T_I)$ was lower at the peak flow rate ($m = 1.0$ kg/s) and corresponded to a more significant convective heat transfer coefficient. In this investigation, parameters such as friction factor, uncertainty analysis, Reynolds number, solar

collector efficiency, Nusselt number, and convective heat transfer coefficient were determined in the solar PTSC system.

2.7. Uncertainty Analysis. For analysis and regression techniques, all experimental values are averaged in numerical and CFD analysis. The uncertainties of the variable effects resulting from derived variables (η_c, Re, Nu, and f) were discovered in the experimental calculation of independent variables (T, Q_g). The standard deviation has been manipulated by derived Equation (12) since each variable has been measured over a minimum of three intervals.

$$\ni_R = \sqrt{\left[\left(\frac{\ni_1 \partial S}{\partial X_1}\right) + \left(\frac{\ni_2 \partial S}{\partial X_2}\right) + \left(\frac{\ni_3 \partial S}{\partial X_3}\right) + \cdots\cdots\cdots \left(\frac{\ni_N \partial S}{\partial X_N}\right)\right]}. \tag{12}$$

Based on Equation (12) [9], the proportional error is calculated as follows:

$$E_R = \frac{\ni_R}{S}\%. \tag{13}$$

Solar PTSC performance depends explicitly on normal direct irradiance, fluid inlet temperature, mass flow rate, and outlet temperature (η_c, Re, Nu, f, T, and Q_g). The following equation gives us clarity regarding the performance of the solar collector, as shown in [9, 18]

$$\eta_c = f\left(T_O, T_I, T, Q_g\right), \tag{14}$$

$$\ni_{\eta_c} = \sqrt{\left[\left(\frac{\partial \eta_c}{\partial Q_g}\ni_{T_O}\right) + \left(\frac{\partial \eta_c}{\partial T_I}\ni_{T_I}\right) + \left(\frac{\partial \eta_c}{\partial T_O}\ni_{Q_g}\right) + \cdots\cdots\cdots \left(\frac{\partial \eta_c}{\partial T}\ni_T\right)\right]}. \tag{15}$$

In Equation (16), flow rate with velocity (m/s) can be expressed as [9]

$$\ni_V = \sqrt{\frac{\partial V}{\partial m}\ni_m}. \tag{16}$$

In Equation (17), Nusselt number (Nu) with Reynolds number can be expressed as [9]

$$\ni_{\mathrm{Nu}} = \sqrt{\frac{\partial \mathrm{Nu}}{\partial\, \mathrm{Re}}\ni_{\mathrm{Re}}}. \tag{17}$$

In Equation (18), Reynolds number (Re) with velocity can be expressed as [9]

$$\ni_{\mathrm{Re}} = \sqrt{\frac{\partial\, \mathrm{Re}}{\partial \ni_V}\ni_V}. \tag{18}$$

In Equation (19), friction factor (f) with pressure drop (ΔP) can be expressed as [9]

$$\ni_f = \sqrt{\frac{\partial f}{\partial \Delta P}\ni_{\Delta P}}. \tag{19}$$

The field under curves was eventually used to compare cases for the collector's overall efficiency index.

3. Results and Discussion

3.1. Flow of Velocity. For validating the experimental analysis with simulation, the developed CFD models' velocity magnitude was compared with the experimental values. Furthermore, there was a positive correlation between the experimental values for CFD analysis, as shown in Figure 4. The magnitude of velocity has been determined in a steady state and utilized to determine the numerical model's prediction efficiency. The magnitude velocity displays the effects of the velocity contour in the dimples tube. The flow behaviour is almost identical in both experimental and CFD analysis, as illustrated in Figure 4. Flow behaviour demonstrates a fair and accurate estimation process and numerical procedure. In the experimental analysis, nanoparticles of SiO_2 containing the volume of concentration 0.1-0.5 percent were used to absorb the SiO_2 levels in a solar dimpled tube. The base fluid, nanoparticles, and nanofluid thermophysical properties are comparatively analyzed.

3.2. Temperature Contour. The dimpled tube temperature contour at different inclination angles with different nanofluid levels for PTSC is shown in Figure 5. The dimpled tube flow is bailment-based, where the SiO_2 nanofluid fills the outer core of the dimpled tube, where the cold water from the tank is passed through the inner core of the dimpled tube. The inclination angle of the PTSC rises from 30° to 60°. At the same time, the dimpled tube temperature decreases because of a reduced buoyancy strength produced in the vicinity of a tube and tank joint. Furthermore, the greatest velocity and temperature have been achieved at a volume fraction of 0.3 percent in all angles. The magnitude plot of 0.1-0.5% nanofluid and three distinct inclination angles at the tube inlet are analyzed. Results showed that the dimpled tube flow velocity at a tilt angle of 45° was recorded to be high. SiO_2 fluid has been assumed to significantly influence thermosiphon phenomena at the analysis phase, contributing to the above results.

3.3. Pressure Contour. The disparity between average Nusselt numbers and volume spacing is shown in Figure 6 for the various inclination angles from 30° to 60°. The average Nusselt number increases for all inclination angle values with the increment in volume fraction. However, the rising inclination angle reduces the mean amount of Nusselt number for the entire volume fraction concentration. This is induced by developing and reducing the mean Nusselt number of the weak secular recirculation at the higher inclination angles. The adjustments in the Nusselt number in the heated walls for 0.5 percent volume at different angles are observed.

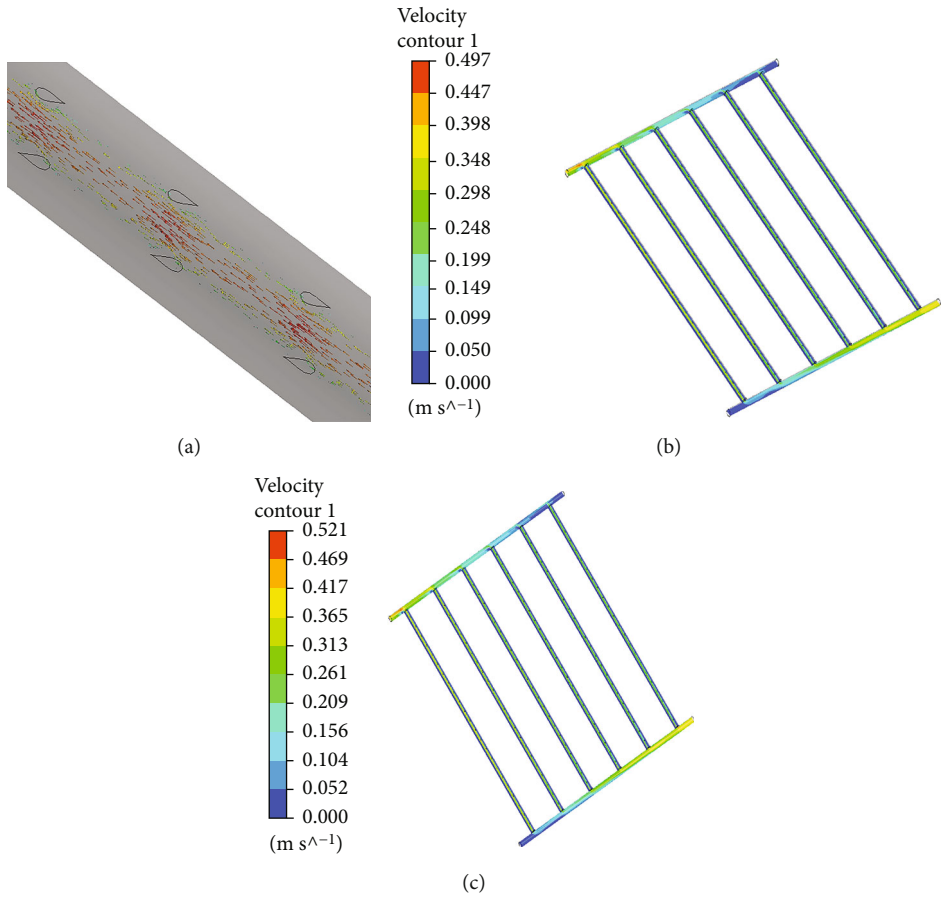

Figure 4: (a) Flow of water in dimpled tube. (b) Low velocity with low flow rate. (c) High velocity with high flow rate.

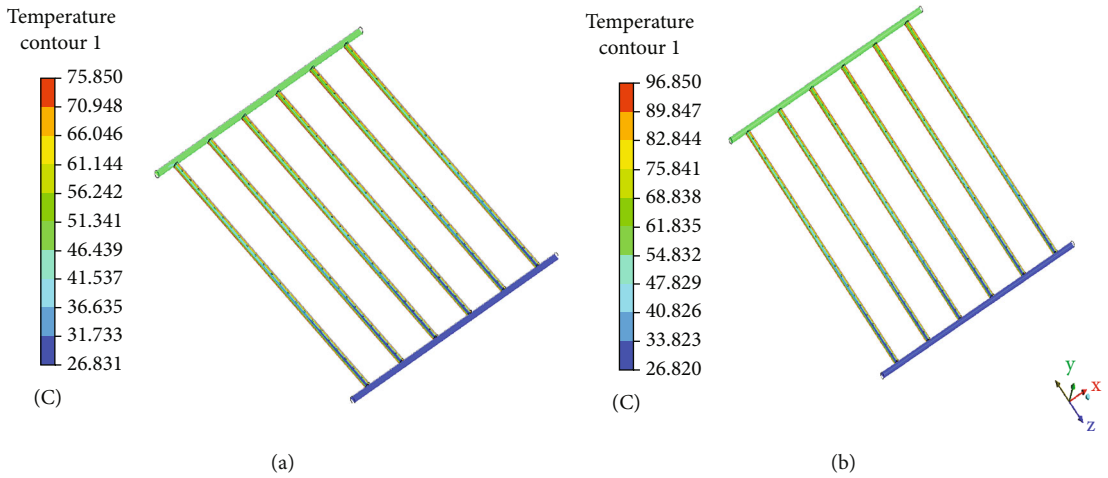

Figure 5: (a) Analysis of low temperature. (b) Analysis of high temperature.

The experimental outcomes confirmed that the higher Nusselt numbers are attained at a small inclination angle.

3.4. Comparison Absolute Energy. Figure 7 shows the energy consumed $\alpha\tau(F_R)$ with the variation in flow velocity for different concentrations of nanoparticles.

A maximum range of 5.43% greater than the base fluid has been observed in the 0.5 kg/min mass flow rate. The inclusion of SiO_2 nanoparticles is utilized to increase the absorbed energy factor, and it depends on the velocity of nanoflows, thermal conductivity, and basic heat power of the operating fluid. The heat absorption of nanoparticles is

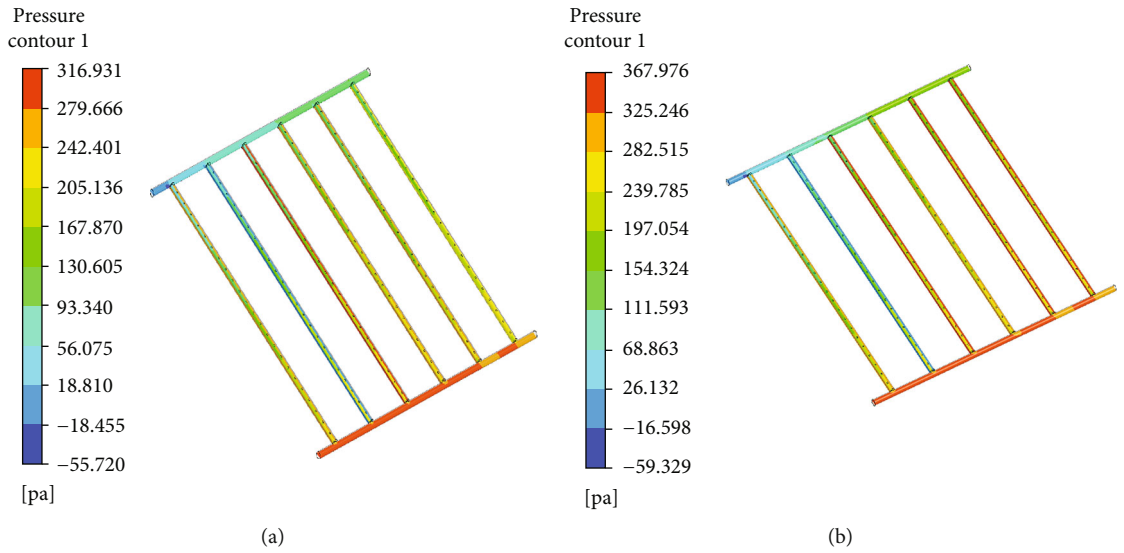

Figure 6: (a) Low-pressure contour. (b) High-pressure contour.

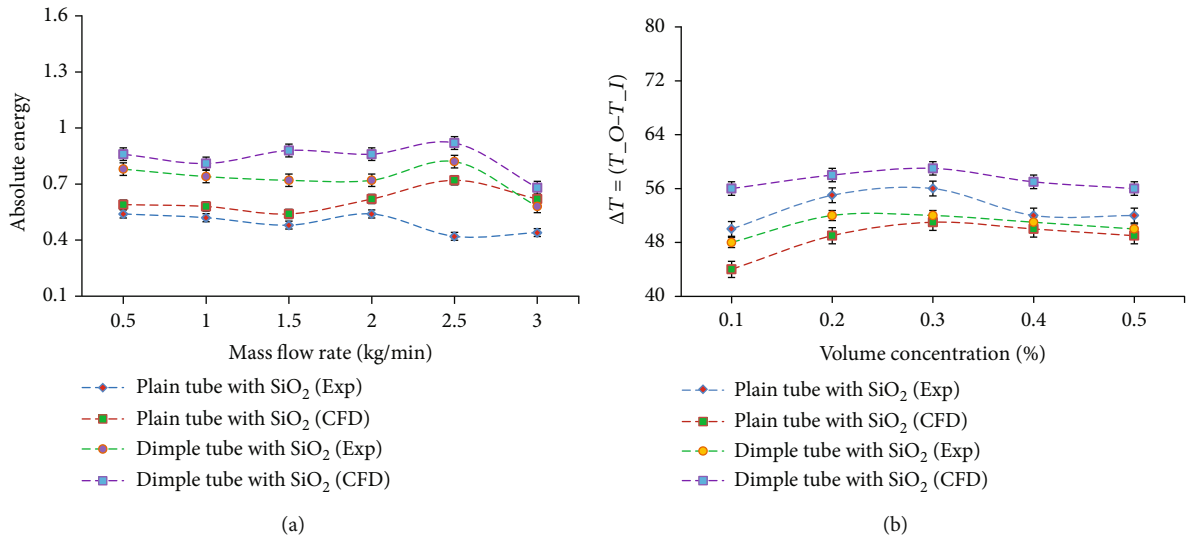

Figure 7: (a) Mass flow rates vs. absolute energy parameter. (b) Volume concentration vs. heat loss.

significantly improved at a volume concentration of 0.3% because the flow rate decreases and the fluid viscosity increases. Furthermore, Reynolds number also decreased. As a result, it contributed to the reduction in the thermal transfer coefficient and reduced the Nusselt number. The energy factor is absorbed for three different flow rates with the relative temperature of PTSC curves (0.5 kg/min-3.0 kg/min). For each of the flow rates, the efficiency is determined by the heat loss parameter $\Delta T = (T_O - T_I)$. The optimum collector efficiency of 62.35% was observed at flow rate of 2.5 kg/min and nanoparticle volume concentration of 0.3%. The variation in Nusselt number and Reynolds number is directly proportional to the heat augmentation rate. The working fluid in the dimpled tube with 0.3% of volume concentration of nanoparticles, at 2.5 kg/min, increases the Nusselt number by 2.5 times compared to the plain tube. It clearly shows that the presence of dimples significantly affected the improvement in heat transfer rate.

3.5. Analysis of Collector Efficiency. Figure 8 shows the collector efficiency improved by 11% and that the convective heat transfer increased by 34.25% relative to the base fluid. The collector efficiency and heat transfer have been enhanced due to increased SiO_2 nanoparticles' absorbance and absorption coefficient. Consequently, a pressure drop in the gradient temperature increased the convective heat transfer coefficient for nanofluids as expressed as $\Delta T = (T_O - T_I)$. For higher volume concentrations (0.1 to 0.5%), there is an 11% improvement in the solar PTSC quality compared with base fluid. The finding shows that the collector efficiency

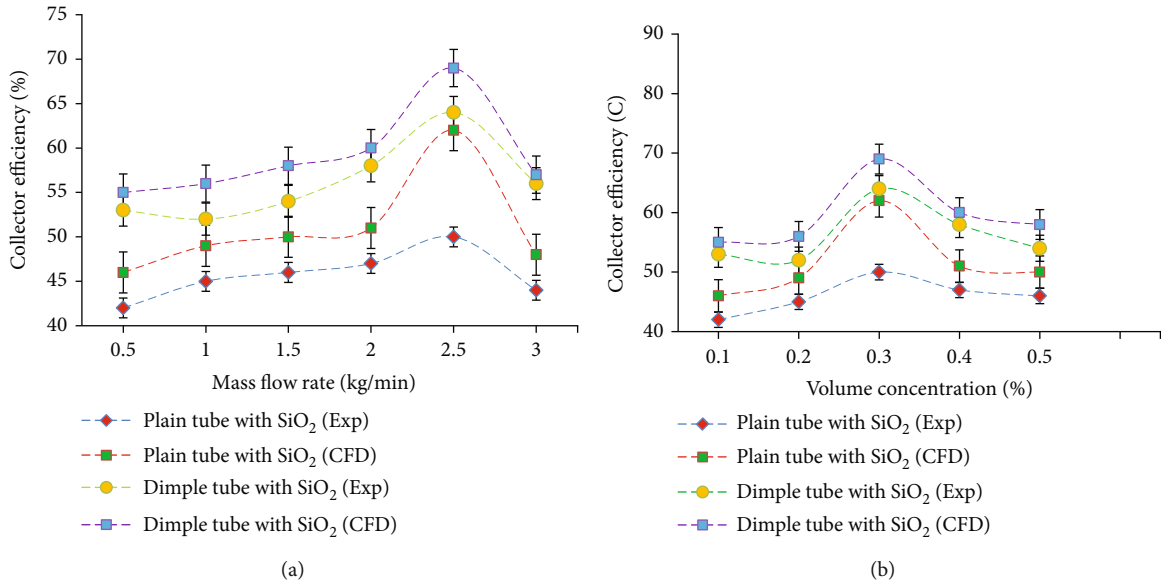

Figure 8: (a) Mass flow rate vs. collector efficiency (%). (b) Volume concentration vs. collector efficiency (%).

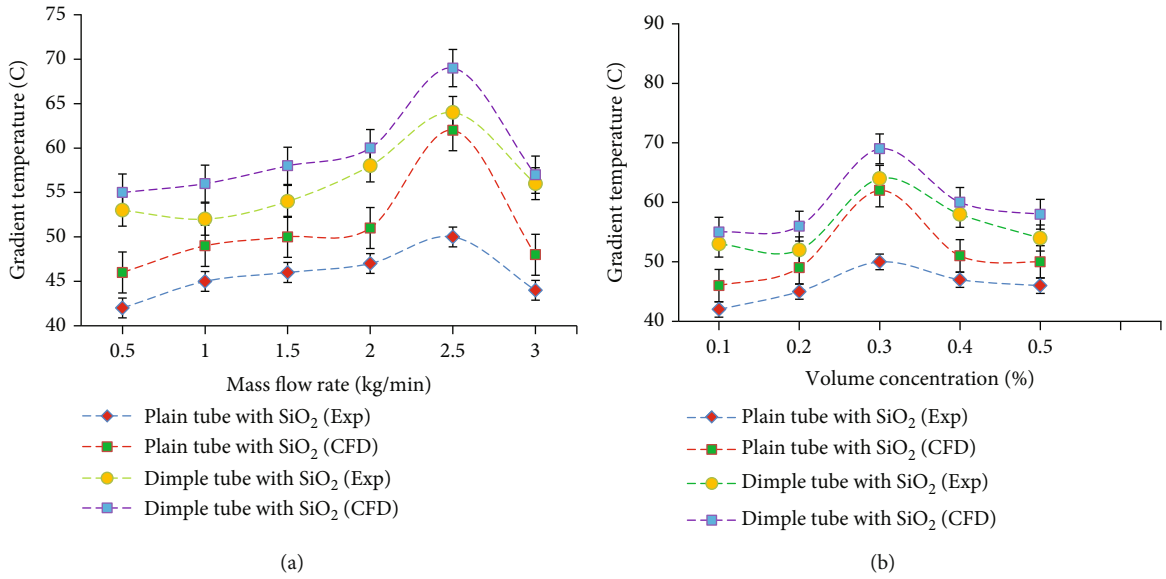

Figure 9: (a) Mass flow rate vs. gradient temperature. (b) Volume concentration vs. gradient temperature.

has been improved by 0.4%, while the volume concentration is rising by 0.5% at the various flow speeds. Since solar PTSC performance increased by an average of 0.5%, the volume's optimum concentration decreased to 0.3%. The flow rate is often shown to be inversely proportional to the temperature of the gradient. As a result, the flow rate increased, and the heat transfer coefficient improved in SiO_2 with the dimpled tube resulting in a significant improvement in the collector's performance.

3.6. Analysis of Gradient Temperature. Figure 9 depicts the temperature gradient maps at varying flow rates and concentrations of SiO_2 nanoparticles and convective heat transfer coefficients at different flow rates. These two graphs would conveniently correlate the temperature, flow rate difference, and heat transmission coefficient. Furthermore, the temperature difference is minimal, and the heat transfer coefficient is proportionally greater at velocity variance. The heat transfer coefficient is smaller during higher flow rates of the contact time on the surface (flow over time). At the same time, the heat transfer coefficient is higher at a lower flow rate. For nanofluids, a temperature gradient of 28.322°C has been achieved at a lower mass flow rate and a temperature gradient of 7.45°C at a higher velocity flow rate.

3.7. Effect of Nusselt Number. The velocity flow and concentration plots are illustrated in Figure 10 for experimental and expected Nusselt numbers. An error value of ±3.12% has

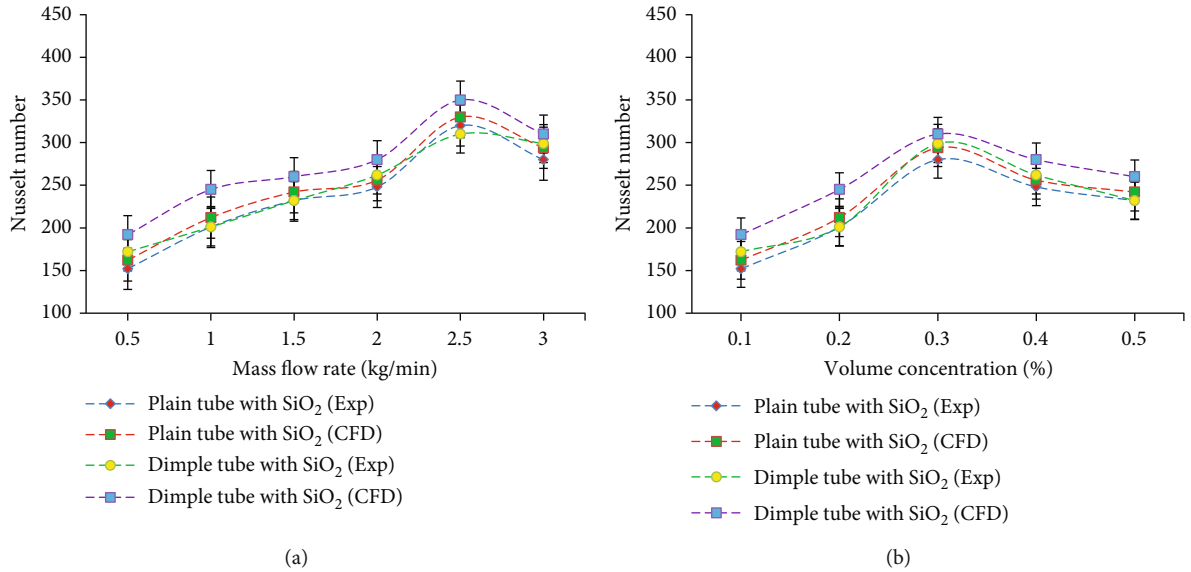

Figure 10: (a) Mass flow rate vs. Nusselt number. (b) Volume concentration vs. Nusselt number.

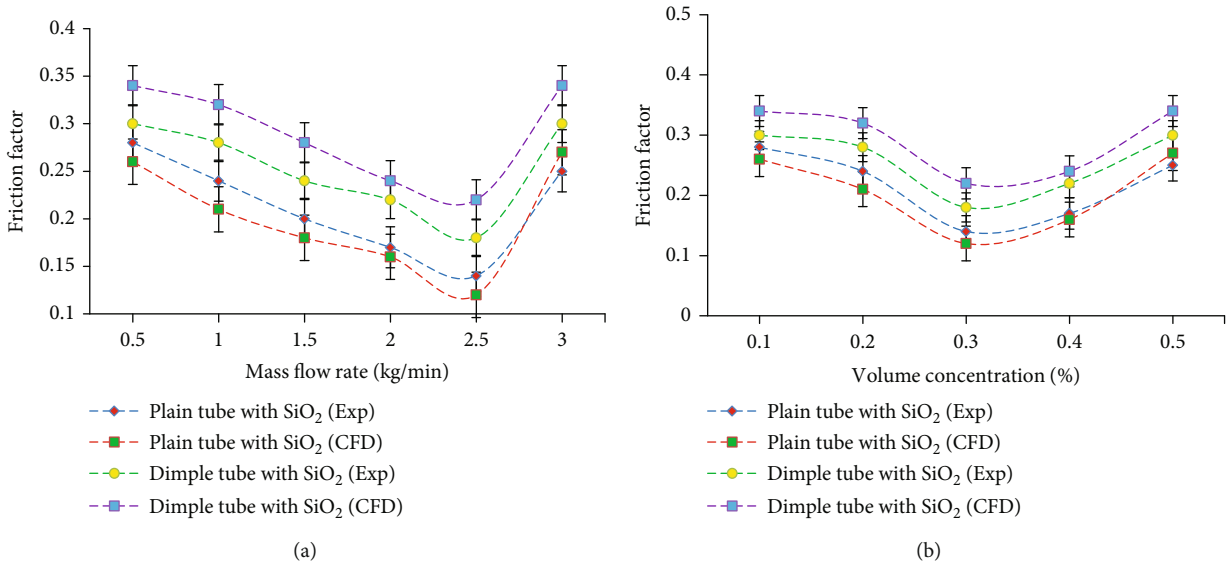

Figure 11: (a) Mass flow rate vs. friction factor. (b) Volume concentration vs. friction factor.

been observed between the CFD analysis and experimental values. Empirical correlation calculations are performed based on varying volume concentrations and velocity flow rates as per Equations (16) and (17) for different Reynolds numbers and Nusselt numbers. The developed model significantly improved the collector efficiency by 62.32% for the Reynolds number range of ($3256 < Re < 9685$) and Prandtl (6.324 to 9.254). Based on the outcomes obtained from CFD and experimental analysis, a volume concentration of 0.3% at 2.5 kg/min exhibits an 11% increment in heat transfer efficiency compared to other flow characteristics.

3.8. Effect of Friction Factor. The experimental and CFD analysis plots for friction factors with various concentrations and flow rates are illustrated in Figure 11. The friction factor is measured as a product of pressure drop and the surface roughness of the dimpled tube. Furthermore, the average pressure drop is recorded as 2.36 kPa for the solar PTSC system. In the current model, the deviation from the estimated friction factor is roughly ±4.62%. The expected friction factor for a higher Reynolds number can deviate in a range of ±11%. The efficiency metrics of experimental and CFD analysis with various flow rates and concentrations of nanoparticles and the deviations can be recorded as approximately ±7.42% percent. It shows efficiency index combinations for different Reynolds numbers and concentrations of nanoparticles. At 0.1-0.5% of the volume concentrations and a volume flow rate of 2.5 kg/min, the maximum output

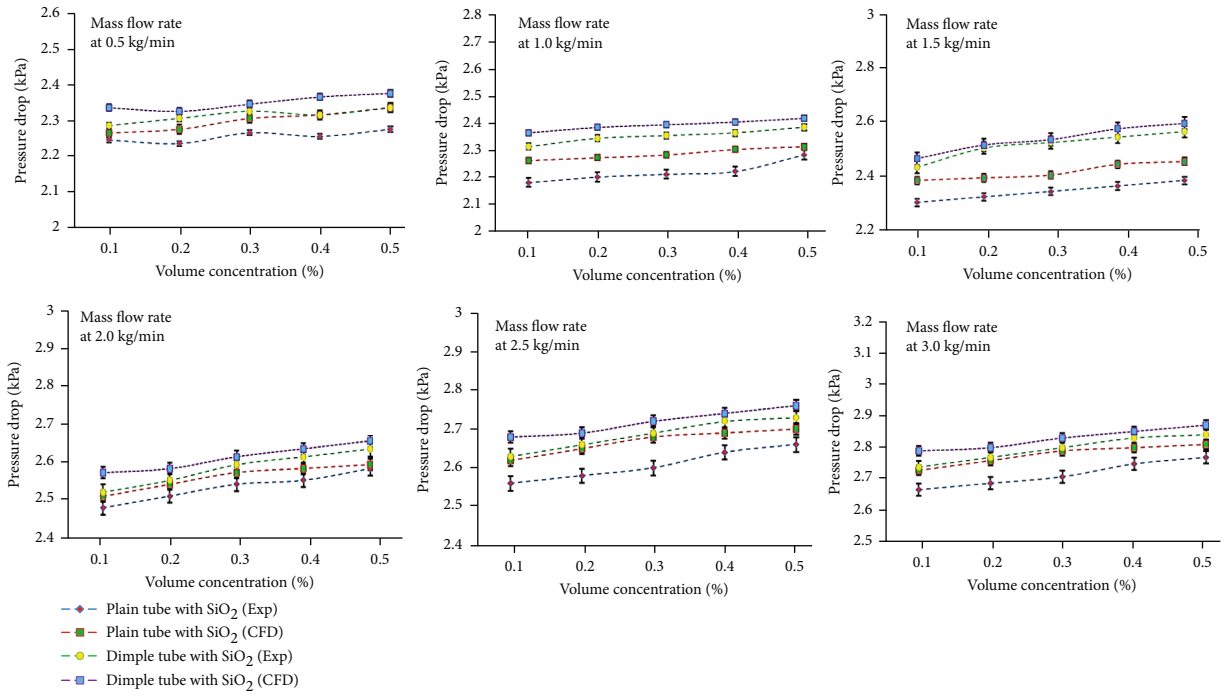

Figure 12: Variation of pressure drop with variation in nanoparticle volume concentration and mass flow rate.

index is 2.42. The SiO_2 nanofluid output index is larger than 1; in the PTSC application, the heat transfer increased in this research. The efficiency variations are based on pH changes and thermophysical nanofluid properties of SiO_2. Particle size affects the solar performances of PTSCs. Nanoparticles of more significant sizes tend to spread and absorb radiation. The measurement of the SiO_2 nanoparticles should be 50 nm to provide efficient heat transfer rates. In this analysis, the average size of the SiO_2 nanoparticles is 50 nm. The heat transfer has been improved in this research, and SiO_2 nanoparticles were efficient for PTSC solar applications.

3.9. Variation of Pressure Drop Concerning Dimpled Texture Tube. Figure 12 portrays the variation of pressure drop with the variation in nanoparticle volume concentration and mass flow rate. From Figure 12, it is observed that with an increase in the concentration of nanoparticles, the pressure drop increases irrespective of the mass flow rate of the water. This is due to the rise in the volume density of the nanoparticles in the nanofluid, which resulted in a more viscous flow of the nanofluid due to an increase in density. From Figure 12, it was also observed that dimpled tubes with SiO_2 nanoparticles exhibited a higher drop in pressure compared to the plain tube with SiO_2. This is due to increased obstacles to fluid flow due to dimple texturing on the tube surface. Apart from this, the dimpled texture offers more drag force to be experienced by the molecules adjacent to the inner tube layer during its dynamic condition. The pressure drop of the solar water heater has increased gradually with the increase in the mass flow rate of water. At a maximum mass flow rate of 3.0 kg/min and 0.5% volume concentration, the pressure drop has been increased by around 5.5% compared to the mass flow rate of 2.5 kg/min. The errors observed in the experiment and simulation are 6.2% and 2.5%, respectively, indicating the linear relationship between the experiment and simulation outcomes. Furthermore, the pressure drop results of the experimental condition are significantly higher than the simulation results.

4. Conclusions

The research analyzed SiO_2 efficiency in heat transfer for solar PTSC applications. Tests were performed using various concentrations of nanoparticles and mass flow rates. The numerical prediction was made on the SiO_2/water nanofluid collector, evacuated by thermosiphon, using commercial ANSYS tools. For various conduit angles, the effect of nanoparticle volume fraction on the collector's thermal efficiency was studied. The most significant conclusions achieved in this study are as follows:

(1) The nanoparticle volume fraction increases the heat conductivity and Nusselt number of solar evacuation pipes

(2) The inclination of 45° plays a significant role in enhancing the thermal efficiency and increases the evacuated tunnel's thermosiphon effect

(3) At the nanoparticle volume fraction and angle of inclination of 0.3 percent and 45 degrees, respectively, the optimum speed and heat transfer change were observed

(4) The nanofluid's output index is 2.42 with a 0.3% mass flow rate and concentration of 2.5 kg/s. The PSPC with SiO_2 nanofluid has a maximum overall

efficiency of 34.25%, which is 11% higher than that of the base fluid

Adopting this technology in operating the solar water heater may enhance heat transfer efficiency. This technology will provide added advantages to commercial solar water heaters in both the industrial and domestic sectors.

Data Availability

The data are available within this manuscript.

Conflicts of Interest

The authors declare that they have no conflict of interest.

Acknowledgments

The authors sincerely thank the Karpagam Academy of Higher Education (KAHE), Coimbatore, India, and Kampala International University, Western Campus, Kampala, Uganda, for providing the necessary facilities to carry out the research.

References

[1] S. T. Hamidi, "A novel application for parabolic trough solar collector based on helical receiver tube and nanofluid with a solar tracking mechanism," *Engineering and Technology Journal*, vol. 38, no. 5, pp. 656–668, 2020.

[2] A. Y. Al-Rabeeah, I. Seres, and I. Farkas, "Thermal improvement in parabolic trough solar collector using receiver tube design and nanofluid," *In International Workshop IFToMM for Sustainable Development Goals*, vol. 108, pp. 30–40, 2021.

[3] A. K. Tiwar, V. Kumar, Z. Said, and H. K. Paliwal, "A review on the application of hybrid nanofluids for parabolic trough collector: Recent progress and outlook," *Journal of Cleaner Production*, vol. 292, article 126031, 2021.

[4] R. Naveenkumar, M. Ravichandran, B. Stalin et al., "Comprehensive review on various parameters that influence the performance of parabolic trough collector," *Environmental Science and Pollution Research*, vol. 28, no. 18, pp. 22310–22333, 2021.

[5] J. Subramani, P. K. Nagarajan, O. Mahian, and R. Sathyamurthy, "Efficiency and heat transfer improvements in a parabolic trough solar collector using TiO_2 nanofluids under turbulent flow regime," *Renewable Energy*, vol. 119, pp. 19–31, 2018.

[6] M. Rezaeian, M. S. Dehaj, M. Z. Mohiabadi, M. Salarmofrad, and S. Shamsi, "Experimental investigation into a parabolic solar collector with direct flow evacuated tube," *Applied Thermal Engineering*, vol. 189, article 116608, 2021.

[7] S. E. Ghasemi, S. Mohsenian, and A. A. Ranjbar, "Numerical analysis on heat transfer of parabolic solar collector operating with nanofluid using Eulerian two-phase approach," *Numerical Heat Transfer, Part A: Applications*, vol. 80, no. 9, pp. 475–484, 2021.

[8] T. Sajid, W. Jamshed, F. Shahzad et al., "Study on heat transfer aspects of solar aircraft wings for the case of Reiner-Philippoff hybrid nanofluid past a parabolic trough: Keller box method," *Physica Scripta*, vol. 96, no. 9, p. 095220, 2021.

[9] M. Arun, D. Barik, K. Sridhar, and G. Vignesh, "Performance analysis of solar water heater using Al_2O_3 nanoparticle with plain-dimple tube design," *Experimental Techniques*, pp. 1–14, 2022.

[10] T. Sajid, W. Jamshed, F. Shahzad, M. R. Eid, E. K. Akgül, and K. S. Nisar, "Entropy analysis and thermal characteristics of Reiner Philippoff hybrid nanofluidic flow via a parabolic trough of solar aircraft wings: Keller box method," vol. 96, p. 9, 2021.

[11] W. Bai, Z. Zhang, W. Tian et al., "Toxicity of zinc oxide nanoparticles to zebrafish embryo: a physicochemical study of toxicity mechanism," *Journal of Nanoparticle Research*, vol. 12, no. 5, pp. 1645–1654, 2010.

[12] M. Moravej, M. V. Bozorg, Y. Guan et al., "Enhancing the efficiency of a symmetric flat-plate solar collector via the use of rutile TiO_2-water nanofluids," *Sustainable Energy Technologies and Assessments*, vol. 40, article 100783, 2020.

[13] O. Mahian, L. Kolsi, M. Amani et al., "Recent advances in modeling and simulation of nanofluid flows-part I: fundamentals and theory," *Physics Reports*, vol. 790, pp. 1–48, 2019.

[14] S. Parvin, R. Nasrin, and M. A. Alim, "Heat transfer and entropy generation through nanofluid filled direct absorption solar collector," *International Journal of Heat and Mass Transfer*, vol. 71, pp. 386–395, 2014.

[15] A. R. Noghrehabadi, E. Hajidavalloo, and M. Moravej, "An experimental investigation on the performance of a symmetric conical solar collector using SiO_2/water nanofluid," *Transp Phenom Nano Micro Scales*, vol. 5, pp. 23–29, 2016.

[16] M. Ghalambaz, A. Behseresht, J. Behseresht, and A. Chamkha, "Effects of nanoparticles diameter and concentration on natural convection of the Al_2O_3-water nanofluids considering variable thermal conductivity around a vertical cone in porous media," *Advanced Powder Technology*, vol. 26, no. 1, pp. 224–235, 2015.

[17] S. V. Sujith, A. K. Solanki, and R. S. Mulik, "Experimental evaluation in thermal conductivity enhancement and heat transfer optimization of eco-friendly Al_2O_3–pure coconut oil based nano fluids," *Journal of Thermal Science and Engineering Applications*, vol. 13, no. 3, article 031005, 2021.

[18] S. K. Verma, A. K. Tiwari, and D. S. Chauhan, "Experimental evaluation of flat plate solar collector using nanofluids," *Energy Conversion and Management*, vol. 134, pp. 103–115, 2017.

[19] S. Yan, F. Wang, Z. Shi, and R. Tian, "Heat transfer property of SiO_2/water nanofluid flow inside solar collector vacuum tubes," *Applied Thermal Engineering*, vol. 118, pp. 385–391, 2017.

[20] T. Yousefi, F. Veysi, E. Shojaeizadeh, and S. Zinadini, "An experimental investigation on the effect of Al_2O_3-H_2O nanofluid on the efficiency of flat-plate solar collectors," *Renewable Energy*, vol. 39, no. 1, pp. 293–298, 2012.

[21] L. S. Sundar and K. V. Sharma, "Numerical analysis of heat transfer and friction factor in a circular tube with Al_2O_3 nanofluid," *International Journal of Dynamics of Fluids*, vol. 4, pp. 121–129, 2008.

[22] R. Ekiciler, "CFD analysis of laminar forced convective heat transfer for TiO_2/water nanofluid in a semicircular cross-sectioned micro-channel," *Journal of Thermal Engineering*, vol. 5, pp. 123–137, 2019.

[23] M. R. Thansekhar and C. Anbumeenakshi, "Experimental investigation of thermal performance of microchannel heat sink with nanofluids Al_2O_3/water and SiO_2/water," *Experimental Techniques*, vol. 41, no. 4, pp. 399–406, 2017.

[24] P. Kalidoss, S. Venkatachalapathy, and S. Suresh, "Optical and thermal properties of Therminol 55-TiO_2 nanofluids for solar energy storage," *International Journal of Photoenergy*, vol. 2020, Article ID 7085497, 9 pages, 2020.

[25] B. N. Cardoso, E. C. Kohlrausch, M. T. Laranjo et al., "Tuning anatase-rutile phase transition temperature: TiO_2/SiO_2 nanoparticles applied in dye-sensitized solar cells," *International Journal of Photoenergy*, vol. 2019, Article ID 7183978, 9 pages, 2019.

[26] A. Ayoobi and M. Ramezanizadeh, "An exhaustive review on a solar still coupled with a flat plate collector," *International Journal of Photoenergy*, vol. 2021, Article ID 9744219, 24 pages, 2021.

[27] Y. Cao, H. Ayed, T. Abdulrazzaq, T. Gul, A. Bariq, and B. Bouallegue, "Effect of the number of nozzles of swirl flow generator utilized in flat plate solar collector: an entropic analysis," *International Journal of Photoenergy*, vol. 2021, Article ID 8320714, 10 pages, 2021.

Hindawi
International Journal of Photoenergy
Volume 2022, Article ID 7543121, 9 pages
https://doi.org/10.1155/2022/7543121

Research Article

Experimental and Analytical Study of a Proton Exchange Membrane Electrolyser Integrated with Thermal Energy Storage for Performance Enhancement

Xiaodong Peng,[1] **Zhanfeng Deng**,[1] **Xueying Zhao**,[1] **Gendi Li**,[1] **Jie Song**,[1] **Danxi Liang**,[1] **Xiaotong Sun**,[1] **Guizhi Xu**,[1] **Wei Kang**,[1] **and Min Liu**[2]

[1]*State Key Laboratory of Advanced Power Transmission Technology, State Grid Smart Grid Research Institute Co., LTD., Changping District, Beijing 102211, China*
[2]*State Grid Electric Power Corporation Co., LTD., Hangzhou 310007, China*

Correspondence should be addressed to Xiaodong Peng; pengxiaodong@geiri.sgcc.com.cn

Received 12 February 2022; Accepted 17 June 2022; Published 4 July 2022

Academic Editor: Kok Keong Chong

To peak carbon dioxide emissions and carbon neutrality, hydrogen energy plays a pivotal role in the energy system dominated by wind power and solar power. The proton exchange membrane (PEM) electrolytic hydrogen production technology has advantages of higher current density, higher hydrogen purity, higher load flexibility, and balanced grid load, becoming one of effective ways to consume renewable energy. Experimental analysis finds that the present PEM electrolyser cannot maintain a stable operating temperature as the input power changes; the polarization curve would distort with the change of temperature. This work proposes a PEM electrolyser coupled with the thermal energy storage device to meet power fluctuation and frequent start and stop caused by renewable resources. Through the involvement of the thermal storage device, electrolytic system is able to operate quickly and persistently in an efficient condition. The coupled system effectively reduces energy consumption in the process of start-stop or load changing, which can effectively adapt to the power fluctuation and frequent start and stop caused by renewable energy.

1. Introduction

The randomness and fluctuation of renewable energy are bringing great challenges to power network security nowadays. How to economically and efficiently use wind or solar power through energy storage technology has become a challenging topic in the global energy field [1]. Hydrogen has attracted widespread attention that it will play an important role in the future as a secondary energy carrier in addition to electricity. Hydrogen energy has the characteristics of large-scale reserves, environmentally friendly, and renewable, which meets the requirements of sustainable development of environment [2, 3]. The electrolysis system converts excess electricity into hydrogen, which can be reused as fuel or converted back into electricity by fuel cells when electric power is needed [4].

The principle technologies of hydrogen production by electrolysis focus on alkaline and proton exchange membrane (PEM). Troostwijk and Diemann first discovered electrolysis in 1789 [5]; so far, Alkaline Electrolysers (AWE) are long established in industry but involve hazardous chemicals and alkaline impurities, and purification is needed before use [6, 7].

In 1966, General Motors developed the first electrolytic cell based on the Solid Polymer Electrolyte (SPE) concept, overcoming the disadvantages of alkaline corrosion and pollution of alkaline electrolytic cells. Solid polymer membranes, also known as proton exchange membranes, provide high electrical conductivity, allowing compact design and high-pressure operation [8]. Figure 1 shows a cross-section of a PEM water electrolyser [9]. PEM cell is compact, mainly composed of anode and cathode plates, diffusion layers,

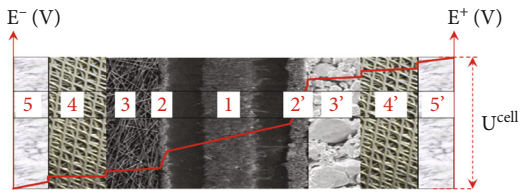

Figure 1: Schematic representation of a PEM water electrolysis cell: 1: proton exchange membrane, 2/2′: catalytic layer, 3/3′: porous transport layer, 4/4′: channel, and 5/5′: plate [9].

catalytic layers, and proton exchange membrane. The catalyst layer can be applied directly to the film or to the porous transport layer (3-3′) to equalize the current distribution. Liquid water is pumped through anodic channels to provide feedstock for the reaction and to expel heat generated during the reaction.

The thickness of proton exchange membrane is around 5~7 mm, which is beneficial to proton conductivity, allowing higher current densities to be achieved [10]. Due to low gas crossover rate of the polymer electrolyte membrane, PEM electrolyser is able to work under a wide range of power density (5%~120%) [11]. The PEM electrolytic hydrogen production technology has advantages, such as higher current density (generally 2~3 A/cm^2), higher hydrogen purity (up to 99.999%), higher load flexibility (5%~120%), and balanced grid load [12].

Significant efforts have been made to improve the performance of the PEM electrolyser by modeling works to discuss the hydrogen crossover through the membrane and difference, such as temperature, mass transfer coefficient, hydrogen concentration in oxygen, and liquid/gas diffusion layer (LGDL) compression and operating pressure [12]. Babar et al. [13] developed an equivalent electrical model for the PEM electrolyser, an input current–voltage (I–V) characteristic for a single PEM electrolyser cell was modeled through a series of experiment, and it has been observed that the electrolysis energy efficiency was in the range of 65–68% at steady-state conditions. Atlam et al. [14], through a single-channel-based three-dimensional CFD model, studied the influence of the key performance parameter of a PEM water electrolyser. The CFD model successfully predicted the current–voltage polarization curve. Carmo et al. [9], Han et al. [15], and Deshmukh and Boehm [16] used similar mathematical models to analyse the effect of current density, temperature, pressure, and membrane properties on the performance of the PEM electrolyser. Their modeling results can help to improve electrolysis system performance. In addition, Ma et al. [17] illustrated temperature distribution along the membrane-electrode assembly under different voltages through the simulation of the internal structure of the electrolytic cell. Three-dimensional (3D) models were also used by Upadhyay et al. [18] and Xu et al. [19]. It is found by Upadhyay et al. that the stack temperature is one of the most influencing parameters and a higher temperature (313 K to 353 K) is optimal for the PEM electrolyser [18]. Through studying the detailed distribution of two phases in anode flow channel, it is found by Xu et al. that the cell performance is improved by 0.171 V at 3 A cm^{-2} by replacing the traditional parallel flow with the new flow field [19].

Another part of the research is based on a combination of experiments and simulations. The thermal effects in the development of electrolyser models were also considered. The common method is to improve or verify the accuracy of the simulation model through experimental test results or empirical formulas [20]. Kim et al. [21] proved the effect of chemical reaction, chemical component thermodynamics, external ambient temperature, and Joule effect on the PEM electrolyser through experimental measurements. The results presented that the dynamic temperature impacted for both current and voltage. Aouali et al. [22] compared modeling results and lab-scale experimental data, and an acceptable mismatch of temperature dynamic performance was found in the PEM electrolyser system.

Water quality is another one of the influencing parameters to the performance of PEM electrolysis. Li et al. [23] investigated long-term Fe^{3+} ion contamination effects on the performance of single PEM cell. Though measuring membrane thickness and fluoride count on the cathode side, it is proved that membrane was attacked by radicals formed from hydrogen peroxide due to the existence of Fe^{3+} ions. The contamination effects of many other cations were also investigated by many researchers, such as Ca^{2+} [24, 25], Na^+ [24, 26], and Cu^{2+} [27].

Drawing on the research history of the PEM electrolyser, there are few studies on power fluctuation and frequent start-stop of electrolytic cell system. This work will discuss the impact of power changes on the PEM electrolyser system and proposed a coupled PEM electrolyser with an energy storage device. Through the combination of solar heat collection device and thermal energy storage device, heat can be used in electrolysis process and keep its efficient operation when input power is fluctuant.

2. System Description

It is found that the PEM electrolyser cannot be maintained in the high-efficiency operating range, when renewable energy is connected to the hydrogen production system, resulting in the increase of overvoltage and instantaneous energy consumption (see details in Section 4.1). A thermal energy storage device can maintain the operating temperature of the PEM electrolyser and drives system in a higher performance. Figure 2 shows the layout of a PEM electrolyser system integrated with thermal energy storage device. The novel system can operate in two modes, namely, normal mode and power fluctuation mode, respectively.

The heat storage is temporarily out of work at normal mode. It should be noted that purified water is required to fill the water loop before the system can be started. When the electrolysis process begins, purified water is continuously pumped through the heat exchanger to the electrolytic cell; in the process of electrolysis, hydrous oxygen is produced at the anode and hydrous hydrogen at the cathode. Hydrogen is stored in a high-pressure tank after separation and purification. The water returns to the relay water tank from

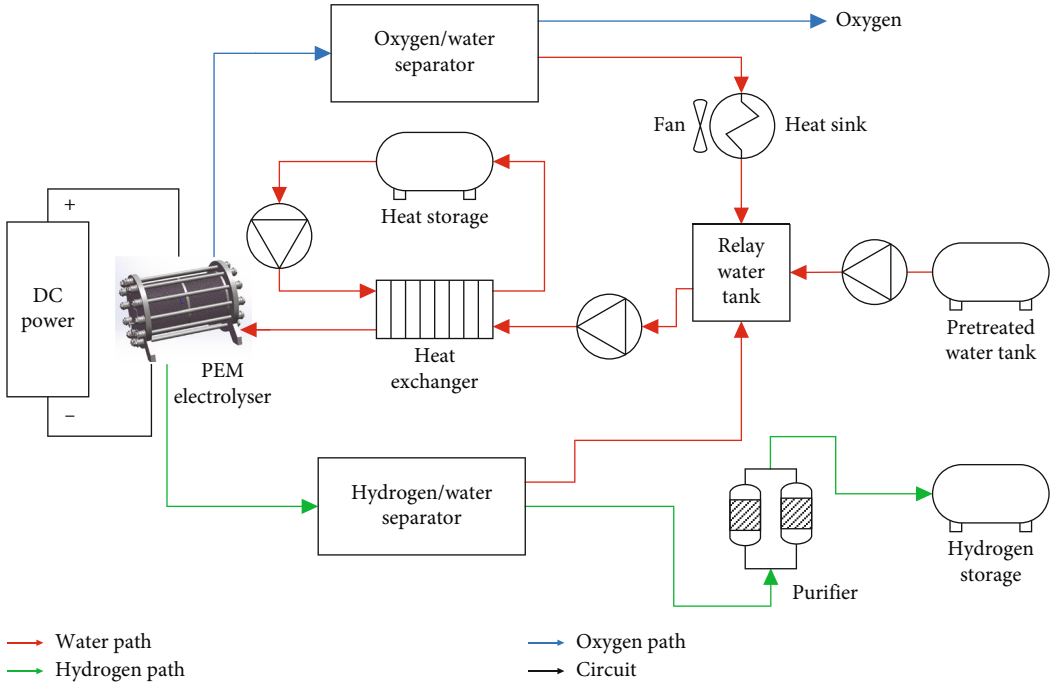

Figure 2: Schematic diagram of the PEM electrolyser system coupled with energy storage device.

the bottom of the separator after oxygen separation, and the oxygen is collected or exhausted from the upper part of the separator.

Power fluctuation mode launches when power fluctuates or system starts. The medium (water) in the energy storage device transfers the heat to the purified water, forcing its temperature to rise rapidly to reach the optimal temperature of the electrolytic cell. Two points should be clarified; one is that pretreated water is pumped to the relay water tank only when its level is low, thus replenishing the PEM electrolyser with the water consumed during the reaction; the second is that the fan is launched when the water is close to the temperature barrier. Due to the characteristics of the catalyst and membrane, the operating temperature of the PEM electrolyser is commonly lower than 90°C, although there are differences of operating temperature in these studies [5, 9, 12].

3. Establishment of the Coupled PEM Electrolyser

According to the coupled PEM electrolyser system selected in this work, the corresponding PEM electrolyser system (hydrogen production test bench) is established, mainly including the PEM electrolyser, water separation subsystem, purification subsystem, heat storage subsystem, pressurizing subsystem, and controlling and monitoring subsystem, as shown in Figure 3. The rated power of the PEM electrolyser system is about 60 kW, affording 3 stacks operating synchronously, and it should be noted that only 1 PEM electrolyser stack is used during the whole experiment. designed hydrogen yield 4 Nm^3/h, and purity is about 99.99%. To ensure the reliability of the experimental system, a throttle valve is used to reduce pressure at the outlet of the oxygen path. Concentration detection and alarm devices are also installed around the platform to ensure the test safety.

3.1. Separation Subsystem. The gas-water separator is used for separating liquid droplets from the gas when the removal rate of liquid impurities in the gas is very high. This subsystem consists of hydrogen separators and oxygen separators, and their structure and function are similar. Hydrogen and oxygen flow out from cathode and anode, respectively, with a certain proportion of liquid water, and enter the primary separator for gas-liquid separation. The function of the separator is to make the gas change direction suddenly in the flow, separating water droplets from the gas. The water droplets gather at the bottom of the separator and flows back to relay water tank. The function of the secondary separator is to further remove water in hydrogen or oxygen after the primary separator; thus, it has the function of gas-liquid separation and cooling and dehumidification. The design parameters of primary and secondary hydrogen separators are listed in Table 1, and Figure 4 shows the real pictures of primary and secondary hydrogen separators and primary and secondary oxygen separators, from left to right, respectively.

3.2. Purification Subsystem. The hydrogen produced by the PEM electrolyser removed almost all liquid water after the separation processes, and the purification subsystem is used to further remove gaseous water from hydrogen to ensure the purity. The hydrogen purification subsystem consists of two adsorption towers in parallel. One adsorption tower is in an adsorption state, and the other is in a regeneration state. The adsorbent is a combination of alumina and molecular sieve, the upper layer of adsorption tower uses molecular sieve, and the lower part uses activated alumina. The

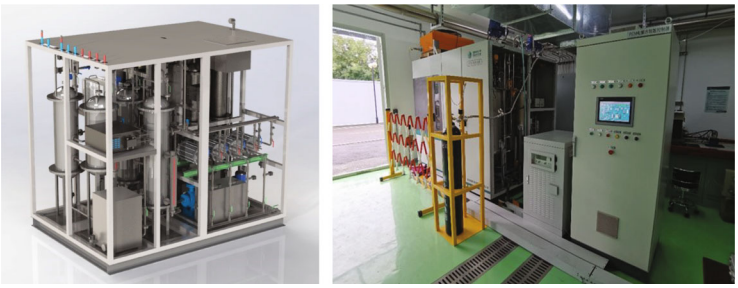

Figure 3: 60 kW PEM electrolyser test bench internal 3D model drawing and actual external view.

Table 1: Main parameters of primary and secondary separators.

Name	Value			
	Primary hydrogen separator	Secondary hydrogen separator	Primary oxygen separator	Secondary oxygen separator
Pressure (MPa)	0.1-3.5	0.1-3.5	0.1-3.5	0.1-3.5
Temperature (°C)	65	20	65	20
Design separation rate (%)	90	90	90	90
Size (mm)	$\Phi 300 \times 1800$	$\Phi 300 \times 1600$	$\Phi 300 \times 1800$	$\Phi 300 \times 1600$

Figure 4: Primary and secondary separators.

rated parameters of purification subsystem are listed in Table 2.

3.3. Heat Storage Subsystem. Heat storage subsystem is used to simulate the process that solar energy or other renewable energy participates in the performance improvement of the PEM electrolyser. Solar or other renewable energy is stored as heat in a subsystem, and the stored heat, through a plate heat exchanger, can be used for PEM electrolysis when input power is fluctuant. The design parameters of circulating water pump are listed in Table 3, and Figure 5 shows the real pictures of the circulating water pump and plate heat exchanger.

3.4. Pressurizing Subsystem. The circulating water pump is a pressurization equipment, through the impeller rotating to form the pressure difference between the inlet and the outlet. It is used to overcome the resistance loss of circulating water system, leading to water continuously flowing in the loop. In a PEM electrolyser system, the circulating water pump is one of the key equipment to steadily provide reaction water,

Table 2: Main parameters of the purification subsystem.

Name	Value
Maximum flow (Nm^3/h)	20
Outlet purify (%)	≥99.99
Pressure range (MPa)	3-3.5
Adsorbent	Alumina, molecular sieve

Table 3: Main parameters of the heat storage subsystem.

Name	Value
Heat transfer medium	Water
Storage temperature (°C)	80-90
Pressure range (MPa)	0.1-0.5
Outlet flow (L/min)	20-40

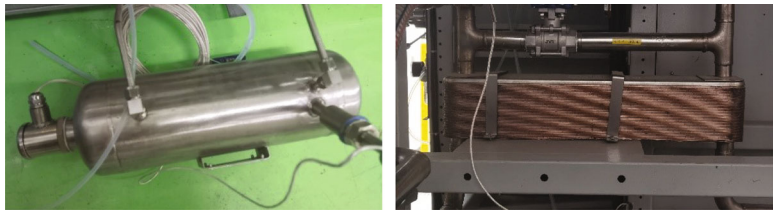

Figure 5: Heat storage and plate heat exchanger.

Table 4: Main parameters of the circulating pump.

Name	Value
Flow range (L/min)	10-50
Temperature range (°C)	5-90
Pressure range (MPa)	0.1-3.5
Lift (m)	10
Motor type	Variable-frequency
Rated power (kW)	1.5

meanwhile, and circulating water can also take heat out of the PEM electrolyser, which is mainly generated by ohmic overpotential [5]. Because the working pressure range of electrolytic cell is 0.1-3.2 MPa, the selected circulating water pump must withstand pressure. The design parameters of the circulating water pump are listed in Table 4, and Figure 6 shows the real pictures of the circulating water pump.

60 kW PEM electrolyser system is mainly used for performance testing of electrochemical reactor polarization curve, electrochemical impedance, electrochemical adsorption area, and hydrogen current density and can monitor the current and voltage of the PEM electrolyser in real time and monitor hydrogen concentration and oxygen concentration to prevent safety problems.

4. Results and Discussions

The testing process of the PEM electrolyser system was divided into two parts: PEM electrolytic process and thermal energy-involved electrolytic process. This section analysed the changes of parameters such as operating temperature of substances at the entrance of the PEM electrolyser during these two processes. Meanwhile, the relevant polarization curves were measured during the two processes. Figure 7 shows the PEM electrolyser used in the experiment, and the details of membrane electrode assembly (MEA) used in the test are shown in Table 5.

4.1. PEM Electrolytic Process. Preparatory works, such as pipeline cleaning or water circulation flowing, should be finished before launching the PEM electrolyser, and this preparatory time was not accounted into the whole test. It should be noted that the PEM electrolyser runs in constant current mode, and the power supply adjusted the voltage continuously according to the characteristics of the PEM electrolytic cell, so that the current was approximately fixed. The water flow into the electrolyser was maintained at 200 mL/min

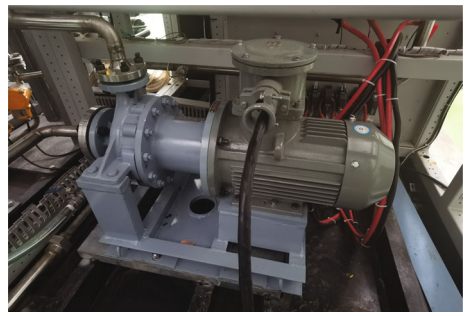

Figure 6: Circulating water pump.

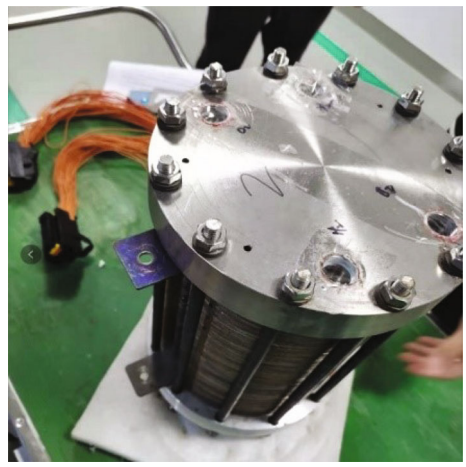

Figure 7: The PEM electrolyser used in the experiment.

per cell. Figures 8 and 9 present the operation process of the test which almost lasts 55 minutes. The current density increased by around 0.2 A/cm^2 each time as the voltage gradually stabilizes until it reached to about 0.715 A/cm^2; the electrolyser continued to operate for 1600 s. During the process of 1600 s operation, load variation tests were done twice at 1800 s and 2250 s, respectively. Then, the current density was gradually increased to the peak value of 0.881 A/cm^2, and after continuous operation for 200 s, the current density was gradually reduced to 0 to complete the whole test.

It can be found that there was no remarkable increase in the water outlet temperature of the cell during the early stage of the test (from 0 to 500 s); obviously, 200 mL/min water flow was excessive for the electrolytic cell at this current density. When the current density increased to a relatively high value, the outlet water temperature gradually rises. In

Table 5: Details of membrane electrode assembly.

Name	Type/value
Proton exchange membrane	Nafion 115
Active area of MEA	160 cm^2
Cathode	Carbon paper
Anode	Titanium fiber felt
Pressure range	0.1-3.2 MPa
Water flow	200 mL/min

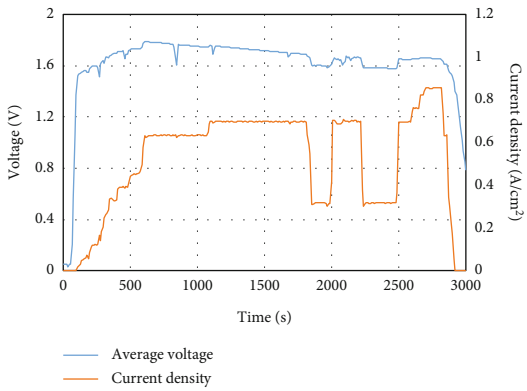

Figure 8: Trends of average voltage and current density of the PEM electrolyser.

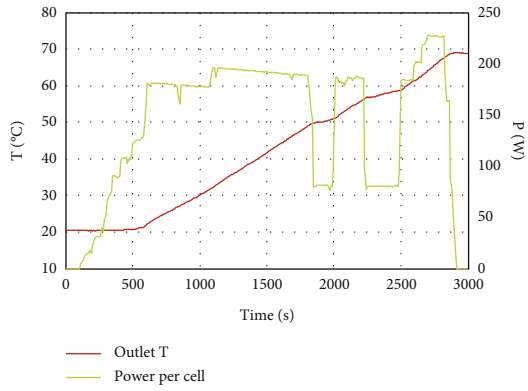

Figure 9: Trends of outlet water temperature and power of the PEM electrolyser.

constant current mode, the voltage dropped slightly as the temperature increases, which was mainly because the activation overpotential and ohmic overpotential presented a significant drop as the temperature increases [5–7], as shown in Figure 10. However, due to the characteristics of the catalyst and membrane, the PEM electrolyser cannot operate persistently without a temperature barrier [5, 10]. It can be concluded that higher temperature is beneficial to reduce the energy consumption of electrolytic cell as long as it is within the temperature limit.

In order to suit the randomness and fluctuation of wind power and solar power, hydrogen production system had to run under variable power for a long time, and its start-stop

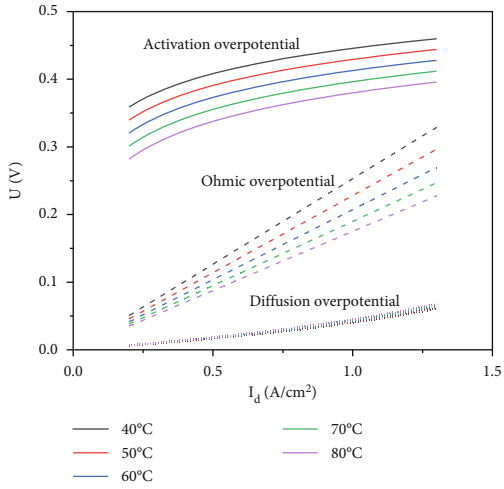

Figure 10: Effect of current density and temperature on activation overpotential, ohmic overpotential, and diffusion overpotential.

frequency is often more than that of hydrogen production system connected to the power grid. Meanwhile, intermittent operation may lead to changes in operating temperature that affect the efficiency of the PEM electrolyser. Figure 11 illustrates the effect of operating temperature on the voltage of the PEM cell, the temperature changes from 20°C to over 60°C in the process of the current density rising from small to large, and the performance improvement was caused by the higher temperature of large current density. It is found that the electrolytic cell cannot maintain a stable operating temperature as the input power changes; the polarization curve would distort with the change of temperature. Therefore, with renewable energy linked to hydrogen production systems, the PEM electrolyser cannot be maintained in the high-efficiency operating range, further resulting in the increase of overvoltage and instantaneous energy consumption. Ignoring errors between simulation and experimental results, dashed lines in Figure 11 clarify the polarization curve of electrolytic cell at constant temperature. In the case of input power fluctuations or continuous start-stop for several times, a renewable energy storage device can maintain the operating temperature of the PEM electrolyser and may keep the system at a higher efficiency.

4.2. Thermal Energy-Involved Electrolytic Process. Before the thermal energy-involved experiment, energy storage device stored solar or other renewable energy in the form of heat in a medium (using purified water in this process) beforehand. The initial temperature of the energy storage device was set at around 85°C. Figures 12 and 13 described the thermal energy-involved electrolytic process. The circulating water temperature reached ~58°C in 30 seconds due to the heat received from the heat storage device. As the current density increases (around 0.63 A/cm^2 in ~380 seconds), the heat generated by the electrolytic cell can maintain the operating temperature, and the heat storage device stops heating. Meanwhile, in order to prevent the electrolytic cell overheating, cooling fan starts to cool down the circulating water.

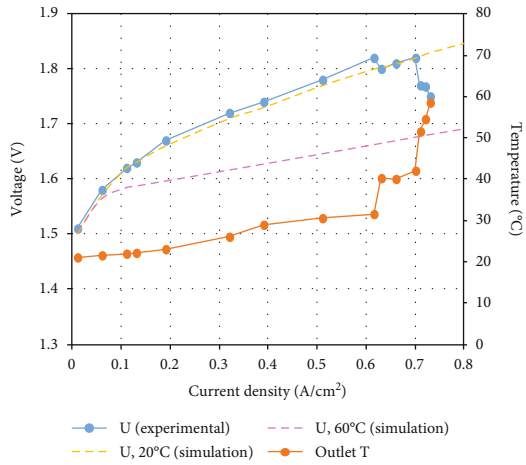

Figure 11: Polarization curves and the effect of operating temperature on the voltage of the PEM cell.

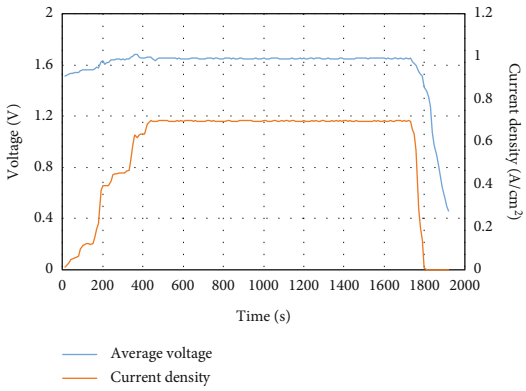

Figure 12: Trends of average voltage and current density of the PEM electrolyser with heat storage involved.

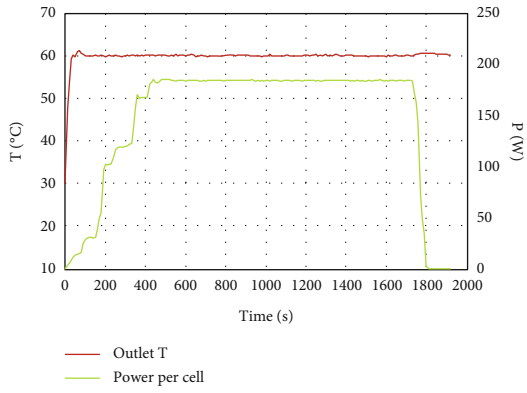

Figure 13: Trends of outlet water temperature and power of the PEM electrolyser with heat storage involved.

The power of the cell was 185 W, and the voltage was about 1.67 V under stable operation condition.

The performance improvement of the PEM electrolyser with heat storage involved is found in Figure 14. With the participation of heat storage device, the polarization curve

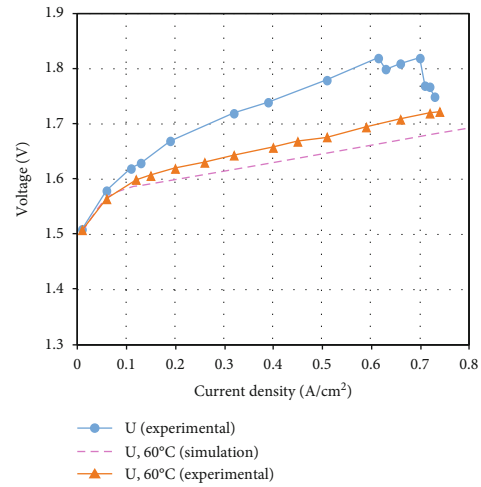

Figure 14: Polarization curves of the PEM cell with thermal storage involved.

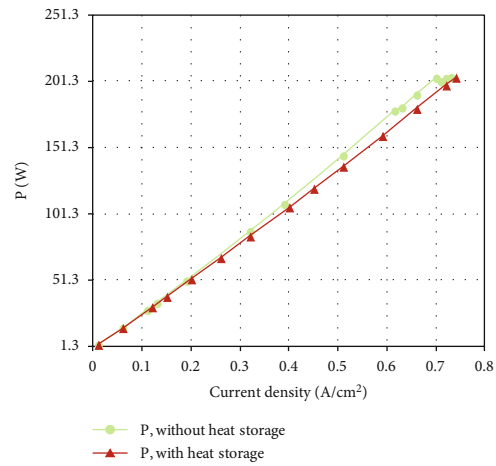

Figure 15: Power consumption comparison with or without energy storage device for the single PEM cell.

of the PEM electrolytic cell showed a similar trend to the simulation results; their errors were less than 3%. The maximum difference of power consumption per cell can reach ~12 W, as shown in Figure 15. The PEM electrolyser installed with heat storage presented a higher current density (more charge transfer) under the same power consumption, which means a higher hydrogen yield (maximum increment of 5.04%). It is concluded that the PEM hydrogen production system coupled with the thermal energy storage device can effectively adapt to the power fluctuation and frequent start and stop caused by renewable energy, so that the hydrogen production system operated in a higher performance range.

5. Conclusions

In this work, a PEM hydrogen production system coupled with the thermal storage device was proposed to meet power fluctuation and frequent start and stop caused by renewable resources. It is found that the present PEM electrolyser

cannot maintain an approximately fixed temperature as the input power changes; the polarization curve would distort with the change of temperature. By optimizing the structure of the PEM system, the inlet water temperature of electrolyser reached ~58°C in 30 seconds and promoted the electrolytic system to run quickly and persistently in an efficient condition. Meanwhile, the coupled system can effectively reduce electrolytic voltages during the process of start-stop or load changing, and the maximum difference of power consumption per cell can reach ~12 W. Therefore, the PEM hydrogen production system coupled with the thermal storage device can effectively adapt to the power fluctuation and frequent start and stop caused by renewable energy.

Data Availability

The data used to support the findings of this study are available from the corresponding author upon request.

Conflicts of Interest

The authors declare that they have no conflicts of interest.

Acknowledgments

The authors would like to acknowledge financial support from Science and Technology Foundation of State Grid Corporation of China (Project No. 4000-202058313A-0-0-00).

References

[1] M. Hirscher, *Handbook of Hydrogen Storage: New Materials for Future Energy Storage*, WILEY-VCH Verlag GmbH & Co. KGaA, Weinheim, Germany, 2009.

[2] T. Wilberforce, F. N. Khatib, E. Ogungbemi, and A. G. Olabi, "Water electrolysis technology," in *Reference Module in Materials Science and Materials Engineering*, Elsevier, 2018.

[3] B. Ahmad, T. Wilberforce, and M. Olabi, "Comprehensive investigation on hydrogen and fuel cell technology in the aviation and aerospace sectors," *Renewable and Sustainable Energy Reviews*, vol. 106, pp. 31–40, 2019.

[4] G. Scherer, T. Momose, and K. Tomiie, "Membrane water electrolysis cells with a fluorinated cation exchange membranes," *Journal of the Electrochemical Society*, vol. 145, p. 780, 1988.

[5] Z. Abdin, C. J. Webb, and E. M. Gray, "Modelling and simulation of a proton exchange membrane (PEM) electrolyser cell," *International Journal of Hydrogen Energy*, vol. 40, no. 39, pp. 13243–13257, 2015.

[6] M. Schalenbach, "A perspective on low-temperature water electrolysis – challenges in alkaline and acidic technology," *International Journal of Electrochemical Science*, vol. 13, pp. 1173–1226, 2018.

[7] M. Balat, "Potential importance of hydrogen as a future solution to environmental and transportation problems," *International Journal of Hydrogen Energy*, vol. 33, no. 15, pp. 4013–4029, 2008.

[8] P. Trinke, B. Bensmann, and R. Hanke-Rauschenbach, "Current density effect on hydrogen permeation in PEM water electrolyzers," *International Journal of Hydrogen Energy*, vol. 42, no. 21, pp. 14355–14366, 2017.

[9] M. Carmo, D. L. Fritz, J. Mergel, and D. Stolten, "A comprehensive review on PEM water electrolysis," *International Journal of Hydrogen Energy*, vol. 38, no. 12, pp. 4901–4934, 2013.

[10] S. Slade, S. Campbell, T. Ralph, and F. Walsh, "Ionic conductivity of an extruded Nafion 1100 EW series of membranes," *Journal of the Electrochemical Society*, vol. 149, pp. 1556–1564, 2002.

[11] F. Barbir, "PEM electrolysis for production of hydrogen from renewable energy sources," *Solar Energy*, vol. 78, no. 5, pp. 661–669, 2005.

[12] R. Omrani and B. Shabani, "Hydrogen crossover in proton exchange membrane electrolysers: the effect of current density, pressure, temperature, and compression," *Electrochimica Acta*, vol. 377, article 138085, 2021.

[13] P. T. Babar, B. S. Pawar, A. C. Lokhande et al., "Annealing temperature dependent catalytic water oxidation activity of iron oxyhydroxide thin films," *Journal of Energy Chemistry*, vol. 26, no. 4, pp. 757–761, 2017.

[14] O. Atlam and M. Kolhe, "Equivalent electrical model for a proton exchange membrane (PEM) electrolyser," *Energy Conversion & Management*, vol. 52, no. 8-9, pp. 2952–2957, 2011.

[15] B. Han, S. M. Steen III, J. Mo, and F. Y. Zhang, "Electrochemical performance modeling of a proton exchange membrane electrolyzer cell for hydrogen energy," *Energy*, vol. 40, no. 22, pp. 7006–7016, 2015.

[16] S. S. Deshmukh and R. F. Boehm, "Review of modeling details related to renewably powered hydrogen systems," *Renewable and Sustainable Energy Reviews*, vol. 12, no. 9, pp. 2301–2330, 2008.

[17] Z. Ma, L. Witteman, J. A. Wrubel, and G. Bender, "A comprehensive modeling method for proton exchange membrane electrolyzer development," *International Journal of Hydrogen Energy*, vol. 46, no. 34, pp. 17627–17643, 2021.

[18] M. Upadhyay, A. Kim, S. Paramanantham et al., "Three-dimensional CFD simulation of proton exchange membrane water electrolyser: performance assessment under different condition," *Applied Energy*, vol. 306, article 118016, 2022.

[19] Y. Xu, G. Zhang, L. Wu, Z. Bao, B. Zu, and K. Jiao, "A 3-D multiphase model of proton exchange membrane electrolyzer based on open-source CFD," *Chemical Engineering*, vol. 1, article 100004, 2021.

[20] R. Garcia-Valverde, N. Espinosa, and A. Urbina, "Simple PEM water electrolyser model and experimental validation," *International Journal of Hydrogen Energy*, vol. 37, no. 2, pp. 1927–1938, 2012.

[21] H. Kim, M. Park, and K. S. Lee, "One-dimensional dynamic modeling of a high-pressure water electrolysis system for hydrogen production," *International Journal of Hydrogen Energy*, vol. 38, no. 6, pp. 2596–2609, 2013.

[22] F. Z. Aouali, M. Becherif, H. S. Ramadan, M. Emziane, A. Khellaf, and K. Mohammedi, "Analytical modelling and experimental validation of proton exchange membrane electrolyser for hydrogen production," *International Journal of Hydrogen Energy*, vol. 42, no. 2, pp. 1366–1374, 2017.

[23] N. Li and S. Simon, "Long-term contamination effect of iron ions on cell performance degradation of proton exchange membrane water electrolyser," *Journal of Power Sources*, vol. 434, article 226755, 2019.

[24] K. Hongsirikarn, J. G. Goodwin, S. Greenway, and S. Creager, "Effect of cations (Na^+, Ca^{2+}, Fe^{3+}) on the conductivity of a Nafion membrane," *Journal of Power Sources*, vol. 195, no. 21, pp. 7213–7220, 2010.

[25] M. A. Uddin, X. Wang, J. Park, U. Pasaogullari, and L. Bonville, "Distributed effects of calcium ion contaminant on polymer electrolyte fuel cell performance," *Journal of Power Sources*, vol. 296, pp. 64–69, 2015.

[26] A. Pozio, R. F. Silva, M. De Francesco, and L. Giorgi, "Nafion degradation in PEFCs from end plate iron contamination," *Electrochimica Acta*, vol. 48, no. 11, pp. 1543–1549, 2003.

[27] T. Okada, Y. Ayato, M. Yuasa, and I. Sekine, "The effect of impurity cations on the transport characteristics of perfluorosulfonated ionomer membranes," *The Journal of Physical Chemistry. B*, vol. 103, no. 17, pp. 3315–3322, 1999.

Hindawi
International Journal of Photoenergy
Volume 2022, Article ID 1890541, 16 pages
https://doi.org/10.1155/2022/1890541

Research Article

Gas Flow Characteristics through Irregular Particle Bed with the Vertical Confined Wall for Waste Heat Recovery

Sizong Zhang,[1,2] **Zhi Wen**,[2] **Xunliang Liu**,[2] **Yi Xing**,[2] **and Hui Zhang**[2]

[1]*School of Energy and Environmental Engineering, University of Science and Technology Beijing, Beijing 100083, China*
[2]*Beijing Key Laboratory of Energy Conservation and Emission Reduction for Metallurgical Industry, University of Science and Technology Beijing, Beijing 100083, China*

Correspondence should be addressed to Sizong Zhang; zhangsizong@ustb.edu.cn

Received 14 April 2022; Accepted 3 June 2022; Published 26 June 2022

Academic Editor: Chuan Li

The vertical waste heat recovery technology of the sinter in the iron and steel industry will be a great driving force for China to realize the "double Carbon" in the near future. For promoting the application of the new technology, the influence of the confined wall on the pressure distribution and pressure drops of the gas flow in the sinter bed was experimentally studied. For the irregular sinter with the rough surface, the gas pressure near the wall is higher than that at the center. Moreover, the radial distribution of the dimensionless pressure is nearly the same at different gas velocities. Therefore, whatever flow state the gas is in, the wall effect on irregular sinters only reduces the pressure drop of the gas flow, which is different from that on spherical particles. The vertical wall limits the randomness and uniformity of the particle accumulation, which is further intensified with the increase of the particle irregularity and particle size. Therefore, the confined wall causes a greater difference in the gas pressure between the wall and the center. With the particle size increasing from 5~10 mm to 55~60 mm, the ratio of the gas pressure between the wall and the center increases from 1.03 to 1.26. If the wall effect is ignored, the pressure drop of the gas flow would be overestimated by 16.01% on average, whereas the correlation of the wall correction can well predict the pressure drop with the mean error and maximum error of 2.74% and 9.48%, respectively.

1. Introduction

To realize the development system of the green economy, China has put forward the targets of the Carbon Peak in 2030 and Carbon Neutrality in 2060. At present, there are mainly two technical routes to solve this problem. On the one hand, it is the large-scale application of the new energy, such as the solar energy. On the other hand, it is the energy conservation and emission reduction of the traditional industry, such as the iron and steel industry [1–3]. The latest statistics show that the energy consumption of the iron and steel industry accounts for about 20% of the whole industry. In all processes of the iron and steel industry, the energy consumption of the sintering process ranks second, which is about 19% higher than the international level. Therefore, the efficient recovery of the waste heat of the sinter is the most promising method to reduce the energy consumption of the iron and steel industry. This will be a great driving force for China to realize the "double Carbon" in the near future.

To improve the rate of the energy-saving and emission reduction, the sinter vertical tank cooling (SVTC) process has been newly proposed by imitating the coke dry quenching (CDQ) process [4]. Compared with the existing annular cooling process, the SVTC process can increase the recovery rate of the sensible heat from 30% to 80% and reduce the air leakage rate from 35~55% to nearly 0%. Before the industrial application, it is necessary to study the feasibility of the SVTC process in the laboratory scale, that is, gas-solid heat transfer characteristics and gas flow characteristics [5, 6].

Gas flow characteristics not only affect the gas-solid heat transfer but also determine the energy consumption of fans, thus affecting the feasibility and economy of the process [5, 7–9]. Therefore, it is of great significance to reliably predict the pressure drop of the gas in the sinter vertical tank.

Since the shape of the sinter is very irregular and its particle size is large, the sinter vertical tank is essentially the packed bed with irregular and large particles [9, 10]. Therefore, some related researches have been carried out to accurately predict the pressure drop of the gas in the sinter bed in recent five years [5–13]. Results show that the pressure drop of the gas increases linearly with the height of the sinter layer increasing, increases in a quadratic relationship with the gas velocity increasing, and declines exponentially with the equivalent particle size increasing. Moreover, considering the influences of the particle size [5, 12], particle size distribution [8, 13], voidage [7], particle shape [10, 12], and wall effect [6, 11], the empirical correlations of the pressure drop are obtained by modifying the Ergun equation. However, the application of the Ergun equation is based on the assumption of the uniform packed bed, which ignores the wall effect of finite packed beds in practice [14–22]. It can only accurately describe infinite packed beds or packed beds with the large ratio of the bed diameter to particle diameter ($D/d_p > 50:1$). Owing to the existence of the confined wall in real beds, particles can only be packed finitely near the wall. This would increase the wetted surface area and the local voidage near the wall. Compared to the predicted value obtained the by the Ergun equation for the same average voidage, the combined effect may lead to the increase or decrease in the pressure drop of the gas flow [20].

For studying the wall effect, a lot of effort has been done. However, different conclusions have been drawn [14–30]. Some researchers have found that the wall effect can increase the pressure drop of the gas flow compared with an identical infinite bed [14], while others have found that this would cause a decline [23]. However, most studies indicate that the effect of the confined wall depends not only on the value of D/d_p, but also on the Reynolds number or the gas flow regime [16, 18, 20, 22, 24, 25]. Whatever the Reynolds number is, the wall effect can be ignored when D/d_p is higher than 50, whereas when D/d_p is lower than 50, the combined influences of the wall friction and the voidage would have opposite results on the pressure drop at different Reynolds numbers. At the low Reynolds number (i.e., laminar flow), the friction effect of the wall plays a prominent role, leading to the increase in the pressure drop of the gas, while the voidage effect is dominant at the high Reynolds number (i.e., turbulent flow), causing a decline in the pressure drop of the gas.

However, most of previous studies on the wall effect are focused on spherical particles. To our best knowledge, there are few studies on irregular particles due to the complexity of the particle shape [31–33]. Although Feng et al. [6] and Tian et al. [11] considered the wall effect to modify the equation of the pressure drop, the influences of the confined wall on the pressure distribution and pressure drops of the gas flow in the sinter bed are still unclear. Therefore, this paper studies experimentally the wall effect on the gas flow characteristics in the bed with irregular sinters under the background of the SVTC process. Furthermore, the accuracy of two correlations without and with the wall correction in predicting the pressure drop is compared.

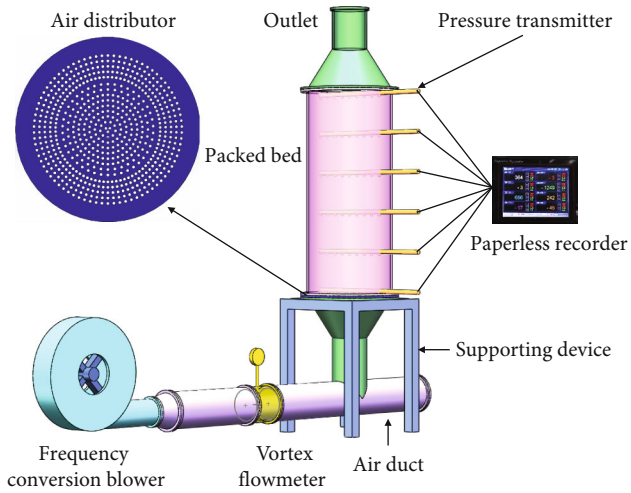

Figure 1: The sketch of the experimental apparatus for measuring the gas pressure in the sinter bed.

2. Experimental Method and Data Processing

2.1. Experimental Apparatus. Figure 1 is a schematic diagram of the experimental apparatus for measuring the gas pressure in the sinter bed. This apparatus is composed of the fan, the cylindrical packed bed, and the system of the measurement and acquisition. The frequency conversion blower is selected for the gas supply to precisely control the gas flow rate in the test. As the main part of the apparatus, the height (H) and inner diameter (D) of the packed bed are 1000 mm and 400 mm, respectively. The vortex flowmeter with the compensation of the temperature and pressure is applied to measure the gas flow rate under the standard condition. To acquire the information of the gas pressure inside the bed, a pressure transmitter with the length of 650 mm is used, and the measured data are collected by the paperless recorder. Basic parameters of above instruments are illustrated in Table 1.

The gas operation state in the experiment is designed according to that of the sinter vertical cooling process. The gas is first blown into the packed bed from the bottom, transported through the sinter layer, and then discharged to the outside of the bed from the outlet. To make the gas flow uniformly distributed on the cross section of the entrance, an air distributor with uniform openings is installed at the bottom. Six pressure taps with an interval of 200 mm are evenly arranged along the vertical direction. For analyzing the influence of the wall effect, thirteen measuring points with an interval of the 25 mm are set uniformly along the radial direction at each pressure tap. Then, these measured data are used to calculate the average gas pressure of the cross section.

Table 1: Basic parameters of experimental instruments.

Instrument	Mode	Range	Accuracy
Frequency conversion blower	HRD 65FU-100/7.5	3720 $m^3 \cdot h^{-1}$, 9 kPa,100 Hz	—
Vortex flowmeter	LUGB1315C-P3Z	150~3000 $m^3 \cdot h^{-1}$	1.0%
Pressure transmitter	CGYL-202	0~10 kPa	0.5%
Paperless recorder	LD-300G	4~20 mA, 8 channels	0.2%

2.2. Experimental Materials and Characterization Methods. The sinter particles are from HBIS Group Hansteel Company in China. All experiments are carried out within the representative particle size range of 5~60 mm [9, 34–36]. It is sieved into 11 kinds of particle sizes in the interval of 5 mm, as shown in Figure 2. It can be seen that the sinter shape is very irregular, and its surface is rough and porous.

To describe the sinter in detail, the particle characteristics are characterized in this paper. Firstly, the apparent density ρ_a for the sinter of each particle size is measured by the displacement method [8, 9, 11], as shown in the following equation:

$$\rho_a = \frac{m_1}{m_3 - (m_2 - m_4)} \rho_{H_2O}, \tag{1}$$

where ρ_{H_2O} is the density of the water; m_1 and m_3 are the mass of the dry sinter and the wet sinter, respectively; m_2 is the mass of the sinter and test basket in the water; m_4 is the mass of the test basket in the water.

Besides, the bulk density ρ_b is measured by the direct weighing method [8, 9, 11], as follows:

$$\rho_b = \frac{(G_1 - G_2)}{V}, \tag{2}$$

where G_1 is the total mass of the sinter and test container; G_2 and V are the mass and volume of the test container, respectively.

The bed voidage ε and shape factor ϕ of sinter particles are determined by Equation (3) [8–11] and Equation (4) [33, 37], respectively, as follows:

$$\varepsilon = 1 - \frac{\rho_b}{\rho_a}, \tag{3}$$

$$\phi = 0.7295\varepsilon^2 - 2.4963\varepsilon + 1.8537. \tag{4}$$

In addition, 50 sinters of each particle size are randomly selected, and the equivalent particle size d_p is obtained by the equal volume method [8–11], as follows:

$$d_p = \sqrt[3]{\frac{6m_s}{\pi\rho_a}}, \tag{5}$$

where m_s is the mean mass of the single sinter.

The particle characteristic parameters of the sinter obtained by above methods are shown in Table 2. A wide range of the gas velocity is also designed for the test condition of each kind of the sinter.

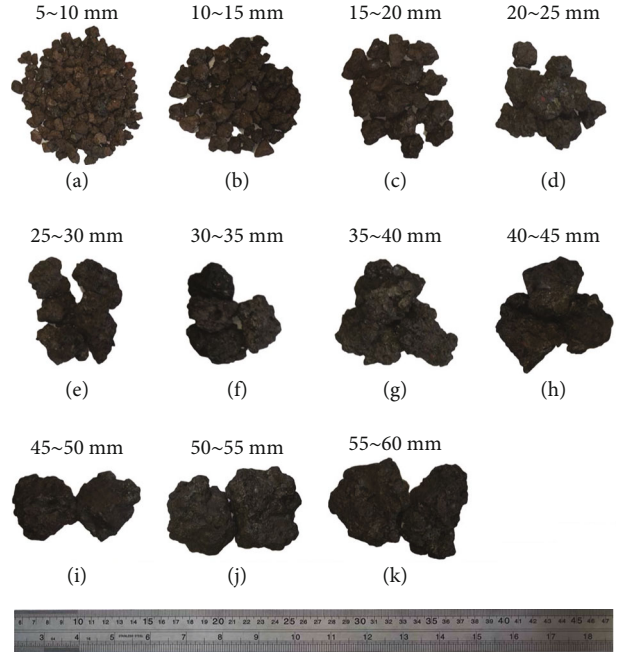

Figure 2: Photographs taken on 11 kinds of the sieved sinter samples within the ranges of (a) 5~10 mm, (b) 10~15 mm, (c) 15~20 mm, (d) 20~25 mm, (e) 25~30 mm, (f) 30~35 mm, (g) 35~40 mm, (h) 40~45 mm, (i) 45~50 mm, (j) 50~55 mm, and (k) 55~60 mm.

2.3. Data Processing. For infinite packed beds with spherical particles, the pressure drop of the gas flow is usually predicted by the Ergun equation, as follows [6, 7, 9, 12]:

$$\frac{\Delta P}{L} = k_1 \frac{(1-\varepsilon)^2 \mu_g \cdot u_g}{\varepsilon^3 {d_p}^2} + k_2 \frac{\rho_g (1-\varepsilon) \cdot {u_g}^2}{\varepsilon^3 d_p}, \tag{6}$$

where k_1 and k_2 are the viscous loss coefficient and the inertial loss coefficient, respectively; ΔP, L, and $\Delta P/L$ are the pressure drop of the gas flow through the sinter layer, the height of the sinter layer, and the pressure drop per unit height, respectively; u_g, ρ_g, and μ_g are the velocity, density, and dynamic viscosity of the gas, respectively.

Table 2: Particle characteristic parameters and test conditions for 11 kinds of sinters.

Particle size (mm)	Equivalent particle size d_p (mm)	Ratio of bed to particle diameter D/d_p	Shape factor ϕ	Apparent density ρ_a (kg·m^{-3})	Bulk density ρ_b (kg·m^{-3})	Voidage ε	Gas velocity u_g (m·s^{-1})
5~10	5.56	71.62	0.663	3847.61	1643.85	0.5727	0.4, 0.8, 1.2, 1.6, 2.0
10~15	10.90	36.69	0.629	3726.41	1513.40	0.5938	0.4, 0.8, 1.2, 1.6, 2.0, 2.4
15~20	14.48	27.62	0.612	3656.28	1448.69	0.6037	0.4, 0.8, 1.2, 1.6, 2.0, 2.4, 2.8
20~25	19.21	20.82	0.607	3614.62	1419.46	0.6073	0.4, 0.8, 1.2, 1.6, 2.0, 2.4, 2.8
25~30	23.28	17.18	0.599	3561.80	1382.78	0.6118	0.4, 0.8, 1.2, 1.6, 2.0, 2.8, 3.2
30~35	26.82	14.91	0.591	3547.14	1359.18	0.6168	0.4, 0.8, 1.2, 1.6, 2.0, 2.8, 3.2
35~40	30.82	12.98	0.586	3536.25	1342.54	0.6204	0.4, 0.8, 1.2, 1.6, 2.0, 2.8, 3.6
40~45	34.99	11.43	0.581	3526.84	1327.55	0.6236	0.4, 0.8, 1.2, 1.6, 2.0, 2.8, 3.6
45~50	38.49	10.39	0.572	3523.35	1306.08	0.6293	0.4, 0.8, 1.2, 1.6, 2.0, 2.8, 3.6
50~55	43.27	9.24	0.568	3523.09	1297.22	0.6318	0.4, 0.8, 1.2, 1.6, 2.0, 2.8, 3.6
55~60	47.39	8.44	0.561	3522.73	1282.11	0.6361	0.4, 0.8, 1.2, 1.6, 2.0, 2.8, 3.6

For irregular particles, the shape factor ϕ is often introduced to modify the correlation of the pressure drop, as follows [10, 12]:

$$\frac{\Delta P}{L} = k_1 \frac{(1-\varepsilon)^2 \mu_g \cdot u_g}{\varepsilon^3 (\phi d_p)^2} + k_2 \frac{\rho_g (1-\varepsilon) \cdot u_g{}^2}{\varepsilon^3 (\phi d_p)}. \tag{7}$$

To facilitate the linear fitting, the dimensionless parameters, i.e., friction pressure drop f_p and particle Reynolds number Re_p, are usually introduced, as follows [6, 7, 9, 12]:

$$\begin{aligned} f_p &= \frac{\Delta P}{L} \frac{\varepsilon^3 (\phi d_p)^2}{(1-\varepsilon)^2 \mu_g u_g}, \\ \mathrm{Re}_p &= \frac{\rho_g u_g (\phi d_p)}{\mu_g (1-\varepsilon)}. \end{aligned} \tag{8}$$

Then, Equation (7) can be simplified to the dimensionless form expressed by

$$f_p = k_1 + k_2 \, \mathrm{Re}_p. \tag{9}$$

For finite packed beds, the wall corrected factor M is introduced as follows [6, 11, 20, 22, 30]:

$$M = 1 + \frac{2 d_p}{3D(1-\varepsilon)}. \tag{10}$$

Then, Equation (9) can be arranged as follows:

$$f_w = k_{1w} + k_{2w} \, \mathrm{Re}_w, \tag{11}$$

where f_w is the wall-modified friction pressure drop, $f_w = f_p/M^2$; Re_w is the wall-modified particle Reynolds number, $\mathrm{Re}_w = \mathrm{Re}_p/M$ [6, 11]; k_{1w} and k_{2w} are the wall-modified viscous loss coefficient and the wall-modified inertial loss coefficient, respectively.

Moreover, Table 3 shows the relative uncertainty of main parameters estimated by the error transfer formula [8–11]. For example, the particle Reynolds number Re_p can be calculated as follows:

$$\begin{aligned} \frac{\delta(\mathrm{Re}_p)}{\mathrm{Re}_p} = \Bigg[&\left(\frac{\delta(\rho_g)}{\rho_g}\right)^2 + \left(\frac{\delta(u_g)}{u_g}\right)^2 + \left(\frac{\delta(d_p)}{d_p}\right)^2 \\ &+ \left(\frac{\delta(\phi)}{\phi}\right)^2 + \left(\frac{\delta(\mu_g)}{\mu_g}\right)^2 + \left(\frac{\delta(1-\varepsilon)}{1-\varepsilon}\right)^2 \Bigg]^{1/2}, \end{aligned} \tag{12}$$

where δ is the absolute uncertainty of the corresponding parameter.

3. Experimental Results and Discussion

3.1. Effect of the Confined Wall on the Bulk Density and Bed Voidage. Figure 3 shows the changes of the bulk density ρ_b

Table 3: Summary of the relative uncertainty of main parameters.

Parameter	Symbol	Uncertainty/%	Parameter	Symbol	Uncertainty/%
Equivalent particle size	d_p	3.07	Pressure drop per unit height	$\Delta P/L$	4.45
Apparent density	ρ_a	1.42	Particle Reynolds number	Re_p	4.87
Bulk density	ρ_b	2.15	Friction pressure drop	f_p	6.52
Voidage	ε	2.58	Wall-modified Reynolds number	Re_w	6.31
Shape factor	ϕ	2.58	Wall-modified friction pressure drop	f_w	7.65

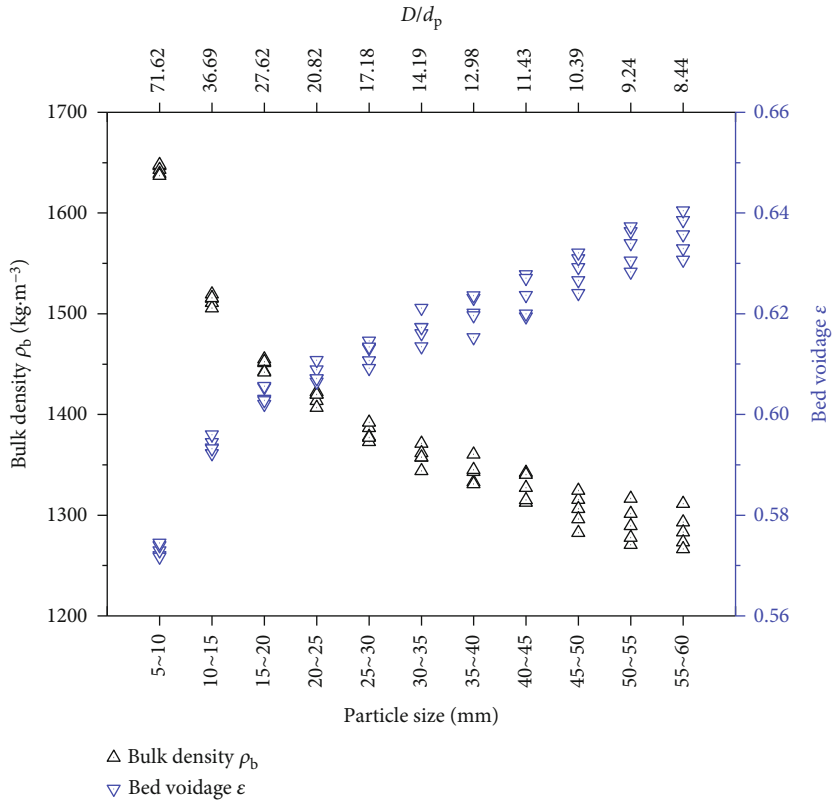

Figure 3: Variation of the bulk density ρ_b and voidage ε of the sinter bed with the particle size under five repeated experiments.

and the bed voidage ε with the particle size under five repeated experiments. With the particle size increasing, ρ_b decreases and ε increases, respectively. This change trend is consistent with the published results [6, 9, 10]. It can be observed from Table 2 that the particle shape factor ϕ gradually reduces with the increase in the particle size. This means that the irregularity of sinters increases, which makes it easier to form bridges when the sinter particles are heaped up. Therefore, the voids between particles in the bed would increase with the increase of the particle size. Besides, it is also found that the reproducibility and uncertainty of ρ_b and ε are getting worse with D/d_p decreasing, which is similar to results obtained by Tian et al. [11] and Raichura [17]. This indicates that the wall effect limits the randomness and uniformity of the particle accumulation in the bed. What's more, the influence of the confined wall becomes more significant with the increase in the particle irregularity and particle size. This further intensifies the nonrandomness and heterogeneity of the particle accumulation.

3.2. Effect of the Confined Wall on the Gas Pressure Distribution. Figure 4 illustrates the radial distribution of the gas pressure (P) at the bed height of $L = 0$ mm under four kinds of particle sizes (i.e., 5~10 mm, 20~25 mm, 40~45 mm, and 55~60 mm). As the radial position (r) moves from the center to the wall, the gas pressure (P) gradually increases at different gas velocities. This indicates that the pressure drop of the gas near the wall is relatively low due to the wall effect for the finite bed of irregular sinters. It is different from the wall effect on spherical particles. The confined wall can increase the viscous loss term of the wall friction effect and decrease the inertial loss term

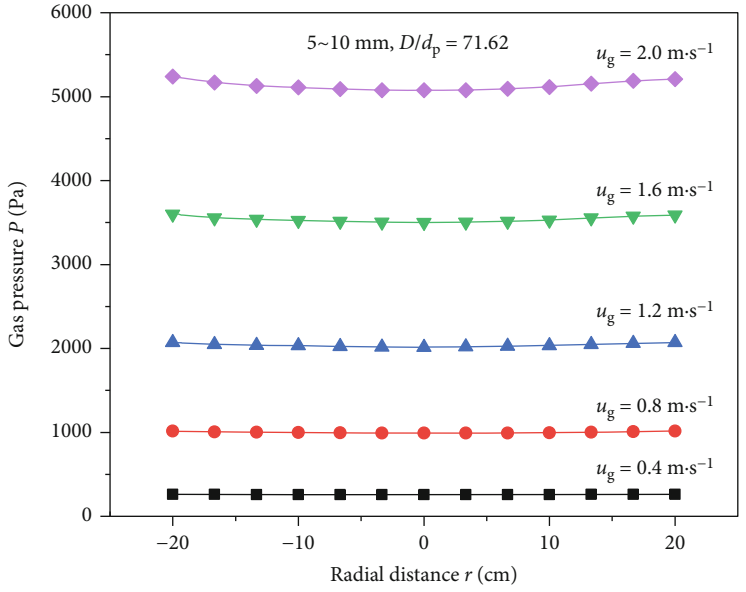

(a)

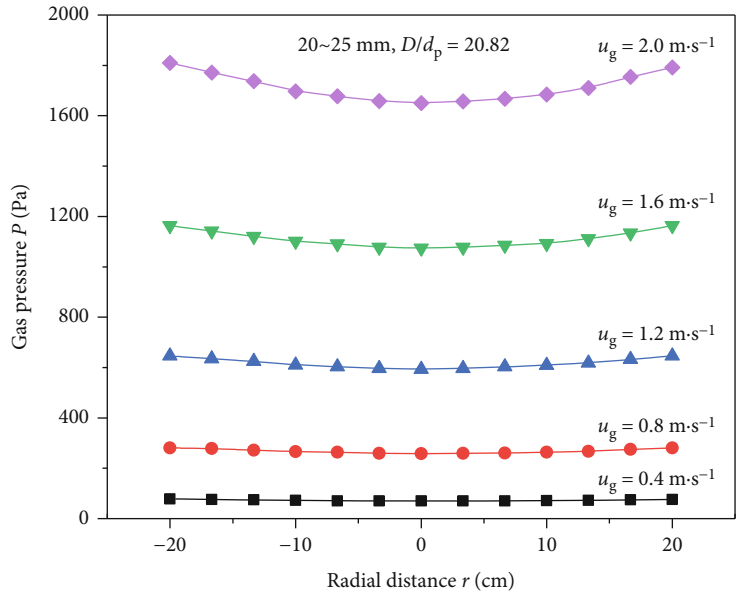

(b)

Figure 4: Continued.

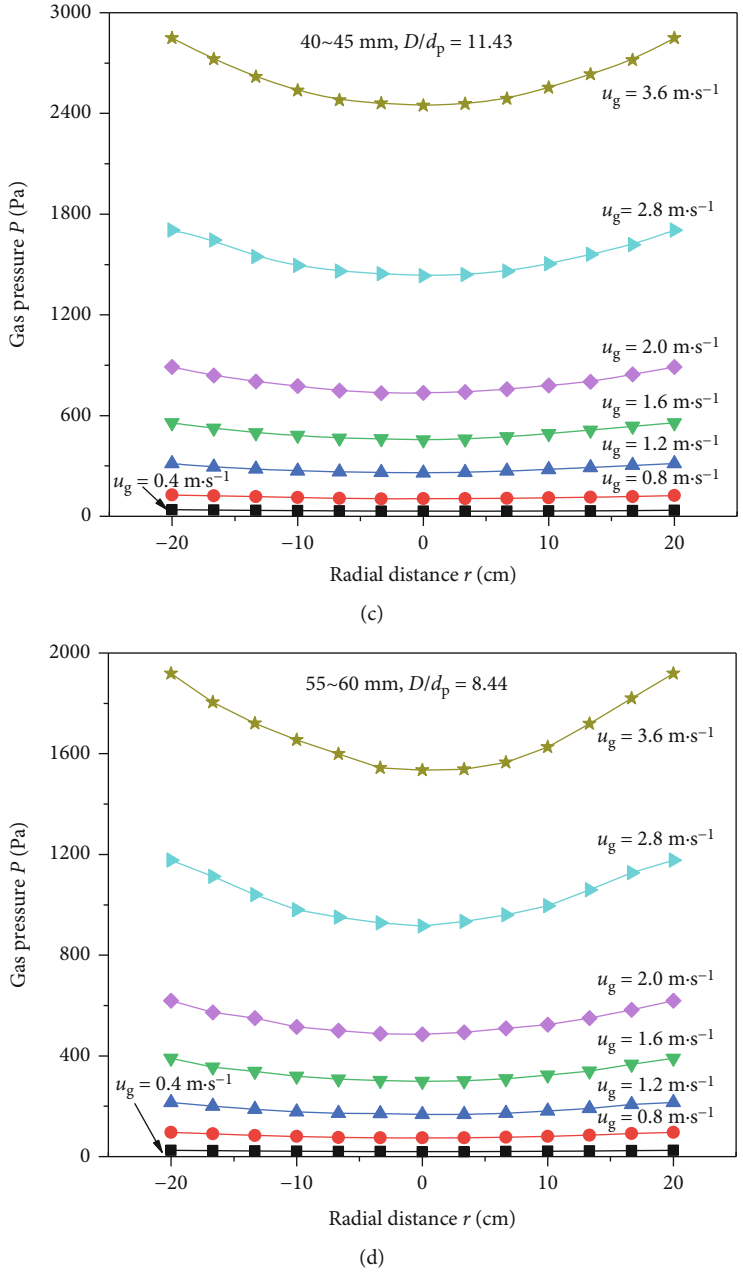

Figure 4: The radial distribution of the gas pressure (P) at the bed height of L = 0 mm under four kinds of particle sizes of (a) 5~10 mm, (b) 20~25 mm, (c) 40~45 mm, and (d) 55~60 mm.

of the voidage effect [16, 18, 20, 24, 25]. Only in the laminar flow, the viscous loss plays a leading role to increase the pressure drop of the gas, whereas under the turbulent flow, the inertial loss is dominant to reduce the pressure drop of the gas [18, 20, 24, 25]. The previous study [11] shows that the gas flow in the sinter bed is easy to reach the turbulent regime or transitional regime due to the irregularity of particles. It is mainly attributed to two aspects. On the one hand, the irregular particles lead to irregular gas channels in the bed, which is easy to destroy the stability of the gas flow. On the other hand, the irregular shape causes the uneven distribution of the gas channel. This would increase of the real velocity of the gas flow in the channel. In addition, the surface of sinter particles is very rough and full of concaves and convexes [9, 10]. Therefore, the friction effect of the confined wall is not necessarily greater than that of the sinter surface. Based on the above two points, the effect of the wall friction on the pressure drop is relatively weak in the irregular sinter bed. Moreover, the bed voidage increases gradually from the center to the wall [38–41]. Therefore, the pressure drop of the gas is relatively low in the region close to the wall. The gas pressure near the wall

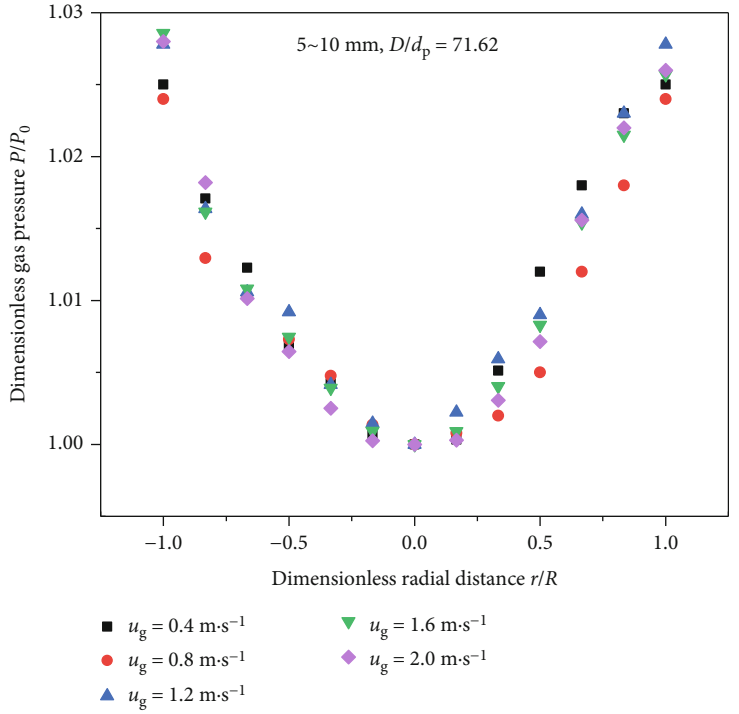

(a)

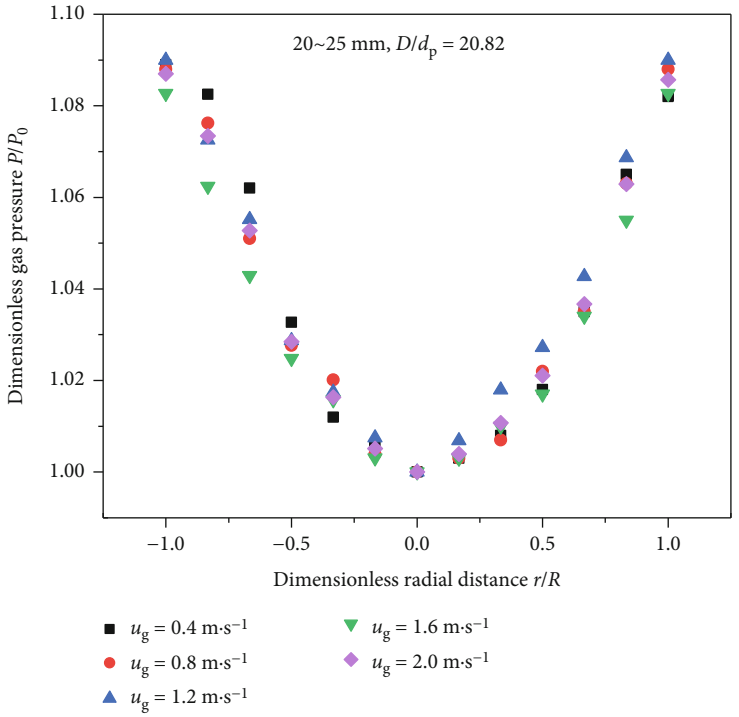

(b)

Figure 5: Continued.

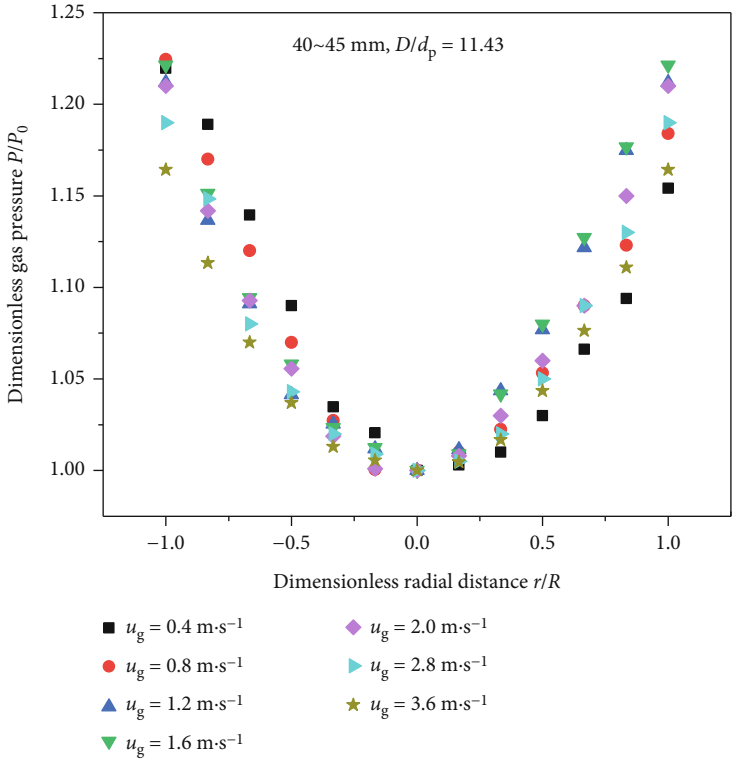

(c)

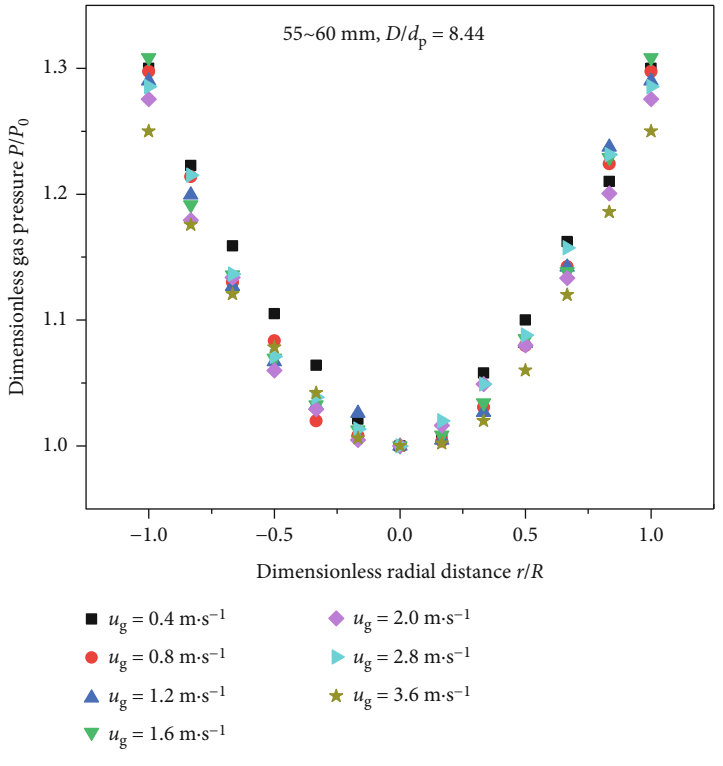

(d)

Figure 5: The radial distribution of the dimensionless gas pressure (P/P_0) at the bed height of $L = 0$ mm under four kinds of particle sizes of (a) 5~10 mm, (b) 20~25 mm, (c) 40~45 mm, and (d) 55~60 mm.

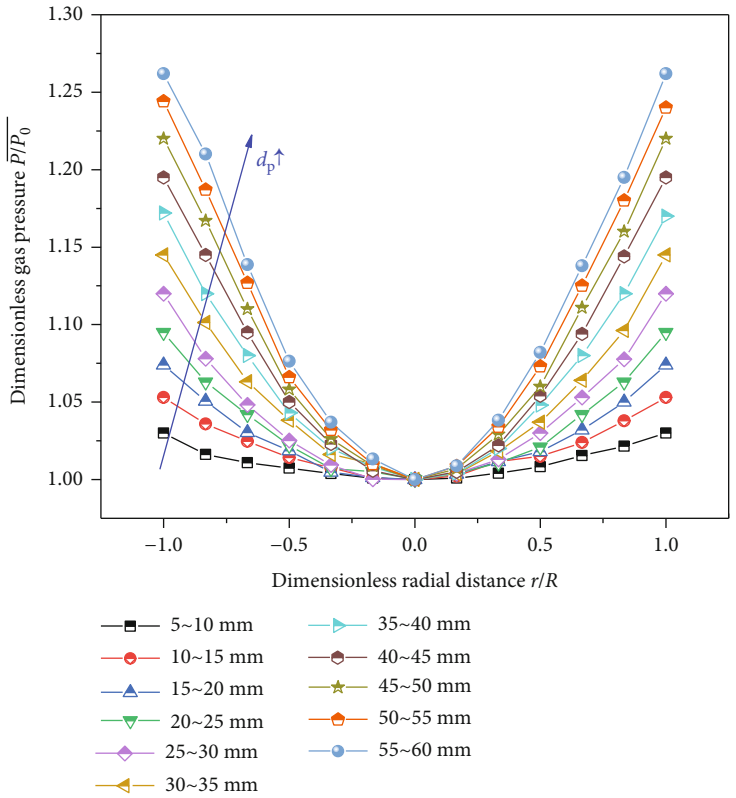

Figure 6: The radial distribution of the average dimensionless gas pressure ($\overline{P/P_0}$) for different gas velocities at the bed height of $L = 0$ mm under 11 kinds of particle sizes.

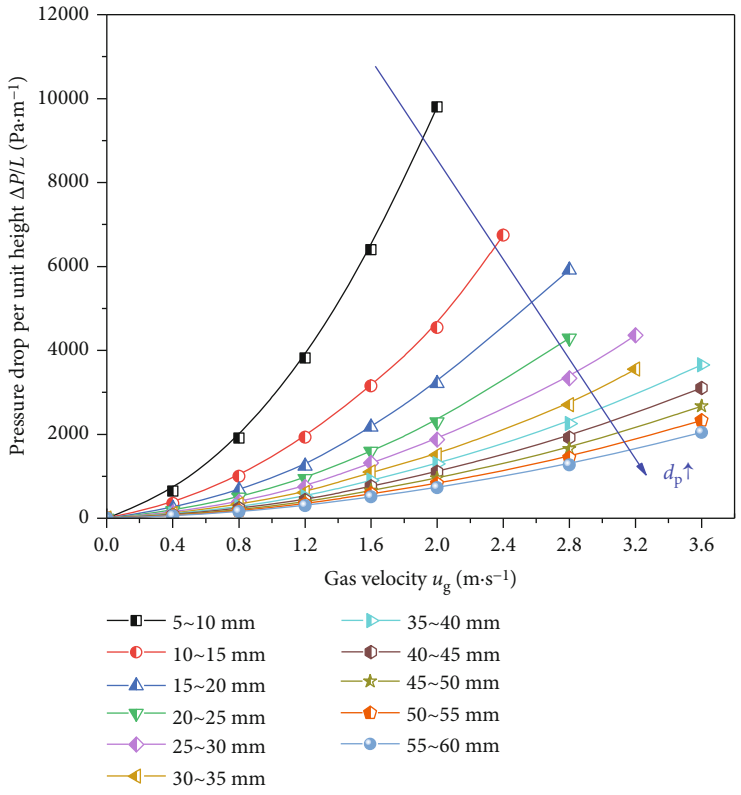

Figure 7: The variation of the pressure drop of the gas flow per unit height ($\Delta P/L$) vs. the gas velocity (u_g) under different particle sizes.

Table 4: Coefficients of the fitting function between the pressure drop per unit height ($\Delta P/L$) and gas velocity (u_g) under 11 kinds of particle sizes.

Particle size (mm)	$\Delta P/L = a \cdot u_g^2 + b \cdot u_g$		Correlation coefficient R^2
	a	b	
5~10	2111.29	659.22	0.99985
10~15	988.75	389.39	0.99808
15~20	645.57	307.56	0.99979
20~25	456.34	251.17	0.99980
25~30	352.03	226.56	0.99941
30~35	283.05	193.26	0.99908
35~40	235.07	164.72	0.99941
40~45	199.09	141.37	0.99951
45~50	170.91	123.26	0.99952
50~55	148.51	109.60	0.99947
55~60	130.01	98.09	0.99959

is larger than that of the interior, especially for the large particle at the high gas velocity.

To further analyze the influence of the gas velocity, Figure 5 illustrates the distribution of the dimensionless gas pressure (P/P_0, P_0 is the gas pressure at the center) with the dimensionless radial distance (r/R, R is the radius of the sinter bed). It is found that the radial dimensionless pressure distribution is nearly the same at different gas velocities. This means that the gas velocity does not change the wall effect on the pressure drop in the bed of the irregular particle. Therefore, whatever state the gas flow is in, the influence of the confined wall on the irregular particle only reduces the pressure drop in the bed.

Figure 6 illustrates the radial distribution of the average dimensionless gas pressure ($\overline{P/P_0}$) at different gas velocities under 11 kinds of particle sizes. It is observed that the values of $\overline{P/P_0}$ increase with the particle size increasing (i.e., the decrease of D/d_p). With the particle size increasing from 5~10 mm to 55~60 mm, $\overline{P/P_0}$ near the wall increases from 1.03 to 1.26. This indicates that the confined wall has a more significant effect on large particles. With the increase in the particle size, the difference of the voidage between the wall and the center becomes larger [38], and the uniformity of the voidage distribution becomes worse [39, 40].

3.3. Effect of the Gas Velocity and Equivalent Particle Size on the Pressure Drop. Figure 7 illustrates the variation of the pressure drop of the gas flow per unit height ($\Delta P/L$) with the gas velocity (u_g) under different particle sizes. Firstly, it is seen that $\Delta P/L$ increases with the increase of u_g, fitting well with the quadratic function in the form of $\Delta P/L = a \cdot u_g^2 + b \cdot u_g$. The correlation coefficients of all fitting curves are greater than 0.99985, as shown in Table 4. This is consistent with the results published [5, 7, 12]. Similar to the Ergun equation, the pressure drop of the gas is composed of the viscous loss linearly related to u_g and the inertial loss of a quadratic relationship with u_g. As u_g increases, the boundary layer gradually disappears and the collision between the gas and particles is increasingly intensified [12, 42]. Therefore, the inertial loss becomes the dominant factor, resulting in a sharp increase in the pressure drop of the gas flow. Moreover, it can be observed from Table 4 that the coefficients of the quadratic function, a and b, decline with the particle size increasing, which is similar with other studies [5, 7, 12]. Also, the bed voidage increases with the increase of d_p, as shown in Figure 3. This causes a reduction in the instability and specific surface area of the gas flow. Therefore, it makes in the inertial loss and viscous loss decrease [42].

3.4. Analysis of the Empirical Correlation of the Pressure Drop

3.4.1. Considering the Wall Effect. According to Equation (11), the relationship between the wall-modified friction pressure drop f_w and the wall-modified particle Reynolds number Re_w can be linearly fitted by the least square method. The obtained wall-modified viscous loss coefficient k_{1w} and inertial loss coefficient k_{2w} for each particle size are shown in Figure 8(a). In addition, Figure 8(a) indicates that k_{1w} decreases and k_{2w} increases with the increase of D/d_p, respectively. This change trend is similar to that obtained by others [11, 17]. Therefore, k_{1w} and k_{2w} are determined as functions of D/d_p,

$$k_{1w} = 540 + 639e^{\left(-0.0581D/d_p\right)},$$
$$k_{2w} = 2.73\text{-}1.883e^{\left(-0.0733D/d_p\right)}. \tag{13}$$

Then, f_w is expressed as follows:

$$f_w = 540 + 639e^{\left(-0.0581D/d_p\right)} + \left[2.73\text{-}1.883e^{\left(-0.0733D/d_p\right)}\right] Re_w. \tag{14}$$

The mean relative error (MRE) between the measured value and the predicted value of the pressure drop per unit height is calculated by

$$\mathrm{MRE}(\%) = \frac{1}{n}\sum_{j=1}^{n}\frac{\left|\Delta P/L_{cal}^{j} - \Delta P/L_{exp}^{j}\right|}{\Delta P/L_{exp}^{j}} \times 100, \tag{15}$$

where j is the serial number of experimental data, $j = 1, 2, \cdots\cdots, n$; n is the number of experimental data; $\Delta P/L_{exp}$ and $\Delta P/L_{cal}$ are the measured value and the predicted value of the pressure drop per unit height, respectively.

It is found that the predicted values by Equation (14) achieve a satisfied agreement with the measured values, as shown in Figure 8(b). The MRE and maximum error are 2.74% and 9.48%, respectively. Therefore, the correlation of the wall correction can well predict the pressure drop of the gas flow through the packed bed of irregular sinters.

3.4.2. Ignoring the Wall Effect. For the comparison, the correlation of the pressure drop without the wall correction is

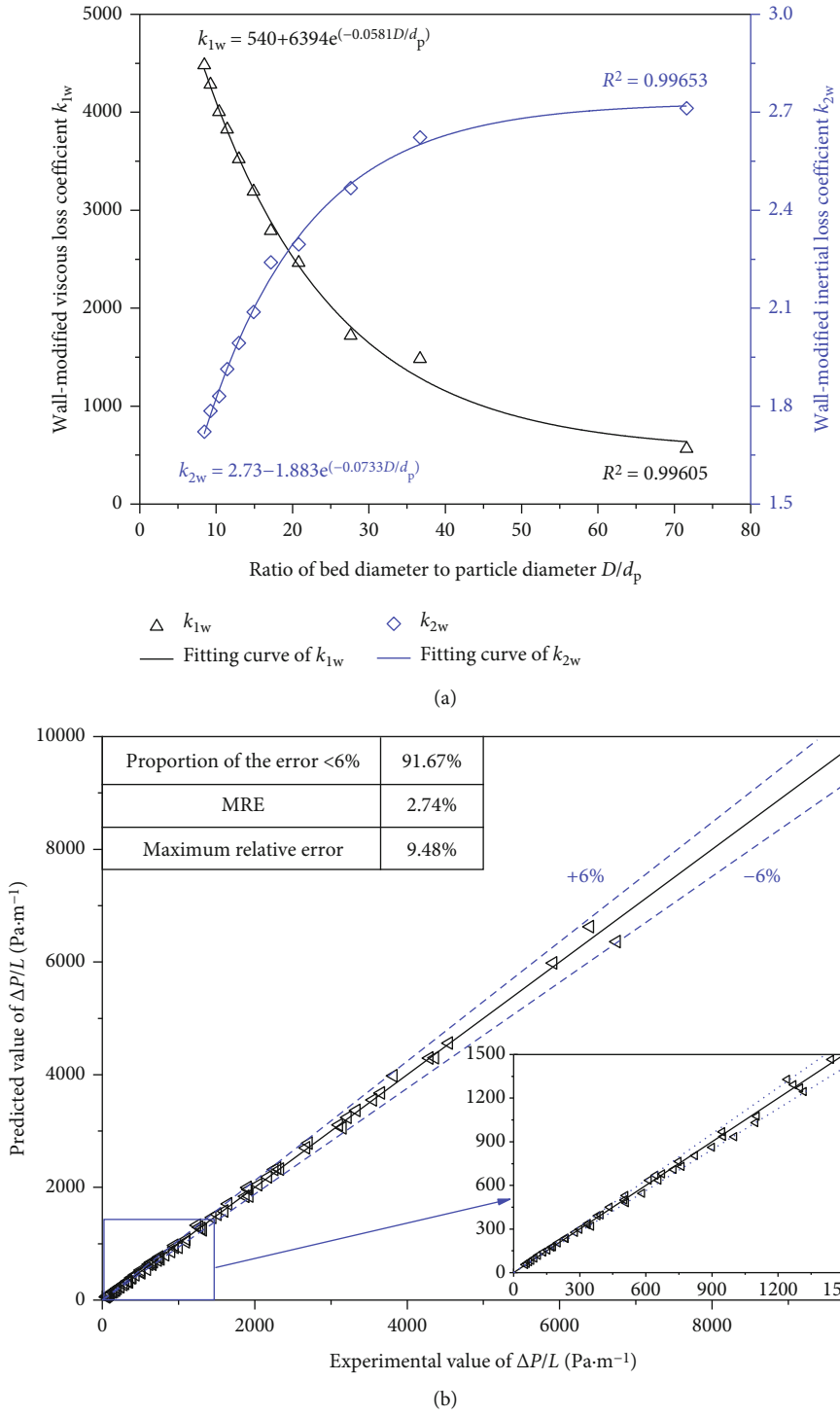

FIGURE 8: Analysis of the wall-modified correlation of the pressure drop: (a) relationship between k_{1w} and k_{2w} vs. D/d_p; (b) comparison between the experimental value and the predicted value of $\Delta P/L$.

also fitted by the least square method according to Equation (9), as shown in Figure 9(a). The correlation of the pressure drop between the friction factor f_p and the particle Reynolds number Re_p is expressed by

$$f_p = 3357 + 2.388\ \mathrm{Re}_p. \quad (16)$$

It is found from Figure 9(b) that most of the predicted values by Equation (16) are larger than the measured values. Since the wall effect leads to the decrease of the pressure drop, the pressure drop of the gas in the sinter bed will be overestimated when it is assumed to be an infinite packed bed. Therefore, the prediction accuracy of the correlation of the pressure drop without the wall correction will decline.

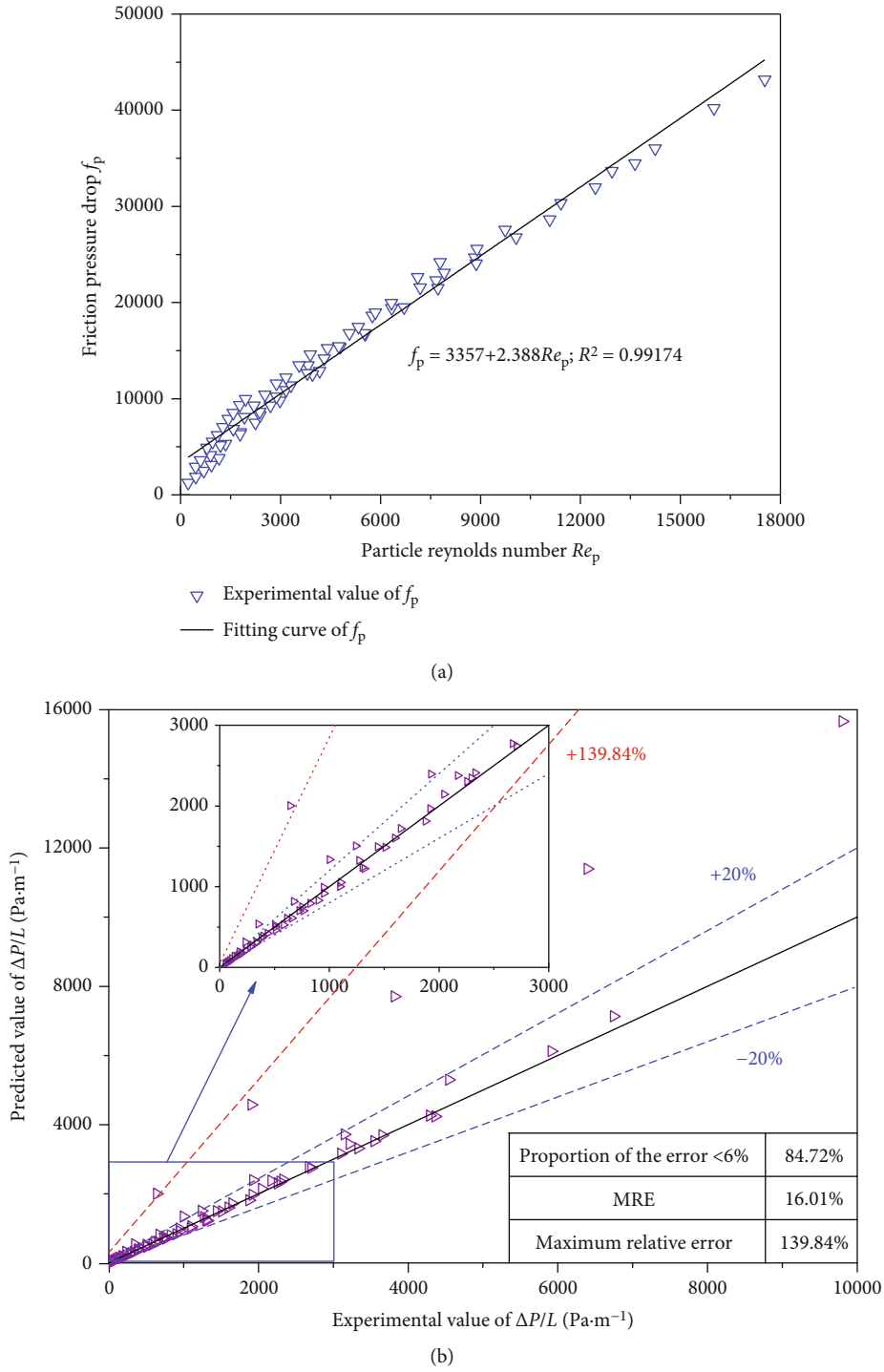

Figure 9: Analysis of the empirical correlation of the pressure drop without the wall correction: (a) relationship between f_p and Re_p; (b) comparison between the experimental value and the predicted value of $\Delta P/L$.

The MRE and maximum error are as high as 16.01% and 139.84%, respectively.

4. Conclusions

The vertical waste heat recovery technology of the sinter will be a great driving force for China to realize the "double Carbon." To promote the application of the new technology, the wall effect on the gas flow characteristic in the bed with irregular sinters was studied by the experimental method.

(1) The irregularity of the sinter increases with the particle size increasing, which causes an increase in the bed voidage. Besides, the vertical wall limits the randomness and uniformity of the particle accumulation. This effect is further intensified with

the increase of the irregularity and particle size, which makes the reproducibility and uncertainty of the voidage become worse

(2) As the radial position moves from the center to the wall, the gas pressure increases gradually. Moreover, the radial distribution of the dimensionless pressure is nearly the same at different gas velocities. Therefore, the wall effect on irregular sinters only reduces the pressure drop of the gas no matter what state the gas flow is in, which is different from the wall effect on spherical particles. Besides, the wall effect is increasing significantly with the particle size increasing (i.e., the decrease of D/d_p). With the particle size increasing from 5~10 mm to 55~60 mm, the dimensionless gas pressure near the wall increases from 1.03 to 1.26

(3) When the wall effect is ignored, the pressure drop of the gas would be overestimated by 16.01% on average, whereas the empirical correlation of the wall correction can well predict the pressure drop of the gas in the packed bed of the irregular sinter with the mean error and maximum error of 2.74% and 9.48%, respectively

Nomenclature

D: Diameter of the sinter bed, m
d_p: Equivalent particle size, m
D/d_p: Ratio of the bed to particle diameter
f_p: Friction pressure drop
f_w: Wall-modified friction pressure drop
H: Height of the packed bed, m
G_1: The total mass of the sinter and test container, kg
G_2: The mass of the test container, kg
k_1: Viscous loss coefficient
k_{1w}: Wall-modified viscous loss coefficient
k_2: Inertial loss coefficient
k_{2w}: Wall-modified inertial loss coefficient
L: Height of the sinter layer, m
m_1: Mass of the dry sinter, kg
m_2: Mass of the sinter and test basket in the water, kg
m_3: Mass of the wet sinter, kg
m_4: Mass of the test basket in the water, kg
m_s: Mean mass of the single sinter, kg
M: Wall correction factor
P: Gas pressure, Pa
P_0: Gas pressure at the centerline, Pa
P/P_0: Dimensionless gas pressure
$\overline{P/P_0}$: Average dimensionless gas pressure
ΔP: Pressure drop of the gas through the sinter bed, Pa
$\Delta P/L$: Pressure drop per unit height, Pa·m^{-1}
$\Delta P/L_{cal}$: Calculated value of the pressure drop per unit height, Pa·m^{-1}
$\Delta P/L_{exp}$: Experimental value of the pressure drop per unit height, Pa·m^{-1}
u_g: Gas velocity, m·s^{-1}
V: Volume of the test container, m^3
r: Radial distance, m
R: Radius of the packed bed, m
Re_p: Particle Reynolds number
Re_w: Wall-modified particle Reynolds number.

Greeks

ρ_a: Apparent density of the sinter, kg·m^{-3}
ρ_b: Bulk density of the sinter, kg·m^{-3}
ρ_g: Density of the gas, kg·m^{-3}
ρ_{H_2O}: Density of the water, kg·m^{-3}
ε: Bed voidage
ϕ: Shape factor
μ_g: Dynamic viscosity of the gas, Pa·s.

Subscripts

p: Particle
g: Gas
w: Wall
cal: Calculation
exp: Experiment.

Abbreviations

MRE: Mean relative error
SVTC: Sinter vertical tank cooling
CDQ: Coke dry quenching.

Data Availability

The data used to support the findings of this study are included within the article.

Conflicts of Interest

We declare that we do not have any commercial or associative interest that represents a conflict of interest in connection with the work submitted.

Acknowledgments

This work is supported by Fundamental Research Funds for the National Natural Science Foundation of China (Nos. 52006008 and 62033014).

References

[1] Q. Xu, K. Wang, Z. W. Zou et al., "A new type of two-supply, one-return, triple pipe-structured heat loss model based on a low temperature district heating system," *Energy*, vol. 218, article 119569, 2021.

[2] Q. Xu, Z. W. Zou, Y. S. Chen et al., "Performance of a novel-type of heat flue in a coke oven based on high- temperature and low-oxygen diffusion combustion technology," *Fuel*, vol. 267, article 117160, 2020.

[3] Q. Xu, L. Liu, J. X. Feng et al., "A comparative investigation on the effect of different nanofluids on the thermal performance of two-phase closed thermosyphon," *International Journal of Heat and Mass Transfer*, vol. 149, article 119189, 2020.

[4] K. Sun, C. Tseng, D. S. Wong et al., "Model predictive control for improving waste heat recovery in coke dry quenching processes," *Energy*, vol. 80, pp. 275–283, 2015.

[5] J. S. Feng, H. Dong, M. M. Li, and J. J. Cai, "Resistance characteristics of fixed bed layer in vertical tank for recovering sinter waste heat," *Journal of Central South University (Science and Technology)*, vol. 45, no. 8, pp. 2566–2571, 2014.

[6] J. S. Feng, S. Zhang, H. Dong, and G. Pei, "Frictional pressure drop characteristics of air flow through sinter bed layer in vertical tank," *Powder Technology*, vol. 344, pp. 177–182, 2019.

[7] J. S. Feng, H. Dong, J. Y. Liu, K. Liang, and J. Y. Gao, "Experimental study of gas flow characteristics in vertical tank for sinter waste heat recovery," *Applied Thermal Engineering*, vol. 91, pp. 73–79, 2015.

[8] F. Y. Tian, L. F. Huang, L. W. Fan, Z. T. Yu, and Y. C. Hu, "Experimental study on pressure drop of packed beds with binary sintered ore particle mixtures," *Journal of Zhejiang University (Engineering Science)*, vol. 50, no. 11, pp. 2077–2086, 2016.

[9] F. Y. Tian, L. F. Huang, L. W. Fan et al., "Pressure drop in a packed bed with sintered ore particles as applied to sinter coolers with a novel vertically arranged design for waste heat recovery," *Journal of Zhejiang University-Science A (Applied Physics & Engineering)*, vol. 17, no. 2, pp. 89–100, 2016.

[10] Y. Liu, J. Y. Wang, Z. L. Cheng, J. Yang, and Q. W. Wang, "Experimental investigation of fluid flow and heat transfer in a randomly packed bed of sinter particles," *International Journal of Heat and Mass Transfer*, vol. 99, pp. 589–598, 2016.

[11] F. Y. Tian, L. F. Huang, L. W. Fan, H. L. Qian, and Z. T. Yu, "Wall effects on the pressure drop in packed beds of irregularly shaped sintered ore particles," *Powder Technology*, vol. 301, pp. 1284–1293, 2016.

[12] J. S. Feng, H. Dong, and H. D. Dong, "Modification of Ergun's correlation in vertical tank for sinter waste heat recovery," *Powder Technology*, vol. 280, pp. 89–93, 2015.

[13] L. S. Pan, X. L. Wei, Y. Peng, X. B. Shi, and H. L. Liu, "Experimental study on convection heat transfer and air drag in sinter layer," *Journal of Central South University*, vol. 22, no. 7, pp. 2841–2848, 2015.

[14] D. Mehta and M. C. Hawley, "Wall effect in packed columns," *Industrial and Engineering Chemistry Process Design and Development*, vol. 8, no. 2, pp. 280–282, 1969.

[15] R. M. Fand and R. Thinakaran, "The influence of the wall on flow through pipes packed with spheres," *Journal of Fluids Engineering*, vol. 112, no. 1, pp. 84–88, 1990.

[16] R. D. Felice and L. G. Gibilaro, "Wall effects for the pressure drop in fixed beds," *Chemical Engineering Science*, vol. 59, no. 14, pp. 3037–3040, 2004.

[17] R. C. Raichura, "Pressure drop and heat transfer in packed beds with small tube-to-particle diameter ratio," *Experimental Heat Transfer*, vol. 12, no. 4, pp. 309–327, 1999.

[18] B. Eisfeld and K. Schnitzlein, "The influence of confining walls on the pressure drop in packed beds," *Chemical Engineering Science*, vol. 56, no. 14, pp. 4321–4329, 2001.

[19] A. Montillet, E. Akkari, and J. Comiti, "About a correlating equation for predicting pressure drops through packed beds of spheres in a large range of Reynolds numbers," *Chemical Engineering and Processing*, vol. 46, no. 4, pp. 329–333, 2007.

[20] Y. S. Choi, S. J. Kim, and D. Kim, "A semi-empirical correlation for pressure drop in packed beds of spherical particles," *Transport in Porous Media*, vol. 75, no. 2, pp. 133–149, 2008.

[21] N. S. Cheng, "Wall effect on pressure drop in packed beds," *Powder Technology*, vol. 210, no. 3, pp. 261–266, 2011.

[22] S. Palle and S. Aliabadi, "Direct simulation of structured wall bounded packed beds using hybrid FE/FV methods," *Computers & Fluids*, vol. 88, pp. 730–742, 2013.

[23] E. A. Foumeny, F. Benyahia, J. A. A. Castro, H. A. Moallemi, and S. Roshani, "Correlations of pressure drop in packed beds taking into account the effect of confining wall," *International Journal of Heat and Mass Transfer*, vol. 36, no. 2, pp. 536–540, 1993.

[24] R. K. Reddy and J. B. Joshi, "CFD modeling of pressure drop and drag coefficient in fixed and expanded beds," *Chemical Engineering Research and Design*, vol. 86, no. 5, pp. 444–453, 2008.

[25] R. K. Reddy and J. B. Joshi, "CFD modeling of pressure drop and drag coefficient in fixed beds: wall effects," *Particuology*, vol. 8, no. 1, pp. 37–43, 2010.

[26] L. D. Harrison, K. M. Brunner, and W. C. Hecker, "A combined packed-bed friction factor equation: extension to higher Reynolds number with wall effects," *AICHE Journal*, vol. 59, no. 3, pp. 703–706, 2013.

[27] T. Atmakidis and E. Y. Kenig, "CFD-based analysis of the wall effect on the pressure drop in packed beds with moderate tube/particle diameter ratios in the laminar flow regime," *Chemical Engineering Journal*, vol. 155, no. 1–2, pp. 404–410, 2009.

[28] Z. H. Guo, Z. N. Sun, N. Zhang, M. Ding, and S. Shi, "CFD analysis of fluid flow and particle-to-fluid heat transfer in packed bed with radial layered configuration," *Chemical Engineering Science*, vol. 197, pp. 357–370, 2019.

[29] Z. H. Guo, Z. N. Sun, N. Zhang, and M. Ding, "Influence of confining wall on pressure drop and particle-to-fluid heat transfer in packed beds with small D/d ratios under high Reynolds number," *Chemical Engineering Science*, vol. 209, p. 115200, 2019.

[30] J. M. Gorman, A. Zheng, and E. M. Sparrow, "Bounding Wall effects on fluid flow and pressure drop through packed beds of spheres," *Chemical Engineering Journal*, vol. 373, pp. 519–530, 2019.

[31] K. G. Allen, T. W. V. Backström, and D. G. Kröger, "Packed bed pressure drop dependence on particle shape, size distribution, packing arrangement and roughness," *Powder Technology*, vol. 246, pp. 590–600, 2013.

[32] M. Mayerhofer, J. Govaerts, N. Parmentier, H. Jeanmart, and L. Helsen, "Experimental investigation of pressure drop in packed beds of irregular shaped wood particles," *Powder Technology*, vol. 205, no. 1–3, pp. 30–35, 2011.

[33] A. Koekemoer and A. Luckos, "Effect of material type and particle size distribution on pressure drop in packed beds of large particles: extending the Ergun equation," *Fuel*, vol. 158, pp. 232–238, 2015.

[34] S. Z. Zhang, Z. Wen, X. L. Liu, X. Liu, S. Wang, and H. Zhang, "Experimental study on the permeability and resistance characteristics in the packed bed with the multi-size irregular particle applied in the sinter vertical waste heat recovery technology," *Powder Technology*, vol. 384, pp. 304–312, 2021.

[35] S. Z. Zhang, Z. Wen, X. L. Liu, H. Zhang, X. H. Liu, and S. Wang, "Effects of particle shape on permeability and resistance coefficients of sinter packed bed," *Journal of Central South University (Science and Technology)*, vol. 52, no. 4, pp. 1066–1075, 2021.

[36] S. Z. Zhang, Z. Wen, X. L. Liu, H. Zhang, S. Wang, and X. H. Liu, "Gas resistance characteristics in vertical tank with irregular sinter for waste heat recovery," *Journal of Central South University (Science and Technology)*, vol. 52, no. 6, pp. 1963–1973, 2021.

[37] M. Hartman, O. Trnka, and K. Svoboda, "Fluidization characteristics of dolomite and calcined dolomite particles," *Chemical Engineering Science*, vol. 55, no. 24, pp. 6269–6274, 2000.

[38] J. S. Feng, H. Dong, Z. Cao, and A. H. Wang, "Voidage distribution properties of bed layer in sinter vertical tank," *Journal of Central South University (Science and Technology)*, vol. 47, no. 1, pp. 8–13, 2016.

[39] C. G. D. Toit, "Analysing the porous structure of packed beds of spheres using a semi-analytical approach," *Powder Technology*, vol. 342, pp. 475–485, 2019.

[40] G. E. Mueller, "A modified packed bed radial porosity correlation," *Powder Technology*, vol. 342, pp. 607–612, 2019.

[41] S. Hamel and W. Krumm, "Near-wall porosity characteristics of fixed beds packed with wood chips," *Powder Technology*, vol. 188, no. 1, pp. 55–63, 2008.

[42] J. S. Feng, H. Dong, H. Z. Li, and J. Y. Gao, "Flow resistance characteristics in vertical tank for sinter waste heat recovery," *Journal of Central South University (Science and Technology)*, vol. 48, no. 4, pp. 867–872, 2017.

Hindawi
International Journal of Photoenergy
Volume 2022, Article ID 3727937, 15 pages
https://doi.org/10.1155/2022/3727937

Research Article

Effects of the Layered Distribution Pattern on the Gas Flow Resistance through the Bed with the Multisize Irregular Particle for the Waste Heat Recovery

Sizong Zhang [1,2]

[1]*School of Energy and Environmental Engineering, University of Science and Technology Beijing, Beijing 100083, China*
[2]*Beijing Key Laboratory of Energy Conservation and Emission Reduction for Metallurgical Industry, University of Science and Technology Beijing, Beijing 100083, China*

Correspondence should be addressed to Sizong Zhang; 513865909@qq.com

Received 15 April 2022; Accepted 2 June 2022; Published 21 June 2022

Academic Editor: Lixin Wang

The application of the sinter vertical cooling technology in the iron and steel industry is conducive to the realization of the double carbon in China. To reduce the energy consumption and improve the economy of the new process, the gas flow resistance in the sinter bed under the layered distribution pattern was experimentally studied. The gas flow resistance of most of the layered distribution modes is lower than that of the random distribution mode. Among all layered arrangement modes, the layered mode with the particle size increasing from the bottom-up has the lowest resistance, followed by the layered mode with the particle size decreasing from the bottom-up. These two modes ensure the feasibility of the application of the layered distribution pattern in the continuous production of the moving bed. Besides, increasing the number of layers benefits the reduction of the gas flow resistance, which has a more significant effect on the layered mode with the particle size increasing from the bottom-up. For the sinter mixture with the equivalent particle diameter of 11.45 mm, the gas resistance of the modes with the particle size increasing and decreasing from the bottom-up decreases by 11.71% and 8.26% with the layer number increasing from three to five, respectively. Also, the effect of the layered distribution pattern on the gas flow resistance progressively weakens with increasing the equivalent particle diameter. For the five-layer distribution mode with the particle size increasing from the bottom-up, the gas resistance decreases by 2.72% with the equivalent particle diameter increasing from 11.45 mm to 15.45 mm, while that decreases by 4.61% with the equivalent particle diameter increasing from 15.45 mm to 19.45 mm. What's more, the change of the equivalent particle diameter has a more significant influence on the layered mode with the particle size decreasing from the bottom-up. With the equivalent particle diameter increasing from 15.45 mm to 19.45 mm under the five-layer distribution pattern, the gas resistance of the layered mode with the particle size increasing from the bottom-up reduces by 4.61%, while that of the mode with the particle size decreasing from the bottom-up reduces by 7.38%.

1. Introduction

For realizing the green economic development system, China has put forward the targets of Carbon Peak in 2030 and Carbon Neutrality in 2060. Apart from vigorously developing the clean energy, including the solar energy, the breakthrough in the energy conversation and emission reduction technology of the traditional industry is a very important aspect, such as the iron and steel industry. The latest statistics show that the energy consumption of the iron and steel industry accounts for about 20% of the whole industry [1–4]. Among all processes, the energy consumption of the sintering process accounts for approximately 10~15% of the iron and steel industry, second only to the ironmaking process [5]. In the sintering process, the sensible heat of the sinter makes up about 70% of the waste heat resource. Therefore, improving the recovery rate of the sensible heat is of great significance for reducing the energy consumption of the sintering process and even the iron and steel industry. This would be a most promising method for China to realize the "double Carbon."

At present, the waste heat recovery of the high-temperature sinter is mainly through the annular cooling process. Since the air leakage rate of the annular cooler is as high as 35~50% and the cooling gas can only be heated to 150~380 °C, the recovery rate of the waste heat from the sinter is less than 30%. Given the shortcomings of the existing process, the vertical tank cooling process of the sinter has been newly proposed based on the coke dry quenching process [6, 7]. It is estimated that the vertical cooling process can increase the temperature of the cooling gas to 500~550 °C and increase the recovery rate from 30% to 80%.

The feasibility of the sinter vertical tank cooling process mainly depends on the gas-solid heat transfer and the gas flow resistance. The gas flow characteristic not only is the basis of the gas-solid heat transfer but also directly determines the pressure of the required fan and the power of the matching motor. For the sintering machine with the annual capacity of 4 million tons of the sinter, the heights of the sinter layer in the annular cooler and the vertical cooler are 0.8~1.5 m [5, 8–11] and 7~10 m [12, 13], respectively. Therefore, the gas flow resistance of the vertical cooler is much higher than that of the annular cooler. The excessive resistance not only makes it difficult for the gas to pass through the sinter layer but also reduces the efficiency of the gas-solid heat transfer and increases the energy consumption. Therefore, how to reduce the gas flow resistance is the key to the application of the sinter vertical tank cooling process.

In recent years, the relevant scholars have carried out some experimental researches on the resistance characteristic of the gas flow in the sinter bed [14–21]. Results showed that the gas flow resistance increased linearly with the bed height increasing [14], increased in a quadratic relationship with the increase of the gas velocity [14, 15], and decreased exponentially with the increase of the particle size and voidage [15]. Tian et al. [16] also found that the wall effect on the gas flow resistance can be ignored for $19 < D/d_p < 35$ (the ratio of the bed diameter D to the particle diameter d_p). However, the wall effect would lead to the reduction of the gas flow resistance for $7 < D/d_p < 19$. When the crushed sinter was added to the sinter mixture, the gas flow resistance in the bed would increase by 2~3 times [19]. In addition, the related studies on other particles are mainly concerned on the influences of the wall effect [22–24], particle shape [25–29], and particle size distribution [28–32] on the gas flow resistance. Therefore, there are few studies on how to reduce the gas flow resistance in the sinter bed.

In the actual production, the particle size of the sinter is nonuniform, but has a wide particle size distribution [17]. Therefore, the traditional distribution pattern, namely, the random distribution pattern, would cause the uneven distribution of the particle size and voidage in the sinter bed [33, 34]. The gas flow in the random bed is very disordered [35], leading to a sharp increase in the gas flow resistance and the uneven cooling of the high-temperature sinter. Besides, the gas flow in the packed bed with the double-size sinter was more disordered than that in the packed bed with the monosize sinter [18]. Compared with the particle bed of the wide particle size distribution, the gas flow in the particle bed of the narrow particle size distribution is more uniform, and the gas flow resistance is lower

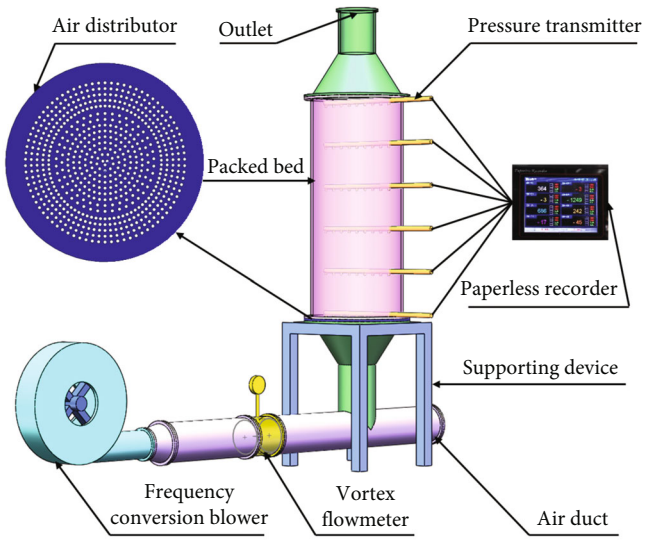

Figure 1: A sketch of the experimental apparatus for measuring the gas flow resistance in the sinter bed.

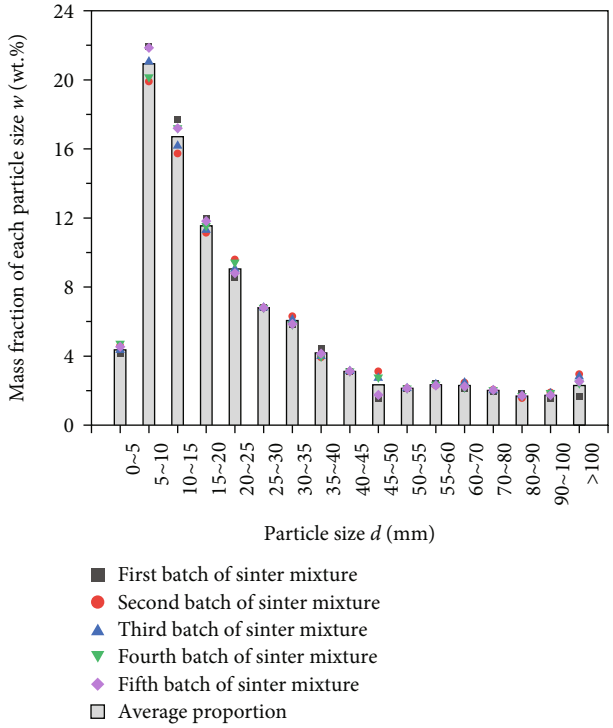

Figure 2: The original particle size distribution of sinter samples.

[36]. Based on the above reason, the layered distribution pattern based on the particle size is proposed [33, 34]; that is, the sinter mixture with the wide particle size distribution is divided into a variety of sinters with the narrow particle size distribution for the layered distribution. The numerical studies showed that the flow field and temperature distribution in the layered bed are relatively uniform [35]. Also, the recovery rate of the waste heat under the layered distribution pattern can be raised by about 14% compared with the random distribution pattern [33, 34].

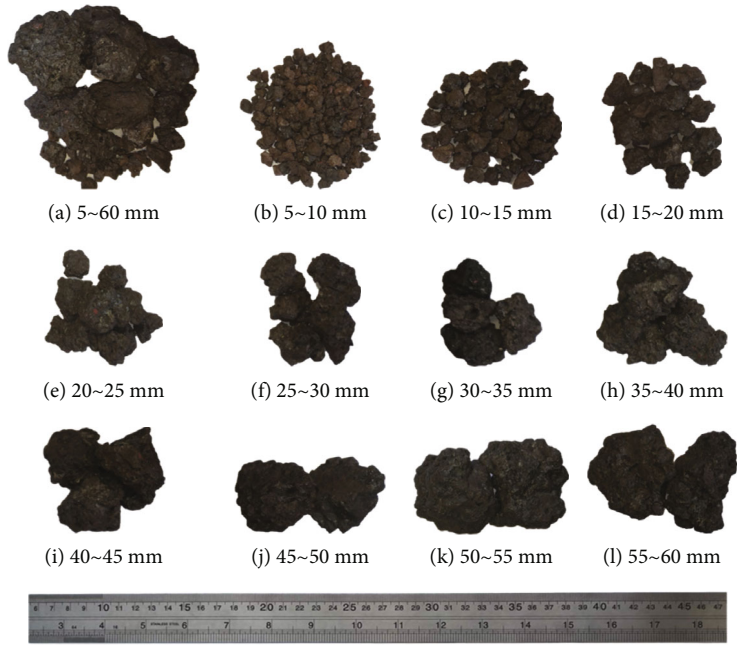

Figure 3: Photographs taken on the sinter of 5 ~60 mm: (a) the unsorted sinter mixture with the multisize; (b–l) 11 kinds of the sieved sinter with the monosize.

Table 1: Expressions of the measured and calculated method for characteristic parameters of sinter particles.

Characteristic parameter	Expression	Equation
Apparent density of the monosize sinter [17, 18]	$\rho_{a,s} = (m_1/m_3 - (m_2 - m_4))\rho_w$	(i)
Equivalent diameter of the monosize sinter [16, 17, 21]	$d_{p,s} = \sqrt[3]{6m_s/\pi\rho_{a,s}}$	(ii)
Apparent density of the sinter mixture [18]	$\rho_{a,m} = \sum_{i=1}^{n} w_i\rho_{a,si}$	(iii)
Equivalent diameter of the sinter mixture [29–31, 36]	$d_{p,m} = \sum_{i=1}^{n} w_i / \sum_{i=1}^{n} w_i/d_{p,si}$	(iv)
Bulk density [17, 18]	$\rho_b = (M_1 - M_2)/V$	(v)
Voidage [16–18, 21]	$\varepsilon = 1 - \rho_b/\rho_a$	(vi)

According to the above findings, the layered distribution pattern is beneficial to improve the uniformity of the gas flow and the sinter temperature in the packed bed. However, it is not known whether the uniform distribution of the gas flow is beneficial to reduce the gas flow resistance in the sinter bed. Therefore, from the viewpoint of reducing the energy consumption, the influence of the layered distribution pattern on the gas flow resistance is studied through experiments, thereby determining the optimal layered distribution mode.

2. Experimental Method

2.1. Experimental System. In this study, the experimental apparatus is constructed to measure the gas flow resistance in the sinter bed, as shown in Figure 1. As the main part of the experimental apparatus, the height and the inner diameter of the cylindrical bed are 1000 mm and 400 mm, respectively. The air distributor with the uniform openings is arranged at the bed bottom to obtain the uniform flow field in the cross-section. Six pressure taps are evenly arranged along the axial direction. For each tap, 9 measuring points are uniformly set along the radial direction to calculate the average pressure of the cross-section. The pressure transmitter (CGYL-202) with the length of 650 mm is selected to acquire the pressure information, the measured range and accuracy of which are 0~5 kPa and 0.5%, respectively. The frequency conversion blower (HRD 65FU-100/7.5) is selected to precisely control the gas flow rate. The vortex flowmeter with the compensation of the temperature and pressure (type: LUGB1315C-P3Z) is used to measure the gas flow rate under the standard condition (273.15 K and 101.325 kPa). The measured range and accuracy of the flowmeter are 150~2500 $Nm^3 \cdot h^{-1}$ and 1.0%, respectively.

2.2. Particle Characteristics of the Sinter. The sinter particles come from HBIS Group Hansteel Company in China. Before the test, five batches of original sinter mixtures are screened to obtain the particle size distribution, as shown in Figure 2.

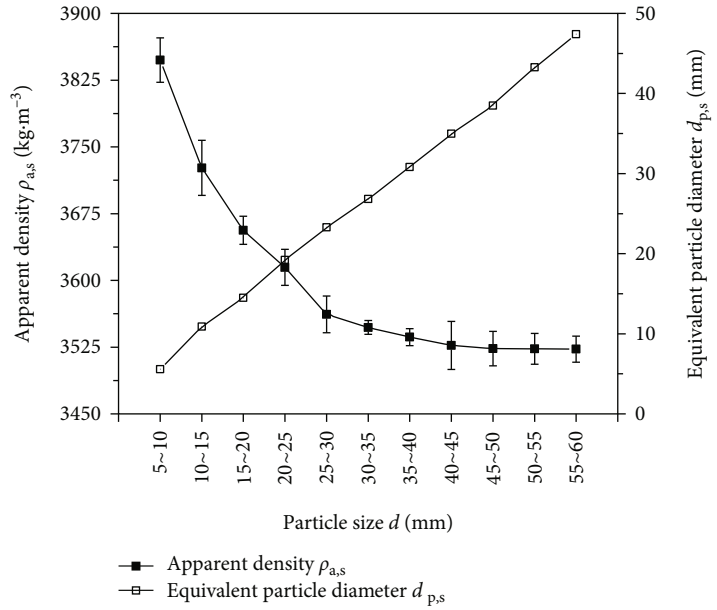

Figure 4: The apparent density $\rho_{a,s}$ and equivalent particle diameter $d_{p,s}$ of the monosize sinter under different particle sizes d.

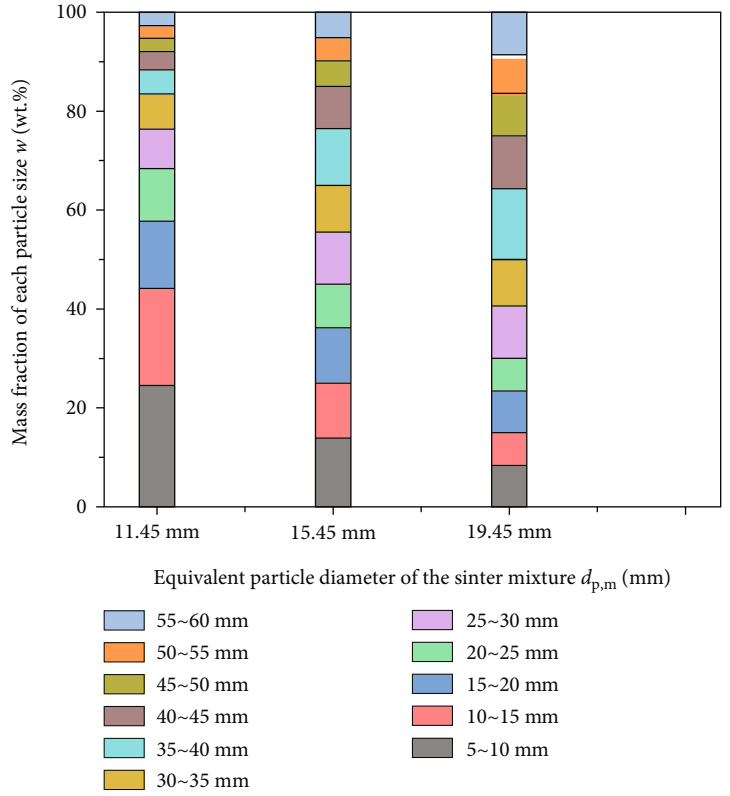

Figure 5: The particle size distribution of the three types of sinter mixtures.

It is observed that the particle size distribution among five batches of sinter mixtures is nearly consistent. Note that the sinter with the particle size range of 5~60 mm accounts for more than 85% of the total weight. Thus, they are taken for the test of the layered distribution, as shown in Figure 3.

To characterize the sinter of each monosize, the apparent density $\rho_{a,s}$ defined as Equation (i) in Table 1 is measured by the drainage method [17, 18], as shown in Figure 4. The equivalent particle diameter $d_{p,s}$ is calculated by Equation (ii) in Table 1 with the equal volume method [16, 17, 21].

Table 2: Characteristic parameters of the three kinds of sinter mixtures.

Equivalent particle diameter $d_{p,m}$ (mm)	Apparent density $\rho_{a,m}$ (kg·m^{-3})	Bulk density $\rho_{b,m}$ (kg·m^{-3})	Total height of the sinter bed L (cm)	Voidage ε
11.45	3676.09	1663.47	45.30	0.5475
15.45	3622.03	1581.00	47.11	0.5635
19.45	3589.73	1512.95	49.23	0.5785

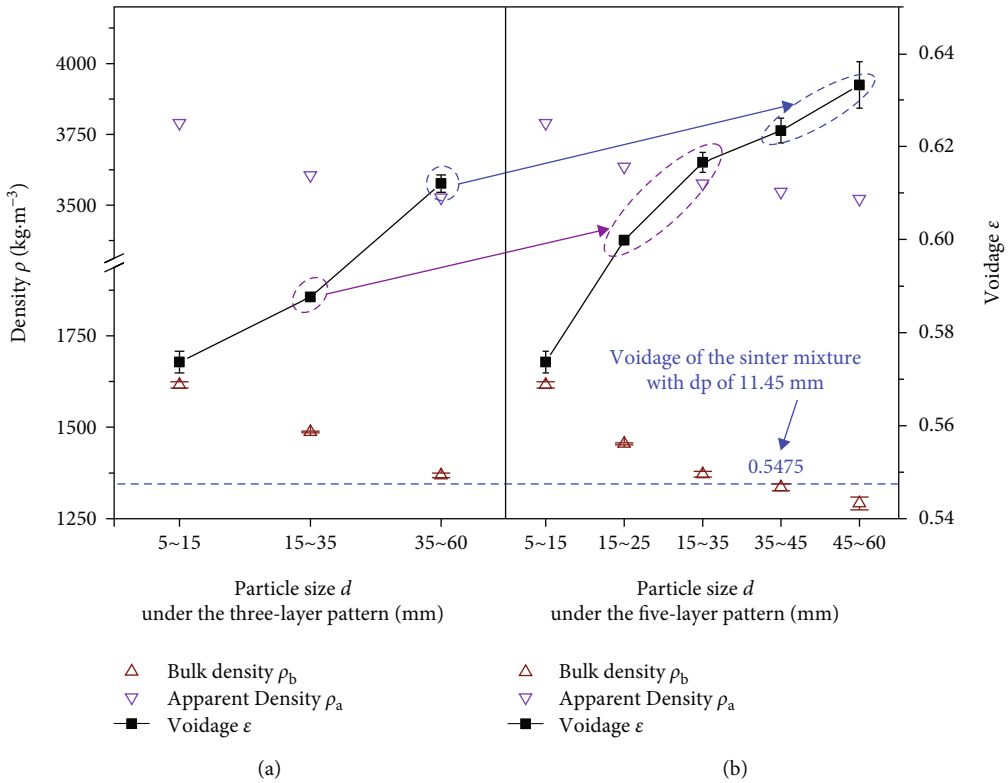

Figure 6: Characteristic parameters of the sinter in each particle size range under the three-layer pattern (a) and the five-layer pattern (b).

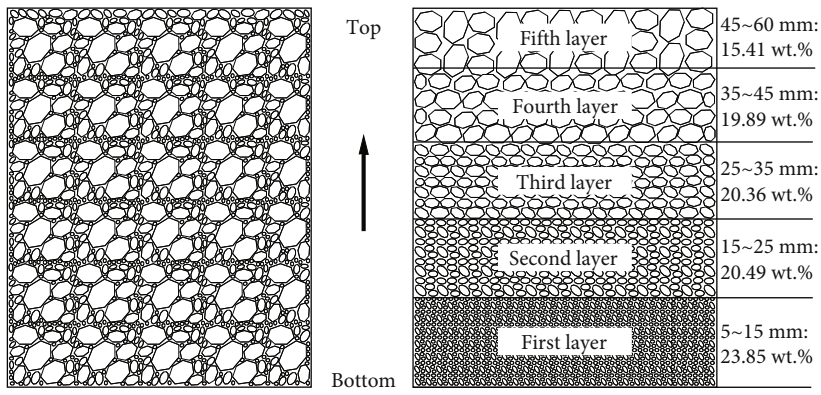

Figure 7: The schematic diagram of the distribution mode: (a) the random distribution mode; (b) the five-layer arrangement mode with the particle size increasing from the bottom-up (i.e., mode 1 in Table 4).

Table 3: All three-layer arrangement modes for the sinter mixture with the equivalent particle diameter of 11.45 mm.

Mode of the layered arrangement	Particle size range of the sinter in each layer d (mm) Bed bottom→bed top			Total height of the sinter layer L (cm)	Ratio of the resistance increase S_k (%)
	First layer	Second layer	Third layer		
0	Random distribution mode (control condition)			45.30	/
1	5~15	15~35	35~60	47.02	-13.99
2	5~15	35~60	15~35	46.54	-6.92
3	15~35	5~15	35~60	46.65	-9.65
4	15~35	35~60	5~15	46.14	-10.95
5	35~60	5~15	15~35	46.03	3.93
6	35~60	15~35	5~15	46.92	-11.89

Table 4: All five-layer arrangement modes for the sinter mixture with the equivalent particle diameter of 11.45 mm.

Mode of the layered arrangement	Particle size range of the sinter in each layer d (mm) Bed bottom→bed top					Total height of the sinter layer L (cm)	Ratio of the resistance increase S_k (%)
	First layer	Second layer	Third layer	Fourth layer	Fifth layer		
0	Random distribution mode (control condition)					45.30	/
1	5~15	15~25	25~35	35~45	45~60	47.36	-25.70
2	15~25	25~35	35~45	45~60	5~15	46.25	-0.56
3	25~35	35~45	45~60	5~15	15~25	47.12	-14.99
4	35~45	45~60	5~15	15~25	25~35	47.27	-10.19
5	45~60	5~15	15~25	25~35	35~45	46.74	-2.93
6	5~15	25~35	45~60	15~25	35~45	46.70	-3.32
7	15~25	35~45	5~15	25~35	45~60	46.58	2.95
8	25~35	45~60	15~25	35~45	5~15	46.37	-2.04
9	35~45	5~15	25~35	45~60	15~25	46.23	-4.63
10	45~60	15~25	35~45	5~15	25~35	45.85	-5.13
11	5~15	35~45	15~25	45~60	25~35	45.25	-1.75
12	15~25	45~60	25~35	5~15	35~45	45.51	-7.09
13	25~35	5~15	35~45	15~25	45~60	46.71	-1.52
14	35~45	15~25	45~60	25~35	5~15	46.16	4.85
15	45~60	25~35	5~15	35~45	15~25	45.84	3.99
16	5~15	45~60	35~45	25~35	15~25	46.02	3.24
17	15~25	5~15	45~60	35~45	25~35	46.04	1.74
18	25~35	15~25	5~15	45~60	35~45	46.22	-10.90
19	35~45	25~35	15~25	5~15	45~60	46.01	-3.91
20	45~60	35~45	25~35	15~25	5~15	46.62	-20.15

Table 5: Summary of the relative uncertainty of parameters in this study.

Parameter	Symbol	Uncertainty (%)	Parameter	Symbol	Uncertainty (%)
Equivalent particle diameter	d_p	1.51	Gas velocity	u_g	1.00
Apparent density	ρ_a	1.42	Voidage	ε	1.81
Bulk density	ρ_b	1.12	Gas resistance	ΔP	0.50

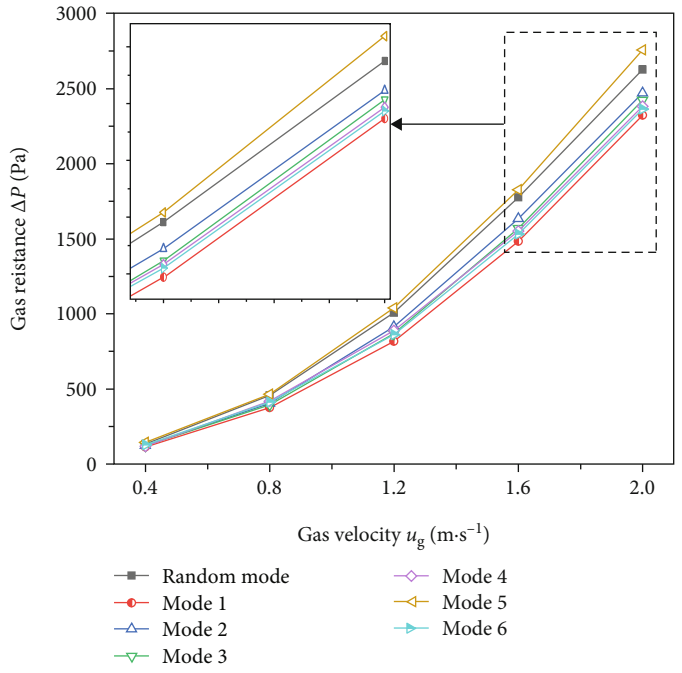

Figure 8: The change of the gas resistance ΔP with the gas velocity u_g under the three-layer layered arrangement modes and the random distribution mode for the sinter mixture with the equivalent particle diameter of 11.45 mm.

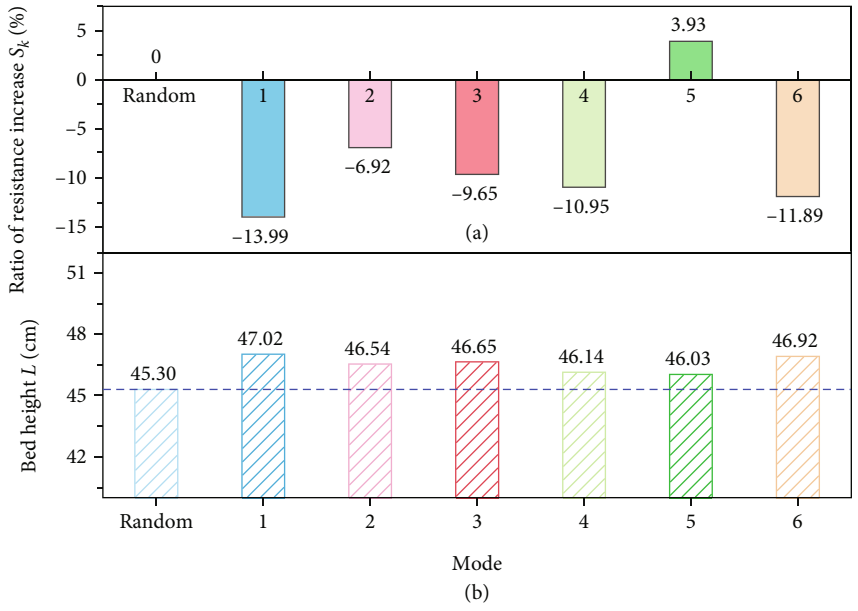

Figure 9: The ratio of the resistance increase S_k (a) and the total height of the sinter bed L (b) under different three-layer arrangement modes for the sinter mixture with the equivalent particle diameter of 11.45 mm.

For the multisize sinter mixture composed of a variety of the monosize sinter, the apparent density $\rho_{a,m}$ and equivalent particle diameter $d_{p,m}$ can be calculated by Equation (iii) in Table 1 [18] with the weighted method and Equation (iv) in Table 1 with the weighted harmonic mean method [29–31, 36], respectively. For multisize sinter mixtures and monosize sinters, the bulk density ρ_b can be measured by the weighing method of Equation (v) in Table 1 [17, 18]. The bed voidage ε can be calculated by Equation (vi) in Table 1 [16–18, 21].

To study the influence of the particle size distribution on the gas flow resistance under the layered distribution

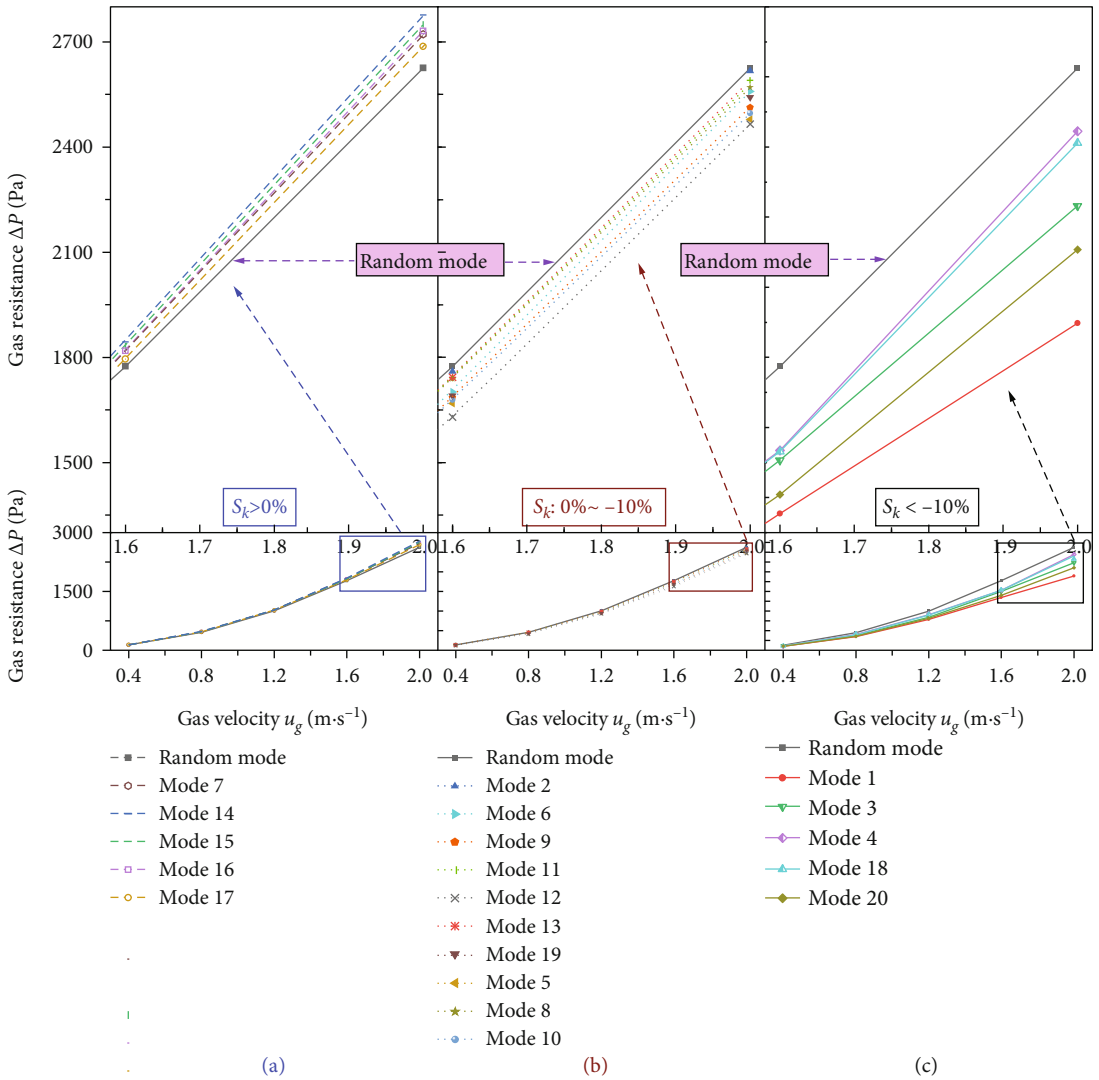

FIGURE 10: The comparison of the gas flow resistance ΔP between the five-layer layered mode and the random distribution mode based on the sinter mixture with the equivalent particle diameter of 11.45 mm: (a) the ratio of the resistance increase $S_k > 0\%$; (b) the ratio of the resistance increase S_k: 0%~-10%; (c) the ratio of the resistance increase S_k <-10%.

pattern, three types of sinter mixtures are designed, as shown in Figure 5. The equivalent particle diameters $d_{p,m}$ of the three kinds of sinter mixtures are 11.45 mm, 15.45 mm, and 19.45 mm, respectively. To ensure the comparability of experimental results, the mass of the three kinds of sinter mixtures is the same, which is 94.30 kg. The characteristic parameters of the sinter mixture obtained by the above methods are shown in Table 2.

To analyze the effect of the layer number on the gas flow resistance, two types of the layered distribution patterns are studied. The first type is divided into three layers, which is composed of the three kinds of sinters with the particle size of 5~15 mm, 15~35 mm, and 35~60 mm. The second type is divided into five layers, which contains the five kinds of sinters with the particle size of 5~15 mm, 15~25 mm, 25~35 mm, 35~45 mm, and 45~60 mm. The bulk density ρ_b, apparent density ρ_a, and voidage ε of the sinter of each particle size are measured by means of the above methods, as shown in Figure 6.

To analyze the effect of the gas velocity u_g, the gas resistance in the layered bed is measured under the five kinds of gas velocities, namely, 0.4, 0.8, 1.2, 1.6, and 2.0 m·s^{-1}. The conventional random distribution pattern is also studied as the control experiment, as shown in Figure 7. To study the effect of the layered arrangement mode, the gas resistance in the bed of the sinter mixture with the equivalent particle diameter of 11.45 mm is measured under 6 kinds of three-layer arrangement modes and 20 kinds of five-layer arrangement modes based on the orthogonal design, as shown in Tables 3 and 4, respectively. Tables also list the ratio of the resistance increase S_k for different layered arrangement modes compared with the random distribution mode, which is defined as follows:

$$S_k = \frac{1}{n}\sum_{i=1}^{n=5}\frac{\Delta P_k^i - \Delta P_r^i}{\Delta P_r^i}, \quad (1)$$

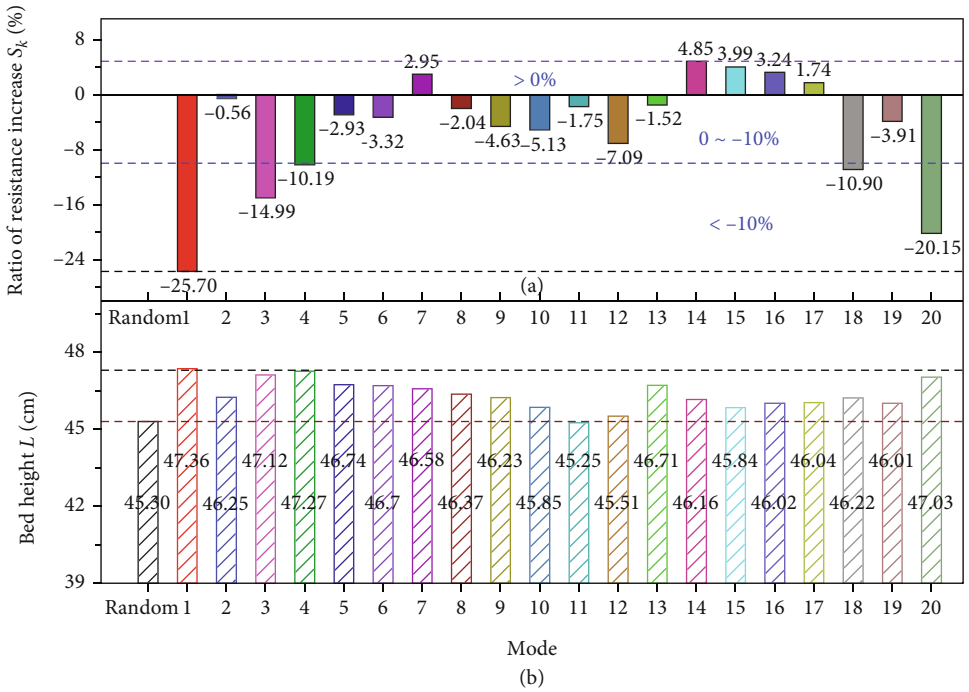

FIGURE 11: The ratio of the resistance increase S_k (a) and the total height of the sinter bed L (b) under different five-layer layered arrangement modes for the sinter mixture with the equivalent particle diameter of 11.45 mm.

where S_k is the ratio of the resistance increase of the k-th layered arrangement mode; ΔP_r^i and ΔP_k^i represent the gas resistance of the i-th gas velocity under the random distribution mode and the k-th layered arrangement mode, respectively; and i is the condition of the i-th gas velocity.

2.3. Uncertainty Analysis. The uncertainty analysis of parameters is calculated by the theory of the error transfer [21, 37–39]. Suppose the relationship between the parameter y and k variables is as follows:

$$y = f(x_1, x_2, x_3, \cdots, x_k), \tag{2}$$

where $x_1, x_2, x_3, \cdots, x_k$ are k independent variables.

Then the absolute uncertainty of y (Δy) can be calculated according to the absolute uncertainty of each independent variable ($\Delta x_1, \Delta x_2, \Delta x_3, \cdots, \Delta x_k$) as follows:

$$\Delta y = \sqrt{\sum_{j=1}^{k} \left(\frac{\partial f}{\partial x_j} \Delta x_j \right)^2}. \tag{3}$$

Therefore, the relative uncertainty of y is expressed as

$$\frac{\Delta y}{y} = \sqrt{\sum_{j=1}^{k} \left(\frac{\Delta x_j}{x_j} \right)^2}. \tag{4}$$

The relative uncertainty of each parameter is shown in Table 5.

3. Experimental Results and Discussion

3.1. Analysis of the Three-Layer Arrangement Mode. Figure 8 shows the change of the gas flow resistance (ΔP) with the gas velocity (u_g) under the three-layer layered mode and the random mode for the sinter mixture with the equivalent particle diameter of 11.45 mm. It can be observed that ΔP increases in a quadratic relationship with the increase of u_g. With the increase of u_g, the collision between the gas and sinter particles will intensify. Therefore, the turbulent degree of the gas flow increases, which makes the gas resistance increase [14].

Based on the data in Figure 8, the ratio of the resistance increase S_k under different three-layer arrangement modes is calculated, as shown in Figure 9(a). It can be found that the gas flow resistance (ΔP) of most of the layered arrangement modes is lower than that of the random distribution mode. On the one hand, the mixing degree of sinters under the layered distribution mode is lower than that of the random distribution mode. Therefore, Figure 6(a) shows that the voidage of each layer under the layered distribution mode is larger than that of the random distribution mode. This reduces the viscous resistance and the inertial resistance of the gas flow [14, 40]. On the other hand, the interval width of the particle size of the sinter in each layer under the layered distribution mode is narrower than that of the random distribution mode. The voidage distribution along the radial direction under the layered bed is more uniform, which reduces the disorder of the gas flow [35, 36].

Also, it can be seen from Figure 9(a) that the gas flow resistance of mode 1 and mode 6 is the smallest, which is 13.99% and 11.89% lower than that of the random distribution mode,

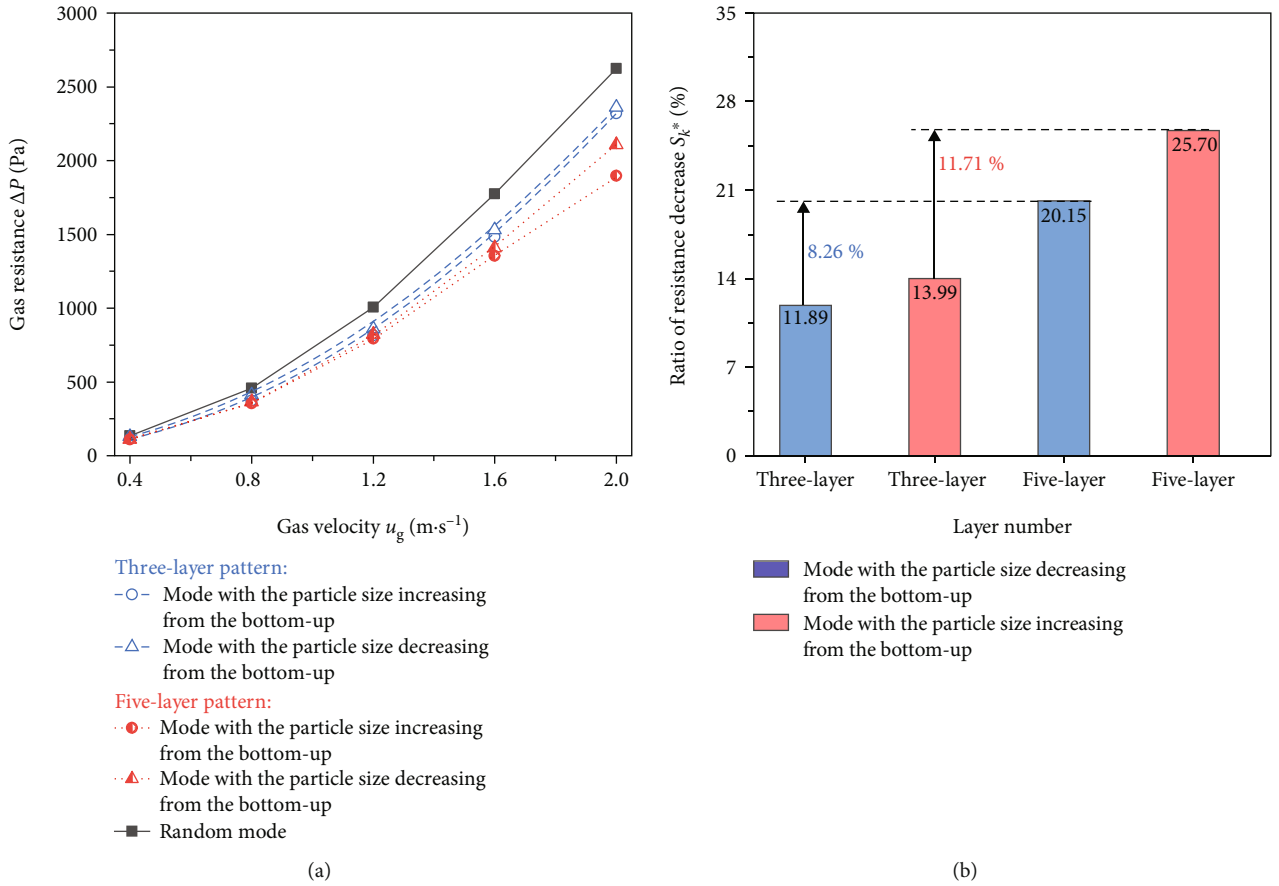

FIGURE 12: The effect of the layer number on the gas flow resistance of the sinter mixture with the equivalent particle diameter of 11.45 mm: (a) the comparison of the gas flow resistance ΔP between two three-layer modes and two five-layer modes; (b) the comparison of the ratio of the resistance decrease $S_k{}^*$ between the two three-layer models and two five-layer models.

respectively. It can be seen from Table 3 that mode 1 and mode 6 are the arrangement modes with the particle size increasing and decreasing from the bed bottom to the bed top, respectively. As can be seen from Figure 9(b), the bed height of these two modes is the highest. This indicates that the mixing degree of particles at the interface of adjacent layers is the lowest due to the continuous change of the particle size. Therefore, the disorder degree of the gas flow through the bed and the local resistance at the interface are relatively the lowest. Unexpectedly, the gas resistance of mode 5 is 3.93% higher than that of the random distribution mode. However, the ratio of the resistance increase is very small. Therefore, the gas flow resistance in the packed bed under the five-layer layered distribution pattern is further studied.

3.2. Analysis of the Five-Layer Arrangement Model. As shown in Figure 10 based on the sinter mixture with the equivalent particle diameter of 11.45 mm, the gas flow resistance ΔP is compared between all five-layer layered modes and the random distribution mode. Notably, Figure 10(a) shows that there are indeed several layered modes, ΔP of which is higher than that of the random distribution mode.

Based on the ratio of the resistance increase S_k of Figure 11(a), all layered modes can be divided into three categories, namely, $S_k > 0\%$, $0 > S_k > -10\%$, and $S_k < -10\%$. According to Figure 11(b), the average bed heights of the layered mode of $S_k > 0\%$, $0 > S_k > -10\%$, and $S_k < -10\%$ are 45.88 cm, 46.41 cm, and 46.88 cm, respectively. For the same batch of the sinter mixture, the bed voidage reduces with the decrease of the bed height. The lower the bed voidage, the greater the gas flow resistance. Besides, it can be seen from Table 4 that the particle size of the sinter between adjacent layers changes greatly under the five layered modes of $S_k > 0\%$. The great change of the particle size between adjacent layers would produce two factors to increase the resistance. On the one hand, the mixing degree of sinter particles between adjacent layers increases. This makes the uniformity of the voidage distribution along the radial distribution reduce, which increases the turbulent degree of the gas flow. On the other hand, the change range of the voidage along the axial direction at the interface of adjacent layers increases. This makes the gas flow expand or contract abruptly at the interface, increasing the local resistance. For the layered mode of $S_k < -10\%$, the particle size of the sinter between adjacent layers changes little, which basically shows the continuous increase or the continuous decrease. The mixing degree of the sinter between adjacent layers reduces. This not only improves the uniformity of the voidage

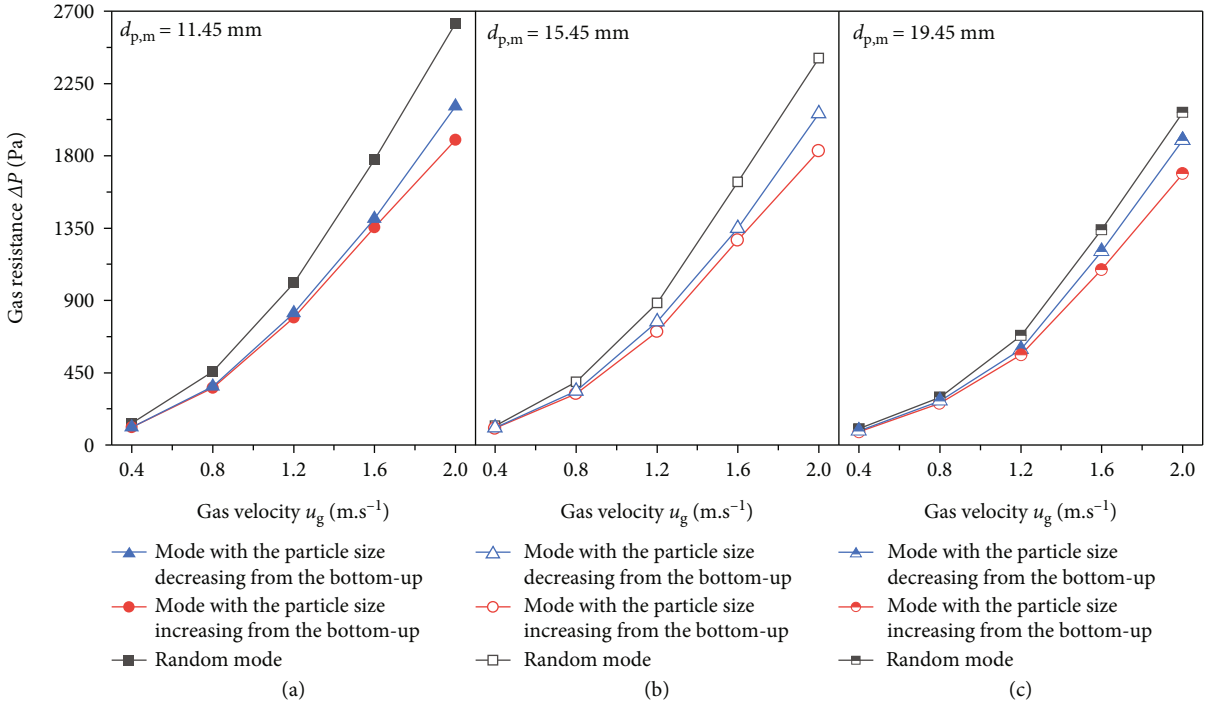

FIGURE 13: The comparison of the gas flow resistance (ΔP) between the random distribution mode and two kinds of five-layer distribution modes under the three kinds of sinter mixtures: (a) $d_{p,m}$ = 11.45 mm; (b) $d_{p,m}$ = 15.45 mm; (c) $d_{p,m}$ = 19.45 mm.

distribution along the radial direction, but also reduces the variation range of the axial voidage at the interface. Therefore, the gas can flow evenly through the sinter layer, which reduces the turbulent degree and the local resistance of the gas flow.

As can be seen from Figure 11(a) for the five-layer distribution pattern, the gas flow resistance of modes with the particle size increasing and decreasing from the bottom-up (i.e., modes 1 and 20) is also the lowest, which is 25.70% and 20.15% lower than that of the random distribution mode, respectively. For the layered distribution pattern, the layered mode with the particle size increasing from the bottom-up has the smallest resistance, followed by the mode with the particle size decreasing from the bottom-up. Compared with the layered mode with the particle size increasing from the bottom-up, the small-size sinter in the upper layer can be easily filled into gaps between the large-size sinters in the lower layer for the mode with the particle size decreasing from the bottom-up. Therefore, the packing structure of the mode with the particle size decreasing from the bottom-up is more complex, intensifying the disorder and resistance of the gas flow.

3.3. Effect of the Layer Number. Figure 12 illustrates the effect of the layer number on the gas flow resistance. In Figure 12(b), S_k^* is defined as the ratio of the resistance decrease of the layered distribution mode compared to the random distribution mode. As seen from Figure 12(a), the gas flow resistance of the three-layer bed is higher than that of the five-layer packed bed under two kinds of layered modes with the particle size increasing and decreasing from the bottom-up. Besides, Figure 12(b) indicates that the gas flow resistance of the mode with the particle size decreasing from the bottom-up declines by 8.26% with the layer number increasing from three to five, while that decreases by 11.71% for the mode with the particle size increasing from the bottom-up. Therefore, the increase of the layer number is not only conducive to further reduce the gas flow resistance, but also has a more significant impact on the mode with the particle size increasing from the bottom-up. This can be attributed to the following two aspects. On the one hand, the sinter with the particle size of 15~35 mm under the three-layer distribution pattern is composed of the sinter with the particle size of 15~25 mm and 25~35 mm under the five-layer distribution pattern. And the sinter with the particle size of 35~60 mm consists of the sinter with the particle size of 35~45 mm and 45~60 mm. Therefore, the packing structure in the three-layer packed bed is more complex. The distribution homogeneity of the voidage and particle size along the radial direction reduces, which increases the disorder degree of the gas flow [36]. On the other hand, Figure 6 shows that the bed voidage of the sinter with the particle size of 15~25 and 25~35 mm is bigger than that of the sinter with the particle size of 15~35 mm. And the voidage of the sinter with the particle size of 35~45 and 45~60 mm is also bigger than that of the sinter of with the particle size of 35~60 mm. Therefore, the overall voidage of the three-layer packed bed is smaller, leading to an increase in the gas flow resistance [40].

3.4. Effect of the Equivalent Particle Diameter. Figure 13 compares the gas flow resistance of the three types of sinter mixtures under the three kinds of distribution modes. The gas flow resistance of the three modes decreases with the

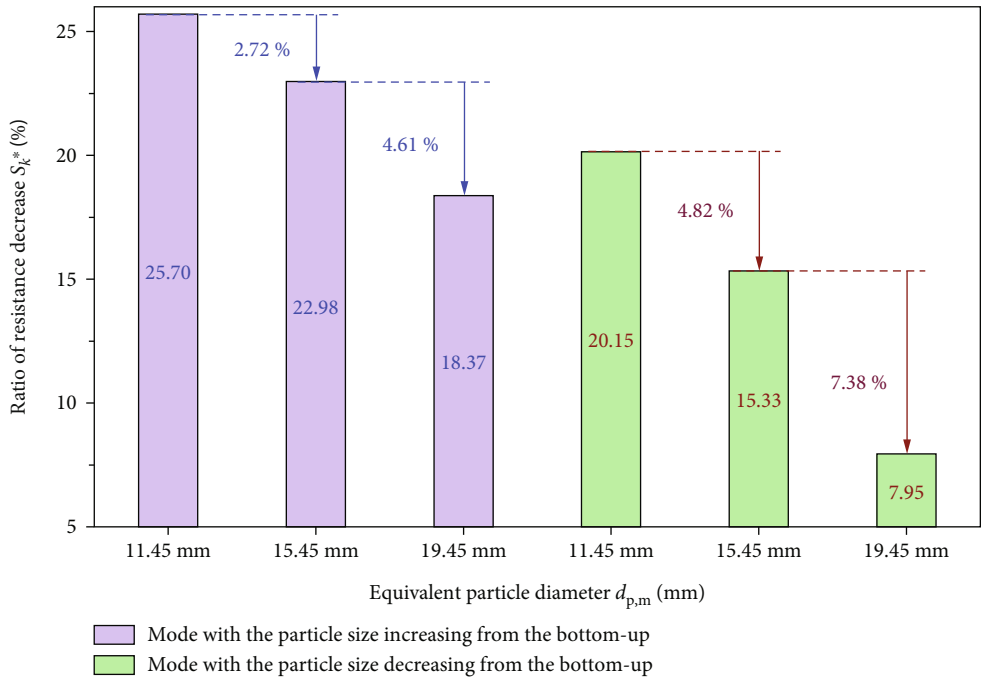

FIGURE 14: Effect of the equivalent particle diameter $d_{p,m}$ on the ratio of the resistance decrease S_k^* under the two five-layer layered arrangement modes.

increase of the equivalent particle diameter $d_{p,m}$. Table 2 shows that the overall voidage of the sinter mixture increases with the increase of $d_{p,m}$. This leads to the reduction of the flow instability and specific surface area, decreasing the inertial resistance and viscous resistance.

Based on the data in Figure 13, the ratio of the resistance decrease S_k^* of the two five-layer modes under the three kinds of equivalent particle diameters $d_{p,m}$ is calculated, as shown in Figure 14. The ratio of the resistance decrease S_k^* under two kinds of layered modes decreases with the increase of the equivalent particle diameter $d_{p,m}$. Moreover, S_k^* of the mode with the particle size increasing from the bottom-up decreases by 2.72% with $d_{p,m}$ increasing from 11.45 mm to 15.45 mm, while that decreases by 4.61% with $d_{p,m}$ increasing from 15.45 mm to 19.45 mm. This indicates that the effect of the layered distribution pattern on the resistance reduction progressively weakens with the increase of $d_{p,m}$. It can be seen from Figure 5 that the proportion of the small-size sinter and the large-size sinter would decrease and increase when the equivalent particle diameter increases, respectively. Therefore, it is easier to form large gaps between particles. For the layered distribution mode, the possibility of the small particle in adjacent layers filling into gaps between large particles under the action of the gravity increases. The nonuniformity of the voidage distribution along the radial direction increases, which makes the layered mode close to the random mode to some extent. Therefore, the increase of the equivalent particle diameter weakens the effect of the layered distribution mode on the disorder degree of the gas flow.

With the increase of the equivalent diameter $d_{p,m}$, Figure 14 also shows that the change range of the ratio of the resistance decrease S_k^* for the mode with the particle size decreasing from the bottom-up is greater than that for the mode with the particle size increasing from the bottom-up. When the equivalent particle diameter $d_{p,m}$ increases from 15.45 mm to 19.45 mm, S_k^* of the mode with the particle size increasing from the bottom-up decreases by 4.61%, while that of the mode with the particle size decreasing from the bottom-up decreases by 7.38%. Hence, the increase of the equivalent particle diameter has a greater influence on the mode with the particle size decreasing from the bottom-up. For the layered mode with the particle size increasing from the bottom-up, the size of the gap between sinters in the lower layer is smaller than that of the sinter in the upper layer. The sinter particles in the upper layer are difficult to fill into gaps in the lower layer. Therefore, the packing structure of the sinters is almost unchanged. The increase of the equivalent particle diameter has little effect on the bed structure of the mode with the particle size increasing from the bottom-up. For the mode with the particle size decreasing from the bottom-up, the probability of the small-size sinter in the upper layer filling into gaps between the large particles in the lower layer increases gradually with the increase of the equivalent particle diameter $d_{p,m}$. The packing structure of the mode with the particle size decreasing from the bottom-up is more similar to that of the random mode. Therefore, the gas resistance of the mode with the particle size decreasing from the bottom-up is more significantly affected by the change of the equivalent particle diameter.

4. Conclusions

The sinter vertical cooling technology is conducive to the realization of the double carbon in the iron and steel industry. To reduce the energy consumption of the new process, the gas flow resistance in the sinter bed under the layered distribution pattern was experimentally studied. The effects of three factors, namely, the layered arrangement mode, the layer number, and the equivalent particle diameter, are carefully discussed.

The results show that the gas flow resistance of most of the layered distribution modes is lower than that of the random distribution mode. This indicates that the application of the layered distribution pattern is beneficial to reduce the gas resistance in the sinter bed. Among all layered modes, the layered mode with the particle size increasing from the bottom-up has the lowest resistance, followed by the mode with the particle size decreasing from the bottom-up. Since the operation state of the sinter vertical cooling process is continuous, these two modes ensure the feasibility of the application of the layered distribution pattern. Besides, the increase of the layer number not only is conducive to reduce the gas resistance but also has a more significant impact on the layered mode with the particle size increasing from the bottom-up. Moreover, the effect of the layered distribution pattern on the gas flow resistance progressively weakens with the increase of the equivalent particle diameter. What's more, the mode with the particle size decreasing from the bottom-up is more significantly affected by the equivalent particle diameter.

This work not only is helpful to understand the effect of the layered distribution pattern on the gas resistance characteristic but also lays a foundation for the application of the layered distribution pattern in the moving bed. However, the bed structure and the mechanism of the gas flow under the layered distribution pattern are still unclear, which is an important research direction in the future.

Nomenclature

D: Diameter of the packed bed (m)
d: Particle size of the sinter (m)
d_p: Equivalent particle diameter of the sinter (m)
$d_{p,s}$: Equivalent particle diameter of the monosize sinter (m)
$d_{p,si}$: Equivalent particle diameter of a certain monosize sinter in the sinter mixture (m)
$d_{p,m}$: Equivalent particle diameter of the sinter mixture (m)
L: Height of the sinter bed (m)
ρ_a: Apparent density of sinter (kg·m^{-3})
m_1: Mass of the dry sinter (kg)
m_2: Mass of the sinter and test basket in water (kg)
m_3: Mass of the wet sinter (kg)
m_4: Mass of the test basket in water (kg)
M_1: Mass of a batch of the sinter and test container (kg)
M_2: Mass of the test container (kg)
ρ_w: Density of the water (kg·m^{-3})
m_s: Mean mass of the single sinter (kg)
$\rho_{a,m}$: Apparent density of the sinter mixture (kg·m^{-3})
$\rho_{a,s}$: Apparent density of the monosize sinter (kg·m^{-3})
$\rho_{a,si}$: Apparent density of a certain monosize sinter in the sinter mixture (kg·m^{-3})
ρ_b: Bulk density of the sinter (kg·m^{-3})
u_g: Gas velocity under the standard condition (m·s^{-1})
V: Volume of the test container (m^3)
w: Mass fraction of the sinter (wt.%)
w_i: Mass fraction of a certain monosize sinter in the sinter mixture (wt.%)
ΔP: Gas flow resistance in the sinter packed bed (Pa)
ΔP_r^i: The gas flow resistance of a certain gas velocity under the random distribution mode (Pa)
ΔP_k^i: Gas flow resistance of a certain gas velocity under a certain layered arrangement mode (Pa)
S_k: Ratio of the resistance increase of a certain layered arrangement mode (%)
S_k^*: The ratio of the resistance decrease of a certain layered arrangement mode (%)

Greeks

ρ: Density (kg·m^{-3})
ε: Voidage

Subscripts

p: Particle
w: Water
g: Gas

Data Availability

The data used to support the findings of this study are included within the article.

Conflicts of Interest

The authors declare that they have no known competing financial interests or personal relationships that could have appeared to influence the work reported in this paper.

Acknowledgments

This work is supported by Basic and Applied Basic Research Fund of Guangdong (2019A1515110743).

References

[1] Y. Li and L. Zhu, "Cost of energy saving and CO_2 emissions reduction in China's iron and steel sector," *Applied Energy*, vol. 130, pp. 603–616, 2014.

[2] Q. Xu, K. Wang, Z. W. Zou et al., "A new type of two-supply, one-return, triple pipe-structured heat loss model based on a low temperature district heating system," *Energy*, vol. 218, article 119569, 2021.

[3] Q. Xu, Z. W. Zou, Y. S. Chen et al., "Performance of a novel-type of heat flue in a coke oven based on high-temperature and low-oxygen diffusion combustion technology," *Fuel*, vol. 267, article 117160, 2020.

[4] Q. Xu, L. Liu, J. X. Feng et al., "A comparative investigation on the effect of different nanofluids on the thermal performance

of two-phase closed thermosyphon," *International Journal of Heat and Mass Transfer*, vol. 149, article 119189, 2020.

[5] X. H. Zhang, Z. Chen, J. Y. Zhang, P. X. Ding, and J. M. Zhou, "Simulation and optimization of waste heat recovery in sinter cooling process," *Applied Thermal Engineering*, vol. 54, no. 1, pp. 7–15, 2013.

[6] Y. H. Feng, X. X. Zhang, Q. Yu et al., "Experimental and numerical investigations of coke descending behavior in a coke dry quenching cooling shaft," *Applied Thermal Engineering*, vol. 28, no. 11-12, pp. 1485–1490, 2008.

[7] K. Sun, C. Tseng, D. S. Wong et al., "Model predictive control for improving waste heat recovery in coke dry quenching processes," *Energy*, vol. 80, pp. 275–283, 2015.

[8] Y. Liu, J. Yang, J. Wang, Z. L. Cheng, and Q. W. Wang, "Energy and exergy analysis for waste heat cascade utilization in sinter cooling bed," *Energy*, vol. 67, pp. 370–380, 2014.

[9] H. J. Feng, L. G. Chen, X. Liu, Z. H. Xie, and F. R. Sun, "Constructal optimization of a sinter cooling process based on exergy output maximization," *Applied Thermal Engineering*, vol. 96, pp. 161–166, 2016.

[10] X. Shen, L. G. Chen, S. J. Xia, and F. R. Sun, "Numerical simulation and analyses for sinter cooling process with convective and radiative heat transfer," *International Journal of Energy and Environment*, vol. 7, no. 4, pp. 303–316, 2016.

[11] S. Zhang, L. Zhao, J. S. Feng, X. F. Luo, and H. Dong, "Parameter optimization of gas-solid heat transfer process in sinter packed bed based on further exergy analysis," *Chemical Engineering Research and Design*, vol. 146, pp. 499–508, 2019.

[12] J. S. Feng, H. Dong, J. Y. Gao, H. Z. Li, and J. Y. Liu, "Numerical investigation of gas-solid heat transfer process in vertical tank for sinter waste heat recovery," *Applied Thermal Engineering*, vol. 107, pp. 135–143, 2016.

[13] J. S. Feng, S. Zhang, H. Dong, and G. Pei, "Effect of gas inlet parameters on exergy transfer performance of sinter cooling process in vertical moving bed," *Applied Thermal Engineering*, vol. 152, pp. 126–134, 2019.

[14] J. S. Feng, H. Dong, and H. D. Dong, "Modification of Ergun's correlation in vertical tank for sinter waste heat recovery," *Powder Technology*, vol. 280, pp. 89–93, 2015.

[15] J. S. Feng, H. Dong, J. Y. Liu, K. Liang, and J. Y. Gao, "Experimental study of gas flow characteristics in vertical tank for sinter waste heat recovery," *Applied Thermal Engineering*, vol. 91, pp. 73–79, 2015.

[16] F. Y. Tian, L. F. Huang, L. W. Fan, H. L. Qian, and Z. T. Yu, "Wall effects on the pressure drop in packed beds of irregularly shaped sintered ore particles," *Powder Technology*, vol. 301, pp. 1284–1293, 2016.

[17] F. Y. Tian, L. F. Huang, L. W. Fan et al., "Pressure drop in a packed bed with sintered ore particles as applied to sinter coolers with a novel vertically arranged design for waste heat recovery," *Journal of Zhejiang University-Science A (Applied Physics & Engineering)*, vol. 17, no. 2, pp. 89–100, 2016.

[18] F. Y. Tian, L. F. Huang, L. W. Fan, Z. T. Yu, and Y. C. Hu, "Experimental study on pressure drop of packed beds with binary sintered ore particle mixtures," *Journal of Zhejiang University (Engineering Science)*, vol. 50, no. 11, pp. 2077–2086, 2016.

[19] L. S. Pan, X. L. Wei, Y. Peng, X. B. Shi, and H. L. Liu, "Experimental study on convection heat transfer and air drag in sinter layer," *Journal of Central South University*, vol. 22, no. 7, pp. 2841–2848, 2015.

[20] J. S. Feng, S. Zhang, H. Dong, and G. Pei, "Frictional pressure drop characteristics of air flow through sinter bed layer in vertical tank," *Powder Technology*, vol. 344, pp. 177–182, 2019.

[21] Y. Liu, J. Y. Wang, Z. L. Cheng, J. Yang, and Q. W. Wang, "Experimental investigation of fluid flow and heat transfer in a randomly packed bed of sinter particles," *International Journal of Heat and Mass Transfer*, vol. 99, pp. 589–598, 2016.

[22] B. Eisfeld and K. Schnitzlein, "The influence of confining walls on the pressure drop in packed beds," *Chemical Engineering Science*, vol. 56, no. 14, pp. 4321–4329, 2001.

[23] Z. H. Guo, Z. N. Sun, N. Zhang, and M. Ding, "Influence of confining wall on pressure drop and particle-to-fluid heat transfer in packed beds with small D/d ratios under high Reynolds number," *Chemical Engineering Science*, vol. 209, article 115200, 2019.

[24] J. M. Gorman, A. Zheng, and E. M. Sparrow, "Bounding Wall effects on fluid flow and pressure drop through packed beds of spheres," *Chemical Engineering Journal*, vol. 373, pp. 519–530, 2019.

[25] D. Nemec and J. Levec, "Flow through packed bed reactors: 1. Single-phase flow," *Chemical Engineering Science*, vol. 60, no. 24, pp. 6947–6957, 2005.

[26] E. Ozahi, M. Y. Gundogdu, and M. Ö. Carpinlioglu, "A modification on Ergun's correlation for use in cylindrical packed beds with non-spherical particles," *Advanced Powder Technology*, vol. 19, no. 4, pp. 369–381, 2008.

[27] M. Mayerhofer, J. Govaerts, N. Parmentier, H. Jeanmart, and L. Helsen, "Experimental investigation of pressure drop in packed beds of irregular shaped wood particles," *Powder Technology*, vol. 205, no. 1–3, pp. 30–35, 2011.

[28] K. G. Allen, T. W. V. Backström, and D. G. Kröger, "Packed bed pressure drop dependence on particle shape, size distribution, packing arrangement and roughness," *Powder Technology*, vol. 246, pp. 590–600, 2013.

[29] A. Koekemoer and A. Luckos, "Effect of material type and particle size distribution on pressure drop in packed beds of large particles: extending the Ergun equation," *Fuel*, vol. 158, pp. 232–238, 2015.

[30] J. H. Park, M. Lee, K. Moriyama, M. H. Kim, E. Kim, and H. S. Park, "Adequacy of effective diameter in predicting pressure gradients of air flow through packed beds with particle size distribution," *Annals of Nuclear Energy*, vol. 112, pp. 769–778, 2018.

[31] L. X. Li and W. M. Ma, "Experimental characterization of the effective particle diameter of a particulate bed packed with multi-diameter spheres," *Nuclear Engineering and Design*, vol. 241, no. 5, pp. 1736–1745, 2011.

[32] L. W. Rong, K. J. Dong, and A. B. Yu, "Lattice-Boltzmann simulation of fluid flow through packed beds of spheres: effect of particle size distribution," *Chemical Engineering Science*, vol. 116, pp. 508–523, 2014.

[33] M. Li, Y. T. Mu, J. Y. Zhang, and D. J. Xie, "Numerical simulation and optimization of sinter cooler in multilayered burden distribution," *Journal of Central South University (Science and Technology)*, vol. 44, no. 3, pp. 1228–1234, 2013.

[34] W. Y. Tian, J. Y. Zhang, C. D. Dai, X. H. Zhang, and J. P. Wang, "Segregation feeding on sinter circular cooler," *Journal of Central South University (Science and Technology)*, vol. 46, no. 4, pp. 1182–1188, 2015.

[35] J. C. Leong, K. W. Jin, J. S. Shiau, T. M. Jeng, and C. H. Tai, "Effect of sinter layer porosity distribution on flow and temperature fields in a sinter cooler," *International Journal of Minerals, Metallurgy and Materials*, vol. 16, no. 3, pp. 265–272, 2009.

[36] M. J. Keyser, M. Conradie, M. Coertzen, and J. C. Van Dyk, "Effect of coal particle size distribution on packed bed pressure drop and gas flow distribution," *Fuel*, vol. 85, no. 10–11, pp. 1439–1445, 2006.

[37] S. Z. Zhang, Z. Wen, X. L. Liu, X. Liu, S. Wang, and H. Zhang, "Experimental study on the permeability and resistance characteristics in the packed bed with the multi-size irregular particle applied in the sinter vertical waste heat recovery technology," *Powder Technology*, vol. 384, pp. 304–312, 2021.

[38] S. Z. Zhang, Z. Wen, X. L. Liu, H. Zhang, X. H. Liu, and S. Wang, "Effects of particle shape on permeability and resistance coefficients of sinter packed bed," *Journal of Central South University (Science and Technology)*, vol. 52, no. 4, pp. 1066–1075, 2021.

[39] S. Z. Zhang, Z. Wen, X. L. Liu, H. Zhang, S. Wang, and X. H. Liu, "Gas resistance characteristics in vertical tank with irregular sinter for waste heat recovery," *Journal of Central South University (Science and Technology)*, vol. 52, no. 6, pp. 1963–1973, 2021.

[40] J. S. Feng, H. Dong, H. Z. Li, and J. Y. Gao, "Flow resistance characteristics in vertical tank for sinter waste heat recovery," *Journal of Central South University (Science and Technology)*, vol. 48, no. 4, pp. 867–872, 2017.

Hindawi
International Journal of Photoenergy
Volume 2022, Article ID 9536772, 17 pages
https://doi.org/10.1155/2022/9536772

Research Article

A Comparative Thermal Performance Assessment of Various Solar Collectors for Domestic Water Heating

Ali Raza Kalair,[1] Mehdi Seyedmahmoudian,[1] Muhammad Shoaib Saleem,[2,3] Naeem Abas,[2] Shoaib Rauf,[2] and Alex Stojcevski[1]

[1]*School of Software and Electrical Engineering, Swinburne University of Technology, Australia*
[2]*Department of Electrical Engineering, University of Gujrat, Hafiz Hayat Campus, Gujrat, Pakistan*
[3]*Department of Electrical Engineering, University of Management and Technology Lahore, Sialkot Campus, Sialkot, Pakistan*

Correspondence should be addressed to Naeem Abas; naeemkalair@uog.edu.pk

Received 13 November 2021; Revised 8 March 2022; Accepted 3 May 2022; Published 16 June 2022

Academic Editor: Qian Xu

Growing population, depleting fossil fuels, economic expansions, and energy intensive life style demand are resulting in higher energy prices. We use energy as of heat and electricity, which can directly be obtained from sun using thermal collectors and solar cells. Solar thermal systems are gaining attention for water and space heating applications due to green aspects of solar energy. A solar thermal collector is a vital part of solar thermal energy system to absorb radiant energy from the sun. In this study, a solar water heating (SWH) system has been designed and simulated in the TRNSYS ® software using thermal and chemical properties of heat transfer fluids using REFPROP for dwellings located on ±31° latitudes (+31 Lahore in Pakistan and -31° Perth in Australia). We present an efficiency parametric optimization-based model for water and space heating. Simulation results for four types of solar thermal collectors are presented, and performance is analyzed on the basis of output temperature (T_{out}), solar fraction (f), and collector efficiency (η). This study evaluates the comparative performance of evacuated tube collector (ETC), flat-plate collector (FPC), compound parabolic concentrator (CPC), and thermosiphon-driven systems. Our findings conclude the evacuated glass tube collector achieves the highest solar fraction, i.e., 50% of demand coverage during August in Pakistan and February in Australia, with an overall average of 43% annually.

1. Introduction

Energy demand is increasing globally due to population growth, fossil fuel depletion, and energy consumptive life styles [1]. US oil consumption was equal to local oil production in the 1950s, double in the 1980s, and equal again in the 2020s due to shale revolution in the 2000s. Energy shortages in winter, high cost of electricity in summer, depletion of conventional fossil fuels, and their environmental effects are leading the world to shift the focus towards renewable energy resources to empower the people beyond 2050 [2]. More than 72% CO_2 emissions are related to energy and 21-37% to food production processes especially tilling, fertilizers, and cattle [3]. Heat and electricity account for 31% of CO_2 emissions [4]. Rock dust in soil can remove 2 to 4 billion tons of CO_2 annually whereas as solar energy can decarbonize energy sector especially 31% fossil fuels produced heat and electricity. Solar energy can easily be converted to useable forms, either solar thermal energy or solar electrical energy. Renewable energy technologies can easily be used for industrial and domestic applications [5]. Hydrogen systems have also shown promising results to be applied as an alternative fuel for domestic and industrial applications [6, 7]. Solar thermal systems are efficient to transform incident solar radiations into useful thermal energy in 40-120°C temperature range [8]. In the near future, application of intermittent renewable energy resources requires load management, power quality delivered, and increased focus on energy storage systems for backup [9–11].

Solar energy can be easily applied at domestic level to minimize gas and electric energy costs to meet water or space heating demands [12, 13]. A recent study shows

1 MW_e peak load shaving may be attained by installing 1000 solar water heaters each with 100-liter volume [14]. Pakistan has large potential to utilize irradiant solar energy for meeting domestic hot water (DHW) demand, and Australia has high sunshine. Wasting coal and gas-fueled plant electricity in presence of abundant of solar energy is not sustainable way of life. Solar collector is a vital part of all the system designs which utilize solar energy, either photovoltaic (PV) or solar thermal energy [15]. Collectors act as a heat exchanging element and convert available solar insolation radiation into beneficial thermal energy. The collected thermal energy is conveyed to thermal storage tank by heat transfer fluid [16]. Heat transfer fluids may be synthetic yet natural refrigerants like water are more sustainable. Addition of table salt in water may increase heat transfer efficiency. The TRNSYS software is used for design of various types of solar collectors for domestic water heating. Flat-plate collector, evacuated glass tube collector, parabolic trough collector, linear Fresnel reflector, and compound parabolic collector are used for 45 to 400°C whereas point and line type solar collectors such as solar tower and parabolic dish are used for 1000 to 1500°C temperature [17, 18]. Flow control by optimum TRNSYS model may enhance effective efficiency up to 7% or more [19]. TRNSYS home models have demonstrated 37% to 68% solar fractions under diverse weather conditions [20]. Integration of PV-driven electromagnetic heating and phase change material storage increases lifecycle cost by 4 to 23% reducing CO_2 emissions by 13 to 26.73 tons [21]. Storage of summer heat for winter heating and winter chill for summer cooling is emerging as yet a remote reality. Seasonal storage of summer heat holds key to elixir of decarbonozation at district heating level in big cities [22].

Thermal collectors are further classified into flat plate, evacuated tube, and concentrating type of collectors with the flat plate being least efficient, but economic, whereas concentrating collectors are employed only for applications requiring high temperatures. Generally, evacuated tube collectors are employed in most applications due to high efficiency and performance. Photovoltaic collectors branch out into 3 generations of solar cells each having their own pros and cons. Generally, in residential applications, only 1st-generation (mono and polycrystalline) silicon cells are being employed due to maturity and efficiency. Newer generation solar cells such as multijunction cells are efficient but currently used in selected areas as the price tag does not justify their use for residential applications. Furthermore, organic cells are promising technology but currently not highly efficient or reliable due to stability issues. Hybrid collectors and their implementations depend on various factors, and their role is ambiguous; some studies claim higher performance as compared to individual technologies, whereas others claim their findings in the favor of using a combination of individual collectors instead of hybrid single enclosure-based collectors. The performance of solar collectors depends on the selective surface, absorptivity (high), emissivity (low), coverings, spacing, and tilt angles $f + 10^\circ$ or $f + 15^\circ$ for domestic water or space heating and $f - 10^\circ$ or $f - 15^\circ$ for refrigeration/absorption due to dust accumulation on collectors. Solar water heaters usually employ FPC, ETC, or CPC with natural or forced circulation. Space heating, cooling, and refrigeration employ FPC, ETC, or CPC with forced circulation [23]. Mean energy efficiency of ETC varies from 80 to 90% compared to FPC from 50 to 60% in high sun countries [24]. ETC outperforms FTC in colder regions due to low conduction losses. ETC efficiency in cold regions is 30-45% but can achieve temperature as high as 170 to 200°C in hot regions. Application of solar energy for cooling and air-conditioning applications is also getting attention of the researchers [25, 26].

Water heating demand accounts for a significant amount of energy consumption in the world. The percentage of energy demand in the water heating process in a household is approximately 10–30%. As a result, selecting an adequate water heating system can have a significant impact on the increase in energy reserve. Using solar technologies as a result of increased energy demand has gotten significant attention because it is a safe, natural, and cost-free process to roll up hot water with solar energy [27, 28]. The performance analysis of solar thermal systems with various collectors, fluids, and conditions is gaining momentum. In this day and age, solar energy is a vital source of energy supply among all renewable energy resources. As a result, considerable progress is being made in harnessing solar energy through the use of technologies, such as solar collectors. Because of its excellent thermal efficiency and good performance in adverse weather condition especially in subzero temperature areas [29], evacuated tube collectors have received a lot of attention. Recent trends include use of nanofluids [30–33], enhancement of heat pipe performance, use of latent heat storage [34], molten salts [35], heat loss reduction designs/insulations [36], geometric heat pipes [37, 38], flow control and design [19, 39–41], and proposing holistic architectures such as CCHP [42–44]. The existing literature emphasizes on individual detailed energy, exergy, and economic studies but lacks a comparative performance of various technologies. This work presents a much needed parametric performance comparison of various solar collectors. These collectors are studied for a typical dwelling. The main contributions of this paper include optimized parametric values for the highest collector efficiency and solar fraction in the specific ambient conditions. This work advocates the trial of multiple technologies to cater thermal needs of a specific area and provides evidence of how certain technologies might not be a good option in one condition but outperform in all other conditions.

2. Background Literature

Solar water heaters collect solar energy and export this irradiant energy to heat transporting medium to warm the water in a storage tank. These systems are efficient up to 70%, and this value is quite higher than the efficiency of PV-based systems, which is around 17% only. Passive and active are two basic categories of water heating system based on their working mechanism. Active systems circulate HTF using a pump, whereas passive systems circulate HTF via gravity forces. A survey presenting working, efficiency, and

arrangements of evacuated tube-based collector is presented in [45]. Al-Joboory compared the enhancement performance of evacuated tube solar water heater systems in multiple configurations [46]. The study employed two identical solar water heaters with 120-liter capacity tanks and methanol as working fluid. One system incorporated thermosyphon and the other with heat pipes. The study revealed that heat pipe systems were better in performance by 22.5% (no load), 42.5% (intermittent loading), and 32.4% (continuous loading) conditions. District heating by employing design of a two-supply/one-return triple pipe structure was proposed by Prof. Xu and his team. The simulation analysis unveiled that distance between heating pipes played a key role in determining total heat loss, i.e., reducing spacing from 114.1 mm to 84.1 mm, and total heat loss reduced from 24.13 w/m to 20.16 w/m but also increased heat exchange between water and pipes [47]. Combination of nanofluids as HTF was tested for two-phase closed thermosyphon (TPCT) by Xu et al. [32] experimentally, and results showed hybrid nanofluid (Al_2O_3-TiO_2-H_2O) showed superior performance by increasing thermal efficiency and heat transfer coefficient. Nanofluids can enhance the performance of molten salts when used as heat storage fluids [33]. In heat transportation, storage, and conversion, the underground pipeline laying technique has gained attention recently because of suitability, quick construction, and low building cost. A study showed heat transfer analysis of large diameter L-type heat pipe network using the flow heat solid coupling method in the ANSYS workbench platform [48].

The sun is a gargantuan fusion reactor empowering wood, water, and wind cycles on earth. More than two-third solar energy is absorbed by ocean waters and less than one-third by land mass. Plants use photosynthesis process to run food supply chain system. The sun uses hydrogen fuel which is the most abundant element in universe. Star science inspired energy systems are under intensive research in USA (NIF), Europe (ITER), and China (EAST). Solar energy consists of light, heat, and radiations. The electromagnetic radiations range from X-rays to radio waves. Solar light spectrum ranges from ultraviolet to infrared. Solar energy is available as heat (IR) and light (visible) which we can harvest using solar thermal collectors and solar cells. Solar collectors use refrigerants/fluids to drive steam turbines, water heating systems, and empower refrigeration cycles for cooling. The energy inside solar spectrum is shown in Figure 1.

A solar thermal collector harvests heat by absorbing sunlight in gas or liquid fluids. Solar collectors are used for trigeneration, i.e., heating, cooling, and power generation applications [50]. Flat plate, evacuated tubes, and flat-plate evacuated solar collectors are preferred for water and space heating or cooling applications, whereas parabolic troughs, parabolic dishes, solar chimneys, and power towers are used for power generation [51]. Concentrating solar power (CSP) systems use lenses and mirrors to convert light into heat to drive heat engines or steam turbines. Solar thermal power plants are usually constructed in remote barren hot regions like Mojave Desert, USA. Solar photovoltaic panels and solar thermal collectors may be installed on rooftops for power generation, water heating, and space cooling in high-sun areas. Rooftop solar cells are common but solar thermal collectors are now becoming popular due to rising natural gas prices. Flat-plate and evacuated tube collectors are used to capture solar heat for water and space heating or cooling with absorption chillers. Solar hot water panels need no extra fluids but solar thermal collectors use refrigerants and heat exchangers to transfer heat to reservoir. All solar collectors may be used for water heating, air conditioning, and power plants at homes and industries.

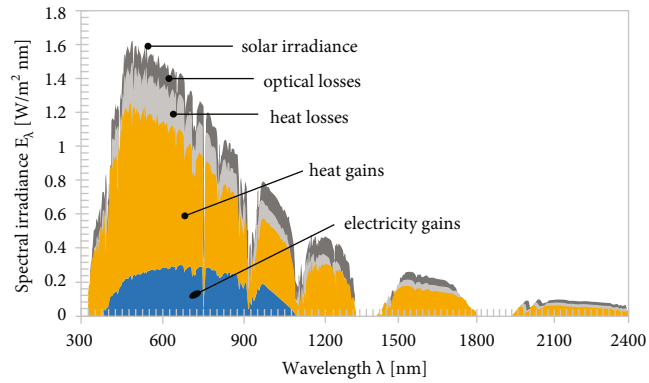

Figure 1: Solar spectrum on PVT collectors (PV 20% and thermal 60%) [49].

2.1. Flat-Plate Collector. A flat-plate collector (FPC) is the most common form of solar thermal technology (80°C). It has insulated glazed absorbing plates that are planted in a casing with an air gap between glazing and plates to trap solar radiation. The cover is made up of sheets of glass. Absorber plates (flay, corrugated, and grooved) are mostly dull and dark (blackened) to absorb maximum radiations. The selective surfaces must be highly shortwave absorbent and transparent to long-wave thermal radiations [52]. Furthermore, the tubes are coated with high absorptive, low emittance layers to exploit maximum radiations. The tubes transfer the heat absorbed to a heat-carrying fluid inside the riser tubes. These riser tubes are connected to main header tubes at both top/bottom ends of the collector or another serpentine tube design. The serpentine tubes are often coupled with a pump as the natural flow is comparatively difficult owing to a complex tube shape. Flat-plate collectors are employed to heat water, refrigerants, air, etc. The collectors have significant life spans but are prone to damage due to extreme climatic conditions like hailing, floods, or thermal expansion that might damage glazing. Generally, copper tubes are the preferred medium of heat transfer owing to good conductivity properties and less prone to corrosion [53]. New polymer-based transparent insulating glazing (TIG) is introduced in literature [54] known as honeycomb collectors. The honeycomb-like structure helps trap air by ceasing rapid circulation, and polymer blocks infrared reradiation thus reducing convectional losses [55].

2.2. Evacuated Tube Collector. Evacuated tube collectors (ETC) employ heat pipes (copper) encapsulated within a vacuum-sealed tube. The ETC can be considered an upgraded form of FPC by creating a vacuum space around

the receiver. The outer tube is transparent, and the inner tube is selectively coated for maximum absorption. Multiple tubes are connected to a common manifold to increase the heat collection area. Fin tubes are used to achieve high temperatures with selective surfaces. Also, evacuated tubes trap more radiations due to vacuum suppression. The design captures both direct and diffused radiations at lower incidence angles as compared to flat-plate collectors. The pipe uses a fluid that undergoes cycles of evaporation/condensation. Volatile liquid/gas is evaporated with radiations and converted into vapors which raised and condensed at sink points releasing its latent energy to another heat transfer fluid at the manifold. Condensed fluid returns due to gravity keeping the circuit alive. The heat transfer fluid through manifold is coupled to a thermal storage tank or directly used via heat exchangers. Temperature ranges from 100 to 130°C. ETCs are the most adopted thermal collectors worldwide with a major 77.8% followed by FPC at 17.9%, unglazed water collectors at 4.1%, and air collectors at 0.2% [56]. The technology is commercially available as shown in Figure 2.

Abas et al. [29] employed supercritical CO_2 as mediating fluid for a solar water heating system and demonstrated a 10% increase in heat transfer efficiency. The thermal performance of ETCs is experimentally investigated by several researchers [57] under identical conditions. These experiments reveal higher efficiency achieved with evacuated collectors compared to other collectors. Nanofluids in heat pipes are getting popular in high population countries like China and India [58, 59]. Water-based CuO was selected as a carrier fluid, and study revealed that the thermal performance of thermosiphon increases by 30% with operating temperature. Li et al. [60] compared heat transfer performance characteristics of nanofluids (ZnO and MgO) in the solar collector and found ZnO as the most suitable option for solar energy utilization. Mahendran et al. [61] proposed a water-titanium oxide nanofluid to increase collector efficiency under clear skies. This study claimed 16.75% increase in efficiency during peak time 2 : 00 pm. A similar study with a slight increase in nanofluid volume concentration (1 to 3%) and modified flow rate claimed an efficiency increase by 42.5%.

2.3. Compound Parabolic Concentrators. Compound parabolic concentrators (CPCs) are nonimaging solar collectors. The CPC collectors use fin type absorbers in the form of flat, bifacial, wedge, or cylindrical configurations. Normally, CPC collectors use fin type absorbers. CPC may be designed with point and line focus and can integrate an inverted or inclined flat-plate absorber by reflecting light on it. Evacuated tube collectors also may be placed at absorber location to get more concentrated light. Line focus CPC collectors are usually preferred for thermal power plants. CPC area concentration ratio depends on acceptance half angle ($C_A = 1/\sin\theta_c$). The CPC collector is not suitable for domestic water heating.

2.4. Evacuated Flat-Plate Collectors (EFPCs). Evacuated flat-plate collectors (EFPCs) combine benefits of both FPC and ETC. An EFPC uses high-vacuum insulation inside and consists of glass and metal materials. EFPCs are most efficient nonconcentrating solar thermal collectors [62]. CERN made the first EFPC and simulation studies show it to be the best solar thermal collectors for air conditioning applications [63]. Solar collectors, due to their outdoor installation, face a wide range of environmental stresses. Apart from windblown objects, the collector materials undergo periodic thermal and humidity stresses. Oxidation of collector material reduces its heat collection efficiency. Silver paint increases reflectivity but soon suffers surface dullness. Mirrors faint over time due to humidity. Our experience shows steel collectors perform better than glass and silver-coated materials. Steel deposits lesser dust on the collector surface that is washed by rains and winds without affecting its overall performance. Evacuated glass tube collectors do not suffer weather wear and tear but easily break during hailing. High windblown objects also strike and break ETC glassware.

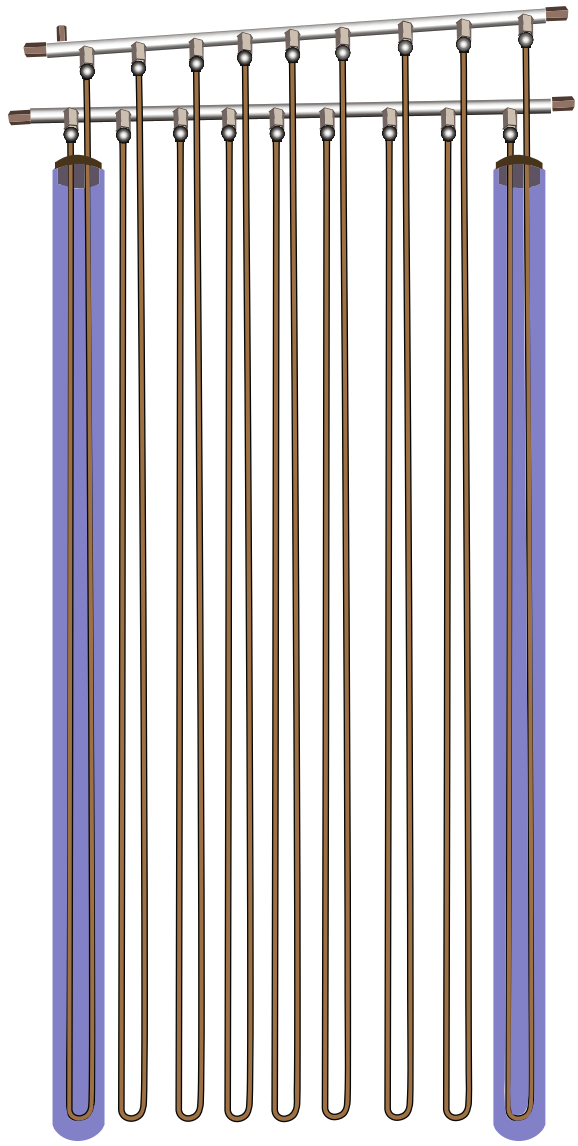

Figure 2: Evacuated glass tube collector with U-shape heat removal tubes.

Solar thermal heat collectors use steel and mirror heliostats. There is an urgent need to research more materials for solar collectors and storage containers. EFPCs are not commonly available in market.

2.5. Synthetic and Natural Refrigerants. During the refrigeration history spread over 160 years, nearly 50 materials had been under use as a heat transport medium. With passaging time, advent of new technologies, and increased environmental concerns, many of them were phased out and reasonable choices remain to be applied depending upon application. Because of the increased risks to the environment, including global warming, ozone depletion, and nuisance emissions, the global community reached at a consensus to stop using ozone damaging immediately and grant a strict time-based permission to replace existing cooling and heating systems with environmentally benign refrigerants. The most recent Paris Accord is a collective effort to limit average global temperature increase below 2°C. [64]. For the achievement of a carbon neutral goal at the earliest, research on replacement of old and development of new refrigerants has got significant attention. Requirement of refrigerants is increasing, and refrigeration technology has become mature and efficient than before. Resurrection of natural refrigerants has open new horizons for the researchers to comply with environmental protection protocols. Every year, 26th June is declared as world refrigeration day to acknowledge remarkable impact to the society made by cooling, air conditioning, and refrigeration technologies [65]. Conventional refrigerants, including chlorofluorocarbons (CFCs) and hydrochlorofluorocarbons (HCFCs), are in use in refrigeration industry for a longer period because of their excellent chemical and heat transfer capabilities. But these fluids are banned after the Montreal Protocol due to damaging effects to the ozone layer and increased global warming. Global protocols mandate nations to work in a unified manner for optimum solutions for existing refrigeration and heating systems [66]. Global Warming Potential (GWP) is a measurement index for the quantity of irradiant energy absorbed by the refrigerant. It is defined as the amount of infrared radiations absorbed by a gas comparative to CO_2 spread over a period of 100 years [67].

In order to replace CFCs and HCFCs, the incumbent refrigerants should have lower flammability and toxicity, smaller atmospheric life span, zero ODP, and ultralow to zero GWP. For thermal and heat transportation systems where refrigerants are applied as mediating fluids, primary parameters for the selection of refrigerant must be GWP and ODP. In addition to CO_2 and NH_3 as purely natural refrigerants, eco-friendly refrigerants R600, R1233zd, R245fa, R410a, and R447a also exhibit great heat transportation outcomes without damaging the environment [68]. Low critical temperature value of 31°C of CO_2 causes transcritical operation and high working pressure. NH3 has a reasonable pressure range, a high critical value of temperature, and higher enthalpy of vaporization. But it is limited due to toxic nature, and extra control mechanism is required for safe operation. [69]. Hydrocarbons occur naturally and possess various properties to be suitable refrigerants being energy efficient, critical point, soluble, and heat transportation. These have sound potential to be used as alternatives CFCs, CFCs, and HCFCs and having nearly zero ODP and relatively lower GWP [70].

3. Comparison of Solar Collector

A solar thermal collector captures heat by absorbing sunshine using synthetic or natural refrigerant. Role of refrigerant is to transfer heat by cooling collector surface. Common water heaters use water and glycol refrigerants. A simple collector may consist of copper spiral on aluminum plate and a working fluid often water. Plate and copper tubes are painted black to capture whole of solar spectrum. Commercial solar collectors may employ control mechanisms to maintain temperature. A solar collector may be concentrating or nonconcentrating type. Absorber area of nonconcentrating solar collector is the same as sunshine capturing area but concentrating solar collector has larger area than the absorber area. Solar air heaters need no refrigerants, and large-scale towers or parabolic collectors are often used in power generation industries. Common residential scale water heating systems employ flat plate [71], evacuated glass tube [72], and evacuated flat-tube collectors [73].

A flat-plate collector is made up of a plate coated with black absorbing medium and pipes to transfer heat at the bottom. A transparent cover is installed at the top and thermally insulated material at the bottom. Black surface absorbs solar energy, and thermal energy is supplied to tank through heat transfer fluid. Efficiency of flat-plate collector lowers in cold, cloudy, and windy environment and further decreases with decay of tubes and the insulation material by weather conditions with the passage of time [74]. Evacuated tube designs among all collector designs have high efficiency due to ability of heat transport in unpleasant weather conditions particularly. These have low cost, simple construction, and easy installation and can be applied for thermal energy requirement ranging from 70 to 120°C [75]. A single evacuated tube is made up of enormously sturdy borosilicate glass material. Outer tube allows radiation to pass through it with high transmission power and low reflectivity. Absorption of radiant heat from sun is increased by applying a layer of selective coating material on the inner tube which also decreases the reflection [29]. Compound parabolic concentrator is constructed like two meeting parabolic reflectors having application where temperature demand is over 100°C [76]. These can collect nondirect radiation using less amount of material in the manufacturing of reflector, and reflectance is increased two-third times [77]. CPC can collect radiation received with large angular spread and then concentrate it on to linear receivers of lesser transverse width. Thermosiphon SWHs have wide application for water heating. These systems work on natural water circulation principle also called thermosiphon effect. A density difference is produced by variations in temperature making the warm water to rise up and the cold water to flow down [78].

This research is intended to perform a comparative analysis of different types of collectors to analyze efficiency to select the best type collector for domestic hot water usage

with higher energy conversion capability. Four types of typical selected collector models evacuated glass tube (type 71), flat plate (type 73), compound parabolic concentrator (type 74) and thermosiphon heating loop system (type 45a) are considered.

4. Thermal Energy Storage

Thermal energy storage be it heat or cold-based employs a heat transfer fluid (HTF) and a medium to store heat to or extract heat from. In some cases, the same HTF can also be employed as a medium. The basic goal of TES is to maintain the temperature of the medium temporarily to be used later. Any increase or decrease of temperature in cold or heat storage results in lower exergy. Exergy in layman terms is the net capability of doing work. If heat storage which is required to maintain heat for a specific purpose loses heat exergy reduces as the system must be supplied the heat that is lost, similarly cold storage in which temperature increases, further electric or other cooling techniques have to be employed to drop back to the desired temperature. The energy storage efficiency of a conventional two-tank system is higher but is not economical as one tank remains empty. Thermocline tanks have replaced two-tank systems with tradeoffs of such as lowered stratification due to water mixing in the same containment. Convective heat transfer between a moving fluid and solid medium is proportional to the heat transfer coefficient, area between fluid, and medium.

$$\dot{Q} = Ah\left(T_f - T_s\right). \tag{1}$$

It is an efficient storage technology that stores heating/cooling in some medium from which it can be extracted later. The stored energy can be passed through a ranking cycle to produce electricity, can be employed in thermoelectric effect, or used directly as hydronic heating. It is usually integrated into distributed generation to promote renewable energy penetration but can be employed as a standalone system in local residential applications as well. This storage technology is capable of shifting peak energy demand and is believed to play a significant role in future demand response protocols [79]. It is also believed that TESS systems can aid in supply/demand mismatch [80]. TESS systems are the ideal candidates for domestic/residential hot water (DHW/RHW) applications, hot water coupled refrigeration systems, space heating, and cooling. The major challenge to be addressed is to prolong the storage duration in these technologies [79] with better insulations, increasing thermal efficiency, promoting passive heating/cooling, and modified architectures. Large-scale projects employ molten salt as storage medium but residential setups use water and directly use it for mentioned purposes. Large-scale projects employ concentrating solar panels (CSP) whereas residential applications employ evacuated glass tube-based solar thermal collectors (STCs) [81]. TESS systems are further classified into three types sensible energy storage (SES), latent heat storage (LHS), and thermochemical storage. The grid-connected capacity of thermal systems is dominated by molten salt thermal storage (MSTS) at 88.11%, followed by chilled water thermal storage (CWTS) at 5.1%, heat thermal storage (HTS) at 4.2%, and ice thermal storage (ITS) at 2.59% [82]. Comparison of solar thermal energy storage with rest of developed alternative technologies is shown in Figure 3.

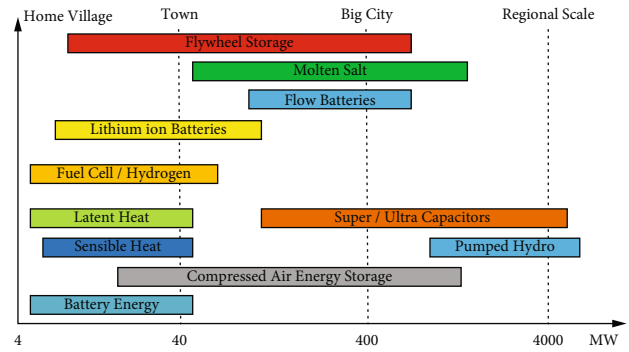

Figure 3: Energy storage technology capacity and preferred installation areas.

4.1. Sensible Heat Storage. Store heat without phase change by heating/cooling a material/medium depending on its heat capacity and thermal diffusivity [83]. The material can be solid (rockbed), liquid (water), or gas (carbon dioxide), and mode of heat transfer can be radiative, convective, and conductive. Sensible heat storage systems (SHS) are believed to be the most appropriate option (70-90% efficient) for storing solar heat. The process is reversible with have high life cycle, no environmental concerns, and residential/commercial deployable technology. The most common residential application includes solar water heater (40 to 80°C) with insulated storage tanks [84] as passive heating as shown in the figure. The water is heated by solar infrared radiations, and through thermosiphon action, it starts circulating to storage or/and heat exchangers. Such setups are coupled with pipes to realize hydronic heating in built environments.

$$Q = \int_{T_i}^{Tf} mC_p dT = mC_\rho C T_f - T_i \Big), \tag{2}$$

where Q accounts for heat stored is equivalent to product of mass of medium and heat capacity integrated over the difference between initial and final times. Other than the residential water thermal storage, there are more types of thermal storage underground thermal storage, molten salt storage, and aquifer thermal storage (ATS). The most notable sensible heat storage installation is near London, the UK, which consists of three 8 boilers and two $2\,\mathrm{MW_{th}}$ CHP with storage with a capacity of $2500\,\mathrm{m^3}$ water providing hot water services to some 3256 residential buildings, 50 commercial buildings, and 3 schools [85]. Rockbed storage systems have low energy density compared to water, thus requires large areas (three times) to accommodate the same amount of heat. A pilot project is presented which was $300\,\mathrm{m^3}$ pebble beds which stored surplus heat from solar collectors during the day to provide hot water and heating services at night [84, 86].

4.2. Stratified Thermal Water Storage. Sensible storages make use of raising/dropping temperature to increase heat storage in a particular medium. The medium solid/liquid/gas should be selected on the basis of high specific heat (c) and high density such that maximum heat is accumulated per volume: water (R718) bearing specific heat (4.2 J/kg.C) and heat content per volume (4.2 MJ/m^{3}K) satisfying both requirements and is potentially harmless. Water-based sensible storage ranges from 0°C to 100°C. Generally employed storage tanks are made up of stainless steel, concrete, plastic, watertight encapsulations preferably with lower heat loss and lower thermal conductivity. Baffle plates are often employed to reflect and trap a certain amount of heat loss. An ideal fluid must be capable of operating at high temperature and low pressure to transfer heat from source (solar collectors) to sink (stratified storage tank).

Hot water storages are designed with few important characteristics in mind being heat storage capacity, heat loss, heat exchange rate, heat exchange capacity, and temperature gradient stratification. Heat content accumulation can be estimated with the product of heat capacity and temperature swing ($T_{\max} - T_{\min}$). Maximizing heat content accumulation reduces storage size. The basic requirement of thermal energy storage is to employ fluid or material with maximum ($\rho.C_p$). A hot fluid at a temperature (T_H) with flow rate ($\dot{m}$) can deliver heat energy with thermal power ($\dot{Q}_T$). We know that sensible energy storage stores heat by increasing its internal energy by creating temperature difference.

$$\begin{aligned} Q &= mc_p\Delta T, \\ \dot{Q}_T &= \dot{m}.C_f(T_H - T_L), \\ (T_2 - T_1).\sum_{i=1}^{n}(M_i.C_{po}) &= (T_2 - T_1).\sum_{i=1}^{n}(V_i.\rho_i.C_{pi}), \end{aligned} \tag{3}$$

where n is the number of materials, M_i is the mass of material (kg), C_{pi} is the specific heat of material (J/kg.K), and ρ_i is the density of material (kg/m^3). The volume required to store Q can be calculated using mass of the storage medium and density in (Kg.m^3).

$$\begin{aligned} V &= \frac{m}{d} = (m^3)\frac{E}{dc_p\Delta T}, \\ \text{Heating energy stored} &= V.Q, \\ \text{Reduction in electrical load} &= \frac{\text{heating energy stored} * \text{peak hour shift}}{3.6}, \\ \text{Annual cost savings} &= (\text{reduction in demand} * \text{demand charges} * \text{CoP}), \\ \text{Payback period} &= \frac{\text{capital investment}}{\text{annual cost savings}}, \end{aligned} \tag{4}$$

The heat exchange capacity and rate should be high both while charging and discharging to attain efficient results.

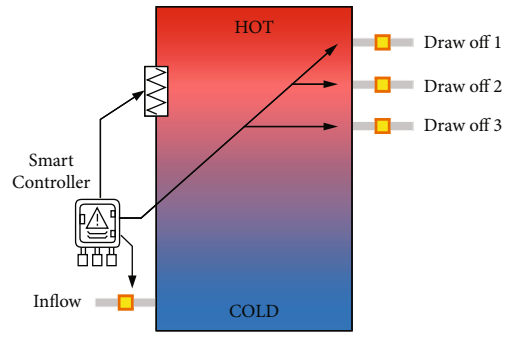

Figure 4: Smart thermal storage tank with auxiliary heater.

Additionally, stratification in both charging/discharging periods improves performance, reduces, or eliminates reliance on auxiliary heating. Collector side temperature should tend to be lower while the extraction side temperature higher comparatively to maintain good stratification. Temperature and pressure influence certain physical properties of fluids. When we increase the temperature of water, its density and viscosity decrease and naturally hot water rises on top of the storage tank. Similarly, the thermal conductivity increases with increased temperature, and stratification is formed quickly. Moreover, it is observed that tall and thin tanks establish and maintain stratification better than bulky and short tanks.

Proper placement of thermal bridges strongly influences the performance of stratified tanks. A thermal bridge applied on the top node hot water side forces the bridge to maintain a higher temperature by causing internal convection from the tank to bridge with higher heat loss at the bridge. The placement of the thermal bridge at the bottom or cold side of the tank forms a cold stagnant layer above the thermal bridge minimizing heat loss. Moreover, rational piping can also improve or deteriorate the performance of the system. Piping installed on the top or sides of hot water stores results in high heat loss through internal circulations, etc. It is suggested to install pipes at the bottom of hot water stores and directed downwards to circumvent/prevent internal circulations. Additionally, heat traps are introduced outside tanks to minimize losses. Furthermore, to avoid thermosyphoning in the pipe loop, it is essential to implement controllable valves that block the piping in the absence of flow [87]. Coldwater inlets need special design attention as to minimize mixing during inflow and draw-offs, and baffle plates are often integrated to reduce mixing losses and improve the overall performance up to 5% [88, 89]. Convective losses from the main storage tank can be captured and accommodated using another sensible storage layer surrounding the main storage with fans and blowers to provide space heating.

The most common form of a storage tank is a steel-based watertight encapsulation for solar domestic hot water (S-DHW) [90]. Geometric rearrangements and modifications in parameters such as height, diameter, length, inlet/outlet positioning, layer thickness, and weight can improve performance up to 20% in certain cases. Research shows that extracting the closest desired temperature from the most appropriate node of stratified varying temperature ranges

Table 1: Insulation materials employed for stratified tanks.

Material types	Composition materials	Thermal conductivity (w.k/m)	Temperature tolerance
Firebrick	Alumina, silica	1	1500 K
Foam glass	Sand, limestone, soda ash	0.05	750 K
Mineral wool	Molten glass, stone, slag	0.5	1000 K
Silica aerogel	Hydrogel siltation	0.01	773 K

improves the performance. Smart storage tanks can satisfy variable draw-offs using rule-based algorithms. Research [88] shows that having multiple draw-off nodes can improve performance by 5%. Moreover, smart tanks are often equipped with auxiliary heating units [91] making use of solar, electric, and gas-based heating in different combinations improving reliability, desirable range of temperatures, and performance improvement up to 25%. A generic illustration of a smart tank is shown in Figure 4.

An ideal thermal storage tank must have no heat losses and be able to draw off the same heat as was stored. But realistically stratified tanks are employed which mix water upon draw-off affecting the temperature of the fluid. Floating controllable insulation baffles are integrated as single stratified tanks to maintain the stored heat and be able to mimic ideal behavior. A tank with height H and vertical coordinate Z form an efficiency equation in which numerator denotes real discharge while denominators denote ideal discharge.

$$\eta = \frac{\int_0^{t_{\text{ref}}} \left[T_{f_{(z=H,t)}} - T_L\right] dt}{(T_H - T_L).t_{\text{ref}}}. \tag{5}$$

For ideal thermal storage ($\eta = 1.0$), the temperature $T_{f_{(z=H,t)}}$ should be maintained to value of T_H which means while charging and discharging the fluid, it maintains its temperature by reducing mixing-based heat losses and other losses. Temperature degradation after draw-off is inevitable due to heat exchange rate between storage medium and fluid. One way if improving efficiency extrinsically is to support systems by using auxiliary heating to preheat the tank to T_H. The other way is to mathematically evaluate and design a comparatively larger system that can accumulate additional heat prior to draw off. Mostly, storage tank is comparatively at a higher temperature than surrounding ambient temperature. This large temperature difference forces heat movement as heat losses. To avoid the losses, insulation has to be provided with materials that have low thermal conductivity (<1 W/m.K) and can sustain high temperatures without degradation of the material layer itself or negatively affecting the efficiency of the process. The prime objective is to minimize losses by regulating temperature. A range of organic (cotton, wool, pulp, cellulose, cane, polymers, fibers, etc.) and inorganic (glass, tock, vermiculite, ceramic, etc.) insulation materials exist. The latest trends include nanostructured aerogels, powdered graphite added to polystyrenes lowering conductivity by 20% [36, 92]. Several commonly employed insulation materials are tabulated in Table 1.

5. Mathematical Modeling

Mathematical equations of output parameters of collectors give outlet heat gain of the respective collector. Collector outlet temperature, storage tank outlet temperature, useful energy gains, and heat produced are monitored and used for the calculation of solar fraction (f) and collector efficiency (η). The thermal performance of ETC array may be estimated by the following [93]:

$$\eta = a_0 - a_1 \frac{(\Delta T)}{I_Y} - a_2 \frac{(\Delta T)^2}{I_Y}. \tag{6}$$

Collector efficiency of a flat-plate collector array is given by the following equation [93]:

$$Q_u = \frac{A}{N_s} \sum_{j=1}^{N_s} F_{R,j}\left(I_T\,(\tau \propto) - U_{L,j}\left(T_{i,j} - T_a\right)\right). \tag{7}$$

Effective reflectance of the compound parabolic concentrating reflector system is defined to be

$$\rho_{\text{eff}} = \frac{I_R}{I_{\text{in}}.\text{CR}}. \tag{8}$$

Temperature of thermosiphon system is investigated by applying Bernoulli's equation and is given by the following equation [93]:

$$T_{CO} = \frac{Q_U}{mC_p} + T_{Ci}. \tag{9}$$

The flow rate at the collector outlet for evacuated, flat plate, and concentric collectors is equal at inlet and outlet valves:

$$\text{md}_{\text{in}} = \text{md}_{\text{out}}. \tag{10}$$

For the calculation of useful energy gain, the following equation is used:

$$Q_u = \text{md} \times C_p \times (T_{\text{out}} - T_{\text{in}}). \tag{11}$$

The energy removal rate from the tank of thermosiphon heating system to supply the load may be given by the following:

$$Q_{\text{load}} = \text{md}_{\text{load}} \times C_p \times \left(T_{\text{top}} - T_{\text{replace}}\right). \tag{12}$$

The rate of energy transfer from the heat source of thermosiphon heating system to the storage tank may be calculated by the following:

$$Q_{\text{in}} = \text{md}_{\text{source}} \times C_p \times (T_{\text{hot}} - T_{\text{source}}). \quad (13)$$

The efficiency of a thermal solar collector is calculated using the Hottel Whillier equation:

$$\eta = \frac{Q_u}{AI_T}, \quad (14)$$

where Q_u is collected heat and I_T is available solar insolation. The solar fraction may be approximated by the following [94]:

$$f = \frac{Q_{\text{load}} - Q_{\text{aux}}}{Q_{\text{aux}}}. \quad (15)$$

Here Q_{load} is the heat produced by collector, and Q_{aux} is the supplementary energy required to meet the DHW demand. A simulation software gives average flow rates for a typical heating and cooling system. Solar water heating and space heating is direct use of solar heat and power in winter. A solar photovoltaic and thermal model was developed for combined water and space heating. Two buildings were selected for water and space heating as shown in Figure 5.

Electric and thermodynamic equations for this model may be written as follows [95]:

$$P_{\text{PV}} = I_{\text{PV}} \times A_{\text{PV}} \times \eta_{\text{PV}}. \quad (16)$$

$W = P \times t$; therefore, $\partial W/\partial t = \dot{W} = P$,

$$\dot{W}_{\text{PV}} = P_{\text{PV}}. \quad (17)$$

Solar thermal [96]

$$P_{ST} = A_T\left[G\eta_o - \alpha(T_m - T_a) - \beta(T_m - T_a)^2\right]. \quad (18)$$

$W = P \times t$; therefore, $\partial W/\partial t = \dot{W} = P_{ST}\,\partial t/\partial t = P_{ST}$,

$$\dot{W}_{ST} = P_{ST}. \quad (19)$$

The mass balance equations ($\dot{m}_{\text{in}} = \dot{m}_{\text{out}}$) for each component of the plant are given by [97]

Solar collector

$$\dot{m}_1 h_1 + \dot{W}_{ST} = \dot{m}_2 h_2. \quad (20)$$

Heat exchanger #1

$$\dot{m}_2 h_2 + \dot{m}_4 h_4 = \dot{m}_5 h_5 + \dot{m}_3 h_3. \quad (21)$$

Heat exchanger #2

$$\dot{m}_3 h_3 + \dot{m}_6 h_6 = \dot{m}_5 h_5 + \dot{m}_9 h_9. \quad (22)$$

Fan-driven air heater

$$\dot{m}_5 h_5 + \dot{m}_8 h_8 + \dot{W}_{PV} = \dot{m}_7 h_7 + \dot{m}_6 h_6. \quad (23)$$

Water tank

$$\dot{m}_9 h_9 = \dot{m}_{10} h_{10}. \quad (24)$$

Water pump

$$\dot{m}_{10} h_{10} + \dot{W}_{\text{PV}} = \dot{m}_1 h_1. \quad (25)$$

6. System Design and Modeling

A solar-assisted water heating system for a typical dwelling house is modeled and simulated in TRNSYS® for the weather of Lahore, Punjab, Pakistan (31.5204° N, 74.3587° E), which also applies to Perth area in Australia. The proposed SWH system comprises an evacuated glass tube solar collector, a fluid filled storage tank with an immersed heat exchanger, and a feed pump to keep heat exchanger fluid flowing in the loop, as shown in Figure 6.

In order to analyze the performance of various types of collectors, it set the initial parameters of the proposed SWH system as a collector area of 5 m^2, optimized flow rate of 3 kg/hr.m^2, and thermal storage tank of volume 0.3 m^3. Water is used as mediating fluid with fluid specific heat 4.19 kJ/kg.K. The hot water inside the thermal storage tank keeps flowing via the load side of the tank. The hot water withdrawing from the water tank passes through an auxiliary heater which warms water at the demanded temperature value for human comfort [98]. During summer in Lahore, ambient temperature is quite high and favorable to harness solar energy for DHW purpose. Hot water usage profile for two to three dwellers of a single family residence was adopted from [99]. Simulations are performed for the metrological data of the whole year (1-8760 hours), and results are presented. Time step for the simulation study is chosen one hour, and the average of monthly values are picked up to represent the output graphs. Parameters selected for system analysis are solar irradiation, collector energy delivery rate, tank energy delivery to load, auxiliary heating rate, collector and tank output temperatures (T_{out}), solar fraction (f), and collector efficiency (η).

7. Results and Discussions

For the analysis of the system designed with optimized parameters, output parameters for the calculation of efficiency and solar fraction are selected. To study the efficiency of the collector and the calculation of solar fraction, temperature at the outlet of the collector, and useful energy gain are measured on the hourly basis. In the thermal loop from storage tank to hot water delivery, temperature at the outlet of the storage tank and energy storage rate are observed. DHW energy requirement, auxiliary heating rate, and solar irradiance are the parameters which are used for the system

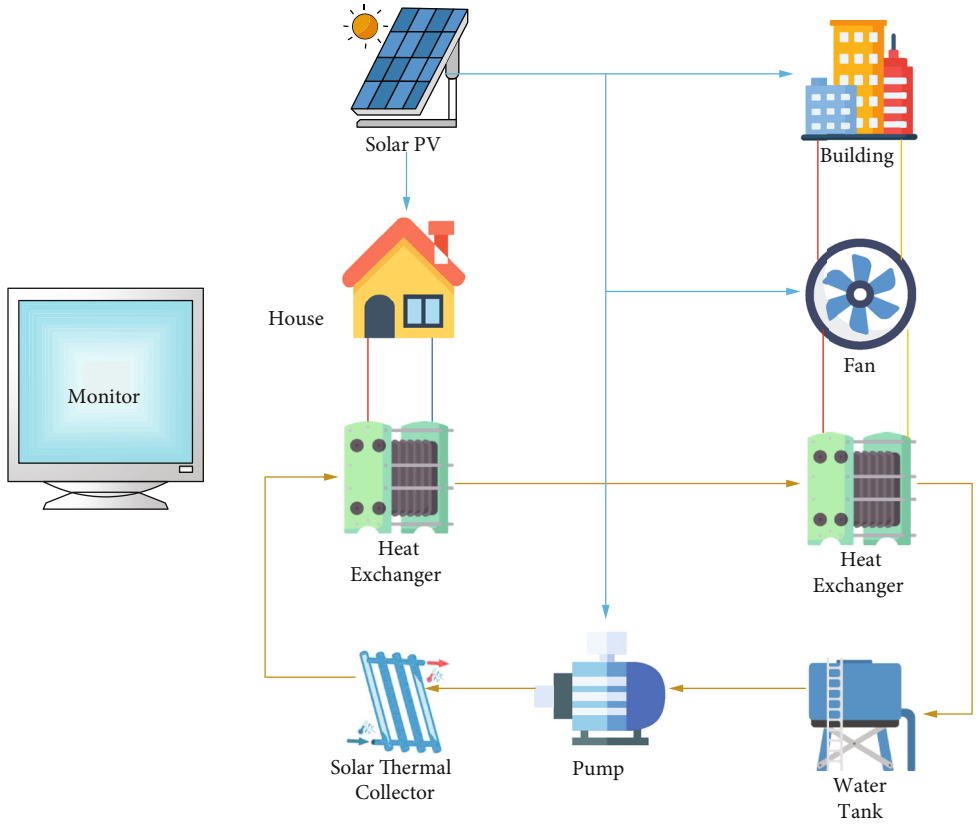

Figure 5: Water and space heating model.

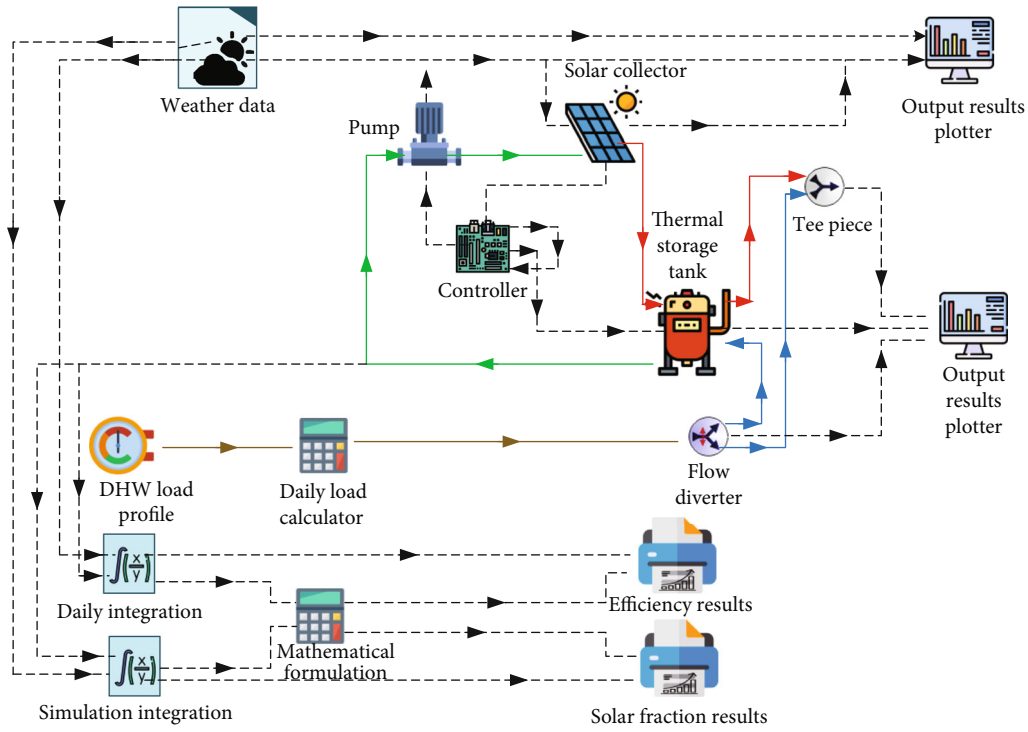

Figure 6: Component diagram of proposed SWH system in TRNSYS.

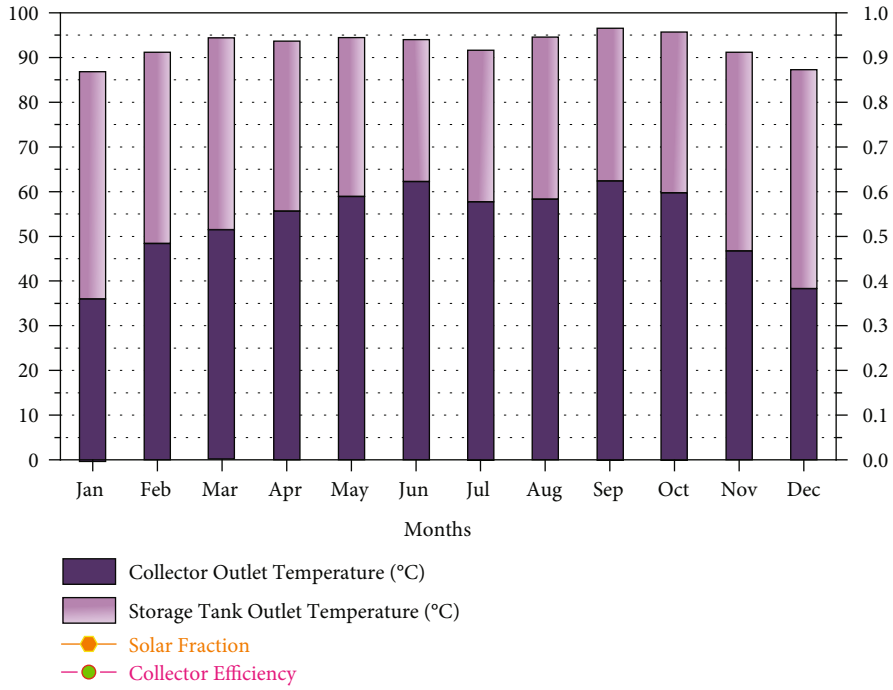

Figure 7: Monthly performance of evacuated glass tube collector.

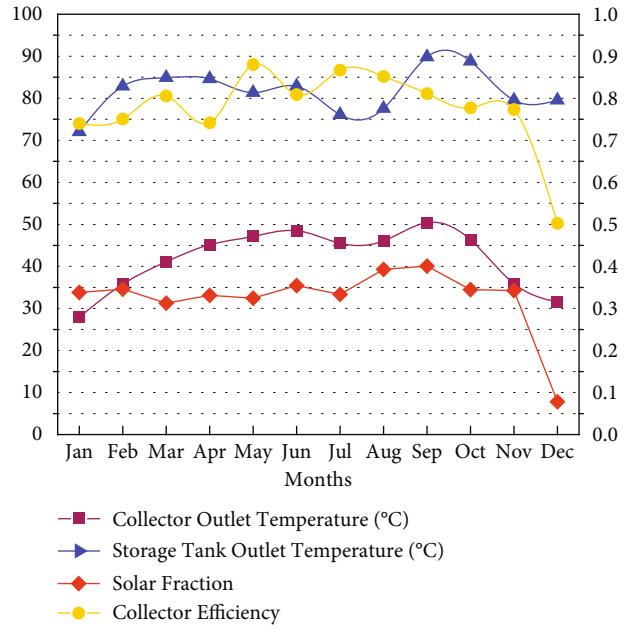

Figure 8: Flat-plate output curves for system efficiency parameters.

performance in the mathematical model explained above. ETC model is employed from standard TESS library type 71 to analyze solar water heater performance under selected weather. Curves of collector and tank outlet temperatures, solar fraction, and collector efficiency for ETC are shown in Figure 7.

A maximum solar fraction value of 0.5 is achieved in August, resulting a collector efficiency of 54%. Average monthly temperatures at the collector outlet are noted from June to September (60-63°C) during peak of summer in Lahore. Tank outlet temperature which is delivered to load is 97°C during this time. It is the temperature of the fluid that flows from the upper half of the stratified storage tank to be delivered to the load. The maximum value of thermal efficiency was observed during month of September during which month wise average of outlet temperatures of the collector and tank attain the maximum values. Significantly lower efficiency is accomplished in the month of December with reduced solar fraction (f) at the value of 0.14 only. Maximum thermal energy delivery was recorded during May to September for water heating loop being the peak summer season having maximum sunshine available.

TRNSYS type 73 module performs a perfect flat-plate collector in simulation environment dynamically. Keeping other parameters as fixed, the type 73 is tested for a year round performance under the same weather to record and compare the results. Figure 8 shows the solar fraction and efficiency reaches a peak value of 0.4 in September, and a good collector efficiency of 88% is observed in May. The maximum value of monthly temperature at collector outlet is recorded 51°C during September. The peak monthly value of fluid temperature that flows towards the outlet node from the tank top was recorded 90°C during this time. System has shown maximum efficiency in the September month for hot water delivery to the residents with the opted parameters.

Various meteorological parameters, including temperature of the ambient, speed of wind, and available solar insolation, may significantly affect the efficiency of the system for year round hot water production.

Parabolic curve model concentrating solar collectors reflects the incident solar radiation on the focal line using surface-coated reflecting materials. Incident solar irradiant

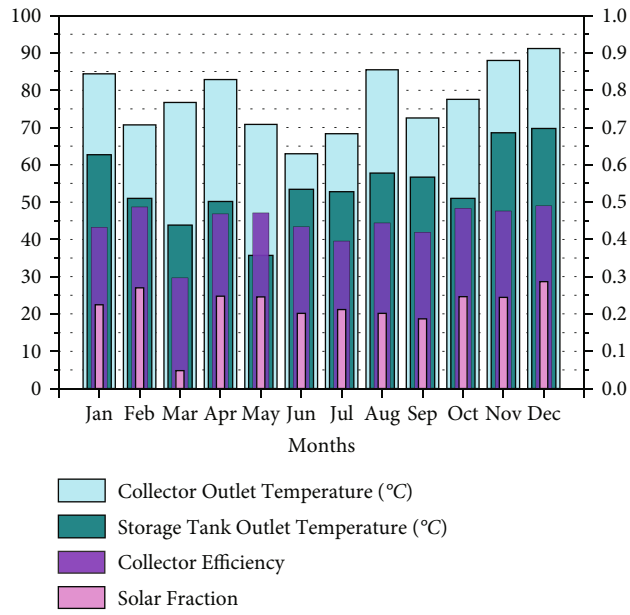

Figure 9: CPC annual performance under Lahore weather.

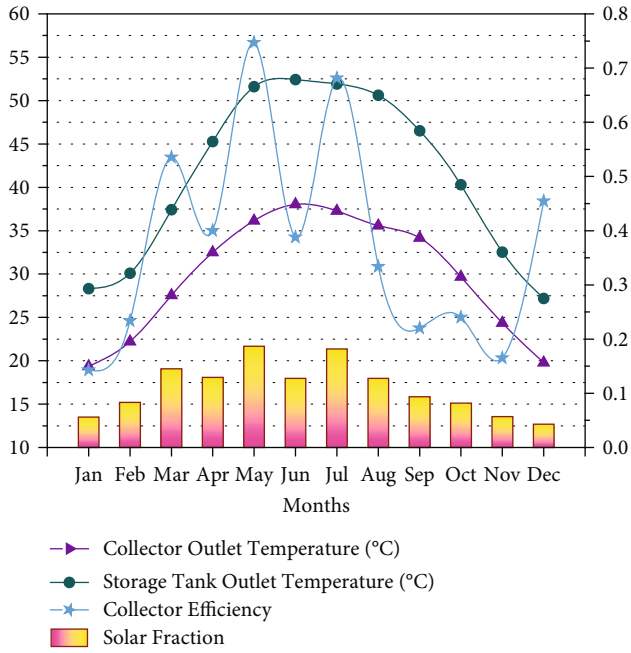

Figure 10: Annual performance of thermosiphon-based SWH system.

energy is concentrated towards the receiver, which raises the temperature of the mediating fluid flowing inside. For achieving maximum efficiency from CPC, it may be installed in a longitudinal plane containing the surface azimuth or in a transverse plane at an angle of 90° from the longitudinal plane. For the analysis of the contracting collector's performance to provide water heating at the domestic level, type 74 module is simulated in TRNSYS simulations. Results of the simulation analysis of CPC collector are shown in Figure 9. The maximum type 74 collector efficiency and solar fractions are noted as 49% and 0.29 during September, respectively. Average monthly temperature at collector outlet is 70°C during September, and the top node temperature of the tank outlet was recorded 91°C. CPC collectors are also used along photovoltaic systems as a hybrid collector, desalination, photo degradation of wastewater, and hydrogen production systems.

Thermosiphon-based system offers more energy efficiency as no need of eternal energy to run the pumps for circulating heat transfer fluid in the loop. Component module type 45a is modeled and simulated in TRNSYS for the analysis of the thermosiphon solar water heating system, and results are presented in Figure 10. Maximum value of collector efficiency and solar fraction are recorded 0.75 and 0.2, respectively, in May, thus exhibiting maximum efficiency of the collector. Maximum monthly temperature at collector outlet is 38°C during June as the peak of summer in Lahore. Tank outlet temperature of the fluid to be provided to load is 52°C during this time.

A comparative graph of solar fraction for all the collector under study is presented in Figure 11. It is observed that the highest value of solar fraction during whole year is attained in case of evacuated glass tube solar collector. This is also validated in literature that evacuated tube-based collectors exhibit greater efficiency on average as compared to flat plate and unglazed collectors [100]. With standard solar radiation available, an EGTC performs 28% more efficiently compared to a flat-plate water heating system [101]. The FPC and CPC stand at second and third number, respectively. Thermosiphon system has shown relatively lower value of solar fraction. Maximum value of f is 0.5 in case of ETC, so 50% of the DWH demand is supplied by the solar collector, and an auxiliary heating unit fulfilled the rest of the demand. These results are in accordance with the collector performance, as reported in literature of previous work.

Solar collector efficiency varies from 45% to 49% with a water-based system, 50% to 53% with nanofluids like Al_2O_3 and 49% to 52% with salty water [102]. Addition of salt in water lowers the freezing point and slightly raises the boiling point. Water heats quickly, yet it has some corrosive actions. Flat-plate collectors show higher efficiency at low temperature and low at higher temperature, whereas conventional evacuated glass tube collectors have moderate efficiencies at all temperatures. [103]. Performance comparison of flat plate and evacuated glass tube is shown in Figure 12.

$$T_i - T_a(^\circ\mathrm{F}). \tag{26}$$

Evacuated glass tubes were 10 to 15% more expensive than flat plate, yet their prices are falling fast. Flat-tube collectors shed ice easily compared to evacuated glass tubes, yet later perform better in rainy winds because of their lower resistance. Earlier studies suggest evacuated glass tube collectors because of their higher efficiency and wider temperature range [104]. Flat-plate collectors heat from 40 to 70°C whereas evacuated glass tubes heat even better.

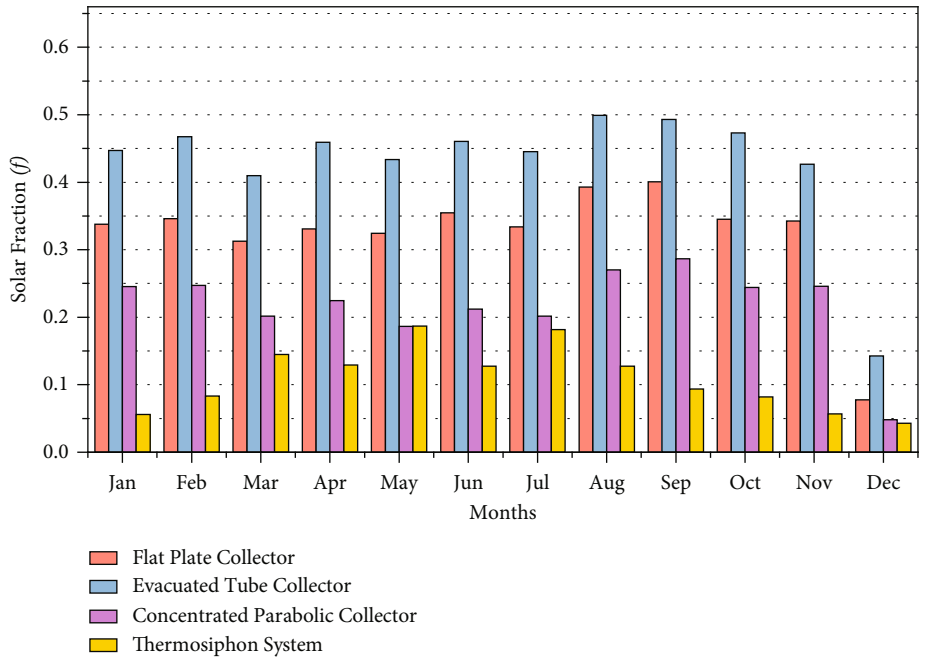

Figure 11: Comparative graph of solar fraction for various collectors.

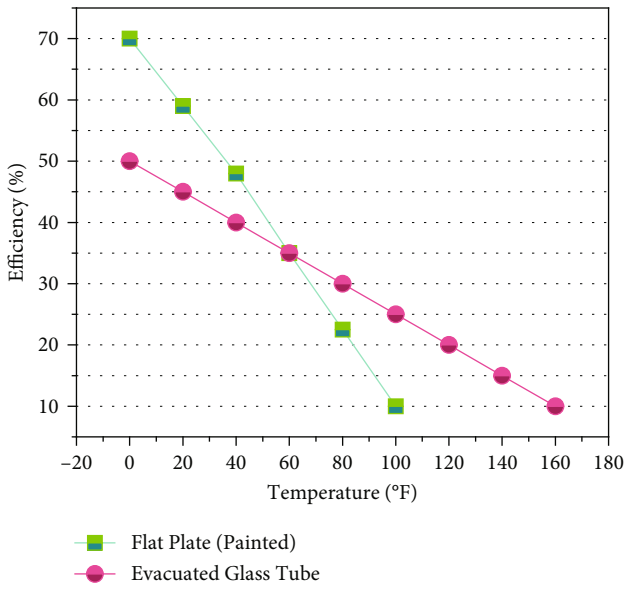

Figure 12: Performance comparison of flat plat and evacuated glass tube.

8. Conclusions

A comparison to evaluate better performance collector from evacuated glass tube, flat plate, compound parabolic concentrating, and thermosiphon is performed on the simulation grounds. A water heating test rig has been designed, modeled, and simulated in the TRNSYS software under weather of Lahore, which are alike Perth, Australia because of similar latitudes. TRNSYS simulation was conducted in Australia, and experiments were performed in Lahore, Pakistan. System performance is studied for parameter solar irradiation, heating requirement, tank energy delivery, and auxiliary heating demand. From these parameters, a mathematical-based model evaluates solar fraction and collector efficiency to fulfill the DHW demand. This TRNSYS simulation study showed a solar fraction of ETC varied from 0.4 to 0.50 peaking to 0.52 in August. The performance of ETC is better than FPC in high sunshine regions, whereas FPC does not function in freezing cold regions. The efficiency at higher temperatures is better for ETC than for FPC. ETC has lower convection and conduction heat losses compared to FPC. ETC temperature range is 60 to 120 degrees compared 60 to 80 degrees by FPC. ETC continues working down to -18°C where FPC freezes and breaks. It is much easier to replace the glass tube compared to expensive repair of the FPC requiring additional heat exchanger. ETC supplies hot water for an average 350 days per year compared to 300 days by FPC. However, the average life of ETC is 11 to 12 years compared to 25 years for FPC. ETC does not require grouting, which is essential for FPC. Results showed that highest solar fraction and collector efficiency values are attained in case of evacuated tube collector compared to flat-tube collector. This system can provide 50% water heating demand for a residential building with two to three occupants. It shows comprising results during the winter season by providing a considerable amount of hot water during the cold season. It is concluded from results that ETC better suits to ±31° latitude metrological conditions worldwide.

Data Availability

Data are available on request.

Conflicts of Interest

The authors declare that they have no conflicts of interest.

Acknowledgments

The author acknowledges Swinburne University of Technology for the Postgraduate Research Scholarship (SUPRA).

References

[1] N. Abas, A. Kalair, and N. Khan, "Review of fossil fuels and future energy technologies," *Futures*, vol. 69, pp. 31–49, 2015.

[2] M. A. Taghikhani, "Renewable resources and storage systems stochastic multi-objective optimal energy scheduling considering load and generation uncertainties," *Journal of Energy Storage*, vol. 43, article 103293, 2021.

[3] C. Mbow and C. Rosenzweig, "Food security," in *Climate Change and Land*, IPCC, 2021.

[4] N. Abas and N. Khan, "Carbon conundrum, climate change, CO2 capture and consumptions," *Journal of CO2 Utilization*, vol. 8, pp. 39–48, 2014.

[5] R. Elarem, T. Alqahtani, S. Mellouli et al., "Numerical study of an evacuated tube solar collector incorporating a Nano-PCM as a latent heat storage system," *Case Studies in Thermal Engineering*, vol. 24, article 100859, 2021.

[6] N. Abas, E. Kalair, A. Kalair, Q. u. Hasan, and N. Khan, "Nature inspired artificial photosynthesis technologies for hydrogen production: barriers and challenges," *International Journal of Hydrogen Energy*, vol. 45, no. 41, pp. 20787–20799, 2020.

[7] M. S. Saleem, N. Abas, A. R. Kalair et al., "Design and optimization of hybrid solar-hydrogen generation system using TRNSYS," *International Journal of Hydrogen Energy*, vol. 45, no. 32, pp. 15814–15830, 2020.

[8] A. Dahash, F. Ochs, M. B. Janetti, and W. Streicher, "Advances in seasonal thermal energy storage for solar district heating applications: a critical review on large-scale hot-water tank and pit thermal energy storage systems," *Applied Energy*, vol. 239, pp. 296–315, 2019.

[9] A. R. Kalair, N. Abas, Q. U. Hasan, M. Seyedmahmoudian, and N. Khan, "Demand side management in hybrid rooftop photovoltaic integrated smart nano grid," *Journal of Cleaner Production*, vol. 258, article 120747, 2020.

[10] N. Abas, S. Dilshad, A. Khalid, M. S. Saleem, and N. Khan, "Power quality improvement using dynamic voltage restorer," *IEEE Access*, vol. 8, pp. 164325–164339, 2020.

[11] A. Kalair, N. Abas, M. S. Saleem, A. R. Kalair, and N. Khan, "Role of energy storage systems in energy transition from fossil fuels to renewables," *Energy Storage*, vol. 8, pp. 1–15, 2021.

[12] M. Irfan, N. Abas, and M. S. Saleem, "Thermal performance analysis of net zero energy home for sub zero temperature areas," *Case Studies in Thermal Engineering*, vol. 12, pp. 789–796, 2018.

[13] L. W. Yang, R. J. Xu, N. Hua et al., "Review of the advances in solar-assisted air source heat pumps for the domestic sector," *Energy Conversion and Management*, vol. 247, article 114710, 2021.

[14] D. Yadav and B. G. Chanchal Sharma, "Study of flat plate solar water heater with force circulating pump," *International Journal of Electrical, Electronics and Data Communication*, vol. 2, no. 7, pp. 1–3, 2014.

[15] C. Mund, S. K. Rathore, and R. K. Sahoo, "A review of solar air collectors about various modifications for performance enhancement," *Solar Energy*, vol. 228, pp. 140–167, 2021.

[16] J. Tarragona, A. L. Pisello, C. Fernández et al., "Analysis of thermal energy storage tanks and PV panels combinations in different buildings controlled through model predictive control," *Energy*, vol. 239, article 122201, 2022.

[17] J. E. Hill and T. Kusuda, *Method of testing for rating solar Collectors Based on Thermal Performance*, , 1986.

[18] A. K. Tiwari, S. Gupta, A. K. Joshi, F. Raval, and M. Sojitra, "TRNSYS simulation of flat plate solar collector based water heating system in Indian climatic condition," *Materials Today: Proceedings*, vol. 46, pp. 5360–5365, 2021.

[19] P. Víg, I. Seres, and P. Vladár, "Improving efficiency of domestic solar thermal systems by a flow control," *Solar Energy*, vol. 230, pp. 779–790, 2021.

[20] C. N. Antoniadis and G. Martinopoulos, "Optimization of a building integrated solar thermal system with seasonal storage using TRNSYS," *Renewable Energy*, vol. 137, pp. 56–66, 2019.

[21] G. Feng, G. Wang, Q. Li, Y. Zhang, and H. Li, "Investigation of a solar heating system assisted by coupling with electromagnetic heating unit and phase change energy storage tank: towards sustainable rural buildings in northern China," *Sustainable Cities and Society*, vol. 80, article 103449, 2022.

[22] M. Yang, Z. Wang, J. Yang, G. Yuan, W. Wang, and W. Shi, "Thermo-economic analysis of solar heating plant with the seasonal thermal storage in Northern China," *Solar Energy*, vol. 232, pp. 212–231, 2022.

[23] L. Evangelisti, R. De Lieto Vollaro, and F. Asdrubali, "Latest advances on solar thermal collectors: a comprehensive review," *Renewable and Sustainable Energy Reviews*, vol. 114, article 109318, 2019.

[24] M. A. Ben Taher, Z. Benseddik, A. Afass, S. Smouh, M. Ahachad, and M. Mahdaoui, "Energy life cycle cost analysis of various solar water heating systems under Middle East and North Africa region," *Case Studies in Thermal Engineering*, vol. 27, article 101262, 2021.

[25] A. R. Kalair, S. Dilshad, N. Abas, M. Seyedmahmoudian, A. Stojcevski, and K. Koh, "Application of business model canvas for solar thermal air conditioners," *Frontiers in Energy Research*, vol. 9, 2021.

[26] A. Rahman, N. Abas, S. Dilshad, and M. S. Saleem, "A case study of thermal analysis of a solar assisted absorption air-conditioning system using R-410A for domestic applications," *Case Studies in Thermal Engineering*, vol. 26, article 101008, 2021.

[27] M. B. J. Bracamonte, J. Parada, J. Dimas, and M. Baritto, "Effect of the collector tilt angle on thermal efficiency and stratification of passive water in glass evacuated tube solar water heater," *Applied Energy*, vol. 155, pp. 648–659, 2015.

[28] M. S. Hossain, R. Saidur, H. Fayaz et al., "Review on solar water heater collector and thermal energy performance of circulating pipe," *Renewable and Sustainable Energy Reviews*, vol. 15, no. 8, pp. 3801–3812, 2011.

[29] N. Abas, A. R. Kalair, M. Seyedmahmoudian, M. Naqvi, P. E. Campana, and N. Khan, "Dynamic simulation of solar water heating system using supercritical CO2 as mediating fluid

under sub-zero temperature conditions," *Applied Thermal Engineering*, vol. 161, article 114152, 2019.

[30] A. N. Al-Shamani, M. H. Yazdi, M. A. Alghoul et al., "Nanofluids for improved efficiency in cooling solar collectors - a review," *Renewable and Sustainable Energy Reviews*, vol. 38, pp. 348–367, 2014.

[31] L. Lu, Z. H. Liu, and H. S. Xiao, "Thermal performance of an open thermosyphon using nanofluids for high-temperature evacuated tubular solar collectors. Part 1: indoor experiment," *Solar Energy*, vol. 85, no. 2, pp. 379–387, 2011.

[32] Q. Xu, L. Liu, J. Feng et al., "International Journal of Heat and Mass Transfer A comparative investigation on the effect of different nanofluids on the thermal performance of two-phase closed thermosyphon," *International Journal of Heat and Mass Transfer*, vol. 149, article 119189, 2020.

[33] Y. Xiong, M. Sun, Y. Wu et al., "Effects of synthesis methods on thermal performance of nitrate salt nanofluids for concentrating solar power," *Energy & Fuels*, vol. 34, no. 9, pp. 11606–11619, 2020.

[34] A. Sharma and R. Chauhan, "Integrated and separate collector storage type low-temperature solar water heating systems with latent heat storage: a review," *Sustainable Energy Technologies and Assessments*, vol. 51, article 101935, 2022.

[35] J. Wang, X. Xie, Y. Lu, B. Liu, and X. Li, "Thermodynamic performance analysis and comparison of a combined cooling heating and power system integrated with two types of thermal energy storage," *Applied Energy*, vol. 219, pp. 114–122, 2018.

[36] P.-W. Li and C. L. Chan, "Thermal insulation of thermal storage containers," in *Thermal Energy Storage Analyses and Designs*, Elsevier, 2017.

[37] R. Senthil, R. M. Elavarasan, R. Pugazhendhi et al., "A holistic review on the integration of heat pipes in solar thermal and photovoltaic systems," *Solar Energy*, vol. 227, pp. 577–605, 2021.

[38] Y. M. Hung, "Effects of geometric design on thermal performance of star-groove micro-heat pipes," *International Journal of Heat and Mass Transfer*, vol. 54, no. 5–6, pp. 1198–1209, 2011.

[39] S. Furbo and L. J. Shah, "How mixing during hot water draw-offs influence the thermal performance of small solar domestic hot water systems," in *Proceedings of the Solar World Congress 2005: Bringing Water to the World, Including Proceedings of 34th ASES Annual Conference and Proceedings of 30th National Passive Solar Conference*, Orlando, Florida, USA, 2005.

[40] G. Ye, L. Ma, F. Alberini, Q. Xu, G. Huang, and Y. Yu, "Numerical studies of the effects of design parameters on flow fields in spiral concentrators," *International Journal of Coal Preparation and Utilization*, vol. 42, no. 1, pp. 67–81, 2022.

[41] E. Saloux and J. A. Candanedo, "Modelling stratified thermal energy storage tanks using an advanced flowrate distribution of the received flow," *Applied Energy*, vol. 241, pp. 34–45, 2019.

[42] J. Wang, Y. Chen, N. Lior, and W. Li, "Energy, exergy and environmental analysis of a hybrid combined cooling heating and power system integrated with compound parabolic concentrated-photovoltaic thermal solar collectors," *Energy*, vol. 185, pp. 463–476, 2019.

[43] E. Gholamian, P. Hanafizadeh, P. Ahmadi, and L. Mazzarella, "A transient optimization and techno-economic assessment of a building integrated combined cooling, heating and power system in Tehran," *Energy Conversion and Management*, vol. 217, p. 112962, 2020.

[44] Q. Xu, L. Li, X. Chen, Y. Huang, K. Luan, and B. Yang, "Optimal economic dispatch of combined cooling, heating and power-type multimicrogrids considering interaction power among microgrids," *IET Smart Grid*, vol. 2, no. 3, pp. 391–398, 2019.

[45] S. M. Tabarhoseini, M. Sheikholeslami, and Z. Said, "Recent advances on the evacuated tube solar collector scrutinizing latest innovations in thermal performance improvement involving economic and environmental analysis," *Solar Energy Materials & Solar Cells*, vol. 241, article 111733, 2022.

[46] H. N. S. Al-Joboory, "Comparative experimental investigation of two evacuated tube solar water heaters of different configurations for domestic application of Baghdad- Iraq," *Energy and Buildings*, vol. 203, article 109437, 2019.

[47] Q. Xu, K. Wang, Z. Zou et al., "A new type of two-supply, one-return, triple pipe-structured heat loss model based on a low temperature district heating system heating system," *Energy*, vol. 218, article 119569, 2021.

[48] Q. Xu and J.-X. Feng, "Effects of different loads on structure deformation of 'L'-type large-diameter buried pipe network based on flow-heat-solid coupling," *Heat Transfer—Asian Research*, vol. 46, no. 8, pp. 1327–1341, 2017.

[49] M.-J. Li, *Utilization of solar spectrum of a PVT collector*, Wikipedia, 2020, https://commons.wikimedia.org/wiki/File:Utilization_of_solar_spectrum_of_a_PVT_collector.svg.

[50] A. Raza Kalair, N. Abas, M. Seyedmahmoudian, A. Stojcevski, and S. Dilshad, "Performance assessment of solar water heating system using CO2 under various climate conditions," *Energy Conversion and Management*, vol. 236, p. 114061, 2021.

[51] B. Norton, *Harnessing Solar Heat*, vol. 18, Springer Netherlands, Dordrecht, 2014.

[52] S. A. Kalogirou, *Solar Energy Engineering: Processes and Systems*, Academic Press, Inc., 2nd ed. edition, 2013.

[53] S. A. Kalogirou, "Nontracking solar collection technologies for solar heating and cooling systems," in *Advances in Solar Heating and Cooling*, pp. 63–80, Elsevier, 2016.

[54] D. Brandl, T. Mach, and C. Hochenauer, "Analysis of the transient thermal behaviour of a solar honeycomb (SHC) façade element with and without integrated PV cells," *Solar Energy*, vol. 123, pp. 1–16, 2016.

[55] M. J. Muhammad, I. A. Muhammad, N. A. Che Sidik, and M. N. A. W. Muhammad Yazid, "Thermal performance enhancement of flat-plate and evacuated tube solar collectors using nanofluid: a review," *International Communications in Heat and Mass Transfer*, vol. 76, pp. 6–15, 2016.

[56] D. Mugnier, "Feature article on PVT systems and collectors, 2020 Annual report," 2020.

[57] E. Zambolin and D. Del Col, "Experimental analysis of thermal performance of flat plate and evacuated tube solar collectors in stationary standard and daily conditions," *Solar Energy*, vol. 84, no. 8, pp. 1382–1396, 2010.

[58] L. Lu, Z.-H. Liu, and H.-S. Xiao, "Thermal performance of an open thermosyphon using nanofluids for high-temperature evacuated tubular solar collectors," *Solar Energy*, vol. 85, no. 2, pp. 379–387, 2011.

[59] M. Mahendran, G. C. Lee, K. V. Sharma, and A. Shahrani, "Performance of evacuated tube solar collector using water-based titanium oxide nanofluid," *Journal of Mechanical Engineering Science*, vol. 3, pp. 301–310, 2012.

[60] Y. Li, H. Q. Xie, W. Yu, and J. Li, "Investigation on heat transfer performances of nanofluids in solar collector," *Materials Science Forum*, vol. 694, pp. 33–36, 2011.

[61] M. Mahendran, T. Z. S. Ali, A. Shahrani, and R. A. Bakar, "The efficiency enhancement on the direct flow evacuated tube solar collector using water-based titanium oxide nanofluids," *Applied Mechanics and Materials*, vol. 465-466, pp. 308–315, 2013.

[62] C. Benvenuti, "The SRB solar thermal panel," *Europhysics News*, vol. 44, no. 3, pp. 16–18, 2013.

[63] A. Buonomano, F. Calise, M. D. d'Accadia et al., "Experimental analysis and dynamic simulation of a novel high-temperature solar cooling system," *Energy Conversion and Management*, vol. 109, pp. 19–39, 2016.

[64] T. L. Cherry, S. Kallbekken, H. Sælen, and S. Aakre, "Can the Paris Agreement deliver ambitious climate cooperation? An experimental investigation of the effectiveness of pledge-and-review and targeting short-lived climate pollutants," *Environmental Science & Policy*, vol. 123, pp. 35–43, 2021.

[65] J. Curlin, *World refrigeration day*, UNEP Ozone Action, 2022.

[66] L. Vaitkus and V. Dagilis, "Analysis of alternatives to high GWP refrigerants for eutectic refrigerating systems," *International Journal of Refrigeration*, vol. 76, pp. 160–169, 2017.

[67] B. O. Bolaji and Z. Huan, "Ozone depletion and global warming: case for the use of natural refrigerant – a review," *Renewable and Sustainable Energy Reviews*, vol. 18, pp. 49–54, 2013.

[68] H. Lv, H. Ma, N. Mao, and T. He, "Boiling heat transfer mechanism of environmental-friendly refrigerants: a review," *International Journal of Refrigeration*, vol. 133, pp. 214–225, 2022.

[69] W. Wu, H. M. Skye, and L. Lin, "Progress in ground-source heat pumps using natural refrigerants," *International Journal of Refrigeration*, vol. 92, pp. 70–85, 2018.

[70] M. Fatouh and M. El Kafafy, "Assessment of propane/commercial butane mixtures as possible alternatives to R134a in domestic refrigerators," *International Conference on Aerospace Sciences and Aviation Technology*, vol. 11, 2011.

[71] M. Sheikholeslami, S. A. Farshad, Z. Ebrahimpour, and Z. Said, "Recent progress on flat plate solar collectors and photovoltaic systems in the presence of nanofluid: a review," *Journal of Cleaner Production*, vol. 293, article 126119, 2021.

[72] A. K. Singh, "A review study of solar desalting units with evacuated tube collectors," *Journal of Cleaner Production*, vol. 279, article 123542, 2021.

[73] J. Fredriksson, M. Eickhoff, L. Giese, and M. Herzog, "A comparison and evaluation of innovative parabolic trough collector concepts for large-scale application," *Solar Energy*, vol. 215, pp. 266–310, 2021.

[74] V. Belessiotis, S. Kalogirou, and E. Delyannis, "Indirect solar desalination (MSF, MED, MVC, TVC)," in *Thermal Solar Desalination*, pp. 283–326, Elsevier, 2016.

[75] J. Gong, Z. Jiang, X. Luo, B. Du, J. Wang, and P. D. Lund, "Straight-through all-glass evacuated tube solar collector for low and medium temperature applications," *Solar Energy*, vol. 201, pp. 935–943, 2020.

[76] A. H. Jaaz, H. A. Hasan, K. Sopian, Haji Ruslan, M. H. B. H. Ruslan, and S. H. Zaidi, "Design and development of compound parabolic concentrating for photovoltaic solar collector: review," *Renewable and Sustainable Energy Reviews*, vol. 76, pp. 1108–1121, 2017.

[77] D. P. Grimmer, "A comparison of compound parabolic and simple parabolic concentrating solar collectors," *Solar Energy*, vol. 22, no. 1, pp. 21–25, 1979.

[78] M. Eltaweel and A. A. Abdel-Rehim, "Energy and exergy analysis of a thermosiphon and forced-circulation flat-plate solar collector using MWCNT/water nanofluid," *Case Studies in Thermal Engineering*, vol. 14, article 100416, 2019.

[79] T. Kousksou, P. Bruel, A. Jamil, T. El Rhafiki, and Y. Zeraouli, "Energy storage: applications and challenges," *Solar Energy Materials & Solar Cells*, vol. 120, pp. 59–80, 2014.

[80] I. Dincer, *Thermal Energy Storage: Systems and Applications*, Wiley, 2011.

[81] Z. Abdin and K. R. Khalilpour, "Single and polystorage technologies for renewable-based hybrid energy systems," in *Polygeneration with Polystorage for Chemical and Energy Hubs*, pp. 77–131, Elsevier, 2019.

[82] N. Khan, S. Dilshad, R. Khalid, A. R. Kalair, and N. Abas, "Review of energy storage and transportation of energy," *Energy Storage*, vol. 1, no. 3, p. e49, 2019.

[83] S. Kuravi, J. Trahan, D. Y. Goswami, M. M. Rahman, and E. K. Stefanakos, "Thermal energy storage technologies and systems for concentrating solar power plants," *Progress in Energy and Combustion Science*, vol. 39, no. 4, pp. 285–319, 2013.

[84] J. Xu, R. Z. Wang, and Y. Li, "A review of available technologies for seasonal thermal energy storage,," *Solar Energy*, vol. 103, pp. 610–638, 2014.

[85] D. Charles, "Stimulus gives DOE billions for carbon-capture projects," *Science*, vol. 323, no. 5918, pp. 1158–1158, 2009.

[86] D. L. Zhao, Y. Li, Y. J. Dai, and R. Z. Wang, "Optimal study of a solar air heating system with pebble bed energy storage," *Energy Conversion and Management*, vol. 52, no. 6, pp. 2392–2400, 2011.

[87] S. Furbo, "Using water for heat storage in thermal energy storage (TES) systems," in *Advances in Thermal Energy Storage Systems*, pp. 31–47, Elsevier, 2015.

[88] U. Jordan and S. Furbo, "Thermal stratification in small solar domestic storage tanks caused by draw-offs," *Solar Energy*, vol. 78, no. 2, pp. 291–300, 2005.

[89] L. J. Shah and S. Furbo, "Entrance effects in solar storage tanks," *Solar Energy*, vol. 75, no. 4, pp. 337–348, 2003.

[90] S. Furbo, *Optimum design of small DHW low flow solar heating systems*, Solar World Congress Proceedings, 1993.

[91] S. Furbo, E. Andersen, A. Thür, L. Jivan Shah, and K. Dyhr Andersen, "Performance improvement by discharge from different levels in solar storage tanks," *Solar Energy*, vol. 79, no. 5, pp. 431–439, 2005.

[92] D. Bozsaky, "Application of nanotechnology based thermal insulation materials in building construction," *Acta Technica Jaurinensis*, vol. 9, no. 1, p. 29, 2016.

[93] Transient System Simulation Tool, *User Manual: TRNSYS 17 a TRaN Sient SYstem Simulation Program*, 2009.

[94] S. A. Klein, W. A. Beckman, and J. A. Duffie, "A design procedure for solar water heating systems," *Solar Energy*, vol. 18, pp. 113–127, 1976.

[95] M. Ozturk and I. Dincer, "An integrated system for ammonia production from renewable hydrogen: a case study," *International Journal of Hydrogen Energy*, vol. 46, no. 8, pp. 5918–5925, 2021.

[96] G. Lorenzini, C. Biserni, and G. Flacco, *Solar Thermal and Biomass Energy*, Wit Press, 2010.

[97] K. Sa, *F-Chart Software*, EES, Engineering equation solver, 2013.

[98] M. S. Saleem, A. Haider, and N. Abas, "Review of solar thermal water heater simulations using TRNSYS," in *2015 Power Generation System and Renewable Energy Technologies (PGSRET)*, IEEE, 2015.

[99] H. E. Babbitt, *Plumbing*, Mcgraw-Hill, 3rd ed. edition, 1960.

[100] N. Abas, N. Khan, A. Haider, and M. S. Saleem, "A thermosyphon solar water heating system for sub zero temperature areas," *Cold Regions Science and Technology*, vol. 143, pp. 81–92, 2017.

[101] D. A. G. Redpath, S. N. G. Lo, and P. C. Eames, "Experimental investigation and optimisation study of a direct thermosyphon heat-pipe evacuated tube solar water heater subjected to a northern maritime climate," *International Journal of Ambient Energy*, vol. 31, no. 2, pp. 91–100, 2010.

[102] P. Visconti, P. Primiceri, P. Costantini, G. Colangelo, and G. Cavalera, "Measurement and control system for thermosolar plant and performance comparison between traditional and nanofluid solar thermal collectors," *International Journal of Smart Sensing and Intelligent Systems*, vol. 9, no. 3, pp. 1220–1242, 2016.

[103] R. Moss, S. Shire, P. Henshall, F. Arya, P. Eames, and T. Hyde, "Performance of evacuated flat plate solar thermal collectors," *Thermal Science and Engineering Progress*, vol. 8, pp. 296–306, 2018.

[104] B. Norton, "Anatomy of a solar collector: developments in materials, components and efficiency improvements in solar thermal collector systems," *Refocus*, vol. 7, no. 3, pp. 32–35, 2006.

Hindawi
International Journal of Photoenergy
Volume 2022, Article ID 9428536, 9 pages
https://doi.org/10.1155/2022/9428536

Research Article

Test Verification of the Standard Compilation of "Energy-Saving Monitoring for Refrigeration Storage System" in Beijing

Jing Ren,[1] **Jinhua Zhang**,[1] **Chunqiang Si**,[2] **Nan Wang**,[3] **Bo Qin**,[4] **Chao Ma**,[2] **Bao Zhang**,[1] **Jianghong Li**,[1] **and Yonghui Li**[1]

[1]*Beijing Building Research Institute Co. Ltd. of CSCEC, Beijing 100076, China*
[2]*Hua Shang International Engineering Co. Ltd., Beijing 100069, China*
[3]*Beijing University of Civil Engineering and Architecture, Beijing 100044, China*
[4]*Beijing Municipal Engineering Consulting Corporation, Beijing 100124, China*

Correspondence should be addressed to Jing Ren; 839410663@qq.com

Received 16 December 2021; Accepted 11 May 2022; Published 7 June 2022

Academic Editor: Qian Xu

In this paper, the feasibility and applicability of the test and evaluation methods for the temperature and energy consumption coefficient in the cold storage system are tested and verified which is specified in the Beijing local standard "Energy Conservation Monitoring of Refrigeration Storage." It also summarizes and analyses the test verification results of the evaluation index of the location of measuring points of temperature in refrigeration storage, data-collecting time interval of temperature in refrigeration storage, energy efficiency coefficient of the refrigeration unit, and energy consumption coefficient of the refrigeration. The study work provides technical support for making the monitor and evaluation methods which applies to the standard.

1. Introduction

Nowadays, with the rapid development of refrigeration and logistics industry, the awareness of the food cold chain is stronger. Refrigeration storage has been the indispensable facility to the food industry. At the same time, with the rise of e-commerce and the implementation of national strategy "One belt and one road," the business of high-end food import and export has achieved great growth and has created a new revenue plate of the cold chain system—large logistics cold storage [1]. According to relevant statistics, the total capacity of cold storage in China has exceeded 43 million tons by the end of 2017. In Beijing, the capital city of China, with the sustained and high-speed economic development, the demand for cold storage has also increased rapidly. It is reported that the capacity of cold storage in Beijing has reached 1574700 tons in 2018 and its capacity and volume rank first in north China [2]. At present, the total capacity of cold storage in China is increasing at an annual average rate of about 20%. Compared with the average capacity of 200 cubic meters per 1000 people in developed countries, the total capacity of cold storage in China has great potential for development [3]. From the view of cold storage energy consumption, the energy consumption level of the same type of cold storage in China is much higher than the average level in developed countries and the energy consumption is 26% and 46% higher than that of Britain and Japan [4].

In view of the rapid growth of cold storage and the high level of energy consumption, the relevant departments in Beijing have organized and compiled the local standard of "Energy-saving Monitoring of Cold Storage System" (hereinafter referred to as "Standard"). The Standard is applicable to the refrigeration which has been put into use and operated normally in Beijing area and provides a standard basis for energy saving monitoring of the refrigeration. In order to cooperate with the compilation of the Standard, the compilation team, taking into account the characteristics and actual situation of Beijing, has carried out feasibility and applicability verification of the monitoring and evaluation

methods in the Standard under the guidance of full investigation, analysis, experimental research, and experts, which provides technical basis for the scientific development of monitoring and evaluation methods in the Standard. The Standard has been compiled through extensive consultation.

This paper mainly summarizes and analyses the test and validation of the temperature and energy consumption coefficient in the cold storage as stipulated in the Standard, including the location of temperature measurement points in the cold storage, the time interval of temperature collection in the cold storage, the COP of refrigeration units, and the evaluation index of energy consumption coefficient in the refrigeration system. This part of the work is an important part of the preparation of the Standards, which provides technical support for the scientific development of monitoring and evaluation methods of the Standards. At the same time, the formulation of this evaluation method also fills in the blank of energy-saving monitoring and evaluation method for domestic cold chain logistics enterprises, which is of great significance to standardize and improve the overall operation level of the cold storage industry.

2. An Overview of the Test Contents

The test and verification work of the Standard mainly focuses on the following contents:

(1) Different types of refrigerators with different storage capacities in Beijing were selected for monitoring and analysis, including ammonia refrigeration system and Freon refrigeration system, as well as civil cold storage and assembled cold storage. Verify the feasibility and applicability of the Standard

(2) The comparative test of the same cold storage is carried out according to different seasons, different recording time intervals, operating temperature, temperature distribution in the storage, collection time intervals, and so on, to verify the applicability of the "Standard" method, test conditions, test time, and other provisions

(3) The test data of all cold storage systems are classified and summarized, and the rationality of the indicators is verified by effective data calculation and coincidence analysis of monitoring indicators

(4) The research work includes the arrangement of temperature points in the cold storage, the test verification of the collection time interval, the test verification of COP of the refrigeration unit, and the evaluation index verification of the energy consumption coefficient of energy-saving monitoring of the refrigeration system

3. Verification of the In-Storage Temperature Test

The "Standard" is to monitor the use of cold storage in operation. Due to the difference of the code and height of the items in the cold storage, the existing national standard GB/T30103.1-2013 "Test Method for Thermal Performance of Cold Storage Part 1: Temperature and Humidity Detection" stipulates the location of the measuring points "at least 3 points in each horizontal direction and at least 3 points in each vertical direction." When the field test or the test conditions are not easy to meet or the operation is not convenient enough and the time interval of current standard data acquisition is different, factors such as compressor start-stop frequency, cold storage type, and test time should be considered comprehensively. This validation work has carried out targeted experimental verification on the location of measurement points and the acquisition time interval.

3.1. Location of Temperature Measuring Points in Cold Storage. In the cold storage, measuring points are arranged in horizontal and vertical directions. Finally, the average values of all measuring points are compared and analyzed with the average values of measuring points in the central region of each vertical direction: testing place #3, cold storage of a food company in Beijing; testing time: 17:20 on November 25, 2017, to 17:20 on November 26, 2017. The results are shown in Table 1.

Comparisons of test results at different time intervals and locations are shown in Figures 1–6.

In Table 1 and Figures 1–6, it can be seen that the working temperature, maximum temperature, and minimum temperature in the cold storage are basically the same and the deviation is not more than 0.3°C. The results show that the average values of all measure points in the height direction are in good agreement with those in the central region. Therefore, the "Standard" stipulates that the temperature measurement point in the height direction is within the range of 40%–60% of the net height of the cold storage, while retaining the requirement of "50 mm–100 mm from the horizontal end measurement point to the wall" in the original national standard, which improves the feasibility of field detection. The test position diagram is shown in Figure 7.

3.2. Time Interval of Data Collection. In the cold storage, measuring points are arranged in horizontal and vertical directions and temperature collection recorders with 5 min and 10 min collection intervals are arranged at the same measuring point. Finally, the average values of different collection intervals are compared and analyzed (including the comparison of different collection intervals for all measurement points and the comparison of different collection intervals for intermediate measurement points): testing place #3, cold storage of a food company in Beijing; testing time: 17:20 on November 25, 2017, to 17:20 on November 26, 2017. The results are shown in Tables 2 and 3.

Tables 2 and 3 show that the working temperature, the highest temperature, and the lowest temperature in the cold storage are basically the same after the stable operation of the cold storage. The maximum deviation is 0.26°C. It shows that the collection time interval of 5 minutes or 10

Table 1: Comparison of the temperature measurement position in storage.

(a)

Collection interval (5 min)	Average value of all measuring points (°C)	Average value of central regional (°C)	Deviation (°C)
Working temperature of cold storage	−17.41	−17.36	−0.05
Highest temperature of cold storage	−14.87	−14.87	0
Lowest temperature of cold storage	−18.68	−18.53	−0.15

(b)

Collection interval (10 min)	Average value of all measuring points (°C)	Average value of central regional (°C)	Deviation (°C)
Working temperature of cold storage	−17.42	−17.37	−0.05
Highest temperature of cold storage	−15.13	−14.89	−0.24
Lowest temperature of cold storage	−18.62	−18.47	−0.15

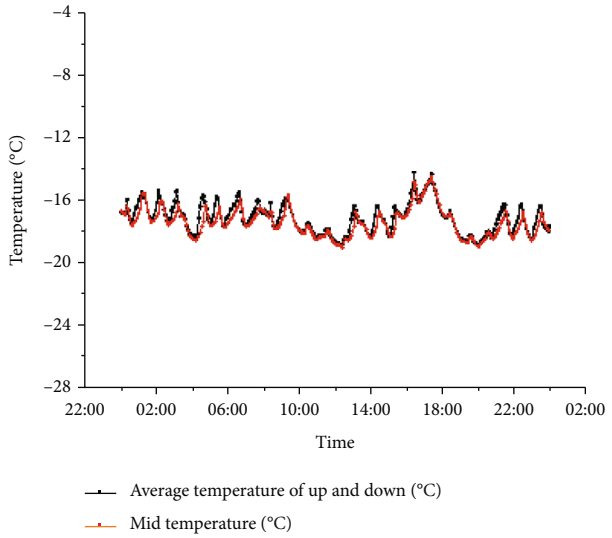

Figure 1: Average temperature and midtemperature of measuring points at vertical position 1.

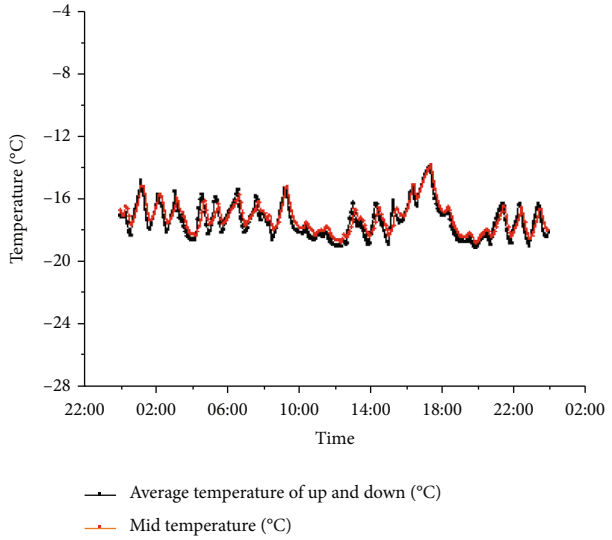

Figure 2: Average temperature and midtemperature of measuring points at vertical position 2.

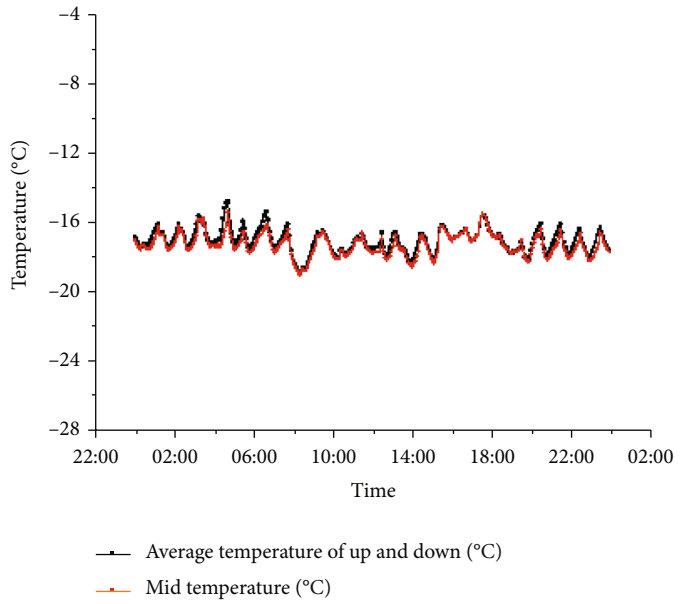

Figure 3: Average temperature and midtemperature of measuring points at vertical position 3.

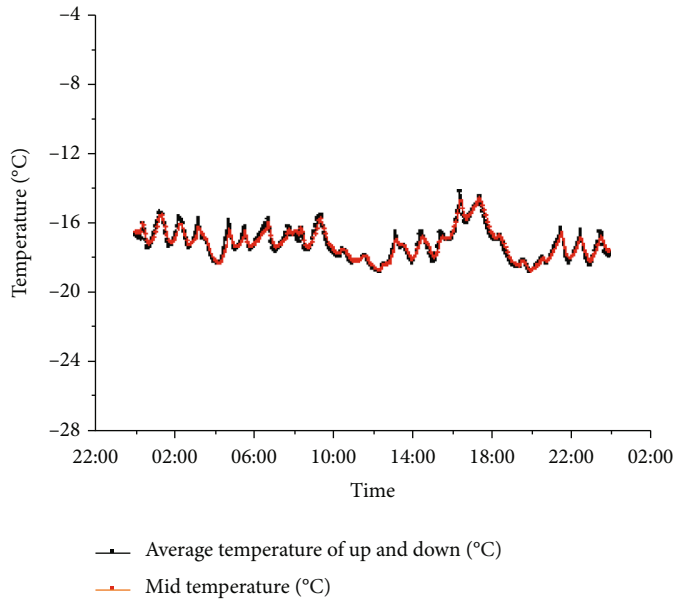

Figure 4: Average temperature and midtemperature of measuring points at vertical position 4.

minutes has little influence on the results. In the process of compiling this Standard, taking into account the factors such as the total test time, compressor operation mode, temperature fluctuation, and the time required for calculating the results, the time interval for temperature collection is stipulated as "not more than 10 minutes, the total test time is not less than 36 hours, and the temperature in the storage should be calculated by the continuous 24-hour data with the minimum temperature difference between the first and the last."

4. COP Test Validation of the Refrigeration Unit

In the process of compiling this standard, the energy consumption coefficient of the cold storage is determined, the refrigeration unit's cooling demand is determined by referring to the calculation method of mechanical load in the design code of the cold storage, and the boundary value of refrigeration electric energy consumption (REC) is calculated based on the relationship with COP. Therefore, the

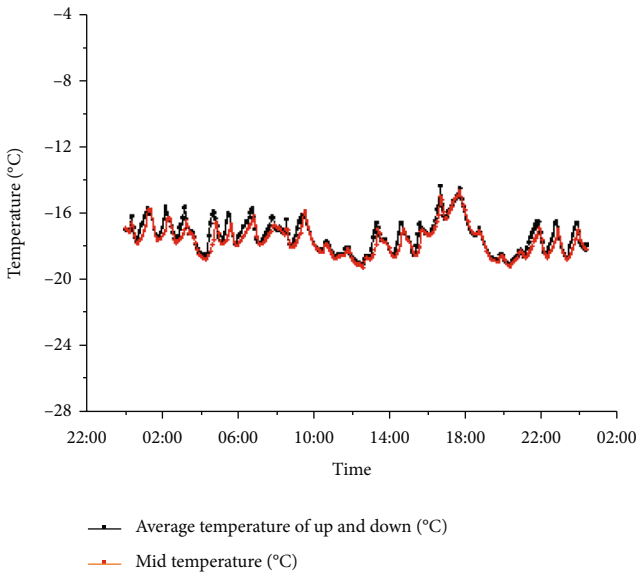

Figure 5: Average temperature and midtemperature of measuring points at vertical position 5.

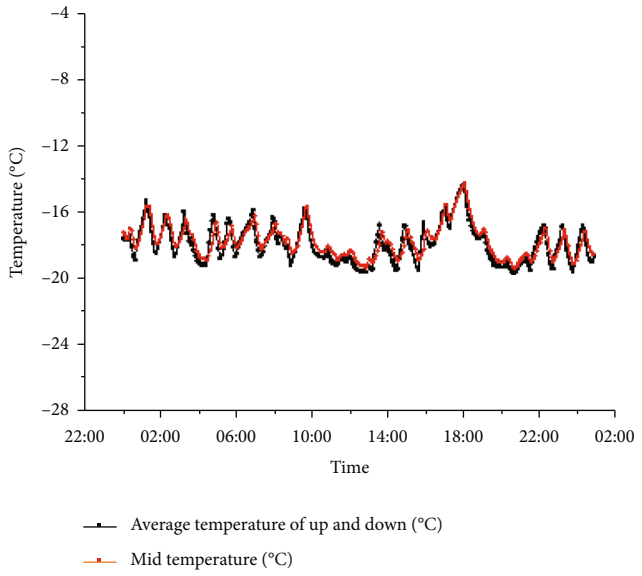

Figure 6: Average temperature and midtemperature of measuring points at vertical position 6.

COP value of the refrigeration unit is very important. In determining the value of COP, this standard adopts the method of combining theoretical calculation with experimental verification.

4.1. Theoretical Calculation of COP in Different Storage Temperature and Refrigerants. Considering the influence of different refrigerant types on COP, the compilation team investigated the use of refrigerant in the research process. Understanding that the United States and other developed countries have been looking beyond the HFC stage, natural

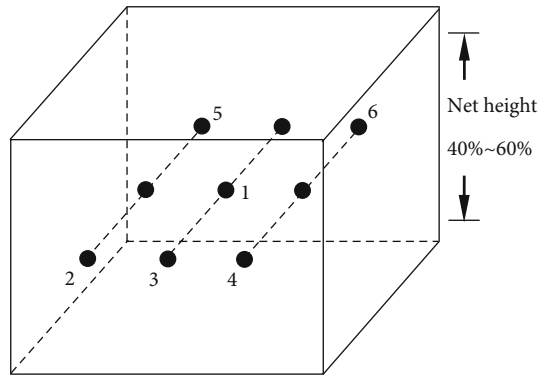

Figure 7: Sketch map of the indoor temperature measurement position.

refrigerants like NH_3 [5] and CO_2 [6, 7] have received unprecedented attention. Research on CO_2 and CO_2 and NH_3 cascade refrigeration is deepening. Besides, more and more practical applications are achieved. Now, there are more than 60 CO_2 systems in operation in the United States [8]. At present, NH_3 and R22 are the most commonly used refrigerants in the refrigeration system of our country. Among them, 80% of the refrigerators use ammonia as refrigerant and 20% of the refrigerators (mostly medium and small refrigerators) use R22 refrigerant.

According to the previous research results, there are four kinds of refrigerants commonly used in Beijing refrigerators: R22, R404 A, R134a, and R717. The theoretical COP of the four refrigerants at different evaporation and condensation temperatures is calculated by the compilation group, and the results are shown in Table 4.

Table 4 shows that COP of the same refrigerant ranges from 1.4 to 3.5 at different evaporation temperatures, while that of the same refrigerant is basically the same at different evaporation temperatures. For example, when the evaporation temperature is −35°C, the COP is 1.37 to 1.47. It can be seen that the theoretical values of COP for different refrigerants at the same evaporation and condensation temperatures are similar. Therefore, in the process of formulating the energy consumption coefficient, this Standard does not take into account the differences caused by different refrigerants. The reference values of COP determined are shown in Table 5.

4.2. COP Reference Value Test Verification. In order to further verify the COP reference value of the refrigeration unit in Table 5, the representative refrigerators were tested in winter and summer, by the compilation group. The sketch map of the location of the measuring points is shown in Figure 8. The seasonal deviation of COP test results and the deviation between COP test results and COP reference values are analyzed. The results are shown in Table 6.

Table 6 shows that the COP of different condensing units shows different trends in winter and summer. For air-cooled condensing units, COP of the system in summer is significantly lower than that in winter. For example, item no. 1 is an air-cooled condensing unit. The seasonal deviation of COP test results is 45.88%. For evaporation condensing units,

Table 2: Comparison of the results of different acquisition time intervals at all temperature measurement points in the cold storage.

Collection interval	Average value of all measuring points in 5 minutes (°C)	Average value of all measuring points in 10 minutes (°C)	Deviation (°C)
Working temperature of cold storage	−17.41	−17.42	0.01
Highest temperature of cold storage	−14.87	−15.13	0.26
Lowest temperature of cold storage	−18.68	−18.62	−0.06

Table 3: Comparison of the results of different collection time intervals at the intermediate temperature measurement points in the cold storage.

Collection interval	Average value of all measuring points in 5 minutes (°C)	Average value of all measuring points in 10 minutes (°C)	Deviation (°C)
Working temperature of cold storage	−17.36	−17.37	0.01
Highest temperature of cold storage	−14.87	−14.89	0.02
Lowest temperature of cold storage	−18.53	−18.47	−0.06

Table 4: COP calculations of four refrigerants at different storage temperatures.

Refrigerants	R22	R134a	R404A	R717	Average value
Design storage temperature (4°C); evaporation temperature (−6°C)	3.52	3.31	3.06	3.93	3.46
Design storage temperature (−5°C); evaporation temperature (−10°C)	3.12	2.87	2.71	3.34	3.01
Design storage temperature (−18°C); evaporation temperature (−28°C)	1.64	/	1.85	1.74	1.74
Design storage temperature (−25°C); evaporation temperature (−35°C)	1.37	/	1.47	1.42	1.42

The abovementioned data are calculated according to the enthalpy and entropy of refrigerant under different evaporation temperature, suction pressure, condensation temperature, and hydraulic pressure. 2.R134a is not applicable in the low-temperature zone.

Table 5: COP reference value for calculating energy consumption coefficient.

COP reference value	Design storage temperature (4°C); evaporation temperature (−6°C)	Design storage temperature (−5°C); evaporation temperature (−10°C)	Design storage temperature (−18°C); evaporation temperature (−28°C)	Design storage temperature (−25°C); evaporation temperature (−35°C)
	3.3	2.3	1.8	1.5

the seasonal deviations of COP test results of units with no. 2 and no. 4 refrigerators are 6.01% and 0.54%, respectively, and the seasonal variation of COP in the system is not obvious. The deviation between the summer test results and COP reference values is in the range of −8.33%~7.78%. In practical use, the summer characteristics of the unit can better reflect its energy consumption level.

5. Test and Verification of the Energy Consumption Coefficient of Cold Storage

In the Standard, the energy consumption coefficient of the cold storage system is defined as "the daily energy consumption per cubic meter storage capacity when the cold storage system runs steadily." To obtain this parameter, the total energy consumption (TEC) of the cold storage system is needed. The total energy consumption (TEC) of the refrigeration system is the sum of refrigeration power consumption (REC) and direct energy consumption (DEC). The refrigeration power consumption (REC) [9–11] is the energy consumption necessary for the refrigeration system within 24 hours, mainly for the refrigeration units and condensers

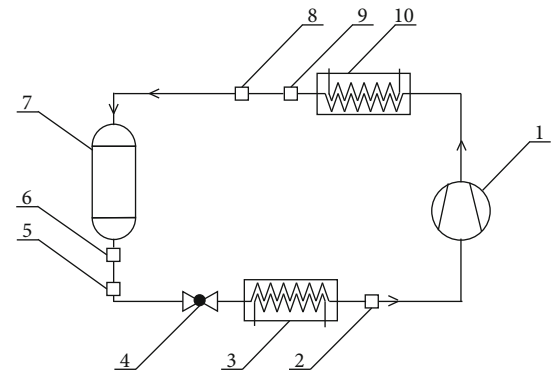

Figure 8: Sketch map of measuring point position where 1: compressor; 2: testing sensor of inspiration temperature; 3: evaporator; 4: throttle valve; 5: temperature measurement sensor for liquid supply after liquid accumulator; 6: refrigerant flow testing instrument after liquid accumulator; 7: liquid accumulator; 8: temperature measurement sensor for liquid supply before liquid accumulator; 9: refrigerant flow testing instrument before liquid accumulator; and 10: condenser. Refrigerant flow rate and temperature test should be preferred at 8 and 9 locations. When this part does not meet the test conditions, choose the location of 5 and 6.

Table 6: COP test results of different seasons and units.

Cold storage number	Project	Refrigerant	Design of cold storage temperature (°C)	Types of condenser units	Test time	COP	Seasonal deviation of COP test results	Deviation from COP reference value
1	A food co. ltd. of Beijing	R22	−18°C	Air-cooled condensing unit	Winter	2.83	45.88%	57.22%
					Summer	1.94		7.78%
2	A food co. ltd. of Beijing	R22	−18°C	Evaporation condensing unit	Winter	1.94	6.01%	7.78%
					Summer	1.83		1.67%
3	A food co. ltd. of Beijing	R22	−18°C	Air-cooled condensing unit	Summer	1.88	—	4.44%
4	A food distribution company of Beijing	R717	−18°C	Evaporation condensing unit	Winter	1.86	0.54%	3.33%
					Summer	1.85		2.78%
5	A cold storage of food refrigeration plant of Beijing	R717	−18°C	Evaporation condensing unit	Summer	1.65	—	−8.33%
6	A by-product market co. ltd. of Beijing	R717	−18°C	Evaporation condensing unit	Summer	1.50	—	−16.67%
7	A college pilot base in China	R22	4°C	Air-cooled condensing unit	Summer	3.43	—	3.94%

(energy consumption necessary for the refrigeration system). Direct electric energy consumption (DEC) refers to the energy consumption of electrical components within 24 hours, including lighting, air cooler, defrosting, wind curtain, automatic control, auxiliary heating equipment, and circulating pump to meet the normal operation of the cold storage system of all ancillary equipment.

5.1. Calculation of the Energy Consumption Coefficient of the Cold Storage System

(1) The refrigeration power consumption (REC) of the cold storage system is calculated according to the following formula:

$$\mathrm{DEC} = \sum_{i=1}^{n} E_i, \tag{1}$$

where DEC is direct power consumption (kWh), E_i is the cumulative power of the ith meter in 24 hours (kWh), and n is the total number of direct energy consumption metering (watt-hour meters)

(2) The direct power consumption (DEC) of the cold storage system is calculated according to the following formula:

$$\mathrm{REC} = Q_s \times \frac{T_c - T_{mrun}}{0.34 \times T_{mrun}}, \tag{2}$$

where REC is refrigeration power consumption (kWh), Q_S is the total refrigeration capacity in 24 hours (kWh), T_{mrun} is the average evaporation temperature (K), and T_c is the condensation temperature (K) (condensation temperature is a constant, 308.15 K)

(3) The total refrigeration capacity Q_S within 24 hours is calculated according to the following formula:

$$Q_S = \frac{G\rho(h_2 - h_1)}{3600}, \tag{3}$$

where Q_S is the 24 h total refrigeration capacity of the refrigeration system (kWh), G is the 24 h cumulative refrigerant flow (m^3), ρ is the refrigerant density (kg/m^3), h_1 is the specific enthalpy of refrigerant (kJ/kg), and h_2 is the specific enthalpy of refrigerant evaporation (kJ/kg). The average evaporation temperature is taken as the average suction temperature

(4) The total energy consumption TEC of the cold storage system for 24 hours is calculated according to the following formula:

$$\mathrm{TEC} = \mathrm{DEC} + \mathrm{REC}, \tag{4}$$

Table 7: Evaluation index value of standard energy consumption coefficient of "Energy Conservation Monitoring of Refrigeration Storage System" in Beijing.

Temperature of the cold storage	Coefficient of energy consumption ($kW{\cdot}h/(m^3{\cdot}24\,h)$)		
	<2000	2000–10000	>10000
+10°C~0°C	0.22	0.18	0.16
−1°C~−10°C	0.32	0.25	0.20
−11°C~−20°C	0.45	0.33	0.27
−21°C~−30°C	0.66	0.55	0.48

where TEC is the sum of refrigeration power consumption and direct power consumption (kWh)

(5) The energy consumption coefficient of the cold storage system is calculated according to the following formula:

$$\varepsilon = \frac{TEC}{V}, \tag{5}$$

where ε is the daily power consumption per cubic meter ($kWh/(m^3{\cdot}24\,h)$) (take the three significant digits after the decimal point) and V is the total storage capacity of the refrigerator (m^3).

In order to obtain a reasonable evaluation index of energy consumption coefficient, the cooling requirement of the unit is determined by referring to the calculation method of mechanical load in the design code of refrigeration storage and the boundary value of refrigeration power consumption (REC) is calculated according to the relationship between COP and the unit. According to the experimental results, the direct energy consumption (DEC) is calculated. Finally, the total energy consumption (TEC) of the cold storage system is obtained, divided by the storage capacity, and the energy consumption coefficient is obtained. Refrigeration power consumption (REC) and unit COP are calculated by theory and verified by test. The index values are validated. The specified index values in the Standard are shown in Table 7.

5.2. Verification Results. In order to verify the rationality of the calculated energy consumption coefficient of Table 7 cold storage, the energy consumption coefficient of typical cold storage with different storage capacities and design temperature is tested. The results are detailed in Table 8.

In the process of testing, it is completely based on the test conditions, the layout of test points, the test methods, the calculation of results, and the evaluation of indicators stipulated in this Standard. Through testing, the measured energy consumption coefficients of different refrigerators are obtained, and finally, reliable test results are obtained to verify the applicability, operability, and rationality of the index formulation of this standard. Through the analysis of the unqualified items in Table 8, the main reasons for the unqualified items are as follows:

Table 8: Statistical table of energy consumption coefficient for different seasons and cold storages.

Storage number	Design of storage temperature	Volume (m^3)	Energy consumption coefficient in winter (kWh/(m^3·24h))	Energy consumption coefficient in summer (kWh/(m^3·24h))	Calculated value of energy consumption coefficient index (kWh/(m^3·24h))	Conclusion
1	−18°C	296	0.288	0.368	0.45	Qualified
2	−18°C	204	/	0.643	0.45	Unqualified
3	−18°C	4847	0.289	0.362	0.33	Unqualified
4	−18°C	131747	0.110	0.213	0.27	Qualified
5	−18°C	84602	/	0.191	0.27	Qualified
6	Mix	72320	/	0.379	0.27	Unqualified
7	4°C	775	/	0.109	0.22	Qualified

(1) Low-temperature reservoir no. 2 and no. 3 with smaller storage capacity do not meet the minimum requirements of the recommended values of design standards because of their poor enclosure structure, and the test results are larger than the index values

(2) The operation of the no. 6 refrigeration system is poor (COP is only 1.5), and the enclosure structure is a rice husk insulation structure. The test results are larger than the index value

6. Conclusion

The experimental verification work described in this paper is an important part of the compilation of the Standard. Through a large number of researches, calculation, analysis, and experimental verification work, the compilation team summarized the energy consumption coefficient evaluation index, which provides a technical basis for the scientific development of the monitoring and evaluation method of the Standard. The energy consumption evaluation index proposed in this Standard will be widely applied to the cold storage systems of storage companies, catering management companies, food distribution companies, food refrigeration plants, and cold chain logistics companies in Beijing. The implementation of this standard can effectively standardize the energy consumption status of refrigeration enterprises in Beijing, and it is of great significance to ensure the energy-saving and efficient operation of the refrigeration system in Beijing.

Data Availability

The data that support the findings of this study are available from the corresponding author upon reasonable request.

Conflicts of Interest

The authors declare that they have no conflicts of interest.

Acknowledgments

The authors are grateful to the financial support of the Key Project of Beijing Natural Science Foundation (under Project Grant no. 3151001), the National 973 Programs (Grant no. 2015CB251303), and the Beijing Advanced Innovation Center for Future Urban Design (Grant no. UDC2016040200).

References

[1] Y. Qin, "China cold chain logistics development report," *China cold chain logistics development report*, pp. 13-14, 2015.

[2] *Distribution Map of National Cold Chain Logistics Enterprises*, China Cold Chain Logistics Alliance, 2018.

[3] K. Lisa, *"Use of cold chains for reducing food losses in developing countries". PEF White Paper No.13-03*, The Postharvest Education Foundation (PEF), 2013.

[4] Y. Zhao, "Energy saving and emission reduction of refrigerator," *Refrigeration Technology*, vol. 30, no. 3, pp. 46–50, 2010.

[5] L. A. Domínguez-Inzunza, J. A. Hernández-Magallanes, M. Sandoval-Reyes, and W. Rivera, "Comparison of the performance of single-effect, half-effect, double-effect in series and inverse and triple-effect absorption cooling systems operating with the NH_3-$LiNO_3$ mixture," *Applied Thermal Engineering*, vol. 66, no. 1–2, pp. 612–620, 2014.

[6] A. H. Mosaffa, L. G. Farshi, C. A. Infante Ferreira, and M. A. Rosen, "Exergoeconomic and environmental analyses of CO_2/NH_3 cascade refrigeration systems equipped with different types of flash tank intercoolers," *Energy Conversion and Management*, vol. 117, pp. 442–453, 2016.

[7] P. Bansal, "A review - status of CO_2 as a low temperature refrigerant: fundamentals and R&D opportunitiesvol. 41, pp. 18–29.

[8] X. Cao, *Research on Refrigeration System Technology of Large Logistics Refrigeration Storage*, Dalian University of Technology, Dalian, 2017.

[9] *Methods of Testing for Thermal Performance on Cold Store—-Part 3, Heat Flux Testing for Envelop Enclosure:GB/T 30103.3-2013*, Ministry of Commerce of the People's Republic of China, 2013.

[10] *Indoor assembled cold storage: SB/T10797-2012*, Ministry of Commerce of the People's Republic of China, Beijing, 2012.

[11] *Refrigerated Display Cabinets-Part2: Classification, Requirements and Test Conditions (ISO23953-2*, International Organization for Standardization (ISO), 1946.

Hindawi
International Journal of Photoenergy
Volume 2022, Article ID 6836686, 7 pages
https://doi.org/10.1155/2022/6836686

Research Article

System Performance and Economic Analysis of a Phase Change Material Based Cold Energy Storage Container for Cold Chain Transportation

Jianwu Zhang, Zixiao Li, and Shanhu Tong

CRRC Shijiazhuang Co., Ltd, No. 168 Yuxiang Street, Luancheng District, Shijiazhuang City, Hebei Province, China 051430.

Correspondence should be addressed to Zixiao Li; 253454473@qq.com

Received 3 March 2022; Accepted 21 May 2022; Published 3 June 2022

Academic Editor: BINJIAN NIE

We studied a shipping container integrated with phase change material (PCM) based thermal energy storage (TES) units for cold chain transportation applications. A 40 ft container was used, which was installed with ten plate-like TES units containing PCM and a charging loop. An appropriate PCM was selected for meeting the requirement of the transportation of fresh vegetables (7-12°C). The charging loop was linked to a separate charging facility via quick coupling valves. The discharging performance of the container under dynamic conditions was investigated. The COP of the system was estimated to be 1.73. Economic analyses showed that energy and operation costs of the PCM-based container were, respectively, 71.3% and 85.6% lower than the same container but powered by a diesel engine (called reefer container). The results also showed that the PCM-based container was able to maintain not only the temperature range (7-12°C) but also the humidity range (85-95%), leading to better quality and longer shelf-life of the goods.

1. Introduction

Currently, cold chain transportation relies on vapour compression refrigeration cycle which is driven by diesel engines [1]. Such technology is expensive due to both high fuel and maintenance costs; it also emits a significant amount of CO_2 and particulate matter thus contributing to global warming.

Taking the advantage of the high energy density [2] and the constant temperature during the phase transition [3], the PCM-based TES is feasible to provide cooling without a constant energy supply. This makes the TES an appropriate method to balance the demand and supply of energy. Besides, the TES can integrate renewable energy well [4]; therefore, it has become ever more attractive in recent years [5].

Some recent studies are using the PCM-based TES for cold chain applications. Michel et al. [6] experimentally and numerically studied a composite layer of PU-PCM foam dedicated to refrigerated vehicles. It was reported that the heat flux across the wall during the "road delivery period" could be reduced by 18% by using the PCM. A refrigeration system incorporating PCM was proposed to achieve the low temperature required for refrigerated trucks [7, 8]. The TES unit was charged by a mechanical refrigeration unit located off the vehicle. When the truck was on duty for delivering products, the PCM discharged and provided cooling. It was concluded that the cost of the PCM integrated refrigeration unit was 86.4% less than conventional systems. An improvement in the temperature control with lower temperature fluctuations and the reduced noise level was also reported.

One can see from the above work when integrating the TES with the conventional cooling system an energy efficiency improvement and the reduction in temperature fluctuations can be achieved. In this work, we introduced the PCM-based TES to the shipping container for cold chain transportation which aimed to investigate the feasibility of the real applications. There is only limited research on integrating the PCM-based TES with shipping containers. Sepe et al. [9] proposed a concept for a 20-feet International Organization Standardization (ISO) container with twelve

eutectic plates. A −26°C eutectic formula was selected as the PCM. The air passing through the plates was cooled first and then cold air was transported for both product freshness preservation and (+4°C- ±1°C) and freeze (−18°C-−20°C). However, the container was also equipped with a refrigeration unit which limited the flexibility. Besides, the authors did not reveal the charging rate which is a concerning aspect for such a container.

A TES container was set up based on the 40 ft ISO shipping container. Up to 10 TES plates containing 1260 kg of PCM were included in one container. The discharging performance was experimentally investigated. The system performance and the economic analysis of the container carrying real items were also revealed in this paper. The system COP, the power, and the cost reduction compared with that of the conventional reefer conditioner were presented.

2. Experimental Set-up

2.1. Material. The PCM RT 5 HC is from Rubitherm Company [10]. It melts at 5°C with a latent heat of 220 kJ/kg. The main thermo-physical properties of the PCM are listed in Table 1.

2.2. Thermal Energy Storage Plate. The TES plate was constructed on the embedded finned tubes which acted as the charging fluid loop. The outer size of a single TES plate is 1800(L) ∗ 1000(W) ∗100(H) mm (see Figure 1).

For each plate, 126 kgs of PCM were filled. Three thermocouples were installed inside each cold TES plate. The location of the thermocouples is shown in Figure 1, with an immersion depth of 0.05 m.

2.3. Container. The dimensions of the container are shown in Figure 2, with 100 mm thickness of polyurethane foam inside the walls as insulation material. Up to 10 plates were installed inside each container, with 9 of them located on the ceiling, and one was installed at the front of the internal wall. There are eight sensors located in two layers, with the height of the first layer (numbers 1, 3, 5, and 7) and the second layer (numbers 2, 4, 6, and 8) from the bottom at 1.8 m and 0.9 m, respectively. In the axial perspective, the sensor was annotated with numbers 7 and 8 located on the door with a distance of 1.2 m from the frame edge. Number 5 and 6 sensors were attached to the internal surface of the door frame, while numbers 3 and 4 were mounted on the middle of the sidewall. The last two sensors, annotated as numbers 1 and 2, were fixed on the frame edge opposite the door. One sensor was placed outside the container to get the ambient temperature and relative humidity. For the dynamic experiments with carrying loads, another three sensors were inserted into the items. The three sensors were installed at the same level (1.2 m to the container bottom), with numbers 9, 10, and 11 having a distance of 12 m, 8 m, and 4 m from the door, respectively.

A data logger system (Hwa Innovate Technology Co. Ltd) was used to record the temperature and relative humidity. The temperature sensors (RTD (PT100) probes) and the RH sensors showed an uncertainty of 1% and 3%, respectively. The internal photo of the shipping container is shown in Figure 3.

Table 1: Thermo-physical characteristics of the PCM.

Density kg/m^3	Latent heat kJ/kg	Phase change point °C	Specific heat capacity kJ/kg.K	Thermal conductivity W/(m.K)
880	220	5	2.0 ± 0.2	0.2

2.4. Charging Process. The charging unit mainly includes an electricity-powered chiller from BITZER, and a centrifugal pump which is used to circulate the HTF between the charging unit and the container. The HTF tank is used to store the pre-cooled heat transfer fluid. It was filled with 14 m^3 EG-water solution that is identified as the HTF shown in Table 2.

By connecting the container with the charging unit through the charging loop, the HTF between the tank and the plates was circulated. Inside the plates, the cold HTF transferred the cold energy to PCMs. The temperature of the outlet and the recirculated HTF was monitored by the wireless data logger system which was provided by Hwa Innovate Technology Co. Ltd. The RTD (PT100) probe with uncertainly at 1%. The flowrate meter with 2% uncertainty was employed to obtain the flowrate of the HTF. The completion of the charging was indicated by the temperature of PCMs which can be obtained by the thermocouples.

3. Performance Index

3.1. Discharging Time. Discharging time is defined as the period of the inside temperature of the container rising from 7 to 12°C. This is because most of the fruits and vegetables can retain freshness within this temperature range [11].

3.2. System COP. The total energy released by heat transfer fluid (HTF, Ethylene glycol-water solution, Q_{EG}) is given as Eq. (1):

$$Q_{EG} = c_{p,EG} * m_{EG} * (T_{o,EG} - T_{i,EG}), \quad (1)$$

where m_{EG} is the HTF mass flow; $c_{p,EG}$ is the specific heat capacity of the HTF; and $T_{o,EG}$ and $T_{i,EG}$ are the HTF temperature at the return and inlet of the charging unit, respectively.

Except for the heat loss to the ambient, the energy transferred by HTF is adsorbed by the PCMs, the moist air inside the container and the aluminium frame of the TES plates. The energy stored by PCMs (Q_{PCM}) can be given as Eq. (2):

$$Q_{PCM} = m_{PCM} * \left[c_{p,EG} * (T_{e,PCM} - T_{s,PCM}) + \Delta H_{PCM}\right], \quad (2)$$

where m_{PCM}, ΔH_{PCM}, and $c_{p,PCM}$ are the mass, latent heat capacity, and specific heat capacity of the PCM, respectively; $T_{e,PCM}$ and $T_{s,PCM}$ are the temperatures of PCM at the end and initial stage of the experiments.

The energy transferred to the aluminium frame of the TES plates, Q_{Al}, can be achieved by Eq. (3).

$$Q_{Al} = m_{Al} * c_{p,Al} * (T_{e,Al} - T_{s,Al}), \quad (3)$$

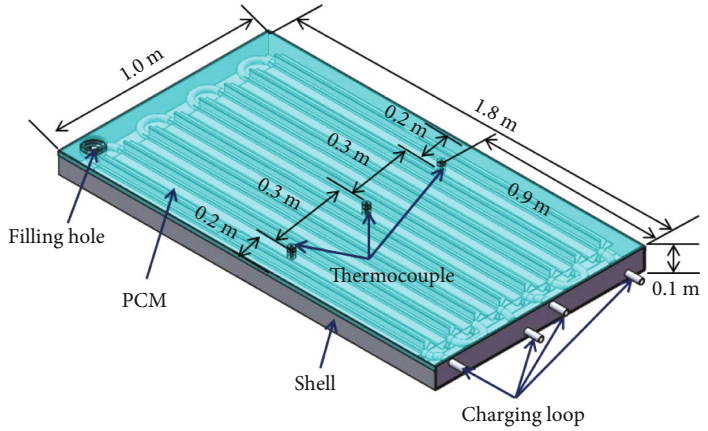

Figure 1: The structural view of a TES plate.

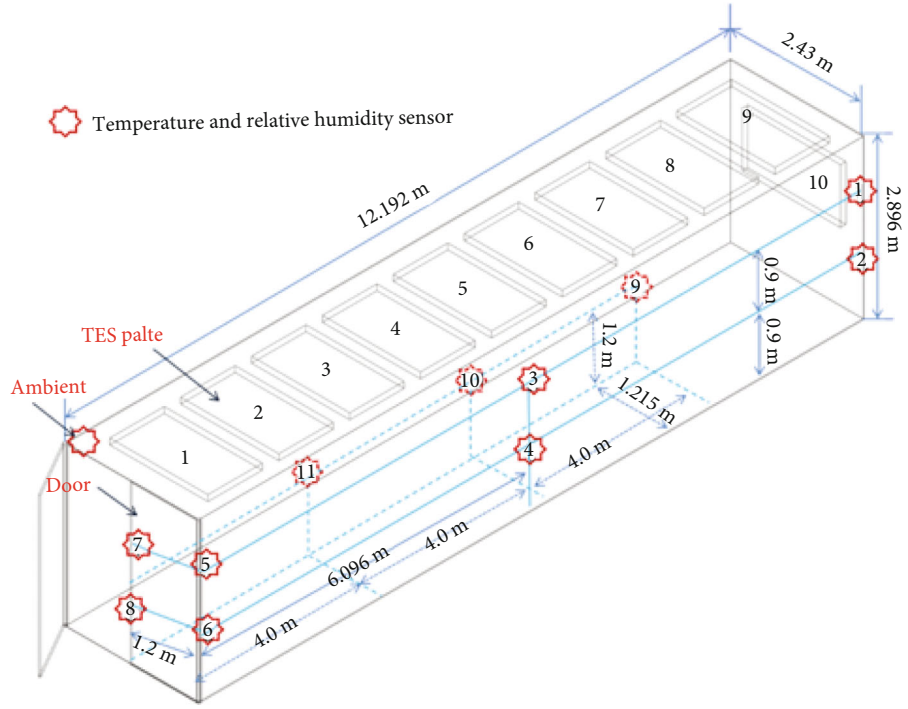

Figure 2: Distributions of TES plates and the sensors of the shipping container.

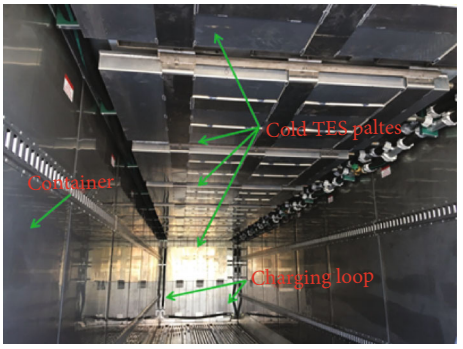

Figure 3: Internal photo of the TES-based container.

where m_{Al} and $c_{p,Al}$ are the mass and specific heat capacity of aluminium, respectively. $T_{e,Al}$ and $T_{s,Al}$ are the temperatures of aluminium at the end and initial stage of the experiments.

The energy absorbed by the moist air (Q_{ma}) is mainly consisted of two parts, with the first part being dry air (Q_a) and the second part being condensed water (Q_w). The Q_{ma} can be obtained through Eqs. (4)~(6) below.

$$Q_{ma} = Q_a + Q_w, \tag{4}$$

$$Q_a = m_a * c_{p,a} * (T_{e,a} - T_{s,a}), \tag{5}$$

$$Q_w = m_w * \Delta H_w, \tag{6}$$

where m_a and $c_{p,a}$ are the mass and specific heat capacity of

Table 2: Comparison of the energy and economic performance of the TES and diesel-powered container.

Properties	The diesel-powered	The TES-based
Delivery distance (km)	2362	
Delivery duration (hour)	53	
Power consumption (kW)	5.4 [14]	1.55
Energy consumption	Diesel(*53*L)	Electircity(*82kWh*)
Diesel consumption (L/h)	1 [15]	0
Diesel price($/L)[a]	0.95	
Electricity price($/kWh)[b]	0.11	
Diesel cost ($)	63.65	0
Electricity cost ($)	0	9.02
Operation cost reduction		85.6%

a: https://www.globalpetrolprices.com/China/diesel_prices/; *b*: https://www.ceicdata.com/en/china/electricity-price?page=4.

dry air, respectively. $T_{e,a}$ and $T_{s,a}$ are the temperatures of dry air at the end and initial stage of the experiments. The m_w and ΔH_w are the mass and condensed enthalpy of water vapour, respectively.

The system COP is defined by:

$$COP = \left| \frac{Q_{PCM} + Q_{Al} + Q_{ma} + Q_{EG,inside}}{W} \right| \quad (7)$$

where W is total electricity consumption during the charging process; Q_{PCM}, Q_{Al}, $Q_{ma,}$ and $Q_{EG,inside}$ are the cold energy released by TES units (PCMs and aluminium frame), the internal moist air, and the sensible cold energy of HTF left inside the charging loop during the cooling process. They can be calculated by Eqs. (1)~(6).

3.3. The Energy Saving and Cost Reduction. The energy saving of the PCM-based TES container compared with that of diesel-powered reefer container can be obtained by Eq. (8).

$$E_s = \left(\frac{P_{Diesel} - P_{PCM}}{P_{Diesel}} \right) * 100\%, \quad (8)$$

where *Es* is the energy saving, P_{Diesel} is power consumption of diesel-powered reefer container, while P_{PCM} is the power consumption of the PCM-based container presented in this study.

The cost reduction of the PCM-based TES container compared with that of diesel-powered reefer container can be calculated by Eq. (9).

$$C_R = \left(\frac{C_{Diesel} - C_{PCM}}{C_{Diesel}} \right) * 100\%, \quad (9)$$

where C_R is the cost reduction, C_{Diesel} is the operation cost of a diesel-powered reefer container, while the C_{PCM} is the operation cost of the PCM-based container presented in this study.

4. Results and Discussion

The container was loaded with 22 tons of grapes and was transferred from *Dunhuang* to *Chengdu*, China, on 03/10/2018-06/10/2018 by road delivery. The loading of grapes into the container was completed at point A in Figures 4(a) and 5(a). The delivery distance and duration is 2362 km and 53 hours, see point B to C. The time evolution of the temperature and RH at the axial and vertical direction within the container can be seen in Figures 4 and 5, respectively.

4.1. Time Evolution of the Temperature and RH of the Container. Figures 4(a) and 4(b), and Figures 5(a) and 5(b) presented the time evolution of the temperature and relative humidity of the loaded container in the axial and the vertical direction, respectively. The temperature (T8) near the door side is the highest. However, in the perspective of the overall temperature distribution, the maximum temperature gap between the sensors is limited to ~2°C which indicates the uniformity of the overall temperature distribution. Besides, one can see that the temperatures close to the door are more sensitive to the door opening. In Figure 4(a), the T8 which is near the door shows the highest temperature change which is from 7°C to nearly 25°C.

By comparing Figures 4(b) and 5(b), the internal relative humidity of the container was found to be between 85% and 95%. The high relative humidity is helpful to keep the freshness of the carrying items.

4.2. Time Evolution of the Temperature and RH inside the Item. The time evolution of temperature inside the carrying items (Figure 6) showed that, during the whole delivery period, the temperature rose slightly until the completion of the delivery. When arriving at the destination, the temperature increased sharply after the doors were opened for unloading. One can notice that there was no obvious fluctuation of temperature in the process of transportation, which is beneficial to keep the freshness of the carrying items. Besides, the relative humidity inside the grapes was nearly 100% which means there is no risk of causing excessive dehydration. Hence, the PCM-based container performs a better temperature and humidity control compared that of the conventional refrigeration container which faces temperature fluctuations [12] and excessive dehydration [13] issues.

4.3. The System COP. The system COP for the dynamic operation carrying item can be calculated by Eq. (7). The total electricity consumed during the charging process is 82 kWh. It was found that the system COP was 1.73.

4.4. The Energy and Cost Reduction. Table 2 shows the energy and economic analyses of the diesel-powered container and the PCM-based container. The electricity consumption of the PCM-based TES container was obtained through the electric meter.

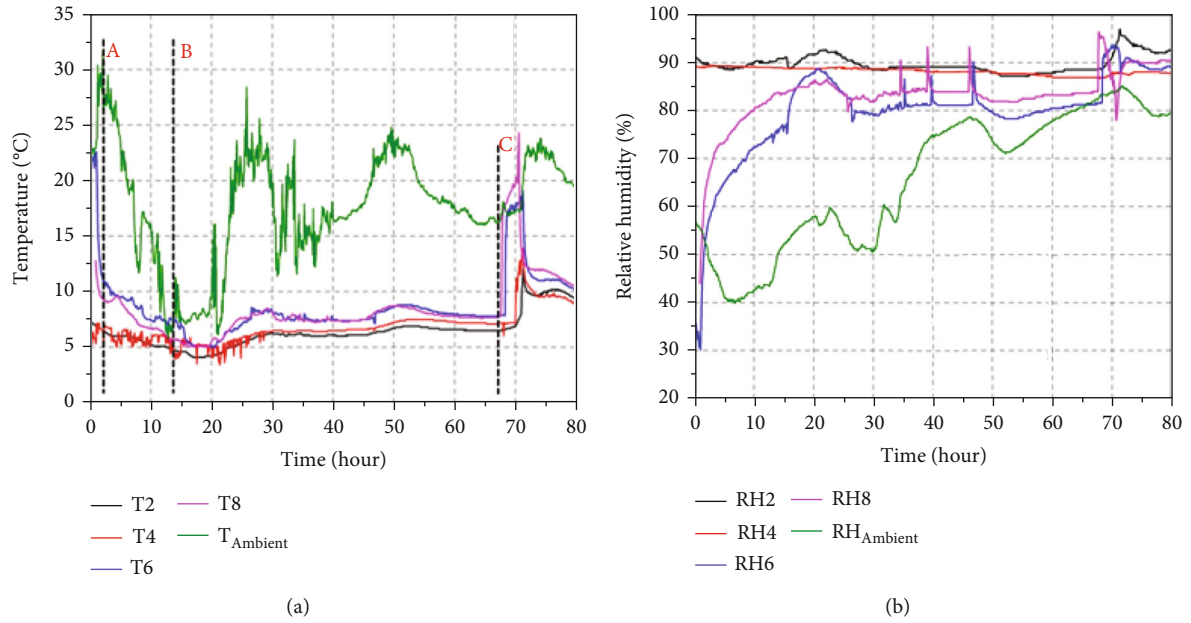

Figure 4: Time evolution of the temperature and RH inside the loaded conditioner under dynamic conditions (axial direction, a: temperature, b: relative humidity).

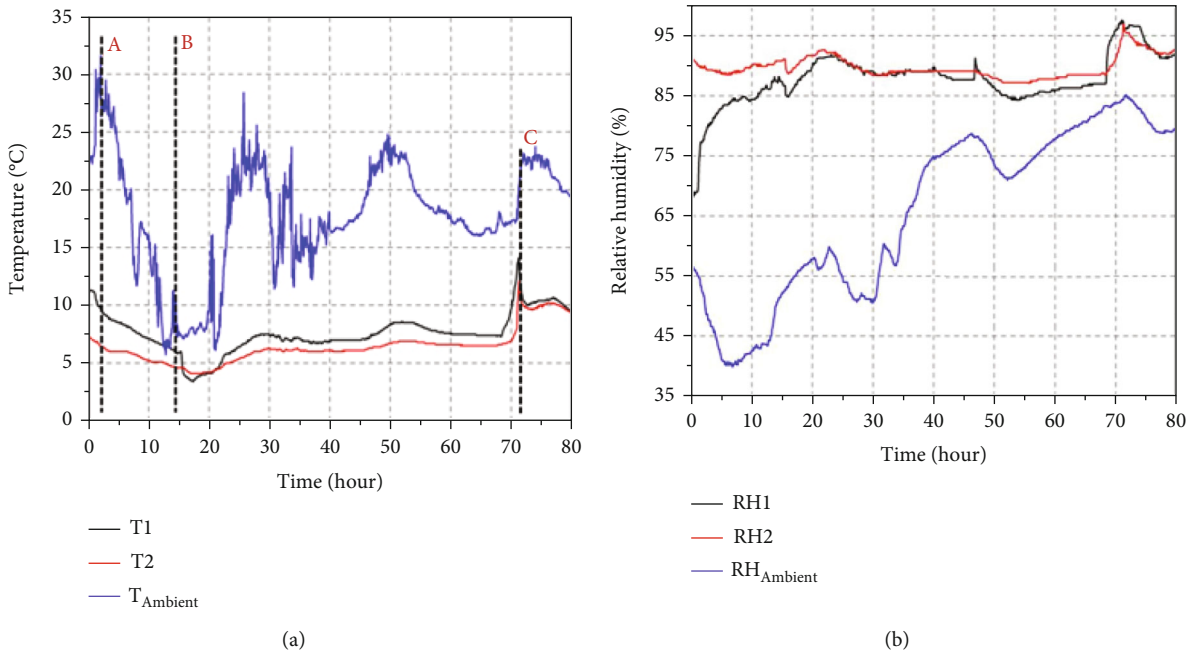

Figure 5: Time evolution of the temperature and RH inside the loaded conditioner under dynamic conditions (vertical direction, a: temperature, b: relative humidity).

The average power consumption of a PCM-based TES container is 1.55 kW, compared with that of the diesel-powered container, and the energy consumption was decreased by 71.3%, which is calculated by Eq. (8). Based on the average electricity tariff and diesel price in China, the cost can be reduced by 85.6%. This indicates the profitable benefit of the PCM-based TES container in the perspective of operation. The payback period was not included in this study as there is still a lack of yearly operations of the newly proposed container.

Both the electricity price and the operating strategy affect the economic performance of the PCM-based container. More profits could be obtained if the system is applied in a location with a peak-load shifting mode.

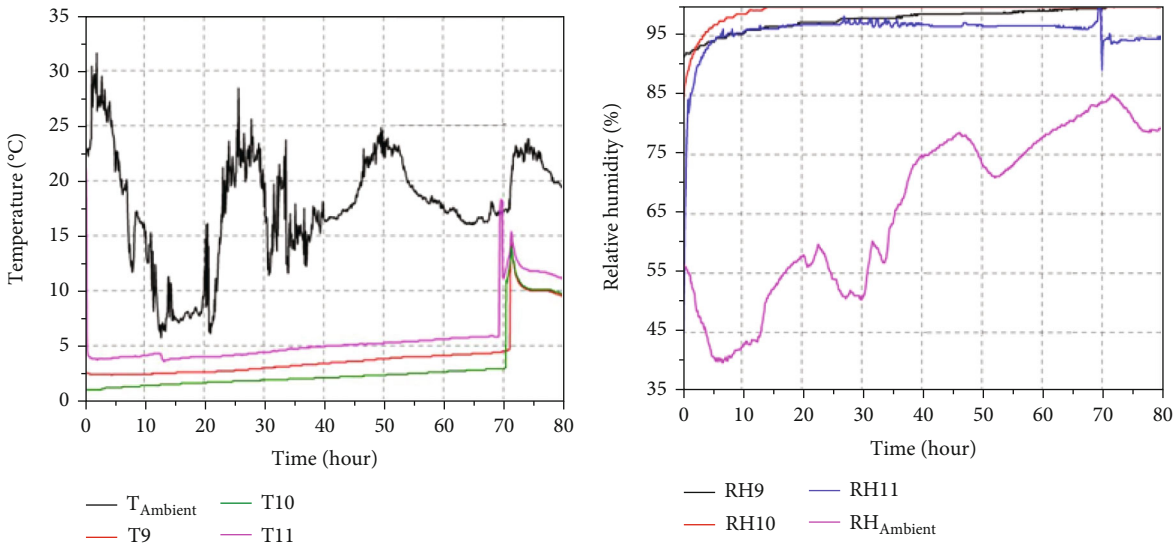

Figure 6: Time evolution of the temperature and RH inside the carrying items under dynamic conditions.

5. Conclusions

This work investigated the performance of a phase change material (PCM) based shipping container for cold chain transportation. The road test performance including the cooling duration and coefficient of the system (COP) of the container carrying items has been presented. Both energy and economic analyses were performed for comparing the diesel-powered and the PCM-based container scenarios in terms of energy consumption and operational cost. It was found that the system COP was 1.73 with the power and operation cost reduction at 71.3% and 85.6% when compared with the diesel-powered reefer container. This indicates the profitable benefit of the PCM-based TES container in the perspective of operation. Furthermore, the container can maintain at a low temperature without an external power supply which enables the container to be transferred flexibly. The improved flexibility and performance enhancement allow the container to be feasible for applications.

Nomenclature

c_p: Specific heat capacity (kJ kg^{-1} K^{-1})
H: Latent heat (kJ kg^{-1})
$\dot{m}$: Mass flow rate (kg s^{-1})
t: Time
m: Mass
T: Temperature (°C K^{-1})
v: Velocity (m s^{-1})
ρ: Density (kg (m$^{3)-1}$)
Q: Energy (kJ)
W: Electrical power (kJ)
\$: US dollar.

Subscripts

PCM: Phase change material
TES: Thermal energy storage
i: Inlet
o: Outlet
e: Ending
s: Starting
P: Power
w: Water vapour
a: Air flow
Al: Aluminium
EG: Ethylene glycol
RH: Relative humidity
Ch: Charging
Dis: Discharging.

Data Availability

The [DATA TYPE] data used to support the findings of this study are included within the article.

Conflicts of Interest

The authors declare that they have no conflicts of interest.

Acknowledgments

The authors acknowledge partial financial support CRRC Shijiazhuang Co., Ltd, CRRC Science and Technology Research and Development Project.

References

[1] M. Ahmed, O. Meade, and M. A. Medina, "Reducing heat transfer across the insulated walls of refrigerated truck trailers by the application of phase change materials," *Energy Conversion and Management*, vol. 51, no. 3, pp. 383–392, 2010.

[2] Z. Khan, Z. Khan, and A. Ghafoor, "A review of performance enhancement of PCM based latent heat storage system within

the context of materials, thermal stability and compatibility," *Energy Conversion and Management*, vol. 115, pp. 132–158, 2016.

[3] S. S. Chandel and T. Agarwal, "Review of current state of research on energy storage, toxicity, health hazards and commercialization of phase changing materials," *Renewable and Sustainable Energy Reviews*, vol. 67, pp. 581–596, 2017.

[4] J. D. Osorio, M. Panwar, A. Rivera-Alvarez et al., "Enabling thermal efficiency improvement and waste heat recovery using liquid air harnessed from offshore renewable energy sources," *Applied Energy*, vol. 275, p. 115351, 2020.

[5] E. Oró, A. de Gracia, A. Castell, M. M. Farid, and L. F. Cabeza, "Review on phase change materials (PCMs) for cold thermal energy storage applications," *Applied Energy*, vol. 99, pp. 513–533, 2012.

[6] B. Michel, P. Glouannec, A. Fuentes, and P. Chauvelon, "Experimental and numerical study of insulation walls containing a composite layer of PU-PCM and dedicated to refrigerated vehicle," *Applied Thermal Engineering*, vol. 116, pp. 382–391, 2017.

[7] M. Liu, W. Saman, and F. Bruno, "Development of a novel refrigeration system for refrigerated trucks incorporating phase change material," *Applied Energy*, vol. 92, pp. 336–342, 2012.

[8] M. Liu, W. Saman, and F. Bruno, "Computer simulation with TRNSYS for a mobile refrigeration system incorporating a phase change thermal storage unit," *Applied Energy*, vol. 132, pp. 226–235, 2014.

[9] R. Sepe, E. Armentani, and A. Pozzi, "Development and stress behaviour of an innovative refrigerated container with PCM for fresh and frozen goods," *Multidiscipline Modeling in Materials and Structures*, vol. 11, no. 2, pp. 202–215, 2015.

[10] "Journal List," in *Current Advances in Immunology*, pp. iii–iv, 2014.

[11] I. N. G. S. Waisnawa, I. D. M. C. Santosa, I. P. W. Sunu, and I. Wirajati, "Model development of cold chains for fresh fruits and vegetables distribution: a case study in Bali Province," *Journal of Physics: Conference Series*, vol. 953, p. 012109, 2018.

[12] N. T. T. Mai, B. Margeirsson, S. Margeirsson, S. G. Bogason, S. Sigurgísladóttir, and S. Arason, "Temperature mapping of fresh fish supply chains-air and sea transport," *Journal of Food Process Engineering*, vol. 35, no. 4, pp. 622–656, 2012.

[13] M. A. Delele, A. Schenk, H. Ramon, B. M. Nicolaï, and P. Verboven, "Evaluation of a chicory root cold store humidification system using computational fluid dynamics," *Journal of Food Engineering*, vol. 94, no. 1, pp. 110–121, 2009.

[14] M. A. Budiyanto and T. Shinoda, "The effect of solar radiation on the energy consumption of refrigerated container," *Case Studies in Thermal Engineering*, vol. 12, pp. 687–695, 2018.

[15] S. A. Tassou, G. De-Lille, and Y. T. Ge, "Food transport refrigeration - approaches to reduce energy consumption and environmental impacts of road transport," *Applied Thermal Engineering*, vol. 29, no. 8-9, pp. 1467–1477, 2009.

Hindawi
International Journal of Photoenergy
Volume 2022, Article ID 8149765, 7 pages
https://doi.org/10.1155/2022/8149765

Research Article

Study on Sunshine Stress Effect of Long-Span and Wide Concrete Box Girder

Wang Cheng,[1] **Zhang Chentian**,[2] **Li Shuo**,[3] **and Li Jianhua**[1]

[1]*CCCC Fourth Highway Engineering Co., Ltd., Beijing 100022, China*
[2]*Planning and Construction Bureau of Management Committee Xiong'an New Area, Hebei 071000, China*
[3]*Key Laboratory of HVAC, Beijing University of Civil Engineering and Architecture, Beijing 100044, China*

Correspondence should be addressed to Wang Cheng; 2918769791@qq.com

Received 30 October 2021; Revised 19 April 2022; Accepted 10 May 2022; Published 31 May 2022

Academic Editor: Alberto Álvarez-Gallegos

In order to further clarify the sunshine stress effect of long-span and wide concrete box girder, the study selected a concrete box girder with 4×42 m span and 33.5 m width, formed the temperature field load through a field test and numerical simulation, established a numerical analysis model by using the finite element program of ANSYS, and comprehensively analyzed the longitudinal temperature stress distribution of a long-span and wide concrete box girder under sunshine. The midspan section of the first span of the box girder is selected for field stress measure, and the field measure results and numerical analysis results are compared and analyzed. The research shows that the results of field measurement and numerical simulation are basically consistent. Sunshine temperature has a great influence on long-span and wide concrete box girder, which should be paid enough attention.

1. Introduction

With the rapid urban development, a long-span and wide concrete box girder is more and more widely used. On the one hand, it has greatly improved the urban operation efficiency and quality of life. On the other hand, it puts forward higher requirements for civil engineering technology. A long-span and wide-width concrete box girder is mostly used in outdoor space, such as large bridge structure and public facility structure, which requires high-temperature adaptability [1, 2]. At the same time, due to the complex structure and large temperature distribution gradient, the influence is more significant [3]. In this paper, the sunshine stress effect of long-span and wide concrete box girder is studied in Zhuhai Hengqin second bridge project.

2. Model Establishment

The Hengqin second bridge is located in the southwest of Zhuhai City. Its south approaching bridge is a cast-in-situ concrete box girder with a standard span of 42 m and a width of 33.5 m for the beam top plate and 17.50 m for the bottom plate. The beam height at the center line is 2.5 m, the top plate is 0.25 m thick, and the bottom plate is 0.25 m thick. It is locally thickened near the fulcrum to meet the stress needs of the structure. Figure 1 is the cross-section diagram of the large-span wide concrete box girder.

The longitudinal length of the bridge structure is much larger than the vertical length and transverse length. If the three-dimensional conduction property of temperature in some areas of the bridge structure is ignored, it can be considered that the temperature change of the bridge along the length direction is consistent. So the three-dimensional heat conduction problem can be simplified to analyze the one-dimensional heat conduction state along the transverse and vertical directions of the bridge [4, 5]. Therefore, only one section along the longitudinal direction of the bridge needs to be selected as a representative. The middle of the first span of the first part (4×42 m) is selected as the temperature and stress measure section, as shown in section A in Figure 2.

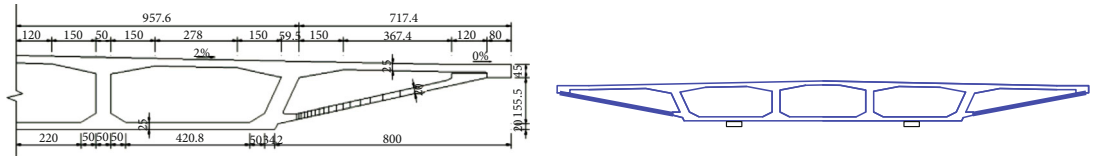

(a) Beam section size (b) Beam section layout

Figure 1: Cross-section diagram of the large-span wide concrete box girder.

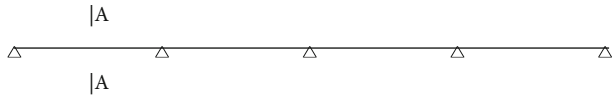

Figure 2: Diagram of the measure section position.

3. Temperature Field Measure

As shown in Figure 2, the temperature measure section is A-A. The temperature sensors are arranged and installed on the upper surface, lower surface, and web of the box girder [6], and the positions are shown in Figure 3.

According to the construction situation of the project, the temperature measure is conducted on a hot day for 24 hours [7]. Figure 4 shows the measured temperature results of the measuring points of the upper surface, lower surface, and web of the box girder within 24 hours.

Under the action of sunshine, the minimum vertical temperature difference occurs at 6 a.m. and the maximum temperature difference occurs at 14 a.m., with a temperature difference value of about 16°C. The transverse temperature difference of the upper surface is relatively uniform, and the maximum temperature difference value is 5°C. The transverse temperature difference of the lower surface is uniform, and the temperature difference value is less than 1°C. The temperature change law of each measuring point changes roughly according to the sinusoidal curve. The internal temperature distribution is uneven, and the temperature of the measuring point near the roof changes greatly during the day.

In order to facilitate engineering application, this study directly uses the field measured temperature value of the boundary as linear interpolation to form the temperature boundary condition of the outer surface of the box girder and then obtains the temperature distribution inside the box girder through steady-state thermal analysis[8, 9]. After the temperature field of the bridge structure is determined, the structural temperature load can be formed according to the thermophysical properties of the material itself [10].

4. Temperature Stress Measure

In order to study the effect of temperature effect, the temperature stress of the box girder is observed while observing the temperature field. The stress measure section of the box girder is the same as the temperature measure section [8], as shown in section A-A in Figure 1.

The layout position of the stress measure sensor is shown in Figure 5. The sensor is bound with the reinforcement and embedded in the structure before concrete pouring.

The measure lasted 24 hours from 14:00 p.m. to 14:00 p.m. the next day. A total of 13 measures were recorded once every two hours. The measure results accurately reflect the change of internal stress of the box girder in one day.

The measure result takes the result at 14:00 at the beginning of the test as the zero point, and the subsequent measure results are the difference from the results at that time. The greater the positive difference, the more it decreases. The greater the negative difference, the more it increases. Therefore, the measured value is not the specific stress but reflects the stress change caused by sunshine temperature [11].

5. Stress Time History Variation

The study selected the solid70 thermal analysis unit provided by ANSYS and ignored the influence of prestressed reinforcement on temperature distribution. The stress distribution of the box girder under the temperature field is calculated and compared with the measured data. The results are shown in Figure 6.

According to the analysis and statistical results of measured and calculated values, under the action of 24-hour solar radiation, the longitudinal compressive stress of the box girder roof gradually decreases with the continuous decrease in temperature. On the contrary, when the temperature rises, the longitudinal compressive stress increases gradually. The variation law and amplitude of measured and calculated values are basically the same, and the maximum error is about 15%. At 14:00 p.m. or 16:00 p.m., the compressive stress at each measuring point of the roof reaches the maximum value. The compressive stress decreases rapidly after dusk and remains at a low level at night and begins to rise rapidly after 8:00 a.m. the next day.

6. Spatial Distribution of Box Girder Stress

6.1. Overall Stress Analysis. Taking 14:00 p.m. with the highest roof temperature and 6:00 a.m. with the lowest temperature difference between roof and floor as examples, Figures 7–14 describe the stress distribution of the roof, lower surface, and the middle section of the first span.

It can be seen from the figure that the roof is subjected to large compressive stress at 14 p.m., the maximum local compressive stress is about 8×10^6 Pa, and the compressive stress of the bottom plate is about 2×10^6 Pa. It can be seen from the midspan section that the middle of the web is under

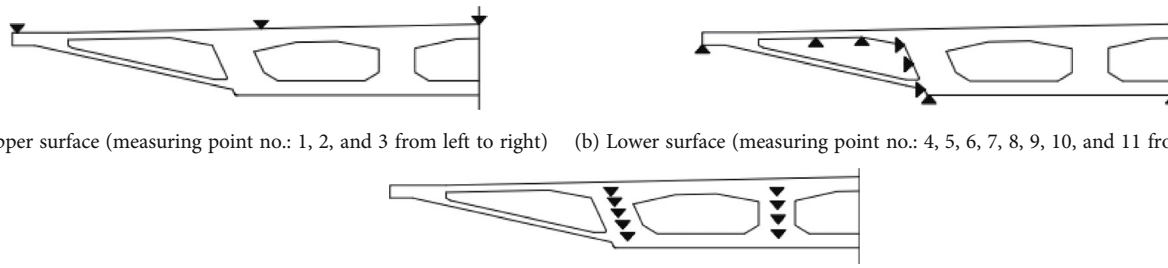

(a) Upper surface (measuring point no.: 1, 2, and 3 from left to right) (b) Lower surface (measuring point no.: 4, 5, 6, 7, 8, 9, 10, and 11 from left to right)

(c) Web (measuring point no.: the left side is 12, 13, 14, 15, and 16 from top to bottom;the right side is 17, 18, 19, and 20 from top to bottom)

Figure 3: Layout diagram of beam temperature measuring points.

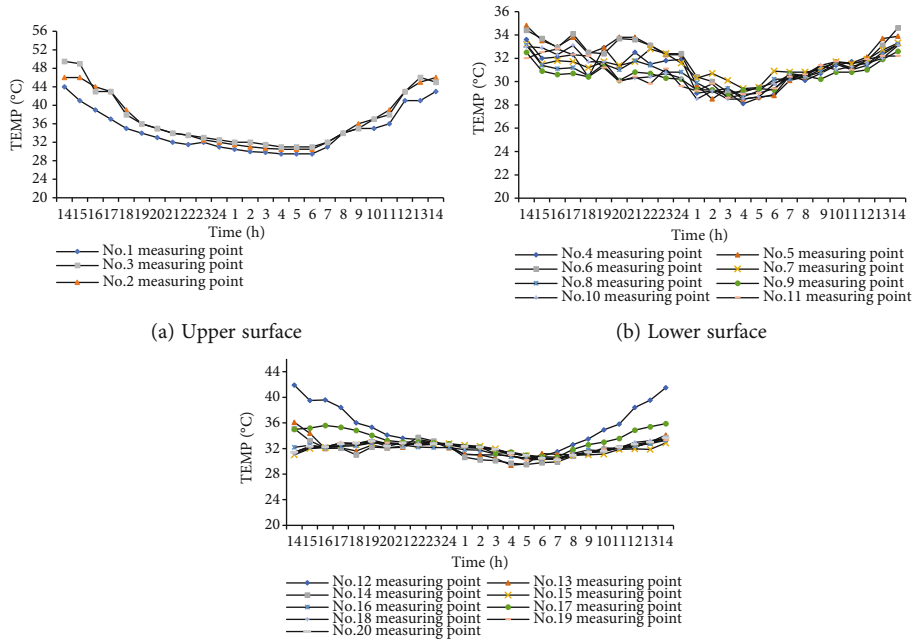

(a) Upper surface (b) Lower surface

(c) Web

Figure 4: Beam temperature measured results.

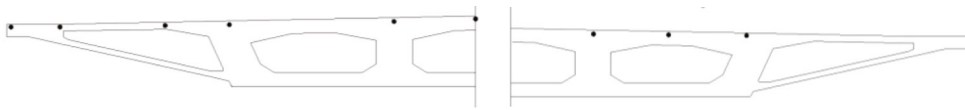

Figure 5: Layout diagram of stress sensor (the horizontal coordinate is 0 at the left end of the cross section).

the action of tensile stress, and there is a large tensile stress at the bottom of the top plate, which is more than 2.5×10^6 Pa. The transverse and longitudinal distribution of stress in the top plate and bottom plate is uneven.

At 6 a.m., the compressive stress value of the top plate is small, the bottom plate is partially compressed and partially tensioned, and the value is small. The horizontal and vertical distribution of the stress in the box is relatively uniform.

6.2. Analysis of Transverse Distribution of Roof Stress. According to the time history stress analysis, the maximum stress of the roof and the maximum vertical stress gradient appeared at 14 p.m.

Figure 15 shows the calculation results of transverse distribution of longitudinal stress of roof at 14 p.m. It can be seen from the results that the roof is in compression, and the longitudinal compressive stress in the middle is the largest, about 8.4×10^6 Pa. The transverse distribution of stress is "V" shape as a whole, and the stress decreases gradually from the middle of the section to both sides.

The main reasons for the uneven transverse distribution of stress are as follows: (1) the shear lag effect of the box girder reduces the longitudinal stress of the cantilever section and (2) the difference of stiffness between the middle and both sides of the roof leads to the difference of transverse stress distribution [12].

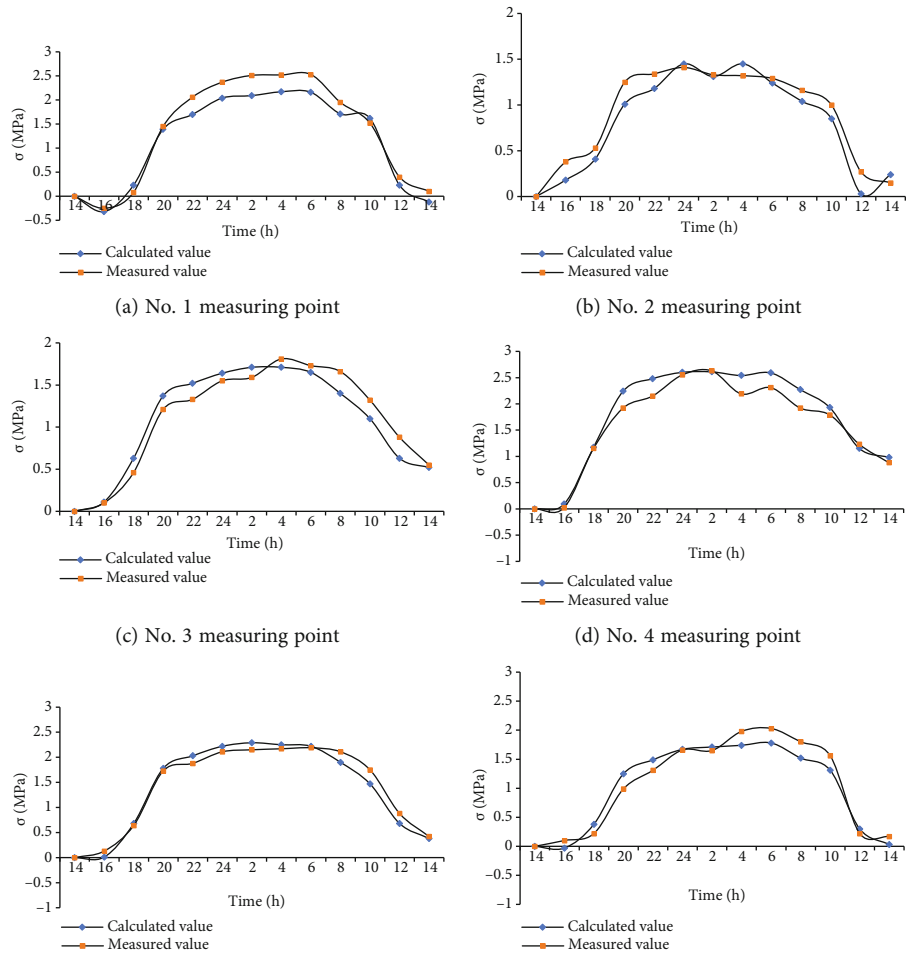

(a) No. 1 measuring point

(b) No. 2 measuring point

(c) No. 3 measuring point

(d) No. 4 measuring point

(e) No. 5 measuring point

(f) No. 6 measuring point

Figure 6: Time history diagram of temperature stress comparison.

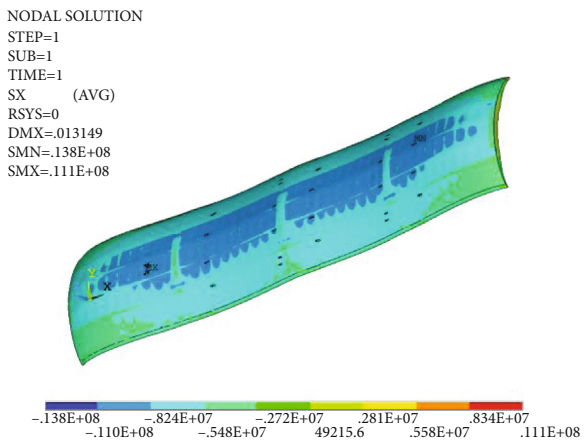

Figure 7: Longitudinal stress distribution at 14 (roof)/Pa.

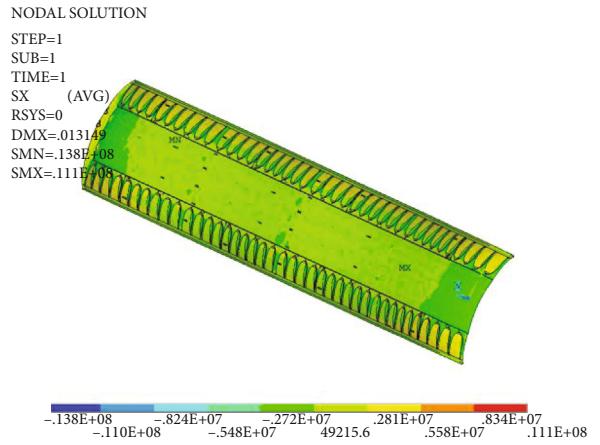

Figure 8: Longitudinal stress distribution at 14 (lower surface)/Pa.

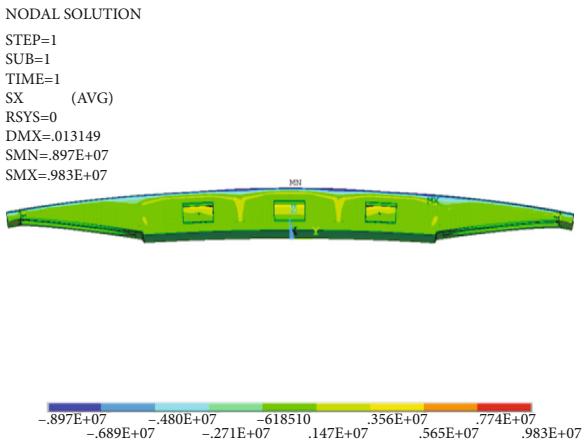

Figure 9: Longitudinal stress distribution at 14 (middle of the first span)/Pa.

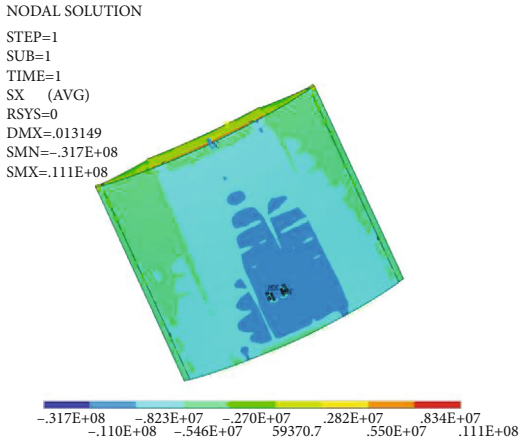

Figure 10: Longitudinal stress distribution at 14 (roof of the first span)/Pa.

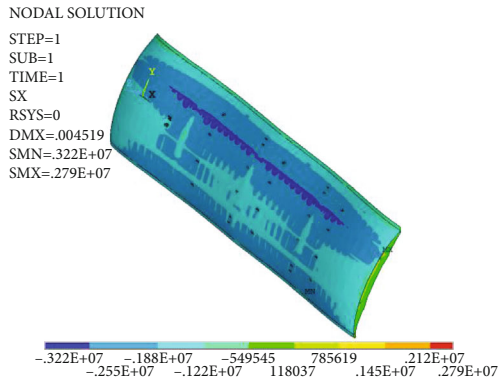

Figure 11: Longitudinal stress distribution at 6 (roof)/Pa.

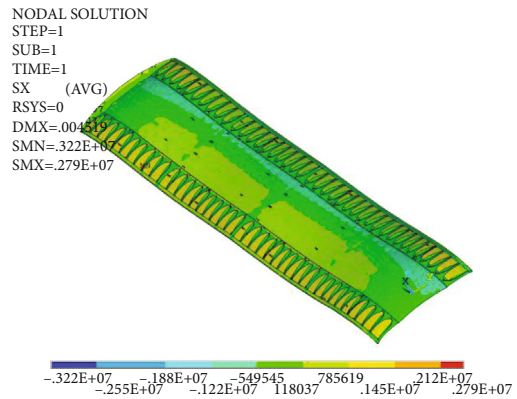

Figure 12: Longitudinal stress distribution at 6 (lower surface)/Pa.

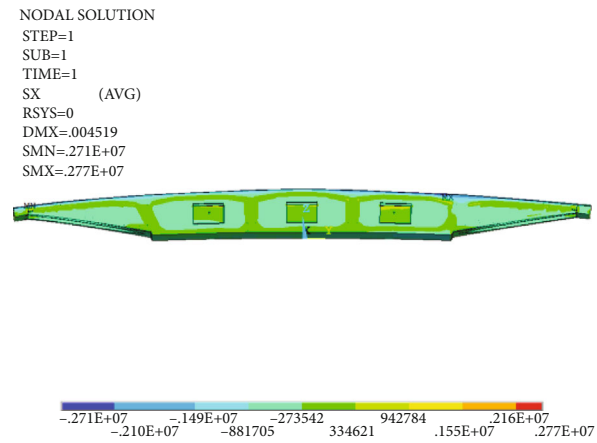

Figure 13: Longitudinal stress distribution at 6 (middle of the first span)/Pa.

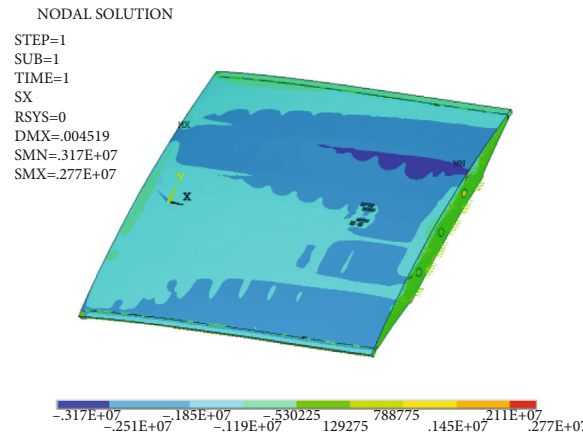

Figure 14: Longitudinal stress distribution at 6 (roof of the first span)/Pa.

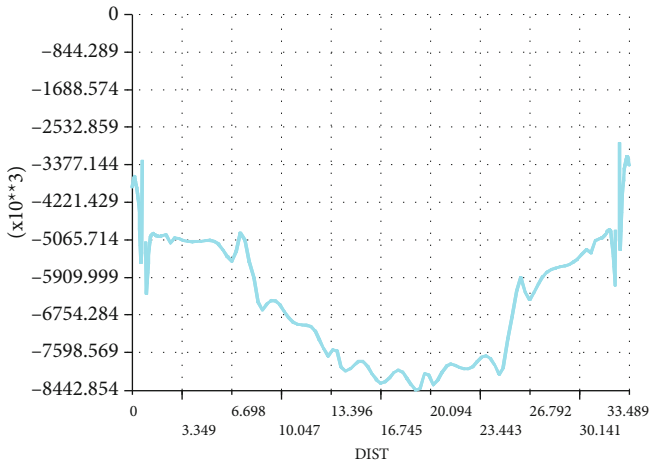

Figure 15: Longitudinal stress distribution of the roof (the ordinate is stress (Pa); the abscissa is distance (m)).

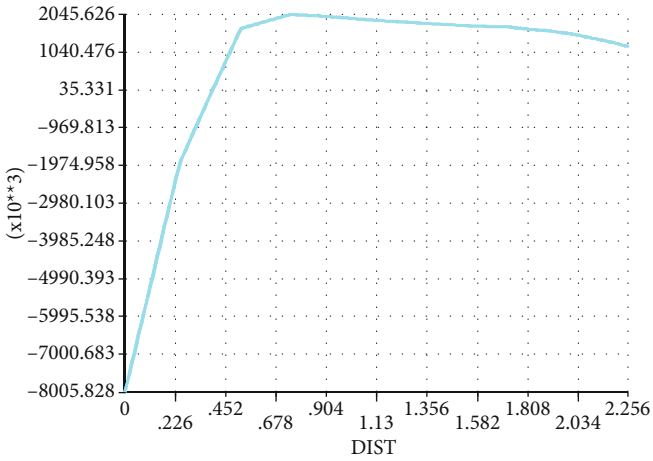

Figure 16: Vertical distribution of longitudinal stress of the web in the middle of the first span (the ordinate is stress (Pa); the abscissa is the distance from the top plate (m)).

6.3. Vertical Stress Distribution of the Box Girder. As can be seen from Figure 16, the compressive stress decreases rapidly with the increase in the distance from the top plate, and the maximum tensile stress appears at the web, which is about 2×10^6 Pa. The critical height point from compressive stress to tensile stress is 30 cm away from the top plate.

7. Conclusion

(1) Based on the field measure and numerical simulation, the time history variation of box girder stress and its uneven spatial distribution are analyzed. Result shows that the simulated value is basically consistent with the measured value, and the maximum error is about 15%. The numerical simulation method is more practical

(2) At 14 p.m., the compressive stress on the top plate of the box girder is large and unevenly distributed, the maximum value of local longitudinal compressive stress is about 8×10^6 Pa, and the stress of the bottom plate is about 2×10^6 Pa. It is necessary to strengthen the structural protection management in different periods of the project site

(3) The transverse distribution of the longitudinal compressive stress of the roof is in a "V" shape as a whole, and the stress decreases gradually from the middle of the section to both sides

(4) The middle and top of the box girder web are subjected to tensile stress. The longitudinal tensile stress at the top of the web is large, exceeding 2.5×10^6 Pa

In short, the sunshine radiation, especially in the case of superimposed dynamic and static loads, has a great impact on the long-span and wide concrete box girder, which should be paid enough attention in the process of design, construction, and use.

Data Availability

The data used to support the findings of this study are available from the corresponding author upon request.

Conflicts of Interest

The authors declare that they have no known competing financial interests or personal relationships that could have appeared to influence the work reported in this paper.

Acknowledgments

The authors are grateful to the financial support of the Scientific Research Program of Beijing Municipal Education Commission (Grant No. KM201910016011) and the Beijing Municipal Natural Science Foundation (3151001).

References

[1] S. Yaqiong and Z. H. Zuo-zhou, "Real-time separation of temperature effect on dynamic strain monitoring and moving load identification of structure," *Engineering Mechanics*, vol. 36, no. 2, pp. 186–194, 2019.

[2] Z. Jianrong, Z. Yuanqiang, L. Jianping, and Z. Zhiyan, "Solar radiation affection on concrete box girder temperature effect," *Journal of Tongji University*, vol. 36, no. 11, pp. 1429–1484, 2008.

[3] W. Gao-xin, D. You-liang, L. Ai, and Z. H. Guang-dong, "Characteristics of transverse temperature differences of steel box girder in run yang cable-stayed bridge using long-term monitoring," *Engineering Mechanics*, vol. 30, no. 1, pp. 163–167, 2013.

[4] L. Yaozhi and D. Shilin, "Mechanical behavior and system changing of cable-truss structures," *Spatial Structures*, vol. 8, no. 4, pp. 45–53, 2002.

[5] L. Yang and W. Z. Y. Yongbin, "Sequentially coupled thermal stress analysis of the prestressed concrete box girder," *Concrete*, vol. 32, no. 10, pp. 139–143, 2015.

[6] L. Lu Jinyu and Q. X. Ding, "Elasto-plastic buckling analysis of novel origami-inspired steel plate shear wall with two-side connections," *Advanced Engineering Sciences*, vol. 50, no. 6, pp. 8–14, 2018.

[7] L. Yong-jian, L. Jiang, and Z. Ning, "Review on solar thermal actions of bridge structures," *China Civil Engineering Journal*, vol. 52, no. 5, pp. 59–78, 2019.

[8] Q. Juntao, Y. Chen, Z. Feng, and L. Xiaoyan, "Study of temperature effect on the composed bridge with corrugated steel webs," *Highway*, vol. 61, no. 3, pp. 54–57, 2016.

[9] D. O. N. G. Xu, D. E. N. G. Zhen-quan, L. I. Shu-chen, G. U. Shou-fa, and Z. H. A. N. G. Feng, "Research on sunlight temperature field and thermal difference effect of long span box girder bridge with corrugated steel webs," *Engineering Mechanics*, vol. 34, no. 9, pp. 230–238, 2017.

[10] J. Vacha, P. Kyzlik, I. Both, and F. Wald, "Beams with corrugated web at elevated temperature, analytical and numerical models for heat transfer," *Fire Safety Journal*, vol. 86, no. 11, pp. 83–94, 2016.

[11] China National Standard, *General Specification for Design of Highway Bridges and Culverts (JTG D60)*, CCCC Highway Planning and Design Institute Co., Ltd., Ed., China Communications Press, 2015.

[12] Chinese National Standard, *Load Code for the Design of Building Structures (GB 5009)*, China Academy of Building Research, Ed., China Construction Industry Press, 2012.

Hindawi
International Journal of Photoenergy
Volume 2022, Article ID 9607545, 6 pages
https://doi.org/10.1155/2022/9607545

Research Article

Intelligent Energy Management System for a Smart Home Integrated with Renewable Energy Resources

Arjun Baliyan,[1] **Isaka J. Mwakitalima**,[2] **Majid Jamil**,[1] **and M. Rizwan**[3]

[1]*Department of Electrical Engineering, Jamia Millia Islamia, New Delhi 110025, India*
[2]*Department of Electrical and Power Engineering, Mbeya University of Science and Technology, P.O. Box 131, Mbeya, Tanzania*
[3]*Department of Electrical Engineering, Delhi Technological University, Delhi 110042, India*

Correspondence should be addressed to Arjun Baliyan; arjunresearch16@gmail.com

Received 24 October 2021; Revised 21 December 2021; Accepted 19 January 2022; Published 8 February 2022

Academic Editor: Yaxuan Xiong

In this paper, an intelligent energy management system for the smart home that combines the solar energy as well as the energy from the battery storage devices has been proposed to reduce the dependency on the power grid and make the system to be more economical. The proposed system manages the energy requirement of the smart home by properly rescheduling and arranging the power flow between the energy storage devices, grid power, and the photovoltaics. The power grid can absorb the excess power from the designed system whenever the load requirement is low, and on the other hand, it can supply the power to the load in case of peak demand. Therefore, in the designed system, a user has the flexibility to sell the extra power for the purpose of revenue. A thorough simulation of the system has been carried out, and the results obtained show the effectiveness of the approach in terms of energy management between the different sources.

1. Introduction

Renewable energy resources (RER) are getting popularity nowadays since they are environmentally friendly and available in abundance. Also, due to the rapid decline in the conventional energy resources, the renewable sources are the best alternative to replace them. A home energy management (HEM) system is basically a system that has been designed with the help of renewable energy resources with an aim to reduce the overall energy consumption. This type of configuration is usually done in order to reduce the electricity bill and manage the peak load demand. Apart from it, the research on converting the power grid into smart grid by combining the already existing grid with the renewable energy resources will further reduce the dependency on the conventional energy resources [1]. In the recent years, research topics focus on home energy management integrated with storage devices and the photovoltaics [2–9]. In [2–5], the authors have considered energy cost minimization as an optimization problem based on the unpredictable behaviour of the output from the renewable energy resources. In [6–8], demand response (DR) programs have been explained for the priority wise rescheduling of the load based on the prediction of renewable energy (RE) output. In [9], the dependence on the battery and its characteristics have been explained and how they can be useful in-home energy management. In [10, 11], the photovoltaic integrated with the home energy management is discussed in detail. Although a lot of discussion on the integration of energy storage units and photovoltaics with the HEM have been explained in the literature [12–14], but still there are certain issues that need to be resolved. For example, how the battery can play an important role in case the power from the solar panel is not sufficient to fed the load and how much benefit the renewable sources of energy can provide in case of peak load demand. This paper resolves one of the such issues by proposing an integration of storage devices and photovoltaics with the HEM that provides surplus power to the grid

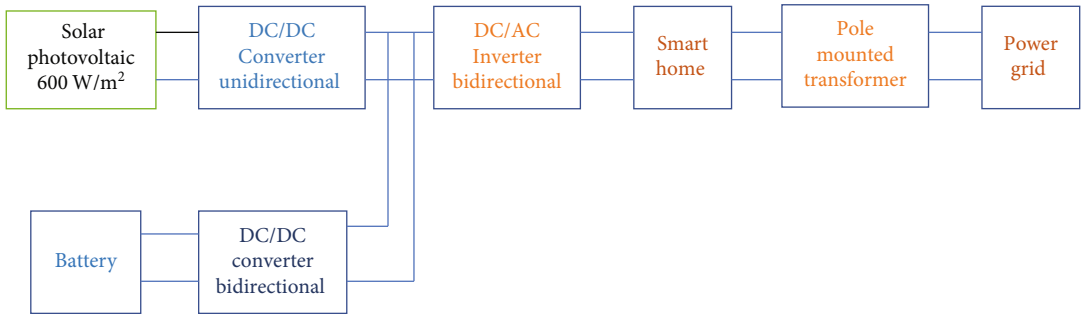

Figure 1: Block diagram of the system.

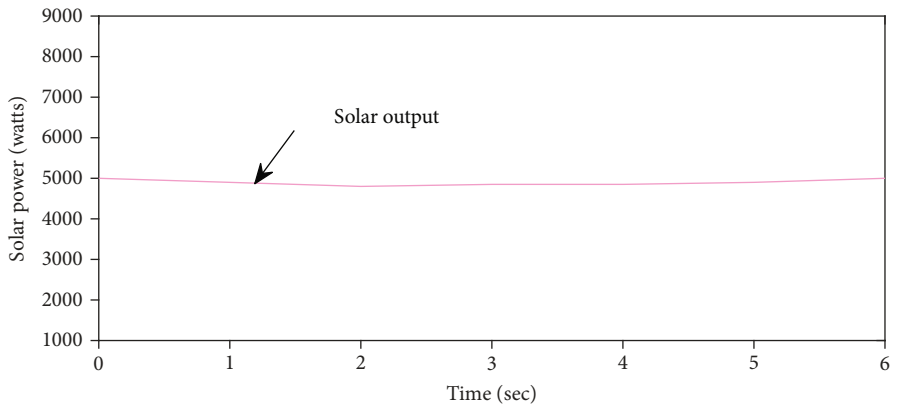

Figure 2: Solar panel output.

Table 1: Battery specifications.

S. no.	Battery parameters	Values
(1)	Nominal voltage	24 V
(2)	Ampere-hour	40 Ah
(3)	State of charge (SOC)	80%
(4)	Fully charged voltage	232.7 V

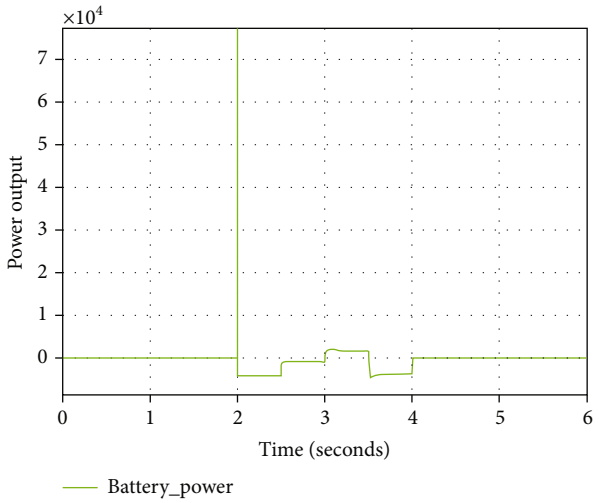

Figure 3: Battery characteristics.

as well as absorb power in case of deficiency. Hence, a perfect balance is maintained to make the system more reliable and economical.

The paper is arranged as per the following sections: Section 2 describes the proposed system, Section 3 explains the obtained simulation results, and Section 4 finally concludes the paper.

2. Simulation Components of Proposed System

This method explains how the existing HEM model can be integrated with the renewable energy resources and the battery storage devices. The block diagram of the above proposed system is given in Figure 1.

Photovoltaics and battery storage devices are working as a complementary power source for a smart home. The rating of photovoltaic system is 5 kW and is described by the current voltage look up table. In order to track the maximum power point, MPPT control algorithm has been used which extracts maximum power under variable system conditions.

2.1. Photovoltaic (PV) System. In this system, PV and the storage device models are developed in order to make the HEM system to operate in integration with the renewable energy resources. To track the maximum power from the solar panel, MPPT technique [15] has been applied which manages the operating point of the array in such a way that

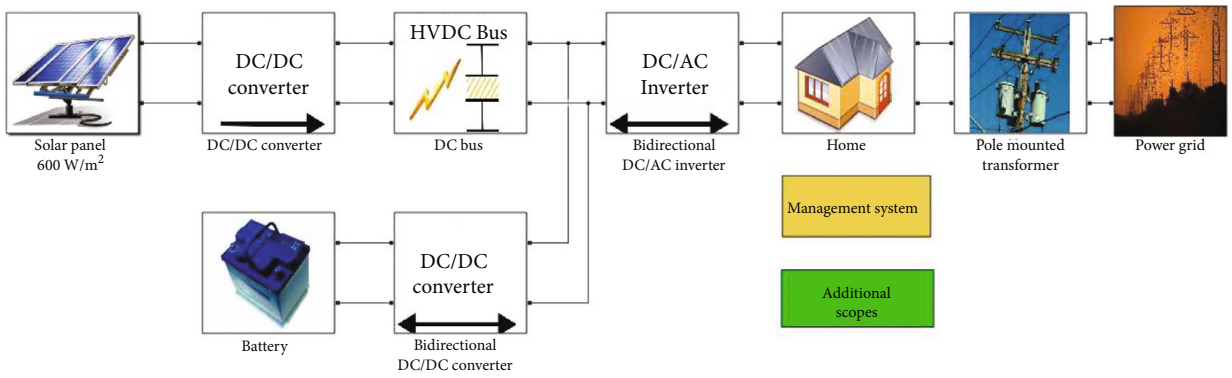

Figure 4: Simulation of the proposed system.

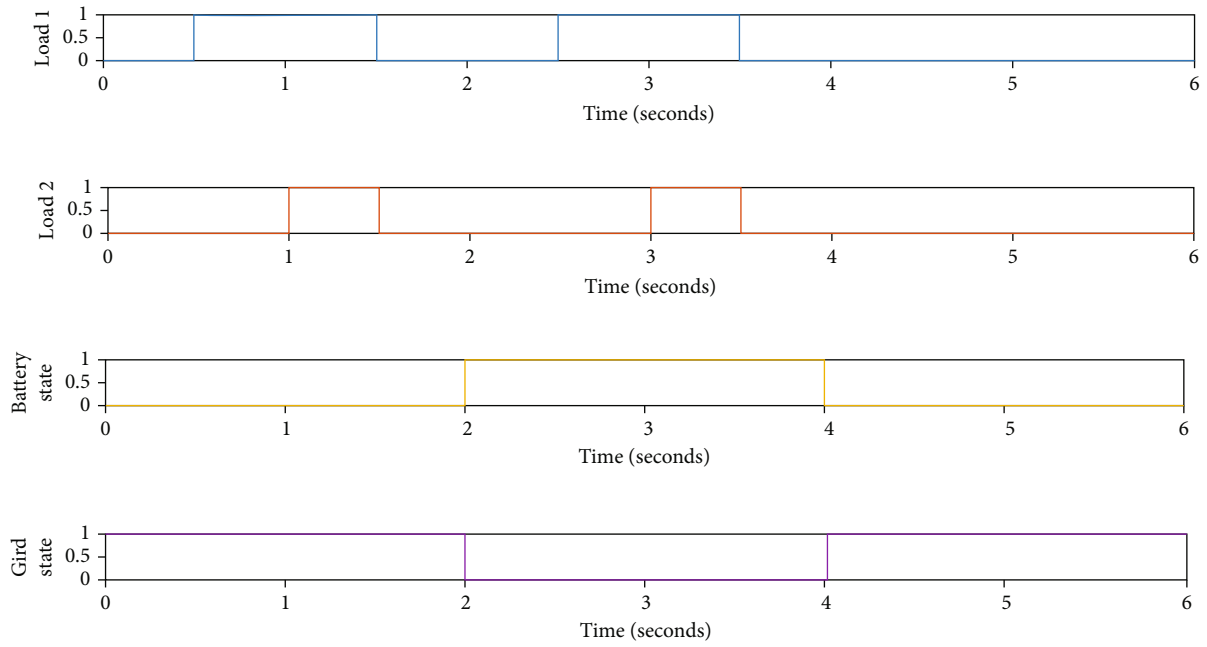

Figure 5: Switching characteristics of loads, battery, and power grid.

it always obtains the maximum power in the different varying conditions.

For photovoltaic system, the energy output or the energy delivered is given by the following

$$E_B = Q\rho_A C_{gt} t\left(1-\delta_p\right)\left(1-\delta_c\right), \quad (1)$$

where Q is the array area in m^2, ρ_A is the average efficiency of an array (%), C_{gt} is the global radiation, T is the time period in secs, δ_p is the PV panel losses (%), and δ_c is the power conditioning losses (%).

And the power absorbed by the grid can be defined as follows:

$$E_{\text{grid}} = E_B * \beta_{\text{inv}} * \beta_{\text{abs}}, \quad (2)$$

where E_B is the energy by PV panel, β_{inv} is the inverter efficiency (%), and β_{abs} is the PV panel energy absorption (%).

Figure 2 shows the output from solar panel which is around 5 kW.

2.2. Battery Characteristics. A 200 V and 40 Ah lithium-ion battery is used as a storage device to provide the power in case of peak load demand. The battery specifications are mentioned in Table 1. The battery is charged and discharged with the help of bidirectional converter that takes power from the solar panel while charging and fed the load when solar panel alone is not enough to feed the total load demand. The battery model that has been used in the paper is explained in [16]. In the proposed system, total loads of 3 kW each are taken, and it was observed that in case when both the loads are ON, the solar panel was not sufficient to provide power, since the total capacity of solar photovoltaic is 5 kW.

The battery output power (W) is shown in Figure 3. It is clear from the figure that from time $t = 0$ to $t = 2$ secs and $t = 4$ sec to $t = 6$ secs the battery is not functioning so the extra power has to be taken from grid for that time instant.

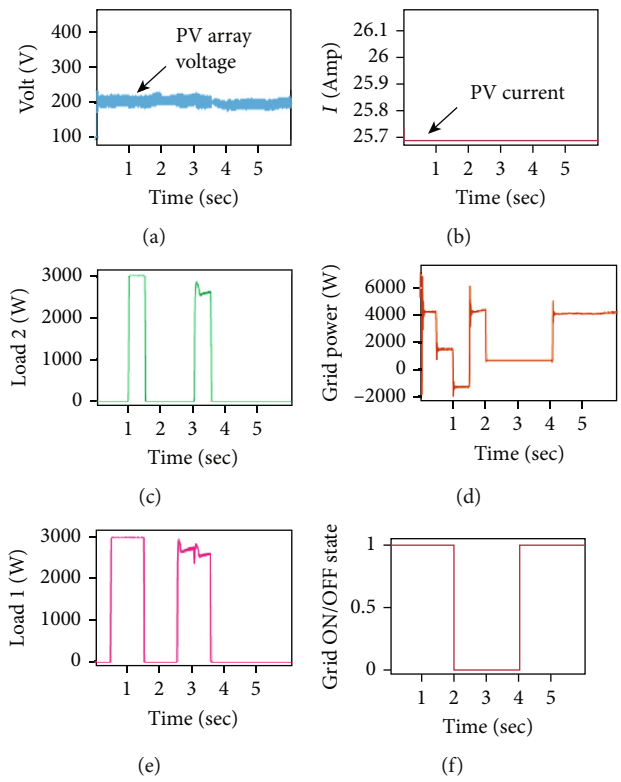

Figure 6: Load, grid, and solar photovoltaic characteristics.

3. Simulation Results

Initially, the battery was not connected to the system, and the loads were also disconnected, so therefore, the total solar power was transferred to the grid. The power generated by the panel was almost constant at 5 kW, and it was obtained by MPPT control algorithm.

Case 1. One of the two loads of 3 kW was turned on, and it was observed that it was consuming more than half of the power produced by the solar panel, and therefore, the excess power is again transferred to the grid.

Case 2. Both the loads are turned on, and the total power demand reaches to 6 kW, so therefore, the solar panel was not sufficient, and hence, the power demand was met by the grid.

Case 3. Now the loads are again disconnected, and the battery is connected which ensures that the total power as the combination of solar energy and storage devices is sufficient to meet the load demand when both the loads are again connected to the system in the same fashion as they were connected.

Figure 4 shows the simulation of the proposed system with renewable sources integrated with the power grid.

From Figure 5, it is clear that initially out of the two loads only one was switched at instant $t = 0.5$ sec and at $t = 1$ secs; both the loads were on, and therefore, the grid has to supply the extra power to meet the load demand. It is also clearly visible that between the time instant $t = 2$ secs to $t = 4$ secs, the battery was delivering the power, and hence, the power delivered by the grid was zero. Figure 6 depicts the photovoltaic, grid power, and the load characteristics.

It can be seen from the figure that at time instant $t = 1$ sec, the total load demand hits 6 kW as clear from Figures 6(c) and 6(e) since the total load adds up at that time instant, but before that, only load 1 was active, and therefore, the grid that was absorbing the surplus power before $t = 1$ sec has to now deliver the power that can be clearly visible from Figure 6(f). But again, at $t = 2$ sec, both the loads are in OFF state, and the battery is now in the on state, so therefore, the power will now be delivered to the grid, and the grid remains in off state. Also, Figure 6(d) shows the continuous power variation that indicates the power absorbed as well as power delivered by the grid for the entire time duration which depends on the changing load conditions. Similarly, Figures 6(a) and 6(b) give the insight of the photovoltaic (PV) voltage and current that is continuously varying according to the solar insolation. Figure 7 depicts the grid power components, solar power that remains almost constant throughout the time period, and load demand.

In the above figure, power delivered from the different renewable energy sources as well as the power absorbed by the load configuration is shown to have a better clarity of the proposed system and how it is able to manage the changing load demand with proper switching between the RER and grid power. In continuation of the above power flow diagram, Figure 7(a) shows the power taken by the grid as well as power supplied in case of changing load conditions

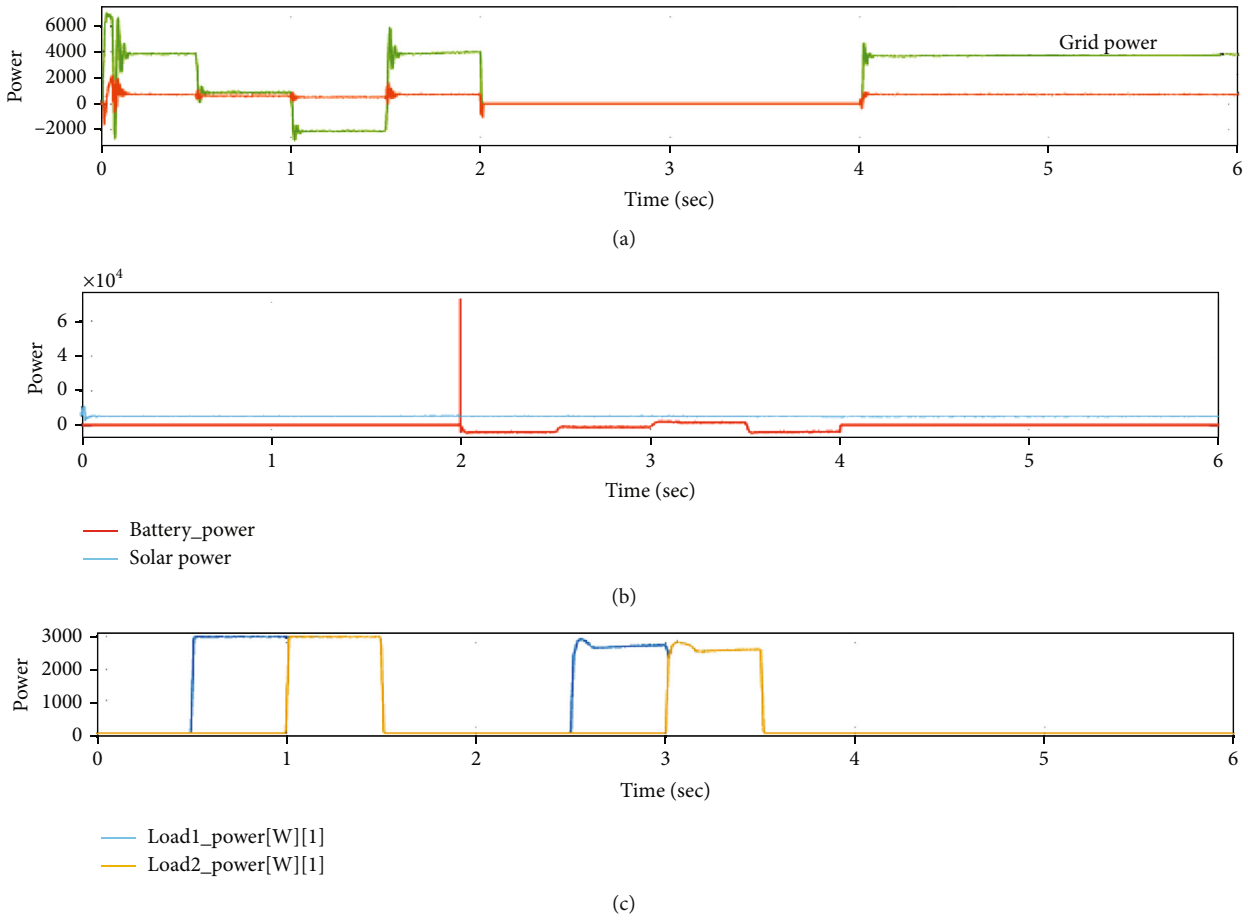

Figure 7: Power flow diagram.

Table 2: System parameters.

S. no	Parameters	Values
(1)	Solar panel	5 kW
(2)	System loads (load 1 and load 2)	6 kW
(3)	Power grid (phase to phase voltage)	66 kV
(4)	Switching frequency	10 kHz
(5)	Reference voltage (V_{dc})	370 V
(6)	Inverter controller gain parameters Tuned with PSO technique	$K_{P1} = 0.01, K_{I1} = 25$ $K_{P2} = 2.5, K_{I2} = 2.5$

and the power availability conditions. Figure 7(b) shows the variation in battery power and the solar power needed to feed the load in case of excess load demand. Similarly, Figure 7(c) illustrates the switching load pattern which clearly shows the maximum and minimum load demand in the entire time duration. The different system parameters and their values are given in Table 2.

4. Conclusion

This paper presents an idea of load management in case of base and peak load demand by integrating the supply with the renewable energy resources. It consists of various energy producing sources that is solar and battery storage devices as well as different energy consuming devices, called loads. Here, the switching between the different energy sources is done for energy management, and the results are shown in MATLAB. It is clear from the above results that the dependency on the grid is minimized, and even the consumer can now provide surplus power to the grid which will ultimately increase the overall revenue. The simulation shows how the HEM integrated with renewable sources is useful for residential load management, and further studies could be done in order to allow HEM to manage the different residential loads with respect to time-of-use pricing.

Data Availability

There is no data taken from any source.

Conflicts of Interest

The authors have no conflicts of interest regarding this article.

References

[1] M. Lissere, T. Sauter, and J. Y. Hung, "Future energy systems: integrating renewable energy sources into the smart power

grid through industrial electronics," *IEEE Industrial Electronics Magazine*, vol. 4, no. 1, pp. 18–37, 2010.

[2] C. Cecati, C. Citro, and P. Siano, "Combined operations of renewable energy systems and responsive demand in a smart grid," *IEEE Transactions on Sustainable Energy*, vol. 2, no. 4, p. 468476, 2011.

[3] Y. Guo, M. Pan, and Y. Fang, "Optimal power management of residential customers in the smart grid," *IEEE Transactions on Parallel and Distributed Systems*, vol. 23, no. 9, pp. 1593–1606, 2012.

[4] H. Wu, M. Shahidehpour, and A. Al-Abdulwahab, "Hourly demand response in day-ahead scheduling for managing the variability of renewable energy," *IET Generation Transmission and Distribution*, vol. 7, no. 3, pp. 226–234, 2013.

[5] Y. Guo, M. Pan, Y. Fang, and P. P. Khargonekar, "Decentralized coordination of energy utilization for residential households in the smart grid," *IEEE Transactions on Smart Grid*, vol. 4, no. 3, pp. 1341–1350, 2013.

[6] A. Papavasiliou and S. S. Oren, "Large-scale integration of deferrable demand and renewable energy sources," *IEEE Transactions on Power Systems*, vol. 29, no. 1, pp. 489–499, 2014.

[7] X. Liu, L. Ivanescu, R. Kang, and M. Maier, "Real-time household load priority scheduling algorithm based on prediction of renewable source availability," *IEEE Transactions on Consumer Electronics*, vol. 58, no. 2, pp. 318–326, 2012.

[8] S. Chen, N. B. Shroff, and P. Sinha, "Heterogeneous delay tolerant task scheduling and energy management in the smart grid with renewable energy," *IEEE Journal on Selected Areas in Communications*, vol. 31, no. 7, pp. 1258–1267, 2013.

[9] J. Byun, I. Hong, and S. Park, "Intelligent cloud home energy management system using household appliance priority-based scheduling based on prediction of renewable energy capability," *IEEE Transactions on Consumer Electronics*, vol. 58, no. 4, p. 11941201, 2012.

[10] P. T. V. B. N. Kumar, S. Suryateja, G. Naveen, M. Singh, and P. Kumar, "Smart home energy management with integration of PV and storage facilities providing grid support," in *2013 IEEE Power & Energy Society General Meeting*, pp. 1–5, Vancouver, BC, Canada, July 2013.

[11] C.-S. Choi, J. I. Lee, and I.-W. Lee, "Complex home energy management system architecture and implementation for green home with Built-in Photovoltaic and motorized blinders," in *2012 International Conference on ICT Convergence (ICTC)*, pp. 295-296, Jeju, Korea (South), Oct 2012.

[12] M. Pipattanasomporn, M. Kuzlu, and S. Rahman, "An algorithm for intelligent home energy management and demand response analysis," *IEEE Transactions on Smart Grid*, vol. 3, no. 4, p. 21662173, 2012.

[13] M. Kuzlu, M. Pipattanasomporn, and S. Rahman, "Hardware demonstration of a home energy management system for demand response applications," *IEEE Transactions on Smart Grid*, vol. 3, no. 4, pp. 1704–1711, 2012.

[14] A. Q. H. Badar and A. Anvari-Moghaddam, "Smart home energy management system – a review," *Advances in Building Energy Research*, vol. 16, no. 1, pp. 1–26, 2020.

[15] L. Xu, R. Cheng, and J. Yang, "A new MPPT technique for fast and efficient tracking under fast varying solar irradiation and load resistance," *International Journal of Photoenergy*, vol. 2020, Article ID 6535372, 18 pages, 2020.

[16] O. Tremblay and L.-A. Dessaint, "Experimental validation of a battery dynamic model for EV applications," *World Electric Vehicle Journal*, vol. 3, 2009.